Doctoral Dissertation

Numerical Simulation of α/γ Phase Fraction in Duplex Stainless Steel Welds

Dong–Cho Kim

June 2021

Division of Materials & Manufacturing Science,
Graduate School of Engineering,
Osaka University

Contents

Chapter 1 Introduction

Duplex stainless steels (DSSs) have various cracks and phase transformation problems during welding. The solidification mode of the DSS is F mode, which is not a big problem because it exhibits good hot cracking susceptibility. It is comparable to FA solidification mode, which exhibits the best hot cracking susceptibility. However, during fusion welding, the weldment is exposed to a welding heat cycle that affects the α/γ phase ratio, resulting in an impaired phase and intermetallic compounds, such as Cr–carbide and nitride, and sigma (σ), and chi (χ) phases get easily precipitate. Consequently, the mechanical properties of the material are deteriorated and the susceptibility to local corrosion is significantly increased.

Therefore, it is necessary to predict and control the α/γ phase transformation in DSS welding.

In this study, we introduced a prediction method through experimental review and phase–field (theoretical) simulation based on kinetics for α/γ phase transformation. Besides, the ultimate goal is to predict the amount of γ in the multi–pass welds in a complete simulation using the phase–field method.

Fig. 1.1 shows the overall flow information for the prediction and control of the phase transformation phenomenon of the DSS welds. Chapter 1 is introduction and Chapter 2 is review of weldability of stainless steels.

In Chapter 3, an equation was derived experimentally based on the kinetics, and the relationship between the temperature dependence of the rate constant for precipitation and dissolution phenomena was revealed. The finite–element analysis model for predicting the γ amount in multi–pass welds was constructed using Quick–welder software (Research Center of Computational Mechanics, Japan). To verify the validity of the calculated results, the actual welds were analyzed. It was confirmed that there was a good correlation between the calculated value and the measured value, and the prediction method used in this study was valid.

In Chapter 4, the phase–field simulation of precipitation and dissolution phenomena was constructed by assuming a multi–component DSS as the Fe–Cr–Ni ternary system. Through the established phase–field simulation, the calculation results for the precipitation and dissolution phenomena of the γ phase were derived, and the relationship between the temperature dependence of the rate constant was revealed. The necessity of introducing a correction factor according to the difference between the ternary system and the multi–component system was investigated in Chapter 5.

In Chapter 5, the introduction of correction factors was reviewed by comparing the results of the temperature dependence of the rate constant for precipitation and dissolution phenomena derived from the phase–field method with the experimental values in Chapter 3. there was a difference in the experimental and calculated values; however, the trend of the values was similar tendency, a correction factor was introduced. The temperature dependence of the rate constant was re–derived through the introduced correction factor, and the result was compared with the experimental value. Besides, to evaluate the applicability of the phase–field method established in this study to other steels, we investigated DSSs with different chemical

compositions.

In Chapter 6, the numerical study was conducted to predict the amount of γ in multi–pass welds using the rate constants for precipitation and dissolution phenomena derived from Chapters 3 (experimental values) and Chapters 4 and 5 (calculated values). In the case of the α/γ phase transformation behavior of the multi–pass welds, it was found that there was a very good correlation between the experimental values and the calculated values. This overcame the limitations that must be derived experimentally based on kinetics depending on the type of steel, and it became possible to semi–quantitative predict the amount of γ of a multi–pass welds using the phase–field method constructed in this study.

In Chapter 7, a microstructure improvement welding process was newly proposed. Since the final welding pass of the multi–pass welds did not receive the heat effect of the subsequent pass, the precipitation of the γ amount was insufficient. So, the microstructure improvement welding process was performed to recover this. The thermal history according to the distance to perform reheat bead welding was derived using computer simulation. The optimal conditions for the microstructure improvement welding process were derived using the derived thermal history and rate constant (experimental values, calculated values). By constructing reheat bead welding under optimized conditions, the amount of γ phase in the final pass was effectively recovered.

Finally, Chapter 8 is the summarized conclusions of this study.

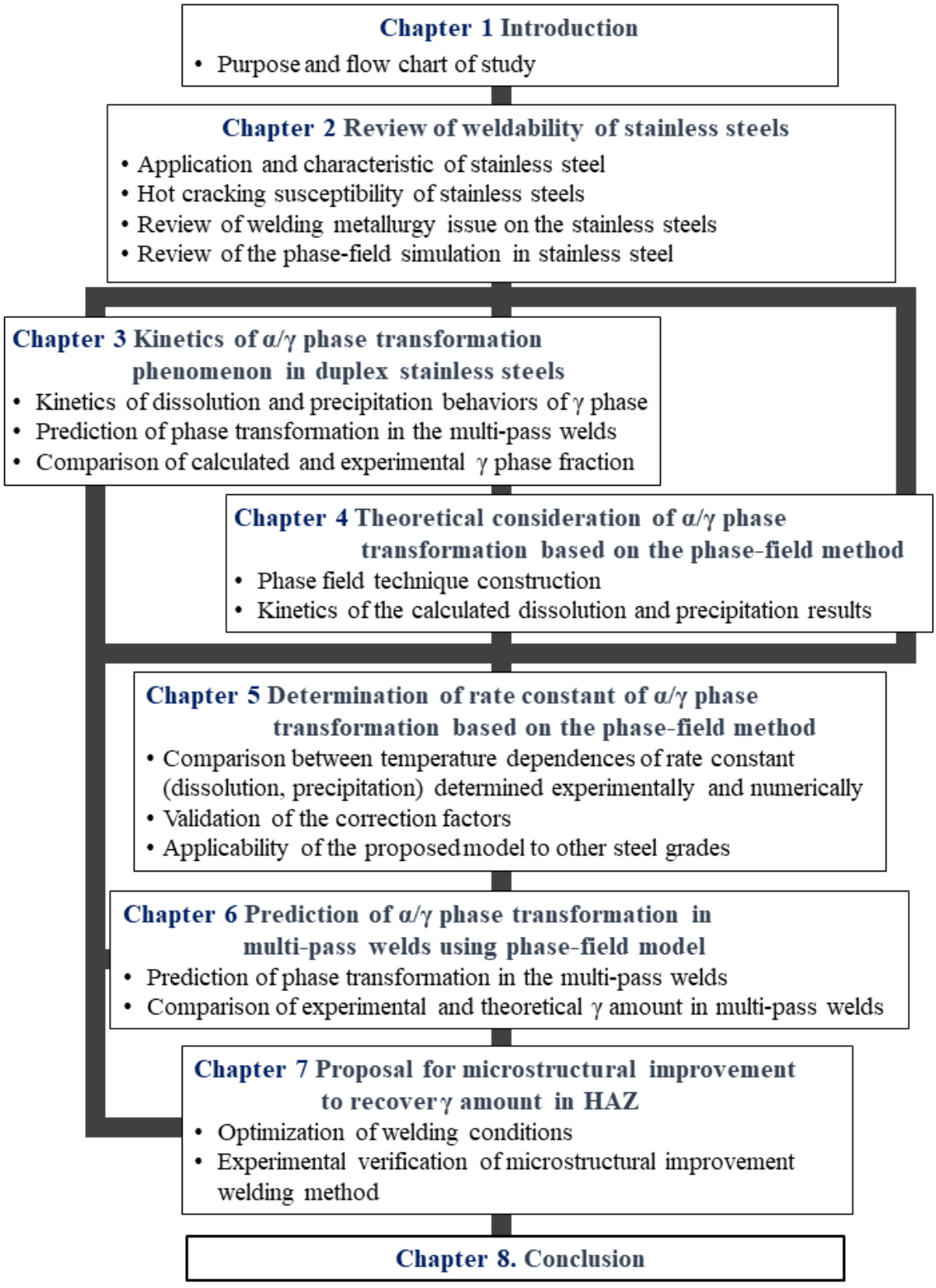

Fig. 1.1 Flow chart of study.

Chapter 2. Review of weldability of stainless steels

2.1 Application and characteristic of stainless steel

Fe–based alloys with a minimum Cr content of 10.5 % are referred to as stainless steel [1].

Cr reacts with oxygen in the air to form a thin passive layer of Cr–rich oxide on the surface, protecting the base metal from corrosion (Fig. 2.1). Resistance to corrosion in high temperature and reductive atmospheres may vary depending on the change in the crystallographic structures due to the addition of an alloying element. Stainless steels can be classified into five major categories based on the structure: austenitic, ferritic, martensitic, duplex (austenite and ferrite), and precipitation hardening [2].

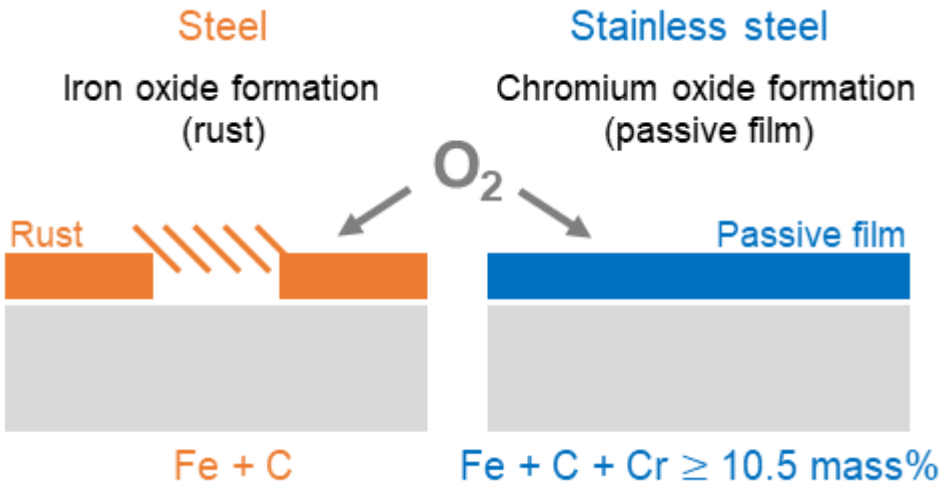

Fig. 2.1 Surface reaction in steel and stainless steel [3].

The ferritic stainless steels predominantly consist of Fe and Cr and they share the same body–centered cubic (bcc) structure as pure Fe. Ferritic stainless steel is resistant to corrosion and has little Ni content, so it is inexpensive and is often used in industrial applications. Exhaust pipes for the automobile industry are one common application [4]. By adding C to the Fe–Cr system martensitic stainless steels are obtained. Martensitic stainless steels are resistant to corrosion and are inexpensive due to its low Ni content. The presence of minor elements, especially C, can significantly displace the boundaries of the austenite and ferrite ranges. The hardness and moderate corrosion resistance of martensitic stainless steels make them suitable for applications such as knives and razor blades [5]. The austenitic stainless steels usually contain Ni in addition to Fe and Cr, which stabilizes the face–centered cubic (fcc) austenite structure at room temperature. When Ni (fcc) is added to the Fe–Cr alloy, the range of austenite (fcc) is widened and stability at low temperatures is increased [6]. Ni can be replaced to some extent by other austenite stabilizing elements such as Mn. The austenitic stainless steels have higher corrosion resistance compared to ferritic and martensitic stainless steels, so they are commonly used in the chemical industry. Other common applications are kitchen appliances.

Austenitic steels that combine excellent formability and corrosion resistance are useful for these applications [5]. The duplex stainless steels (DSSs) consists of austenite and ferrite.

Combining some of the good properties of the two phases, it has higher stress corrosion resistance and yield strength than austenitic stainless steel and has better ductility and toughness than ferritic stainless steel. These properties make the duplex stainless steels (DSSs) attractive for load–bearing applications in corrosive atmospheres, e.g. in the off–shore industry [2]. The fifth grade of stainless steel is a precipitation hardening alloy. Depending on their structure, they can be divided into three subgroups (austenite, martensite or semi–austenite). Precipitation hardened alloys improve the strength of the basic structure by forming precipitates during aging.

However, because precipitation hardening alloys are expensive, they are mainly used for special applications in high–tech industries [2]. Various problems arise during the manufacturing process such as stainless steel welding with these advantages. When welding stainless steel, hot cracking occurs frequently, so whether or not hot cracking occurs can influence the characteristics of the welds [7]. Besides, due to the influence of the thermal cycle during welding, the phase ratio may change and intermetallic compounds such as Cr–carbide, nitride, and sigma (σ) may be generated [8]. Therefore, understanding the basic mechanism of hot cracking and the phase transformation phenomenon is most important.

2.2 Hot cracking susceptibility of stainless steels

2.2.1 Hot cracking theories

Hot cracking is intergranular or interdendritic material imperfecti–ons, evolving and growing in a weld pool near zone during the execution of a fusion welding process or/and occurs in reheated weld metal during multi–pass welding. It can be divided into weld metal cracks (SC) and heat–affected zone cracks (LC) depending on the location and size of the occurrence, and this is also called "microcracking or HAZ cracking". Ductility dip cracks (DDC) are hot cracking that occurs due to a decrease in the ductility of a solid material within a temperature range somewhat lower than that of solidification cracking and liquation cracking [9]. Hemsworth et al. [10] presented the classification of hot cracking as shown in Fig 2.2. It can be divided into solidification cracks and liquation cracks (Type I) that occur in the solidification section near the liquidus temperature, and DDC (Type II) that occur before and after the recrystallization temperature after the end of solidification. The effect

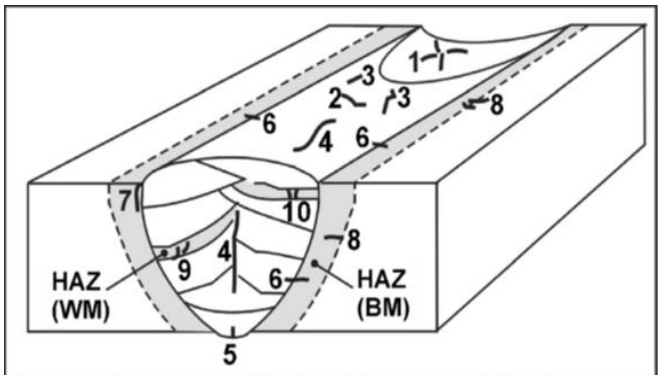

1. Crater crack (SC)	Type 1A	6. Transverse cravk (LC)	Type 1B
2. Transverse crack (SC)	Type 1A	7. Edge crack (LC)	Type 1B
3. Longitudinal Crack (SC)	Type 1A	8. DDC in HAZ	Type 2A
4. Centre crack (SC) in longitudinal section and in transverse section	Type 1A	9. DDC in HAZ (multi-run weld)	Type 2C
5. Root crack (SC)	Type 1A	10. DDC in HAZ (single-run weld)	Type 2B

Fig. 2.2 Designation of hot cracks according to their location in the weld metal (WM) or in the heat–affected zone (HAZ) following [10].

of welding metallurgy during the solidification process and the phenomenological approach to hot cracking were investigated by researchers such as Wolf et al. [11], Lippold et al. [2], and Böllinghaus et al [12–14]. From Fig. 2.3, it can be seen that the hot cracking resistance is related to the welding process and welding parameters. Therefore, hot cracking behavior can be directly influenced by the welding process and welding parameters [15–17].

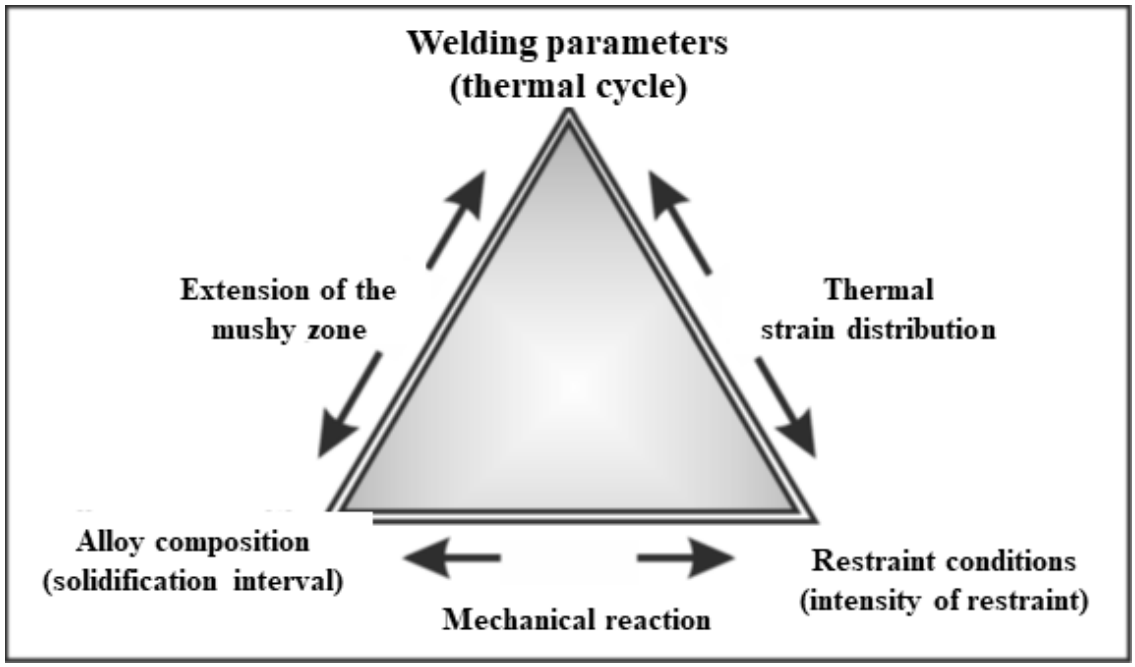

Fig. 2.3 Variables influencing hot cracking [18].

2.2.2 Understanding the solidification behavior of stainless steel

To understand the solidification behavior of stainless steel welds, a study of the Fe–Cr–Ni phase diagram is required. Fig. 2.4 shows the liquidus and solidus projections of the Fe–Cr–Ni system along with the constituent binaries [19]. Fe–Cr system is isomorphous down to temperatures well below the solidification range. The Cr–Ni system exhibits eutectic at 1618 K and 49 mass % Ni. In the Fe–Ni system, the δ–ferrite phase on the Fe side forms a short peritectic loop, after which it is completely soluble to 100 mass % Ni. Thus, in the Fe–Cr–Ni ternary system, the liquidus projection

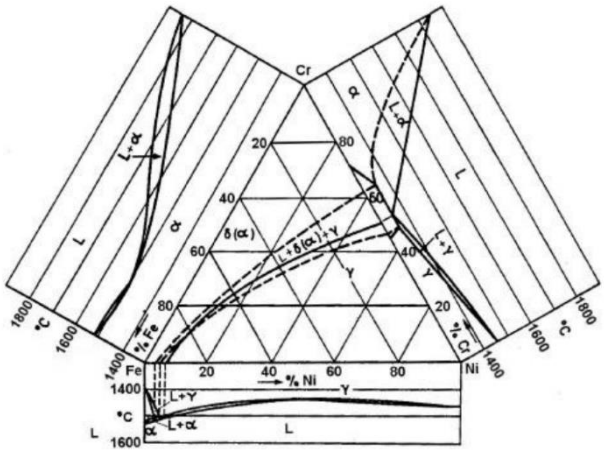

Fig. 2.4 Liquidus and solidus projections of the Fe–Cr–Ni system shown along with the constituent binaries [19].

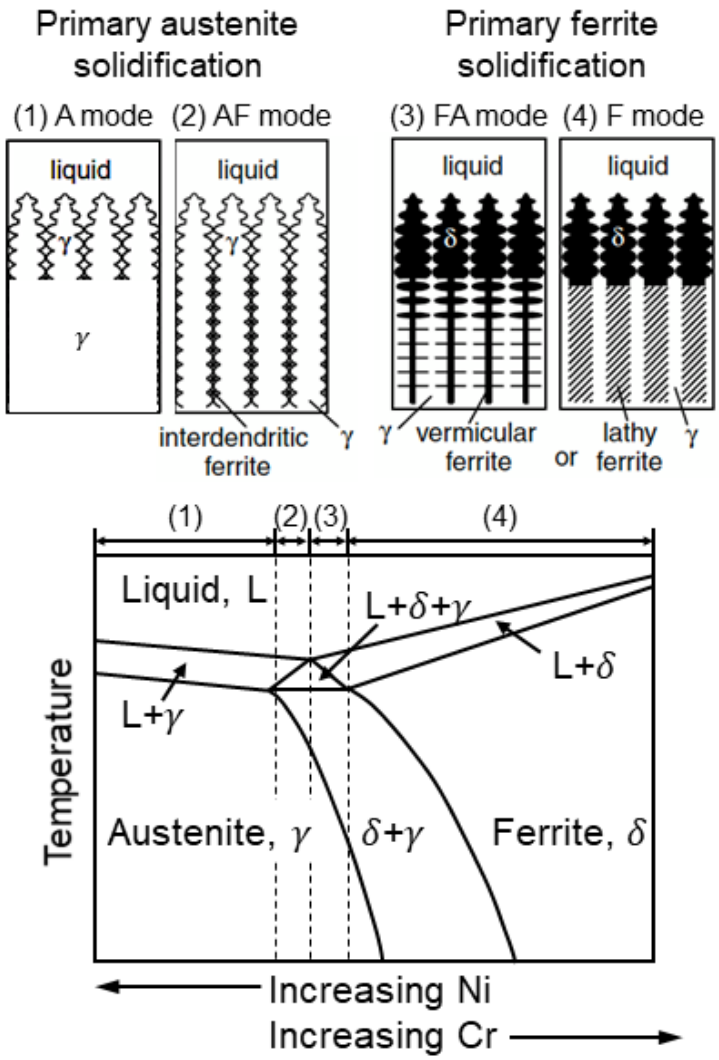

Fig. 2.5 Schematic diagram of solidification mode in Fe–Cr–Ni welds [20].

starts with the peritectic reaction for the Fe–Ni system ($\delta + L \leftrightarrow \gamma$) and moves to the eutectic reaction for ($L \leftrightarrow \delta + \gamma$). The initial solidification phase is determined by the position of the alloy relative to the liquid surface, which under equilibrium conditions proceeds towards the eutectic/peritectic before solidification is complete. Most of the widely used stainless steel compositions arise from the Fe–rich side of the ternary system, with 50 to 70 % by mass % Fe.

The ternary 70 mass % Fe isopleth shown in Fig. 2.5 is typically used to identify the primary solidification phase or solidification mode for various compositions. In general, four modes are considered: austenitic (A), austenitic–ferritic or primary austenitic (AF), ferritic–austenitic or primary ferritic (FA) and ferritic (F). The approximate compositional range and microstructure morphology in which these modes occur are schematically shown in Fig. 2.5. Koseki [24] investigated the segregation of major alloying elements in stainless steel welding. Alloys that solidify in A mode remain unchanged at low temperatures, and alloys that solidify with AF form some eutectic ferrite. In fully austenitic stainless steels, the interdendritic area is slightly concentrated in both Cr and Ni, whereas in AF mode weld metals, a significant concentration of Cr and depletion of Ni occurs in the interdendritic area. In the Cr–rich and Ni–depleted

regions, ferrite nuclei appear as non–equilibrium stages. For compositions that solidify in FA and F modes, it can pass through the ferrite–austenite two–phase region and re–enter the single–phase austenite field. If the ratio of Cr/Ni is higher, the equilibrium structure at room temperature can hold a significant amount of δ–ferrite as in duplex stainless steels (DSSs). In Fe–Cr–Ni alloys, the transition from peritectic to eutectic reaction occurs at 17.2 mass % Cr and 11.9 mass % Ni [21]. In equilibrium conditions, the peritectic reaction occurs only with Fe content above 75 mass %, but quenching experiments have shown that even at higher alloy content, the peritectic reaction can occur, possibly due to segregation [22]. Solidification of alloys such as Type 304 tends to be peritectic, while higher alloy grades undergo eutectic type reactions. The transfer moves to a lower Cr level by adding Mo [21]. The occurrence of a peritectic reaction is important because the heterogeneous grain boundaries formed at the liquid junction of the peritectic system can delay wetting and crack formation [23].

2.2.3 Solidification of stainless steel welds

Segregation changes the product phase and its composition under the non–equilibrium solidification conditions during welding. The segregation of major alloying elements in stainless steel welds has been investigated by Koseki [24]. For fully austenitic stainless steels, the interdendritic region is slightly concentrated in both Cr and Ni, whereas in AF mode weld metals, a significant concentration of Cr and depletion of Ni occurs in the interdendritic region.

In addition, for FA and F mode solidification, the dendrites core is significantly enriched in Cr and depleted of Ni. The segregation of Cr to ferrite and Ni to austenite during solidification plays an important role in stabilizing ferrite during subsequent solid–state transformation. An important aspect of weld solidification is the effect of solidification mechanics on the formed phase. In stainless steel, the relatively small difference in the thermodynamic stability of the two–phase (δ and γ) near the eutectic allows non–equilibrium solidification into the metastable phase obtained by extrapolating the equilibrium phase boundary [25]. Therefore, the weld microstructure of stainless steel is highly dependent on the cooling rate and kinetic factors such as epitaxy, except for equilibrium stability considerations [26]. In FA or F mode weld metals, 70–100 % δ–ferrite may be formed at the end of solidification, which transforms almost completely to austenite in the solid–state on cooling. Ferrite retention of up to 15–20 % in austenitic stainless steel weld metals is supported by two factors: the Cr and Ni segregation patterns after solidification and the prevention of Cr and Ni diffusion through rapid cooling during welding. There are many studies on the prediction of δ–ferrite in stainless steel weld metals. When predicting ferrite, the influence of various alloying elements and the need to take into account the prevailing non–equilibrium conditions during welding gave rise to the concept of Cr_{eq} and Ni_{eq}. The evolution of the construction diagram for ferrite prediction was reviewed by Olson [27]. While considering cracking susceptibility, in addition to room temperature ferrite content, information about the solidification mode is more relevant. Hammar and Svensson performed quenching experiments on many alloys at melting temperatures, freezing the predominant structure immediately after solidification [28]. They just developed the

following equivalent formula for solidification prediction. Cr_{eq} = Cr +1.37Mo + 1.5Si + 2Nb + 3Ti and Ni_{eq} = Ni + 22C + 14.2Ni + 0.31Mn + Cu. According to this formula, the transition from AF mode to FA mode occurs at a Cr_{eq}/Ni_{eq} ratio of 1.55. In addition, some studies satisfactorily predict the solidification mode of the above equivalents and based on this, solidification paths for a large number of compositions were determined [29,30]. Siewert [31] proposed a new ferrite diagram that predicted ferrite up to 100FN and thus covered the complete range of austenitic and duplex stainless steels. Fig. 2.6 shows the result of a diagram known as the WRC–92 diagram [32]. This diagram is better than the accuracy of the DeLong diagram because the bias due to higher coefficients for N has been eliminated. In addition, since the solidification mode boundary is included, it can be judged to be more important from the viewpoint of cracking. Recent theoretical approaches to ferrite prediction using thermodynamic phase stability and using artificial neural networks have led to greater improvements in the accuracy of ferrite prediction over that offered by the WRC–92 diagram [33,34].

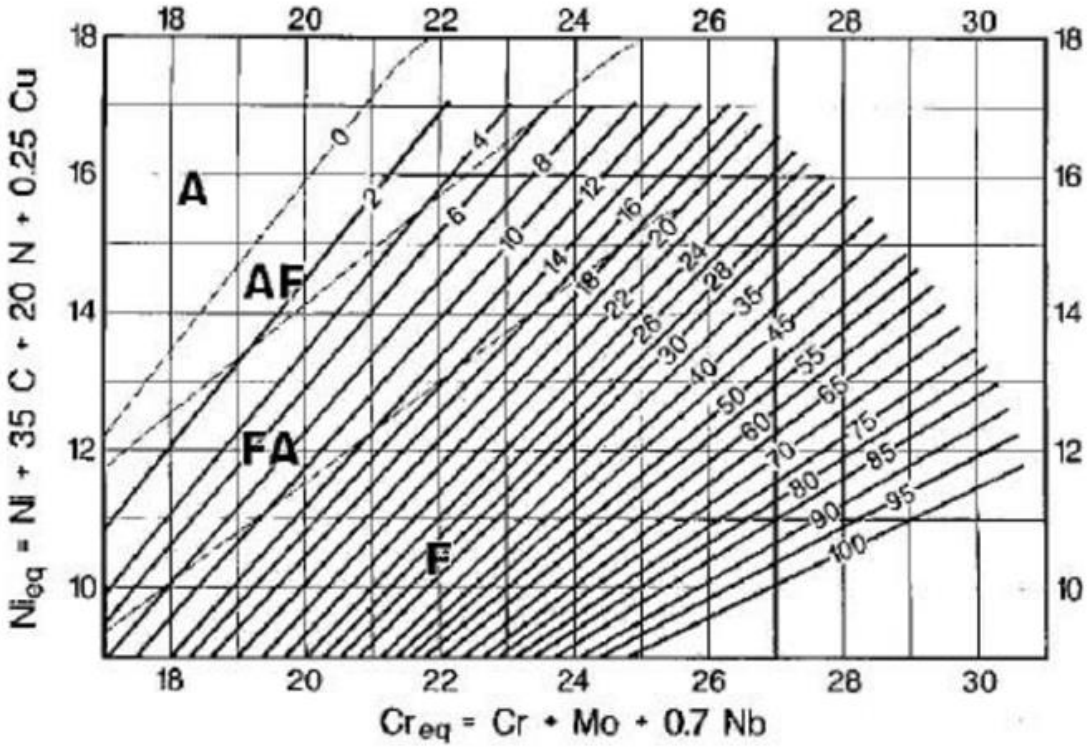

Fig 2.6 The WRC–92 constitution diagram for weld metal ferrite, including solidification mode boundaries [32].

2.2.4 Forms of solidification cracking

Weld solidification cracking occurs preferentially in the fusion zone at the end of solidification, along the solidification grain boundary (SGB), and sometimes along the sub–grain boundary (SSGB) of the fusion zone. Weld solidification cracking occurs preferentially in the fusion zone at the end of solidification, along the SGB, and sometimes along the sub–grain boundary (SSGB) of the fusion zone. At least three different boundary types can be observed metallographically, as shown schematically in Fig. 2.7. Since SGB is caused by the intersection of packets or groups of sub–particles, it is a direct result of competitive growth that occurs along the trailing edge of the weld pool. Because each sub–grains packet has a different growth direction and orientation, the crossing direction becomes a boundary with high angular misorientation, which is often referred to as a "high–angle" grain boundary. The SGB also exhibits a compositional component resulting from solute redistribution during solidification.

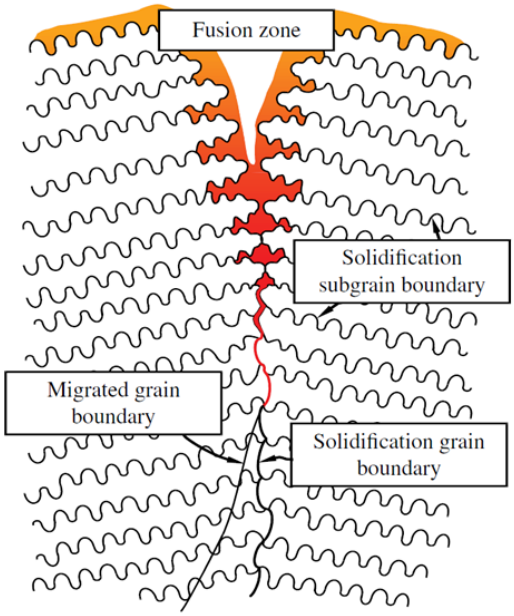

Fig 2.7 Schematic representation of the boundaries in single–phase weld metals [35].

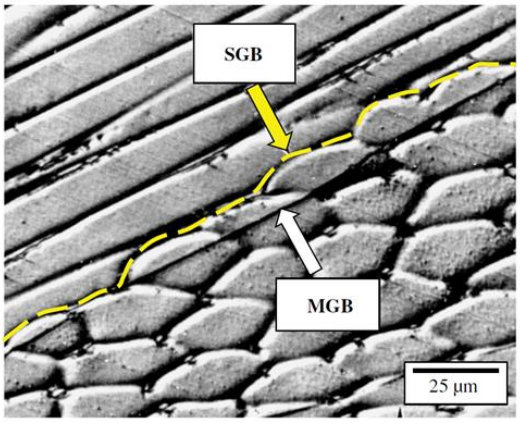

Fig 2.8 Examples of boundaries in the fusion zone of a fully austenitic (fcc) stainless steel [35].

This compositional partitioning can form a low melting liquid film along the SGBs at the end of solidification, an example of which is shown in Fig. 2.8. SSGB generally exist as cells or dendrites, and the boundary separating adjacent sub–grains is called SSGB, and represents the finest structure that can be resolved with an optical microscope. Solute redistribution that creates this compositional gradient at the SSGB is dictated by microscopic solute redistribution, as described in the SGB. An example of a solidification crack in a martensitic stainless steel (Alloy HT9) is shown in Fig 2.9. Note that there is evidence of liquid films along the SGBs in this weld metal. Electron probe microanalysis shows strong segregation of alloying elements Cr and Mo to these boundaries, along with the impurity element P. Based on the previous above, methods for eliminating or reducing susceptibility to solidification cracking are somewhat apparent. Control of solidification behavior, when possible, is always desirable. With steels, solidification as ferrite (bcc crystal structure) will

result in an improvement in cracking resistance relative to solidification as austenite (fcc).

When that option is not available, such as with some austenitic stainless steels, reduction of impurity elements (S, P, and C) is helpful. The effects of solidification mode and composition on hot cracking will be discussed in detail in subsequent sections.

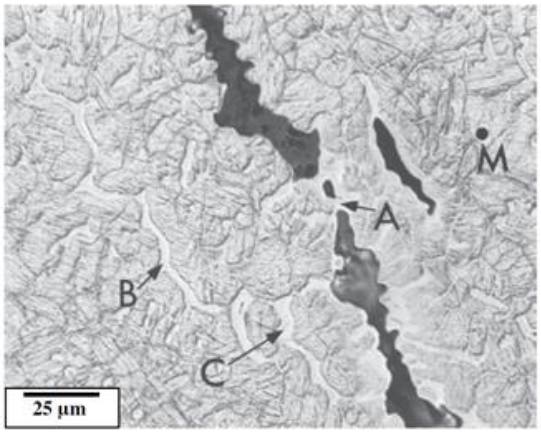

(a) Region of crack.

Element	A	B	C	M
Cr	18.2	17.0	17.2	12.0
Mo	2.9	2.5	2.4	0.9
Ni	0.5	0.5	0.4	0.4
Mn	0.8	0.7	0.8	0.6
V	0.7	0.6	0.6	0.3
W	0.7	0.7	0.7	0.4
S	0.04	0.08	0.05	0.04
P	0.24	0.27	0.19	0.02

(b) Composition (in wt %) along solidification grain boundaries.

Fig 2.9 Solidification cracking in a martensitic stainless steel.

2.2.5 Effect of δ–ferrite and solidification mode on solidification cracking

There are studies on the effects of various *δ*–ferrite contents on the cracking of stainless steel [36]. For the fully austenitic compositions, it was found that the cracking susceptibility was high, but the specimens with 5–30 % ferrite were quite resistant to cracking. In general, since harmful impurities such as S and P are more soluble in *δ*–ferrite than austenite (Table 2.1), the presence of significant amounts of *δ*–ferrite can reduce the concentration of these impurities at the austenite grain boundary and the damaging effects on solidification cracks [38–43]. In addition, it is believed that when *δ*–ferrite is the first solidification step, the substantial boundary region between *δ*–ferrite and austenite acts as a sink for S and P. When ferrite content was increased further, the cracking sensitivity was again increased. Masumoto [44] found that the FA/F solidification mode was essential for reducing cracking rather than residual ferrite content after welding. In addition, various investigations were conducted using the hot cracking test for various compositions.

Table 2.1 Solubility of sulfur and phosphorus in ferrite and austenite (mass %) [37].

	In δ–Ferrite	In Austenite
Sulfur	0.18	0.05
Phosphorus	2.8	0.25

Kujanpaa [45] plotted crack data from the literature on a map of the P + S vs. Cr_{eq}/Ni_{eq} ratio. In this map, they displayed crack data from several studies, as shown in Fig. 2.10. They found that highly susceptible compositions lay bounded by a curve with a lower limit of 0.01–0.015 mass % P + S, and limited on the Cr_{eq}/Ni_{eq} axis by a value of 1.5, up to which a primary austenitic solidification mode exists. Thus, compositions with Cr_{eq}/Ni_{eq} greater than 1.5 or with P + S < 0.01 mass % were 'not susceptible'. However, when the Cr_{eq}/Ni_{eq} ratio was less than 1.5, the cracking tendency increased sharply, unless the P + S content was less than 0.01 mass %.

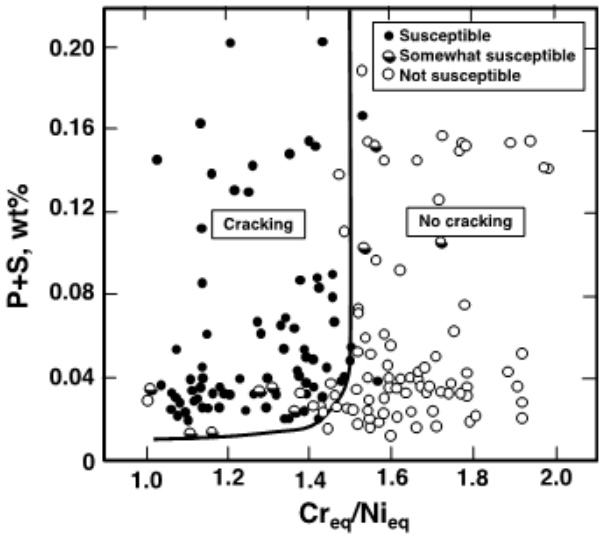

Fig 2.10 Solidification cracking behavior in austenitic stainless steel welds as a function of Schaeffler Cr_{eq}/Ni_{eq} ratio and P+S levels [17].

Recently, it became possible to theoretically predict the solidification crack susceptibility (solidification brittle temperature range, BTR) by calculating the solid–liquid coexistence temperature range based on the supercooling and the solidification segregation phenomenon.

A model considering the solidification mode and solidification form was constructed, and at the same time, the effects of solidification mode solidification form and δ–ferrite amount on BTR were revealed by numerical analysis [46,47]. Meanwhile, Lundin modified the diagram and shown in Fig. 2.11 to represent longitudinal varestraint test data on 3mm thick specimens [48]. Lundin determined the composition based on total crack length (TCL) in a varestraint test at 4 % strain. 'highly susceptible' for TCL> 2.5mm, 'susceptible' for TCL between 1.5–2.5mm, 'No susceptible' for TCL less than 1.5mm. The equivalent formula used here is the formula of Hammar and Svensson [28]. When the data were plotted on this diagram, the mixed solidification mode FA region, in which Cr_{eq}/Ni_{eq} ratio is 1.5–1.6, was identified as having a cracking susceptibility intermediate between that of the A mode and FA or F mode materials.

In this region, cracking was sensitive to P + S levels. FA/F mode materials with Cr_{eq}/Ni_{eq} above 1.6 are very resistant to impurity elements even above 0.04 mass %, whereas in A mode materials (Cr_{eq}/Ni_{eq} < 1.5), cracking is high when P + S is greater than about 0.015 mass %.

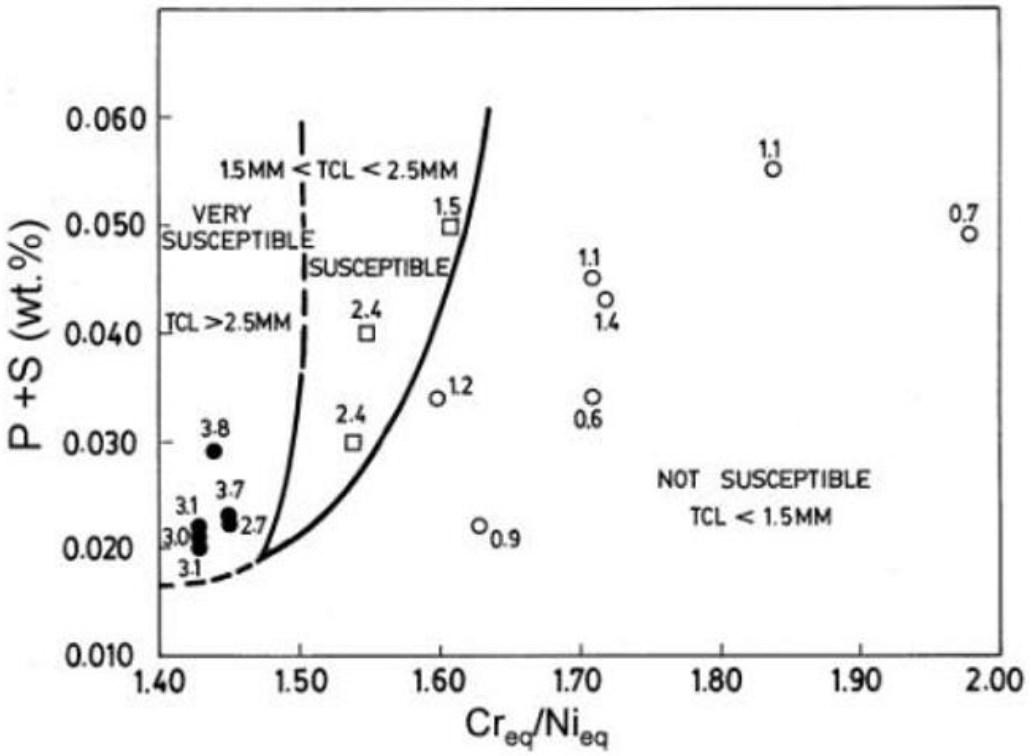

Fig 2.11 Solidification cracking behavior in austenitic stainless steel welds as a function of Hammar–Svensson Cr_{eq}/Ni_{eq} ratio and P+S levels [17].

2.2.6 Effects of sulfur and phosphorus

After examining the influence of several factors on cracking sensitivity, it was found that S, P, B, Nb, Ti, and Si were the most harmful [39,49]. These elements form a low–melting eutectics with Fe, Cr, or Ni as indicated in Table 2.2, it is strongly divided into liquid and has low solubility in solidified steel. Low eutectic temperatures can lead to a lower solidus temperature due to eutectic formation. S is known as an impurity that adversely affects stainless steel welding due to the formation of a low–melting sulfide film along the interdendritic and grain boundary regions. S is virtually insoluble in all three major components of stainless steel, viz. Fe, Cr, and Ni. While austenite solidifies, S is strongly rejected as a liquid, which quickly lowers the melting point of the interdendritic liquid. Therefore, even with a very low austenite content (< 0.005 mass %), the potential to form a low–melting point process is still strong [52].

On the other hand, δ–ferrite exhibits higher solubility for elements such as S and P. Solidification in FA mode is known to increase resistance to S content by up to 0.05 mass % without hot cracking. Lundin [53] investigated the weldability of stainless steel and found that when the ferritic solidification mode was maintained, satisfactory weldability was exhibited even if the S content was 0.35 mass %. On the other hand, in the case of the type 310 steel solidified in the austenitic mode, it was confirmed that the sulfide film was present even at 0.005 mass % S and the brittle temperature range was increased with P. Kujanpaa [54] found 2000 times the S concentration in HAZ cracks in type 310 stainless steel. Therefore, the harmful role of S in hot cracking is clear. In the case of P, which forms a low–melting eutectic with Fe,

Cr, and Ni, as in S, the maximum solubility of P in austenite at the eutectic point (1423K) with Fe is 0.25 mass % and that in ferrite is 2.8 mass % at 1323 K. Brooks [55] has found that P is particularly harmful in fully austenitic stainless steels because it has a strong tendency to spread into a liquid film. It has also been found that even at high temperatures, the low diffusivity of P in both austenite and ferrite phases virtually impedes homogenization [19].

Due to the harmful effects of S and P, work has been done to add other factors that hinder the impact. To reduce the effect of P and S, there is a study result of reduced cracking by forming a molten MnS–γ eutectic higher than FeS through the addition of Mn [49]. In addition, research results are showing that the addition of lanthanum and other rare earth is very effective in binding P and S as stable compounds [56].

Table 2.2 Partition coefficients of elements promoting hot cracking in austenite and ferrite, constitution and melting points of possible low–melting phases [19,50,51].

Constituent	Temp. (K)	Partition coefficient		Low–melting phases	
		δ	γ	Structure	Melting points (K)
Sulfur	1638	0.091	0.035	Eutectic Fe–FeS	1261
				Eutectic Ni–NiS	903
phosphorus	1523	0.23	0.13	Eutectic Fe–Fe_3P	1321
				Eutectic Ni–Ni_3P	1148
Boron	1654	0.125	0.001	Eutectic Fe–Fe_2B	1450
				Eutectic Ni–Ni_2B	1413
				Eutectic $(Fe,Cr)_2B$–γ	1453
Niobium	1573	0.28	–	Eutectic Fe–Fe_2Nb	1643
				Eutectic NbC–γ	1588
				Nb–Ni rich phase	1433
Titanium	1573	0.57	–	Eutectic Fe–Fe_2Ti	1563
				Eutectic TiC–γ	1593
Silicon	1573	0.77	0.52	Eutectic Fe–Fe_2Si	1485
				Eutectic NiSi–Ni_3Si_2	1237
				NiSi–γ	1269

2.2.7 Effects of nitrogen on solidification cracking

Several studies point to the fact that N increases hot cracking by changing the solidification mode from ferrite to austenite [57–59]. Matsuda [59] investigated cracking in type 304 weld metal with N addition and concluded that the addition of N reduced the amount of primary ferrite and the residual ferrite content as well. It was also found that increasing amounts of P and S at the grain boundaries with the addition of N promote hot cracking. Hot cracking is characterized by a brittle temperature range (BTR), which increases with N content, reaching a value similar to fully austenitic type 310. On the other hand, studies on 316 weld metals did not find any detrimental effects [60]. Zhitnikov [61] reported that if the ferrite content is kept constant, the increase in N levels is not detrimental to hot cracking resistance and may have some beneficial effect, but no information is provided on the P and S content. The effect of N

in weld metals containing ferrite (or ferritic solidification mode) seems to be related to the level of impurity elements.

Thus, N can be harmful in high–impurity weld metals (> 0.04 mass %), but in relatively pure compositions it can have a neutral or beneficial effect. While stainless steels with an addition of up to 0.2 mass % N reported beneficial effects [61], Arata [57] found that N content up to 0.16 mass % did not significantly affect the hot cracking of type 310. In recent work, N additions enhanced cracking in fully austenitic 316L weld metal with high S (0.012 mass %) but did not increase cracking in low S (0.001 mass %) weld metal. The P levels in these steels are 0.035 mass % and 0.031 mass % respectively. It was concluded in this study that at high S levels, N acts synergistically with S to increase cracking [17].

2.3 Review of welding metallurgy issue on the stainless steels

Stainless steels are a class of Fe–base alloys that are noted for their high corrosion and oxidation resistance. They usually contain from 12 to 27 mass % Cr and 1 to 2 mass % Mn by weight, with the addition of Ni in some grades. A small amount of C is also present, either deliberately added or as an unavoidable impurity. Stainless steel can be classified into the main categories of ferritic, martensitic, austenitic, and duplex based on its structure [2]. This chapter was discussed the current status of research on the phase transformation phenomenon of stainless steel and the problems that arise during welding.

2.3.1 Ferritic stainless steels

Ferritic stainless steels are generally considered to be less weldable than austenitic stainless steels while having the advantage of low cost and excellent corrosion resistance to stress corrosion cracking. These are composed mainly of a bcc phase. As shown in Fig. 2.12(a), Cr (bcc) stabilizes α–Fe (bcc) and its high–temperature counterpart δ–Fe (bcc) to form a closed γ loop [62]. It can be said that ferritic stainless steels have metallurgical properties similar to Fe–Cr alloys containing enough (about 12 mass % or more) Cr to remain outside the γ loop. They are essentially ferritic over the whole solid–state temperature range.

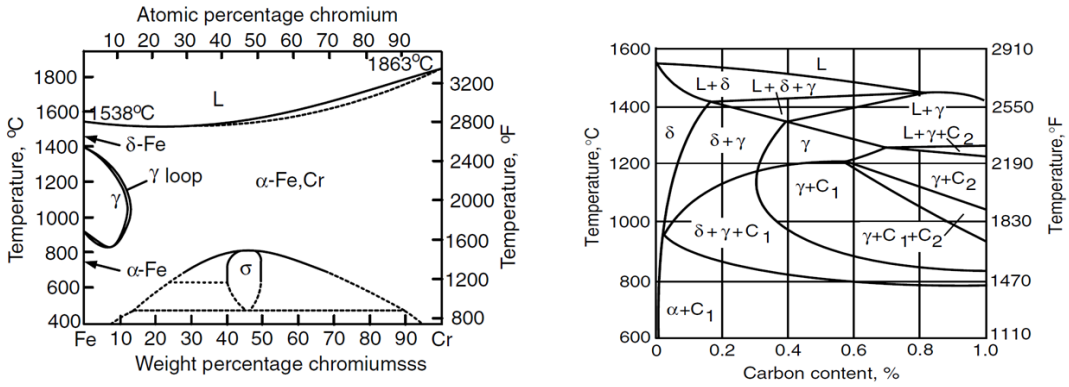

(a). (b).

Fig. 2.12 Phase diagrams: (a) Fe–C; (b) Fe–Cr–C phase diagram at 17 mass % Cr [62, 63].

Ferritic stainless steel generally has a Cr content of less than 27 mass % to prevent formation of a large amount of sigma (σ) phase. However, to prevent the formation of excessive amounts of brittle sigma (σ) phase, the maximum Cr content of ferritic stainless steels is generally kept below 27 mass %. The most commonly used ferritic stainless steel perhaps is the 430 type, which usually contains about 17 mass % Cr and 0.05–0.12 mass % C. Fig. 2.12(b) is a vertical section of the Fe–Cr–C phase diagram at 17 mass % Cr [63]. The sensitivity range of ferritic stainless steels is greater than 1198 K, and resistance to intergranular corrosion is restored by annealing in the range of 923–1088 K for approximately 10–60 min [64]. This is quite different from the sensitivity of austenitic stainless steels (not stabilized like 304). This temperature is essentially the opposite of austenitic stainless steels, and weld decay also occurs close to the weld metal, not as far away as is the case with austenitic stainless steels. In the case of corrosion protection, even though 430 stainless steel has a C content of 0.009 mass % C, it is still vulnerable to welding corrosion, and unlike austenitic stainless steel, a decrease in C content does not have much effect.

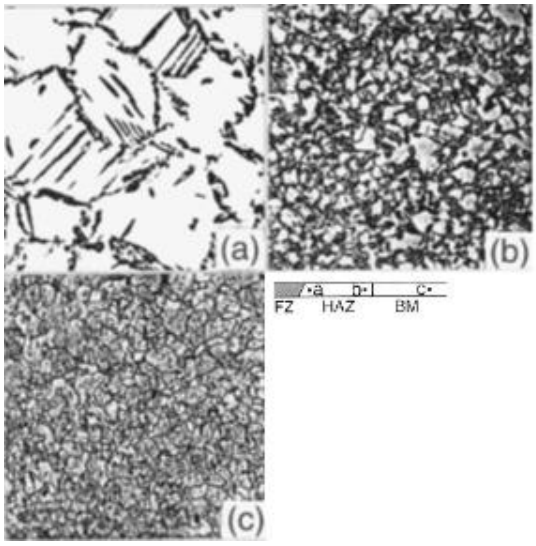

Fig. 2.13 Microstructure of 430 stainless steel: (a) near fusion boundary; (b) near base metal; (c) base metal [65].

However, the addition of Ti or Nb was found to help prevent corrosion [64]. Since the diffusion rates of C and Cr are much higher in ferrite (bcc) than in austenite (fcc), rapid cooling above 1198 K during welding does not inhibit the precipitation of Cr carbide at the grain boundaries of ferritic stainless steels. Likewise, unless the C content is extremely low (eg 0.002 mass % C in 446 stainless steel), lowering the C content cannot effectively prevent Cr carbide precipitation. According to Uhlig [64], post–weld annealing in the range of 923–1088 K helps to reset the uniform Cr composition to resist intergranular corrosion by promoting the diffusion of Cr atoms into Cr depleted regions adjacent to Cr carbide deposits. Fig. 2.13 shows the microstructure of 430 stainless steel in the base metal and the HAZ [65]. Position b (away from the fusion boundary) reaches the austenite formation ranges ($\delta + \gamma +$ C1 and $\delta + \gamma$) of the phase diagram (Fig. 2.12(b) at about 0.08 mass % C). Here, austenite is formed along the grain boundary and transforms into martensite through rapid cooling during welding (Fig. 2.13(b)).

Position a (near the fusion boundary) reached the δ–ferrite range and excessive grain growth occurred. During cooling, the formation of austenite begins, and large particles of needle–shaped austenite are formed due to the high cooling rate. During cooling to room temperature, the needle–shaped austenite turns into martensite. Because of excessive grain coarsening and formation of needlelike martensite at grain boundaries, the notch toughness of as–welded 430 stainless steel is poor. Post–weld heat treatment at 1073 K (martensite tempering) significantly

improves the notch toughness. Suppressing martensite formation by adding 0.5 mass % Ti or 1 mass % Nb also helps [63]. This is probably because both Ti and Nb increase the stability of δ–ferrite, thus suppressing the formation of austenite. Furthermore, as mentioned previously, they tend to form carbides at high temperatures. Therefore, the C content is reduced, and the tendency to form martensite decreases. Excessive grain growth can be avoided, of course, by using lower welding heat inputs. It has also been suggested that nitride and carbide formers such as B, Al, V, and Zr can be added to ferritic stainless steels to suppress grain growth during welding [66].

2.3.2 Martensitic stainless steels

Martensitic stainless steel is well known for its high strength and excellent corrosion resistance. The most commonly used are martensitic stainless steels with 13 mass % Cr containing more than 0.08 mass % C. Fig. 2.14 shows a vertical section of the Fe–Cr–C at 13 mass % Cr [63]. This diagram is somewhat similar to that shown in Fig. 2.12(b) at 17 mass % Cr, but the temperature and composition range of the austenite phase (γ) is much wider for the 13 mass % Cr steel. The hardness of martensitic stainless steels increases rather significantly with increasing C content.

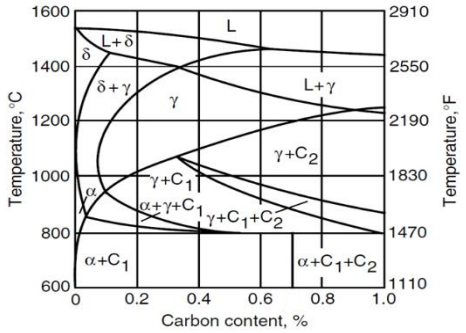

Fig. 2.14 Phase diagram of Fe–Cr–C phase diagram at 13 mass % Cr [63].

For 12 mass % Cr steel quenched from 1323 K, for instance, the hardness increases from 364 HV at 0.07 mass % C to 620 HV at 0.60 mass % C [63]. On the other hand, when H is present during welding, martensitic steel having a high C content is susceptible to under–bead cracking. Martensitic stainless steel with a C content of 0.25–0.3 mass % or more is generally difficult to weld. Under–bead cracking can still occur even if relatively low limits are applied during welding due to internal stresses induced by the volume increase associated with the austenite–martensite transformation

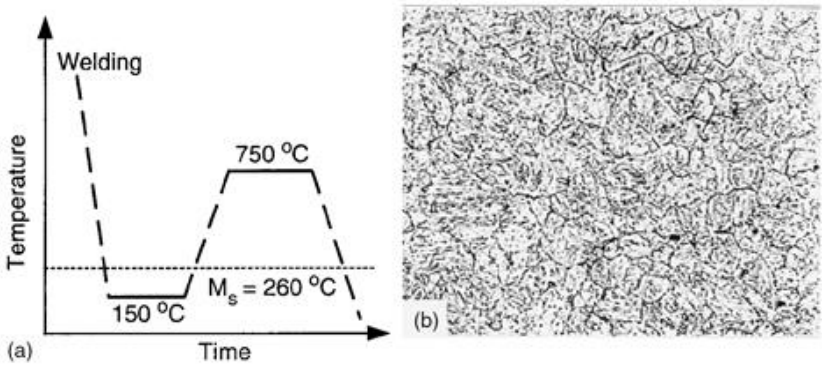

Fig. 2.15 Proper post–weld heat treatment and resultant microstructure of a 12 mass % Cr [63].

Tempering (873 to 1123 K) is usually used after preheating and welding to prevent under–bead cracking. Fig. 2.15 shows the post–weld heat treatment for a creep–resistant 12 mass % Cr steel (12 mass % Cr–0.2 mass % C–1 mass % Mo–0.4 mass % W–0.3 mass % V) and the resultant microstructure [63]. Upon the completion of welding, keep the welded part at 423 K to prevent cracking. After that, heat treatment at 1023 K for 4 h forms a tempered HAZ with a martensitic structure. Fig 2.16 shows a different post–weld heat treatment and the resultant microstructure [63]. It is recommended to keep the welding area at a temperature higher than M_S (573 K) to prevent martensite from forming after welding to avoid the possibility of under–bead cracking. However, during post–heat treatment at 1023 K, the unmodified austenite phase decomposes, and the microstructure of HAZ ferrites together with the agglomerated carbides settled at the grain boundaries, which is inferior to tempered martensite and breaks better.

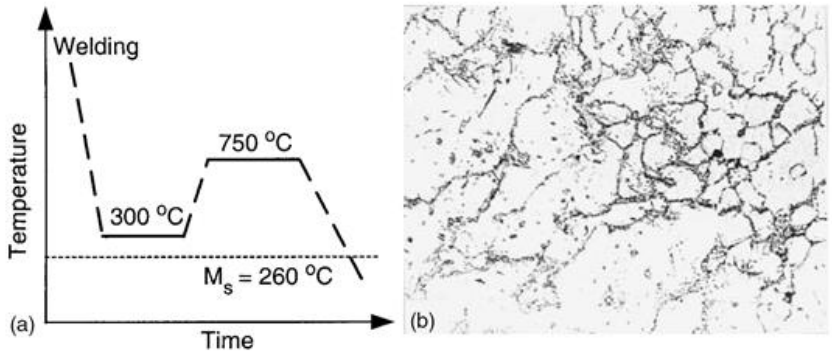

Fig. 2.16 Improper post–weld heat treatment and resultant microstructure of a 12 mass % Cr martensitic steel [63].

2.3.3 Austenitic stainless steels

Fig. 2.17 shows the phase diagram of Fe–Cr and Fe–Cr–Ni. When Ni (fcc) is added to the Fe–Cr alloy, the range of austenite (fcc) is broadened, and stability at low temperatures tends to increase [6]. Typical austenitic stainless steels contain a Cr content of at least 15 mass % and a sufficient Ni content, thus maintaining a stable austenite structure in the temperature range from 1373 K to room temperature without martensite formation [63]. The most commonly used stainless steel is 304 stainless steel also known as 18–8 stainless steel, because it consists of 18 mass % Cr and 8 mass % Ni.

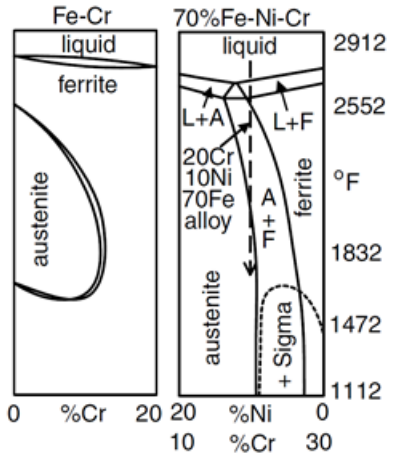

Fig. 2.17 Phase diagrams: (a) Fe–Cr; (b) Fe–Cr–Ni at 70 mass % Fe [6].

Fig. 2.18 shows the microstructure of a 0.05 mass % C 304 austenitic stainless steel in HAZ subjected to accelerated corrosion testing [67]. As can be seen from the results, the attack at the grain boundary is certain. In the case of austenitic stainless steel, sensitization occurs

due to the precipitation of Cr carbide at the grain boundary. HAZ of austenitic stainless steels containing more than about 0.05 mass % C may be susceptible to a form of intergranular corrosion called weld decay [68]. A schematic diagram of the Cr depletion area is shown in Fig. 2.19. These areas become anodes to the rest of the grain and are preferentially attacked by corrosive substances, causing intergranular corrosion.

Fig. 2.20 shows the solvus curves of $Cr_{23}C_6$ and TiC (and NbC) in 18 mass % Cr–8 mass % Ni stainless steel [69]. The precipitation temperature of carbides is about 873–1123 K for $Cr_{23}C_6$ and up to about 1373 K for TiC.

Cr carbide dissolves at temperatures above the solvus curve, but if cooled slowly, there is a possibility of reprecipitation of Cr carbide. However, at high cooling rates, the Cr carbide can become supersaturated with free C. The location of weld decay can be predicted through the schematic diagram of the thermal cycle during welding in Fig. 2.21. Weld decay does not occur at the peak temperature (fusion boundary) during welding, but at a shorter distance where the peak temperature is much lower. That is, the material at position 1 near the fusion boundary exhibits the highest temperature and cooling rate. As a result, the cooling rate through the precipitation range is so high that Cr carbide precipitation occurs. At location 2 further away from the fusion line, the retention time of the material over the sensitization temperature range is long enough for precipitation to occur. In position 3, the maximum temperature is too low to allow precipitation. In addition, the C content can also influence the degree of sensitization of the material. As shown in Fig. 2.22, sensitization takes place more rapidly in 304 stainless steel as its C content is increased [70]. In addition, Ikawa et al. [70] also reported that as the heat input increased, the area of weld decay became wider. As for a method of preventing weld decay for austenitic stainless steels where these problems occur, post–weld heat treatment, reduction of C content, the addition of strong carbide formers have been proposed [64,71,72].

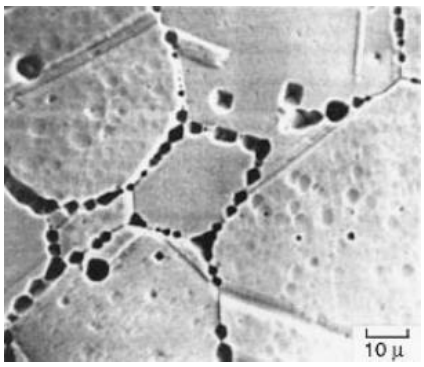

Fig. 2.18 Intergranular corrosion in HAZ of a 304 stainless steel containing 0.05 mass % C [67].

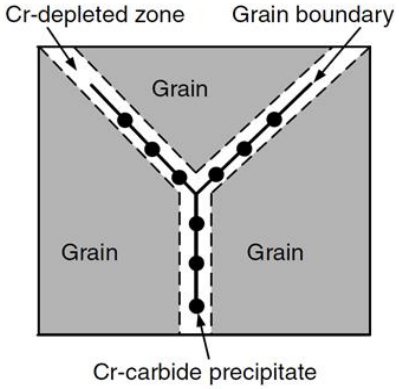

Fig. 2.19 Grain boundary micro structure in sensitized austenite stainless steel [68].

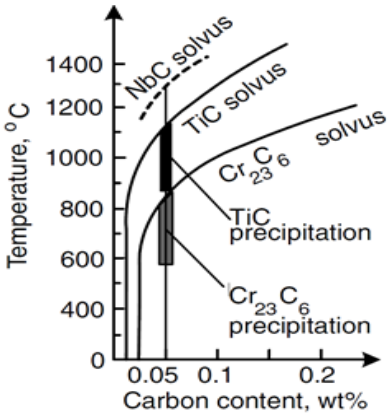

Fig. 2.20 Solvus curves for $Cr_{23}C_6$ and TiC in 304 stainless steel [69].

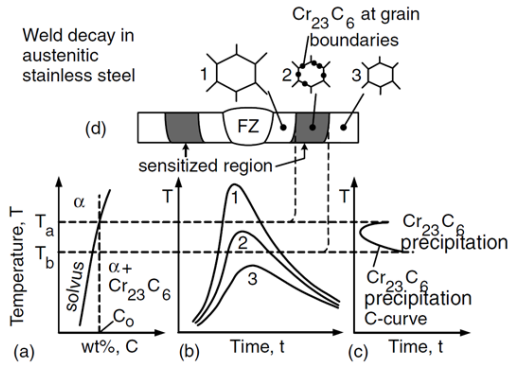

Fig. 2.21 Sensitization in austenitic stainless steel: (a) phase diagram; (b) thermal cycle [68].

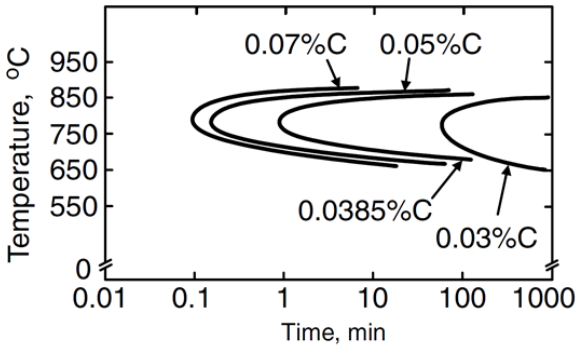

Fig. 2.22 Effect of C content on isothermal precipitation of $Cr_{23}C_6$ in 304 stainless steel [70].

2.3.4 Duplex stainless steels

Duplex stainless steels (DSSs) has been designed to have 50 % δ–ferrite/50 % γ–austenite microstructure, there chemistry is characterized by significant contents of (Cr + Mo) while Ni content remains about 50 mass % of the austenitic grades with similar corrosion resistance properties. DSSs (austenite/ferrite) is classified into a wide range of product groups by composition, from lower alloyed lean DSS to highly–alloyed super DSS and hyper DSS grades.

Among them, the most common DSS grade is EN1.4462 or 2205 (UNS S31803/S32205), which contains 22 mass % Cr–5 mass % Ni–3 mass % Mo–0.16 mass % N chemical composition, are used in a variety of applications and product types. It also exhibits more than twice the yield strength compared to AISI Type 304, 316, and 317 austenitic stainless steels. In recent years a number of so–called lean DSS have attracted a lot of interest as cost–efficient alternatives to standard austenitic grades such as 304L (1.4307) and 316L (1.4401). Lean DSS grades are competitive by replacing some of the Ni with a combination of Mn and N while maintaining strength, corrosion resistance, and proper phase balance, and generally have corrosion resistance equivalent to or better than standard austenitic grades [73,74]. Likewise, Super DSS is a super austenitic alternative and an alternative to expensive Ni alloys [75]. The main reason to use DSS is its excellent resistance to oxidation, corrosion, and stress corrosion while maintaining good mechanical properties. DSS is classified by calculating the chemical composition using the formula resistance equivalent PRE (Table 2.3), but it is not applicable to all environments. It is also called PREN because it takes into account the N content. [76]

$$PREN = [mass\ \%\ Cr] + 3.3[mass\ \%\ Mo] + 16[mass\ \%\ N] \qquad (2.2)$$

The addition of W in some DSS can increase corrosion resistance, for these grades a PREW is expressed as follow:

$$PREW = [mass\ \%\ Cr] + 3.3[mass\ \%\ Mo] + 1.65[mass\ \%\ W] + 16[mass\ \%\ N] \qquad (2.3)$$

PREN and PREW value is often used to distinguish the family to which alloy belongs. The classification taking in account the PRE is as follow:

- For Lean DSS lower than 30.
- Standard DSS having 30 as PRE.
- Super DSS with 40.
- Hyper DSS >45.

DSS with these characteristics is used in various fields described below:

- Gas extraction applications
- Oil production
- Heat exchangers
- Crude distillation
- Petrochemicals
- Desalination plants

Table 2.3 Chemical compositions in mass % of some most common wrought duplex stainless steel grades arranged with ascending PREN value [77].

Grade	Cr	Mo	Ni	N	Other elements	PREN
2101 (UNS S 32101)	21	0.3	1.5	0.22	–	25
2202 (UNS S 32202)	22	–	2	0.20	–	26.5
2304 (UNS S 32304)	23	0.2	4.0	0.10	–	25
2205 (UNS S 31803)	22	3.0	5.3	0.17	–	35
2507 (UNS S 32750)	25	4	7.0	0.27	–	>40
Zenon100 (UNS S 32760)	25	3.6	7.0	0.25	0.7 Cu, 0.7 W	41
2707 HD (UNS S 32707)	27	4.8	6.5	0.4	–	49
3207 HD (UNS S 33207)	32	3.5	7.0	0.5	–	50

The chemical composition of DSS has been adjusted to reach the 50 % ferrite and 50 % austenite base metal microstructure. Fig. 2.23 shows the Fe–Cr–Ni ternary phase diagram. It shows that when DSS solidifies into ferrite and the temperature cools to about 1273 K, some of it turns into austenite [78]. Since austenite is thermodynamically formed from ferrite, the alloy can't exceed the equilibrium level of austenite. However, assuming continued cooling to low temperatures, carbides, nitrides, sigma (σ), and other intermetallic compounds are possible microstructural components. This change in composition can have a great influence on the

volume fraction of δ–ferrite and γ phase. It is important to maintain the desired phase ratio by appropriately controlling the contents of Cr, Mo, Ni, and N and thermal history. In addition, since the cooling rate determines the amount of δ–ferrite that can turn into γ, the cooling rate following high temperature exposure has a significant effect on the phase balance [79]. In the case of N, it is an element that increases the temperature at which austenite starts to form δ–ferrite. Therefore, it is almost possible to reach the equilibrium level of γ even at a relative cooling rate.

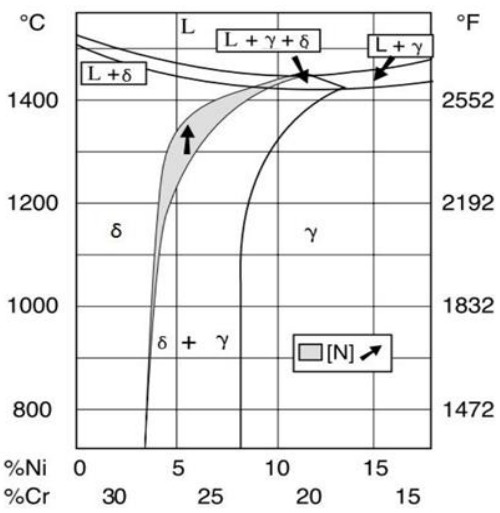

Fig. 2.23 Fe–Cr–Ni ternary phase diagram at 68 mass % Fe [78].

However, the use of N implies that Cr nitride can be formed with δ/δ and/or δ/γ boundaries. Other detrimental phases, such as sigma (σ), alpha prime (α'), and carbides can form in a matter of minutes at certain temperatures. Fig. 2.24 is the result showing the precipitation diagram for the second phase. The precipitation of the Cr nitride, sigma (σ), and chi (χ) phases begins at a relatively "slow" time of 1 to 2 minutes at temperature, which has a slower precipitation time compared to the ferritic and austenitic grades. This advantage is due, in part, to the high solubility of C and N in the low Ni austenite phase and possibly to a retarded effect of N on the carbide precipitation. As a result, DSS has a very advantage in sensitization during cooling, and the kinetics of formation of carbides and nitrides change depending on Cr, Mo, and Ni. Sigma (σ) and chi (χ) precipitation occur simultaneously with carbide and nitride precipitation while reaching higher temperatures. DSS grades with higher Cr, Mo and Ni content exhibit faster sigma (σ), and chi (χ) kinetics. In DSS ferrite phase is essentially unstable because of the high content of alloying elements. Therefore, a large variety of secondary phases may precipitate in DSS in the temperature range of 573–1273 K during isothermal aging or other heat treatment. Precipitation of secondary phases in DSS is usually considered in two separate temperature regions as shown in Fig. 2.25, which may occur below 873 K and from 873 to 1273 K. Additionally, spinodal decomposition of ferrite can occur in the temperature range of 573–773 K. The following phases observed: sigma (σ) phase, Cr_2N, CrN, secondary austenite γ_2, chi (χ) phase, R phase, π phase, M_7C_3, $M_{23}C_6$, and τ phase.

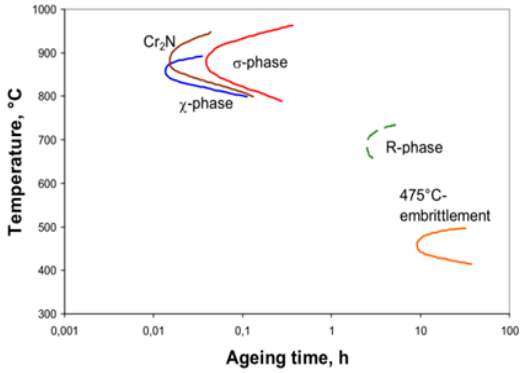

Fig. 2.24 Experimentally determined TTT diagram of SAF 2507 showing the C–curves of Cr_2N, χ–phase, σ–phase, R–phase and spinodal decomposition [79].

On the other hand, for the lean DSS, there is no precipitation of sigma (σ) phases because the content of Cr and Mo, which causes the δ–ferrite to remain in excess after solidification and promotes the precipitation of the sigma (σ) phase, is significantly lower than that of other DSSs. Fig. 2.26 shows the microstructure results of a DSS treated at 1223 K for 90 min. The precipitates are mainly located in the vicinity of the grain boundaries between ferrite and austenite, but were also identified within the austenitic grains.

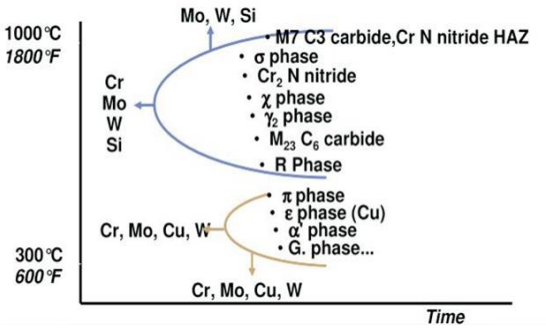

Fig. 2.25 Phase precipitation which may occur in DSS grades [80].

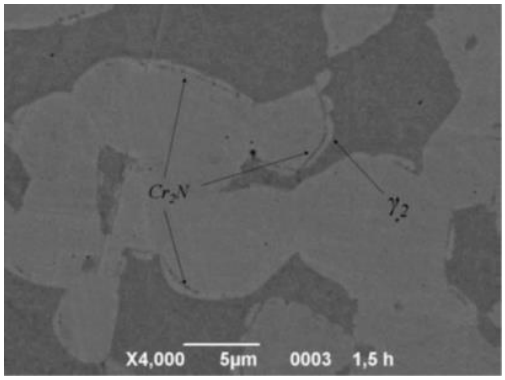

Fig. 2.26 SEM–BSE micrographs of nitrides precipitation in 2304 DSS treated at 1023 K for 90 min [81].

This can be explained by the fact that, as a result of the treatments, the precipitation of nitrides has occurred together with the formation of secondary austenite. Fig. 2.27 shows the secondary electron (SE) image and back–scattered electron (BS) image of scanning electron micrographs obtained from the sample solution–treated at 1353 K. The formation of sigma (σ) phase is intimately associated with the δ/γ interface of duplex structure. Individual sigma (σ) phases were precipitated at the interfaces of δ/γ and penetrated into the δ–ferrite (Fig. 2.27(a) or grew along the δ/γ–interface as a shape of butterfly (Fig. 2.27b). The preferential precipitation of sigma (σ) phase from δ–ferrite is well known due to the richness of Cr and Mo in δ–ferrite. Sigma (σ) phase is undoubtedly the most important of the listed secondary phases because of its significant volume fraction and its strong influence on toughness and corrosion behavior, besides 4 vol. % of the sigma (σ) phase can result in a decrease of impact toughness down to the value of less than 27 J from 230–300 J.

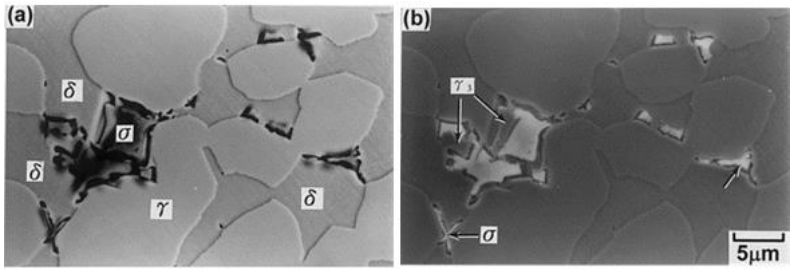

(a) SE images. (b) BS images.

Fig. 2.27. Scanning electron micrographs showing σ phase located at the δ/γ–interface [82].

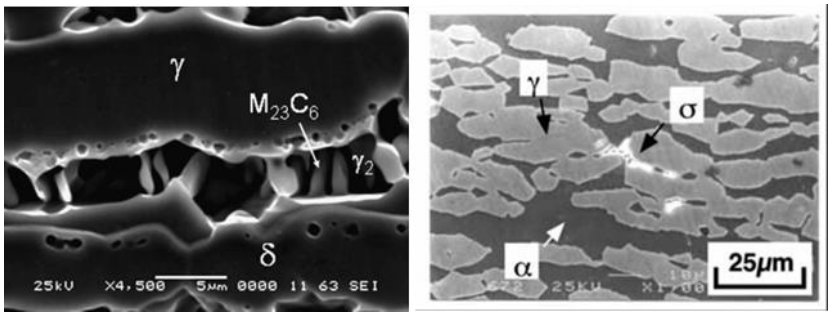

(a) $M_{23}C_6$ phase. (b) sigma (σ) phase.

Fig. 2.28 Change in microstructure of the HAZ in DSSs [97,98].

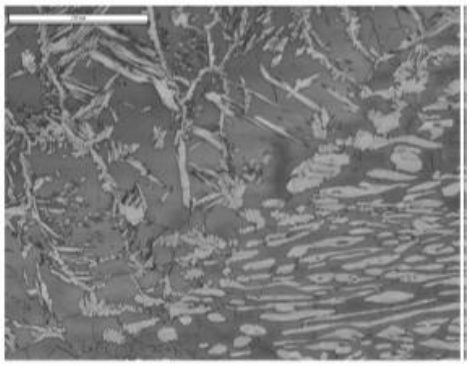

Fig.2.29 Optical micrographs of the welds [81].

During fusion welding, the DSS base material is subjected to a series of thermal cycles. Therefore, microstructural transformations occur, affecting the α/γ balance in the steel [83–94]. In the HAZs, this difference of α/γ ratio causes intermetallic compounds to be easily precipitated (Fig. 2.28), and adversely affects mechanical properties and corrosion resistance [95–113]. Moreover, the microstructure of the weld metal (WM) differs from that of the base metal because the WM solidifies into single–phase alpha (F mode) to precipitate Widmanstätten γ [94]. The heat affected zone (HAZ) adjacent to the fusion line (Fig. 2.29) presents a lower amount of austenite compared to the melted zone, while the ferrite matrix content increases dramatic liken in the weld zone approximately 65 %. During the welding procedure the structure in this region is fully transformed to ferrite, and the austenite grains then reform on cooling to room temperature. The Cr during the weld thermal cycles has insufficient time to diffuse through the ferrite phase; consequently, the α/γ transformation occurs partially during cooling. Furthermore, the adjacent zone to the base metal (Fig. 2.29) has a major grain growth than the melt zone; coarser austenitic grains are presented within a ferrite matrix. Therefore, to ensure the quality of the welds, the formation of the secondary phases and the quantitative evaluation and prediction of the α/γ phase transformation are required. Accordingly, there are active movements to attempt quantitative evaluation and prediction through kinetics. The foundation of models describing time dependent phase transformations were laid in the late 1930s. Johnson and Mehl [114], Avrami [115,116] and Kolmogorov [117] developed a model for phase transformation during isothermal conditions analytically, and Austin and Rickett [118] developed a model based on experiments. These models are usually referred to as the JMAK–equation and the AR–equation. It was reported that the growth of sigma (σ) phase and γ precipitation phenomenon accords to the JMAK–equation or the AR–equation. It was clarified that the above equations were applicable to explain the experimental results concerning the dependence of temperature on growth properties.

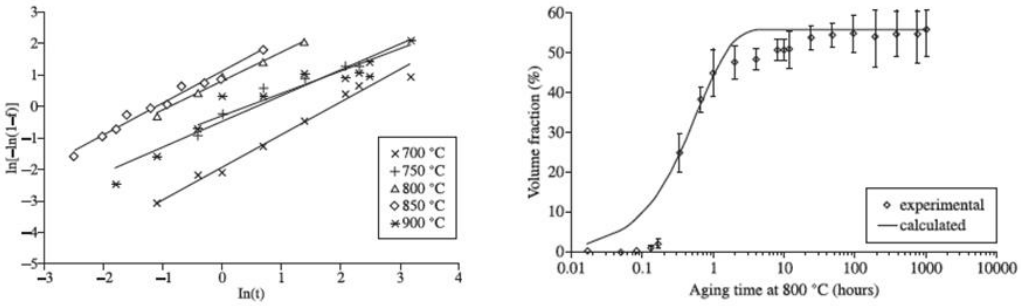

(a) JMA plot of sigma (σ) phase. (b) Comparison of measured and calculated values.

Fig. 2.30 Phase transformation behavior of sigma (σ) phase [119].

Magnabosco et al. [119,120] described the determination of the Time–Temperature–Precipitation (TTP) diagram for the sigma (σ) phase, and proposed a model that predicts the formation of the sigma (σ) phase using an equation of Johnson–Mehl–Avrami–Kolmorgorov (JMAK) type. The JMAK type equation was determined to estimate the fraction of sigma (σ) phases formed during isothermal aging of DSS, and there was a high correlation between the experimental data and the predicted results (Fig. 2.30). P. Ferro et al [121]. also developed a prediction model based on the modified JMAK type equation by comparing the study data of Wilson and Nilsson [122]. The computer model, based on the modified JMAK type of equation, uses information from isothermal experiments of sigma (σ) phase transformation and predicted the transformation kinetics during a cooling process. R. Badji et al [97]. investigated the effect of the solution treatment temperature before aging treatment on the transformation of δ–ferrite in DSS welding. The JMAK theory was then used to conduct a detailed study of the sigma (σ) phase precipitation kinetics to develop a quantitative understanding of the δ–ferrite transformation kinetics in such materials. They found that increasing the solution–treatment temperature from 1323 to 1523 K delays sigma (σ) phase formation and favours precipitation of intergranular secondary austenite. Meanwhile, in the case of α/γ phase transformation, it is reported that the growth of the γ phase is due to the impingement effect explained by the Austin–Rickett equation, which clearly explains the transformation behavior of the γ phase in the over–cooled α phase [123]. Besides, isothermal heating data was used to predict γ phase formation (Fig. 2.31) in the continuously cooled HAZ [124,125].

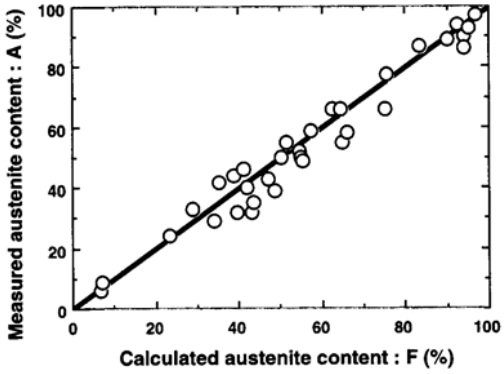

Fig. 2.31 Comparison between calculated and measured austenite contents in weld metals [125].

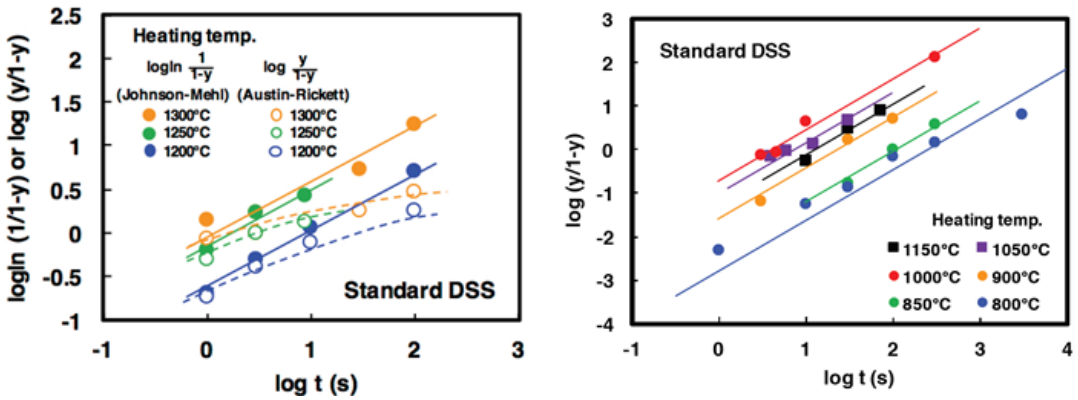

(a) Dissolution. (b) Precipitation.

Fig. 2.32 Austin–Rickett plots of dissolution and precipitation behavior of γ phase [127].

However, only the precipitation phenomenon was considered—and that in a limited temperature range—and to use it to predict the γ amount of a multi–pass weld is unreasonable if both precipitation and dissolution phenomena are not considered in multiple temperature ranges. In a recent study [126,127], the authors evaluated the kinetics of α/γ phase transformation (precipitation and dissolution of γ phase) in the HAZ of DSS welds (standard, lean, and super). The amount of γ in the single–welded HAZ section was derived by numerical analysis and compared according to the composition of the DSS. As a result, it was confirmed that the behavior of the γ phase precipitation and dissolution followed the Austin–Rickett type equation, and the kinetics of phase transformation was clarified by revealing the relationship with the temperature dependence of the rate constant (Fig. 2.32). However, as described above, the microstructure of the weld metal (WM) may be different from that of the HAZ (base material). Moreover, it is difficult to predict quantitatively in the case of welds with a much more complex thermal history, such as multi–pass welding.

In this doctoral dissertation, the research content of predicting the amount of γ phase of multi–pass welds was included by conducting kinetics of the α/γ phase transformation phenomenon of the HAZ (base material) and weld metal (WM) of DSSs, reflecting the above research backgrounds.

2.4 Review of the phase–field simulation in stainless steels

2.4.1 Description and characteristic of the phase–field method

Currently, simulation based on the phase–field model is one of the most actively researched and developed methods among the existing computer simulation technologies for predicting the microstructure and phase transformation of materials. The advantage of the phase–field model is that the parameters related to the free–energy equation and diffusion included in the governing equation can be applied for predicting the microstructure of the material using a commercially available database. Moreover, this model can consider all the changes (phase transformations) that occur in the microstructure of the material owing to external environmental variables (heat, stress, magnetic field, etc.) in terms of conservative (mass) and non–conservative (phase, interface, anisotropy, etc.) parameters. The phase–field model is being extensively applied in various natural and applied science studies since it was first proposed by Fix [128] and Langer [129]. Recently, it has been applied to the prediction and analysis of non–diffusion phase transformation processes, such as dislocation kinetics [130,131], crack propagation [132,133], and martensitic transformation, and to almost all the phase transformations involving solid–solid phase transformation, grain growth [134], and recrystallization precipitation diffusion. The Phase–field model is a mathematical modeling technique to analyze the interface problem of materials. In the existing phase transformation model introduced in the previous section, the interface was treated as a sharp interface with a thickness of 0 to simplify it into a one–dimensional problem, but the biggest difference is that the phase–field model treats the interface as a diffuse interface with a finite thickness. Existing sharp interface by using the concept of the diffuse interface, it became possible to simulate and predict all microstructure changes that the model could not solve. In the phase–field model, the boundary condition at the interface is expressed by a partial differential equation as a variable of the phase–field with several–dimensional order parameters. Here, the phase–field is recognized as a domain with distinct values. For example, in the solidification problem, the phase–field is expressed in the form of 1 for liquid and 0 for solid (Fig. 2.33).

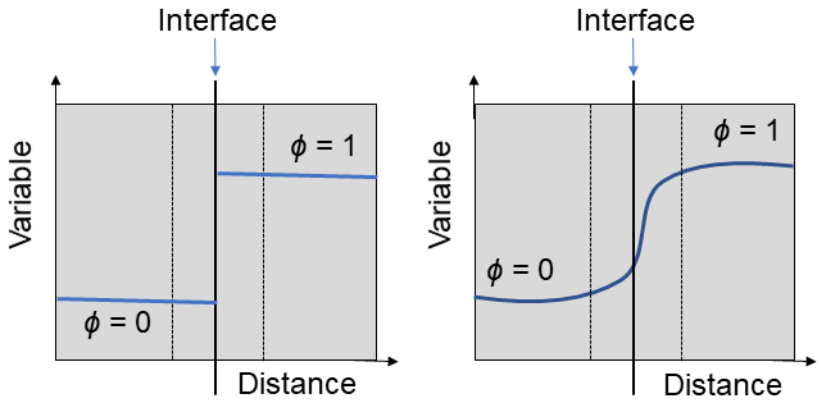

(a) Sharp interface. (b) Diffuse interface.

Fig. 2.33 The concept of the diffuse interface in the phase field model.

In general, phase–field variables related to the crystal structure, orientation, composition, temperature, etc. have almost constant values within one region but gradually change at the diffuse interface of a crystal interface having a finite thickness. At this time, the position of the interface is defined based on the position where the phase–field has a certain value (for example, 0.5). In the phase–field, these boundary problems are solved by numerically solving the Allen–Cahn and Cahn–Hilliard equations.

2.4.2 Application of phase–field simulation

Modeling of the solidification process through the phase–field method was introduced about 20 years ago [128,129,135]. It was motivated by the desire to predict the complicated dendritic patterns during solidification without explicitly tracking the solid–liquid interfaces. It was first demonstrated by realistically simulating a three–dimensional dendrite using a phase– field model from Kobayashi [136]. Böttger [137,138] analyzed the hot ductility during continuous casting and conducted a study on micro–segregation in AA6061 and A356 aluminum alloys. Regarding magnesium alloys, the anisotropy of hexagonal crystals has attracted the attention of researchers. Eiken [139] studied the growth behavior of magnesium by performing a three–dimensional phase–field simulation to analyze the grain growth rate according to the direction and the resulting solidification mechanism; it was found that several grains dominated the overall growth rate. Besides, the influence of structural defects such as dislocations was also considered. Recently, a diffusion interface model was proposed from Hu and Chen that reflects the elastic fields produced from coherent compositional inhomogeneities and general structural defects including dislocations [140]. It is a unique feature of this model that the elastic field from dislocations and coherent compositional

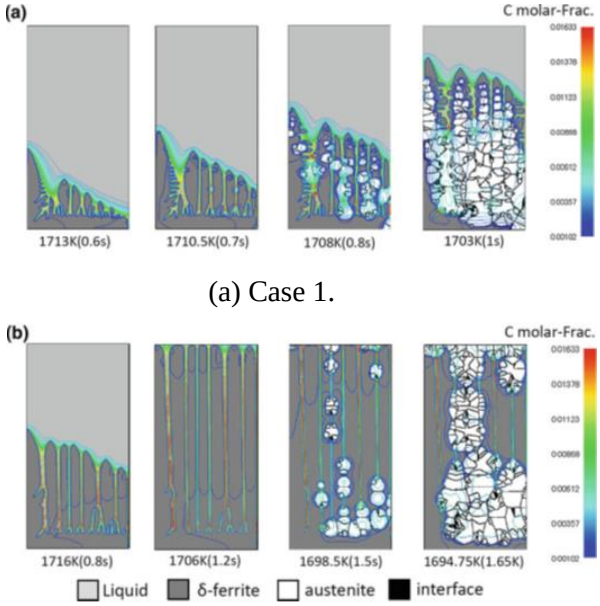

(a) Case 1.

(b) Case 2.

Fig. 2.34 Phase and C molar–fraction distribution in DSSs. [144].

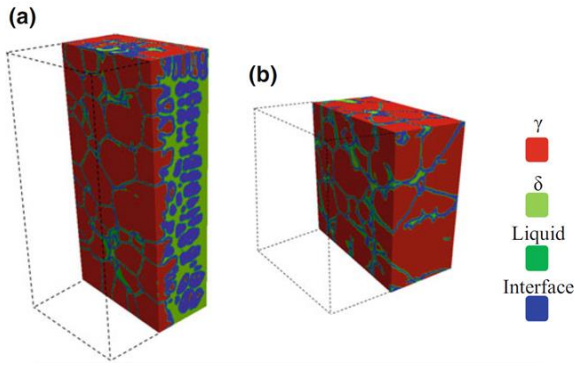

Fig. 2.35 Center cross section of (a) columnar and (b) equiaxed microstructure calculated by MPF method. [145].

inhomogeneity is obtained within the same formulation using the concept of eigenstrains in micromechanical. For crack propagation, Aranson et al. [141] and Karma et al. [142] et al. recently studied how to apply a phase–field model to the tricky problem of crack propagation in amorphous solid. For example, on a crack surface, the phase–field varies from 0 to 1, while a value of 1 in the phase–field represents a solid region and 0 represents a crack with zero density [141] or with all atomic bonds broken [142]. The Allen–Cahn equation for the above listing is combined with the elastodynamics equation for the phase–field. The evolution of the phase–field is driven by the applied stress or strain, but the evolution of the phase–field is determined by local criteria. The local density is below a certain critical density [141] or the local deformation is above the critical value [142].

The crack propagation simulation using the phase–field method seems to capture the main phenomenological features of crack propagation observed experimentally, but the quantitative modeling of crack propagation kinetics requires further development. Nomoto et al. have developed a multi–phase field (MPF) in conjunction with the CALPHAD thermodynamic database for solidification simulation of Fe–Cr–Ni–Mo–C duplex stainless steel. They have two different compositional conditions (Case 1: Fe–16 mass % Cr–2 mass % Mo–10 mass % Ni–0.08 mass % C and Case 2: Fe–17 mass % Cr–2 mass % Mo–9 mass % Ni–0.08 mass % C) successfully calculated the microstructure of solidification (Fig. 2.34) after nucleation of the γ phase [143]. Besides, MPF method coupled with CALPHAD database was used to simulate microstructure evolution by columnar and equiaxed (Fig. 2.35) solidifications during continuous casting. Moreover, the microstructure of recrystallization by the hot rolling process was also predicted by combining with various commercial simulations including the MPF method [144].

2.4.3 Application examples of phase–field in phase transformation phenomenon

Recently, a study was conducted to predict the change of microstructure according to the cooling rate by using the phase–field simulation parameter value [145].

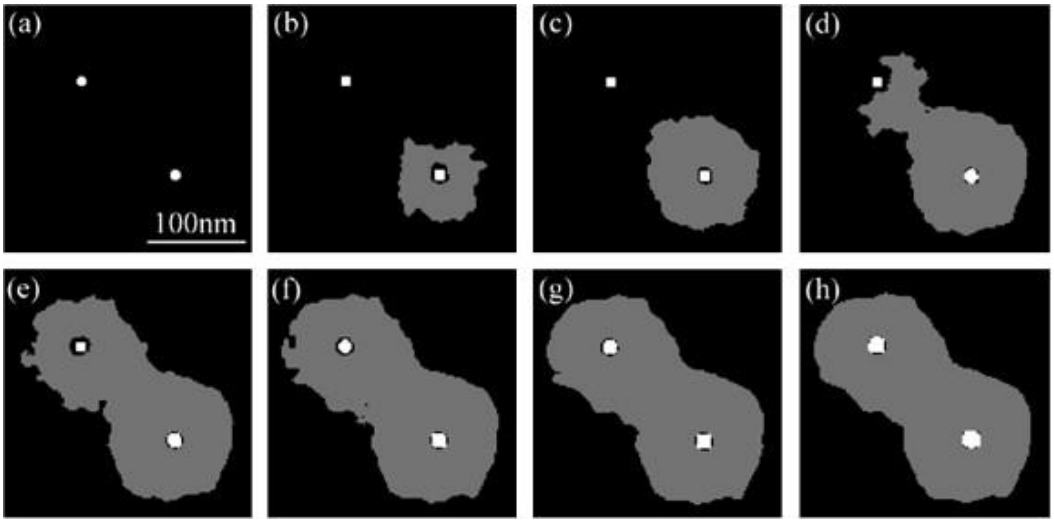

Fig. 2.36 Change of mole fraction of $M_{23}C_6$ carbide phase and α phase with time [150].

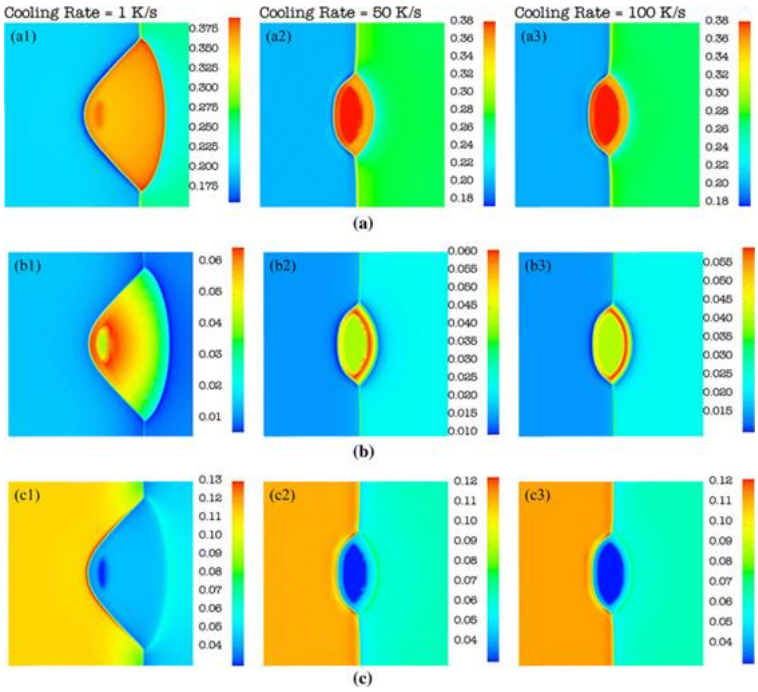

Fig. 2.37 Changes in the composition profile of (a) Cr, (b) Mo, and (c) Ni according to the cooling rate. Austenite on the left side, ferrite on the right side, and sigma in the middle [151].

The ferrite nucleation process and grain growth direction were predicted and verified through comparison with the experimentally observed microstructure. It also provides insight into the nature of phase transformations concerning interface control or diffusion control mode.

Yeon et al. [146] simulated the isothermal austenite to ferrite transformation in a Fe–Mn–C system under para–equilibrium. Using the model of Steinbach et al., Pariser et al. [147] modeled the austenite to ferrite transformation in ultra–low carbon steel and in interstitial–free steel during cooling at a medium cooling rate. In addition, Koyama et al. [148,149] investigated the phase decomposition of elemental Ni and Mn during the spinodal decomposition in Fe–Cu–Ni–Mn quaternary alloys. In Type 304 steel, simultaneous nucleation and growth simulation of $M_{23}C_6$ carbide and ferromagnetic α phase were predicted during the creep process using the phase–field method. Changes in the relative amounts of these two product phases, during the creep process in Type 304 steel, are first reproduced using the phase–field method, and then the correlation of the dislocation density with the phase transformation was investigated (Fig. 2.36). They found a high correlation between the precipitation behavior of the α phase and the dislocation density during the creep process. It has been proven that the phase–field model is useful for investigating the stochastic and kinetic phenomena of the phase transformation [150]. In the case of DSS, Malik et al [151]. applied a phase–field simulation to the precipitation of the sigma (σ) phase in SDSS 2507 under continuous cooling. The simulation results observed that the precipitation of the sigma (σ) phase was characterized by the accumulation of Cr and Mo at the austenite–ferrite and ferrite–ferrite boundaries (Fig. 2.37).

Moreover, it was found that the slow cooling rate promotes the growth of the sigma (σ) phase, while the high cooling rate limits it and eventually preserves the duplex structure in the SDSS 2507 (Fig. 2.38).

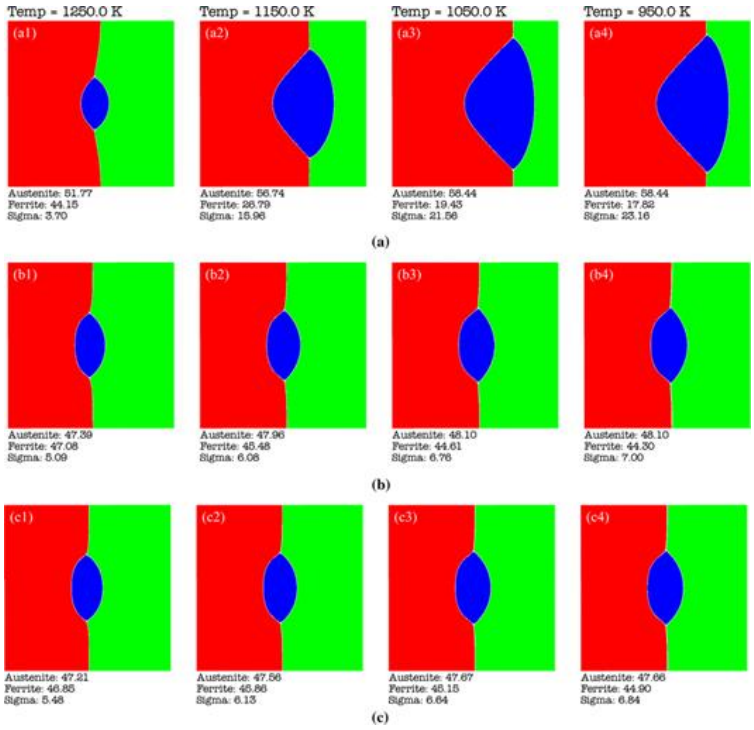

Fig. 2.38 Changes in microstructure according to cooling rate. Red is austenite, green is ferrite and blue is sigma (σ) phase. Numbers at the bottom depict volume fraction of each phase in percentage [151].

Based on the above, they proved that the morphological characteristics and compositional profiles of the overall predicted deformation are in good agreement with empirical data. Yeddu et al [152]. developed a multi–length scale model to study stress assisted martensitic deformation. It can be observed that, as the transformation progresses, the pre–existing spherical martensitic embryo transforms into an ellipsoid–shaped martensite unit (Fig. 2.39). It was proved that the martensitic microstructure predicted by the model is in good agreement with the experimental results obtained for stainless steels of similar composition. Bhogireddy [153] studied the growth process of the γ phase during quenching of a DSS assumed to be a ternary system using a phase–field simulation. The equilibrated system was quenched by 20K, and the phase shift was observed by solving the governing equation over 100 time steps with a time interval of 10^{-6} s, and the output observed at this stage was used to observe the α/γ transformation in the Fe–Cr–Ni system (Fig. 2.40). They evaluated that the simulations show the growth of the austenite phase during quenching as well as in real systems.

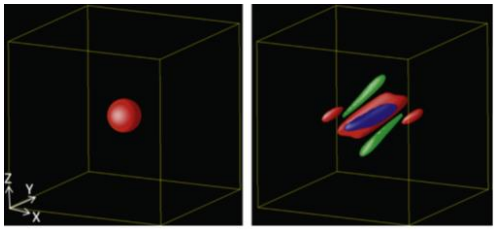

(a) t* = 0. (b) t* = 5.

(c) t* = 10. (d) t* = 75.

Fig. 2.39 Martensitic microstructure evolution during a thermal martensitic transformation. [152].

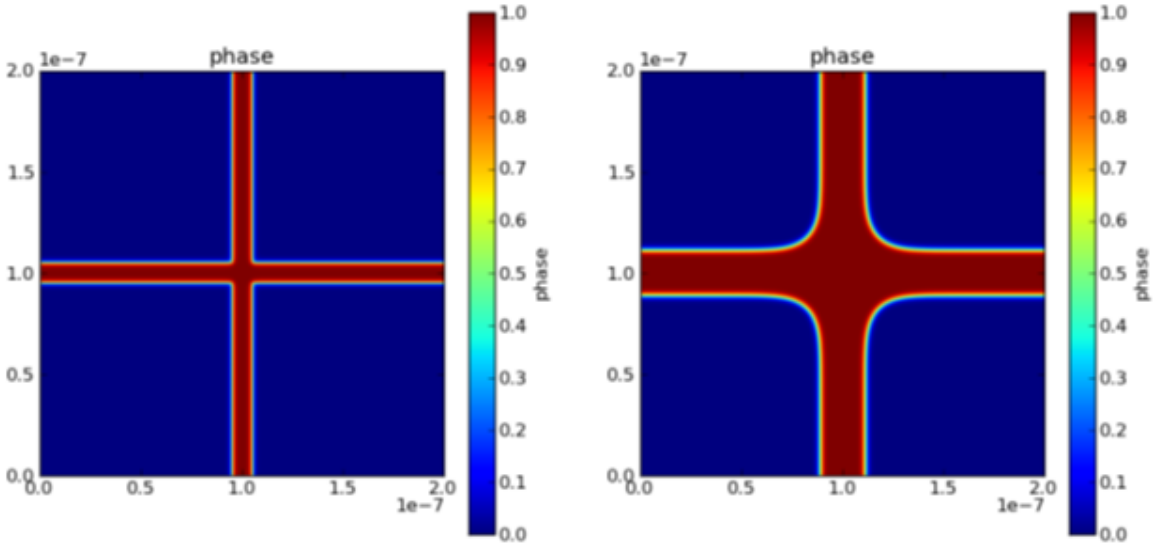

(a) Before quenching. (b) After quenching.

Fig. 2.40 Growth process of γ phase during quenching. [153].

2.4.4 Phase–field simulation challenges and future prospects

Phase–field simulation is a predictive technique with many advantages. First of all, the interface can model the evolution of arbitrary shapes and complex microstructures without explicit tracking. This is especially true for predicting three–dimensional microstructures.

Second, it can be applied to a wide variety of microstructure problems by appropriately selecting the variable parameters. Third, the phase–field model can explain various phenomena such as phase transformation and particle coarsening within the same formulation. Finally, it is possible to link phase–field models with thermodynamic and kinetic databases for obtaining the materials parameters [148, 154–160] or to derive the free energy models from microscopic models [161–163]. However, one of the major drawbacks of the phase–field approach is the fact that the method is still computationally intensive, especially for three–dimensional systems.

Therefore, it is essential to develop and implement efficient and accurate numerical algorithms. Despite the effort to increase the artificial interfacial width that one can employ in a phase–field model, for example, using the thin–interface analysis, in many cases, numerical methods using uniform grid sizes will not be sufficient to perform three–dimensional phase–field simulations with the desired system size. Developing algorithms for systems where interfaces are rich in microstructures and involving long–range interactions such as elastic interactions will be a long–term challenge. Currently, various researchers are actively researching the phase–field. The phase–field model simulation technology is closely constructively linked to the material database, and the microstructure prediction process serves as a link for predicting characteristics in mesoscale and macroscale. Considering the fact that the microstructure prediction results determine the final characteristics of materials and parts and the life prediction results, the technology development in this field is expected to proceed even faster.

Chapter 3 Kinetics of α/γ phase transformation phenomenon in duplex stainless steels

3.1 Introduction

Duplex stainless steel (DSS) has wide applications in various industries, such as chemical, energy, and offshore plants. DSS has a microstructure composed of a balanced austenite (γ) and ferrite (α) phase and has excellent properties, such as high strength and toughness, high corrosion resistance, and good weldability. However, during welding and depending on the thermal cycles, DSS undergoes complex microstructural and phase changes that affect the α/γ phase balance [83–94]. For this reason, secondary phases such as Cr–carbide and nitride, Sigma (σ) and chi (χ) phases get easily precipitated [92, 95–103], so the mechanical properties and corrosion resistance of DSS are greatly influenced by the α/γ balance [86, 93, 99, 105, 107–111]. Therefore, it is important to quantitatively review the prediction and control of α/γ phase transformation in DSS welding. There are some studies on the phase transformation behavior of DSS and the nucleation and growth mechanisms of the secondary phases. On the other hand, few studies have investigated the kinetics of α/γ phase transformation [94,164–166]. In recent studies [126–127], the authors evaluated the kinetics of α/γ phase transformation (precipitation and dissolution of γ phase) in the HAZ of DSS welds (standard, lean, and super). The amount of γ in the single–welded HAZ section was derived by numerical analysis and compared according to the composition of the DSS. As a result, it was confirmed that the behaviors of the γ phase precipitation and dissolution were followed by the Austin–Rickett type equation, and the kinetics of phase transformation were clarified by revealing the relationship with the temperature dependence of the rate constant. However, in multi–pass welds, the weld metal (WM) and HAZ are reheated several times by subsequent welding thermal cycles, and as such, the dissolution and precipitation of the γ phase take place alternately during the welding process.

Moreover, due to microstructural changes, the kinetics of the γ phase, dissolution and precipitation, will be different in the multi–pass WM and HAZ (base material). Therefore, due to this complex phase transformation behavior during the thermal cycle, the α/γ phase transformation in the multi–pass welds is difficult to predict in a quantitative manner.

In the present study, the kinetic approach was made to the α/γ phase transformation phenomena in the multi–pass welds of DSSs. Both of the dissolution and precipitation behaviors of γ phase were kinetically investigated for the reheated WM as well as the base metal HAZ, and the γ phase fraction in multi–pass welds of DSSs was numerically calculated by coupling with the heat conduction analysis during multi–pass welding. Finally, the predicted results of α/γ phase transformation in multi–pass welds were verified by the experimental examination.

3.2 Materials and experimental procedures

3.2.1 Materials used

Three types of DSSs, lean, standard and super DSSs, were used for the base metal. Table 3.1 shows the chemical compositions of the base metals used in this study. All DSSs were heat–treated at 1323 K×5 min after hot rolling. The autogenous filler metals (diameter, 1.2 mm) were used for gas tungsten arc welding (GTAW). The chemical compositions of filler metals are shown in Table 3.2. The γ phase fraction of as–received base metals of DSSs was approx. 50–60 %. The dimensions of DSS plates were 50 mm × 70 mm × 4 mm^t (for single pass melt–run welding). Table 3.3 shows GTA melt–run weld conditions and welding specifications were as follows: 90 A; arc voltage, 14 A; welding speed, 1mm/s; shielding gas, Ar+2 % N_2 (flow rate, 15 L/min).

Table 3.1 Chemical composition of the duplex stainless steels in this study (mass %).

Steel	C	Si	Mn	P	S	Ni	Cr	Mo	Cu	N	Fe
Lean DSS (type 821L1)	0.017	0.42	3.21	0.024	<0.001	2.24	20.88	0.48	1.05	0.17	Bal.
Standard DSS (type 329J3L)	0.008	0.56	1.82	0.025	0.0002	5.75	22.55	3.08	0.16	0.161	Bal.
Super DSS (type 327L1)	0.009	0.31	0.51	0.024	0.0009	6.56	25.11	3.72	0.21	0.259	Bal.
Lean DSS (lab)	0.014	0.35	1.49	0.024	0.0004	3.06	20.85	0.30	0.09	0.177	Bal.
Super DSS (type 329J4L)	0.025	0.33	0.73	0.031	<0.001	6.33	24.69	3.21	0.06	0.17	Bal.

Table 3.2 Chemical composition of the filler metals in this study (mass %).

Steel	C	Si	Mn	P	S	Ni	Cr	Mo	Cu	N	Fe
Lean DSS (type 821L1)	0.01	0.38	1.43	0.017	–	8.62	23.11	3.27	0.06	0.15	Bal.
Standard DSS (type 329J3L)	0.012	0.56	1.81	0.024	0.0005	5.72	22.46	3.07	0.17	0.169	Bal.
Super DSS (type 327L1)	0.013	0.31	0.48	0.025	0.0005	6.83	24.98	4.03	0.2	0.265	Bal.
Lean DSS (lab)	0.014	0.35	1.49	0.024	0.0004	3.06	20.85	0.30	0.09	0.177	Bal.
Super DSS (type 329J4L)	0.014	0.34	0.59	0.02	<0.001	9.75	25.35	3.94	0.06	0.24	Bal.

Table 3.3 Conditions of GTA melt–run weld.

Parameters	Values
Arc voltage	14 V
Arc current	90 A
Welding speed	1 mm/s
Electrode extension	2.0 mm
Arc length	2.0 mm
Shield gas	Ar + 2 % N_2
Shield gas flow rate	15 L/min
Filler wire	None

3.2.2 Heat treatment and metallography

The full weld metal specimen for isothermal heat treatment was machined from the melt–run welded plate. The dimensions of specimen were 3 mm × 8 mm × 1.5 mm^t (Fig. 3.1). On the other hand, the base metal specimen for isothermal heat treatment was directly machined from the as–received plate. The dimensions of specimen were 3 mm × 3 mm × 4 mm^t (Fig. 3.2). Isothermal heat treatment of the DSS specimen was performed in an Ar atmosphere using a high–frequency induction heating device. The heat treatment conditions, including the thermal cycle pattern, are summarized in Table. 3.4. The heating rates (HR) of the solution and precipitation treatments were constant at 100 K/s, and then water quenching (W.Q.) was performed. For the dissolution heat treatment of the base materials, it was carried out at a temperature of 1373–1633 K, and in the case of precipitation heat treatment was performed at a temperature of 1073–1423 K after performing alpha single-phase heat treatment in advance. On the other hand, in the case of the dissolution heat treatment of the weld metals, the α/γ phase ratio is very complicated because the specimens for heat treatment were cut from the TIG melt-run weld. Therefore, after heat treatment at 1273–1323 K to precipitate γ amount up to 50 % of the original base materials after alpha single-phase heat treatment, dissolution heat treatment was performed. For the precipitation heat treatment, it is the same as the precipitation heat treatment method of the base materials. A change in the isothermal heat treatment was carried out for the kinetic investigation of the dissolution and precipitation behavior of the γ phase. The microstructure of the specimens etched by electrolytic polishing with a voltage of 15.0 V for 15 s using 10 % oxalic acid solution was observed using an optical microscope (OM) and a scanning electron microscope (SEM). Electron back scattered diffraction (EBSD) analysis was performed using a JEOL JSM–7001FA field emission gun–SEM. The sample was tilted 70° to the incident beam at a 20 kV acceleration voltage. The working distance was 15 mm, and the scan step size was 0.8 μm.

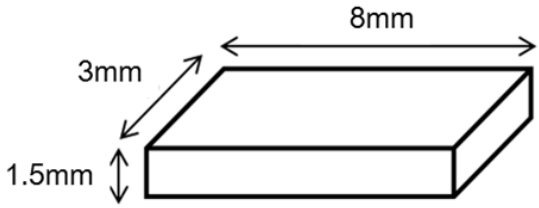

Fig. 3.1 Schematic diagram of specimen for isothermal heat treatment test of WM.

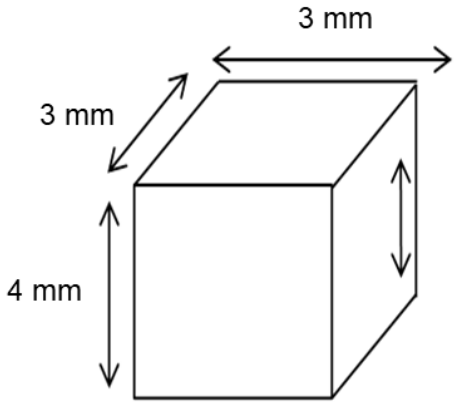

Fig. 3.2 Schematic diagram of specimen for isothermal heat treatment test of HAZ.

Table 3.4 Conditions of isothermal heat treatment.

Heat treatment		Thermal cycle	Conditions	
Base metal (Base metal HAZ)	Solution treatment	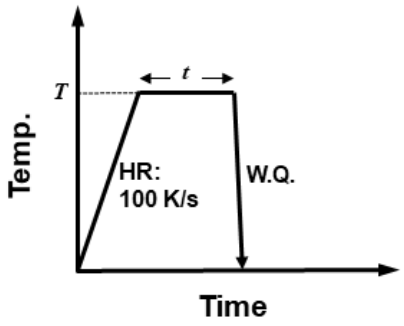	Heating temp., T	1373–1633 K
			Holding time, t	0–3000 s
	Precipitation treatment	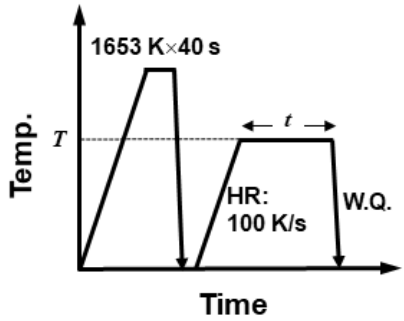	Heating temp., T	1073–1423 K
			Holding time, t	0–3000 s
Weld metal (Reheated WM)	Solution treatment	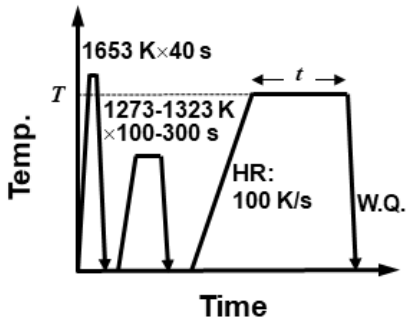	Heating temp., T	1473–1623 K
			Holding time, t	0–30 s
	Precipitation treatment	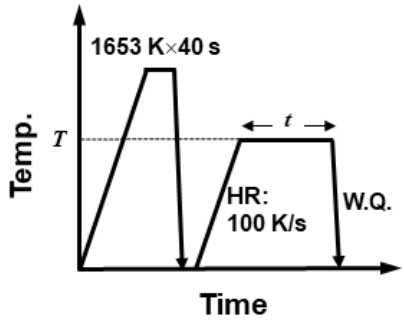	Heating temp., T	1123–1423 K
			Holding time, t	0–1000 s

3.2.3 Multi–pass gas tungsten arc welding

Multi–pass gas tungsten arc welding (GTAW) was performed to investigate the microstructure and fraction of the γ phase in welding. Table 3.5 shows a schematic and welding conditions of the multi–pass welding specimen. The multi–pass welding specifications were as follows: arc current, 150 A; arc voltage, 12 V; welding speed, 27 cm/min (root pass); arc current, 220 A; arc voltage, 12 V; welding speed, 27 cm/min (other passes); shielding gas, Ar + 2 % N_2 (flow rate, 15 L/min); inter–pass temperature, 373 K; U–groove (angle, 50°; root face, 1 mm). In the multi–pass welding, the total number of welding passes was 15.

Table 3.5 Welding conditions and a schematic of the joint.

<table>
<tr><th colspan="2">Welding conditions</th><th>Schematic of the joint</th></tr>
<tr><td rowspan="2">Arc current</td><td>1st pass: 150 A</td><td rowspan="5"> 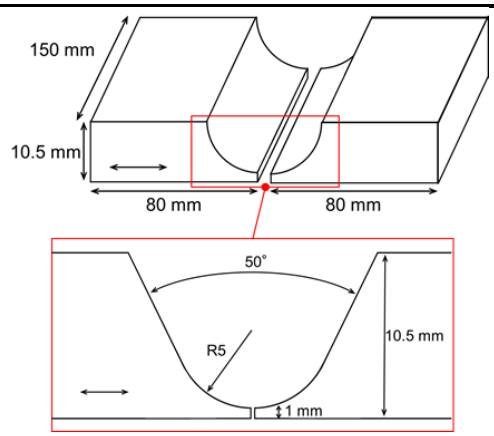
</td></tr>
<tr><td>2nd–15th pass: 220 A</td></tr>
<tr><td>Welding speed</td><td>1.5 mm/s</td></tr>
<tr><td>Shield gas</td><td>Ar + 2 % N_2</td></tr>
<tr><td>Shield gas flow rate</td><td>15 L/min</td></tr>
</table>

3.3 Kinetics of the phase transformation behavior in DSSs

3.3.1 Kinetics of γ dissolution phenomenon of the base materials

The change in microstructure of DSSs during the solution treatment was investigated.

Fig.3.3 shows an example of microstructural change (phase mapping by EBSD analysis) in lean DSS (type 821L1) with the solution treatment condition. The red regions indicate a γ phase, green ones a α phase and yellow ones a σ phase in the microstructure. A typical microstructure of DSS could be observed in all specimens, namely, a γ phase was aligned along the rolling direction. The amount of γ phase decreased with an increase in the heating temperature. It has been confirmed that similar dissolution behavior was observed in standard and super DSSs.

The area fraction of γ phase in the phase map was measured for all steels with varying the heat treatment condition. Fig. 3.4 shows the effects of heat temperature and holding time on the volume fraction of γ phase in lean (lab), standard (type 329J3L), super (type 327L1), lean (type 821L1), and super (type 329J4L) DSSs. The fraction of γ phase was increased with an increase in the heat temperature and holding time, and saturated at an equilibrium fraction in all steels. Previous studies [126–127] have reported that the precipitation of the γ phase was followed by the Austin–Rickett equation, which is presented in Eqs. (3.1) and (3.2) [123–125].

$$\frac{y}{1-y} = (kt)^n \tag{3.1}$$

$$\log\left(\frac{y}{1-y}\right) = n\log k + n\log t \tag{3.2}$$

where, y is the fraction transformed, k is a rate constant, t is time, and n is the time exponent. In this case, the y can be expressed as Eq. 3.3.

$$y = \frac{f - f_0}{f_{eq} - f_0} \tag{3.3}$$

where, f : γ precipitation (dissolution) amount, f_0 : initial γ precipitation (dissolution) amount, f_{eq} : equilibrium γ (α) amount. Therefore, the applicability of the equations reported in the previous study to evaluation of the dissolution of the γ phase was investigated. Fig. 3.5 shows Austin–Rickett plots for the dissolution behavior of the γ phase in the investigated DSSs.

The plots indicate a good linear relationship, and the slope of the lines is almost the same regardless of the heating temperature. The time exponents (n) can be derived according to temperature from the aforementioned Austin–Rickett plots in Fig. 3.5, and the results are presented in Table 3.6. The time exponents (n) for lean, standard, and super DSSs were determined to be 0.93, 0.64, 0.72, 0.49, and 0.77, respectively. Consequently, the dissolution kinetics of the γ phase in all base metal HAZs were followed by the Austin–Rickett equation.

To investigate the temperature dependence of the rate of dissolution in the γ phase, we used the equation of rate constant $k(T)$, which can be expressed using an Arrhenius–type equation Eq. (3.4).

$$k(T) = k_0 \exp\left(-\frac{Q}{RT}\right) \tag{3.4}$$

where k_0 is the frequency factor, Q is the activation energy, T is the absolute temperature and R is the gas constant. The results of the Arrhenius plots for the dissolution rate of DSSs are depicted in Fig. 3.6. From the figure, it can be seen that ln k and $1/T$ have a good linear relationship. Then, the temperature dependencies of the dissolution rate of the γ phase in lean, standard, and super DSSs were investigated, and the results are presented in Table 3.6.

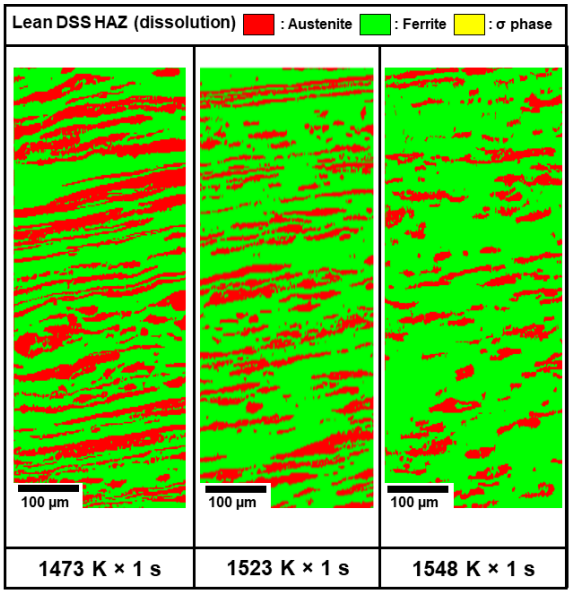

Fig. 3.3 Change in microstructure of lean DSS (type 821L1) with solution treatment.

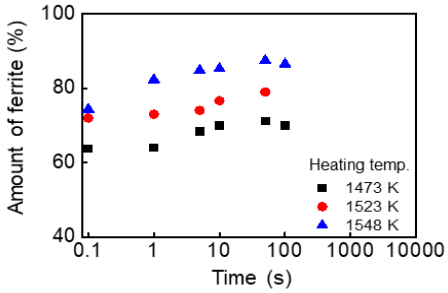

(a) Lean DSS (type 821L1).

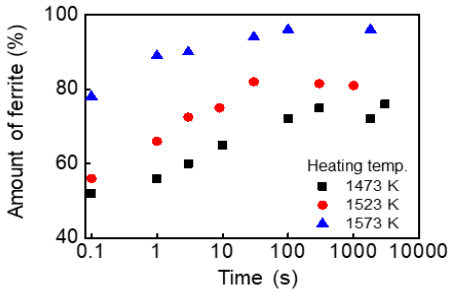

(b) Standard DSS (type 329J3L).

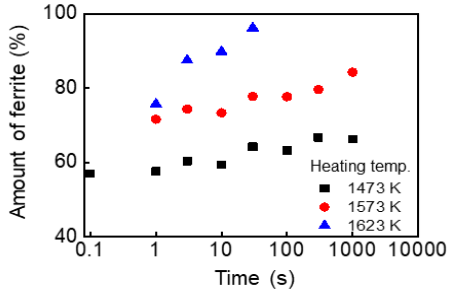

(c) Super DSS (type 327L1).

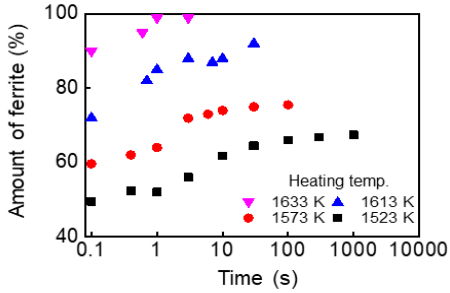

(d) Lean DSS (lab).

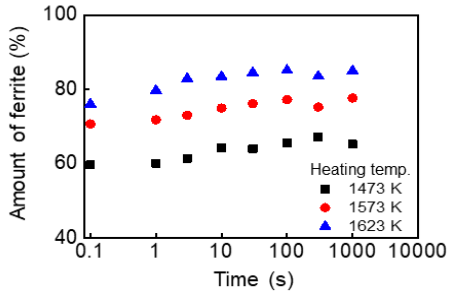

(e) Super DSS (type 329J4L).

Fig. 3.4 Changes in the dissolved γ fraction for the DSSs at different temperatures.

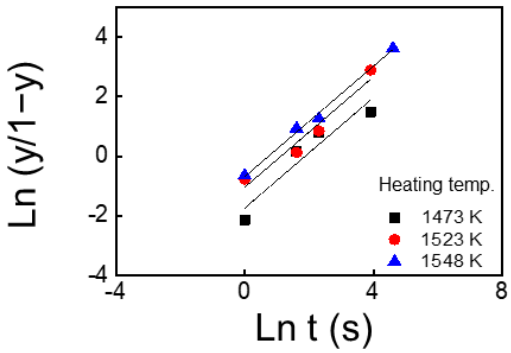

(a) Lean DSS (type 821L1).

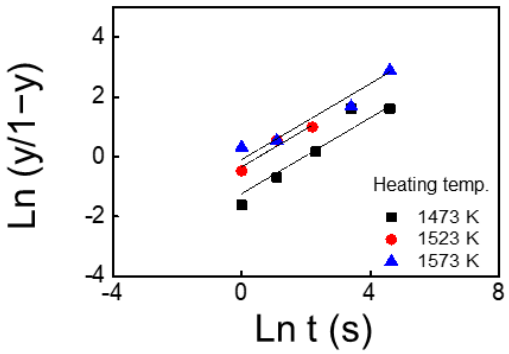

(b) Standard DSS (type 329J3L).

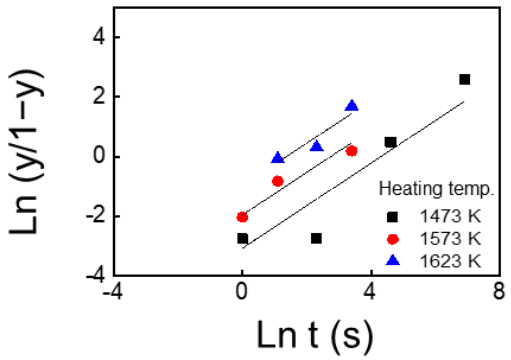

(c) Super DSS (type 327L1).

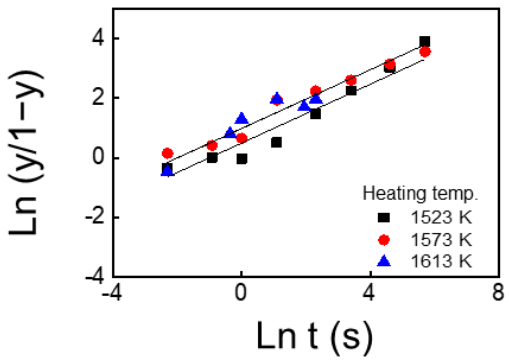

(d) Lean DSS (lab).

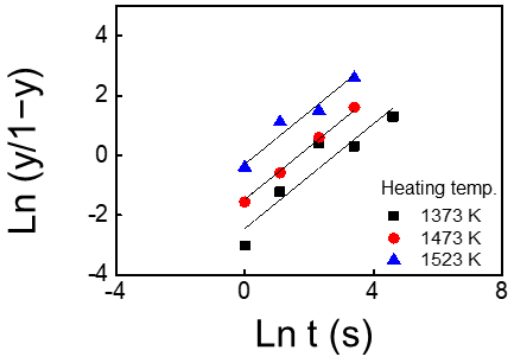

(e) Super DSS (type 329J4L).

Fig. 3.5 Austin–Rickett plots of the γ phase dissolution behavior in the base material HAZs for the DSSs at different temperatures.

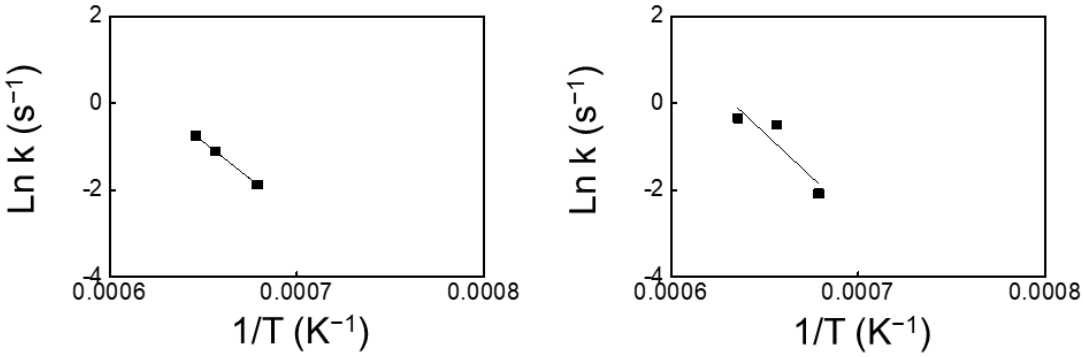

(a) Lean DSS (type 821L1).

(b) Standard DSS (type 329J3L).

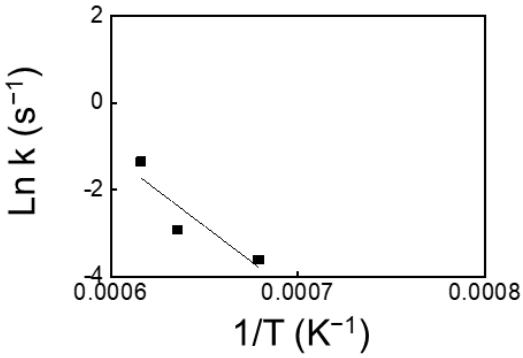

(c) Super DSS (type 327L1).

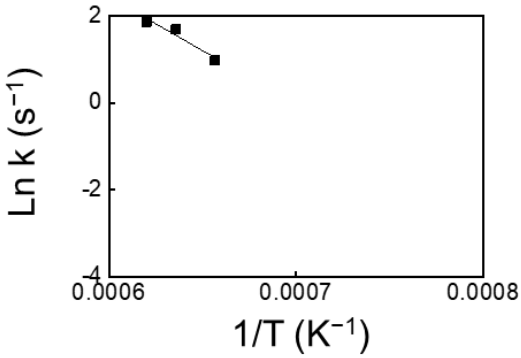

(d) Lean DSS (lab).

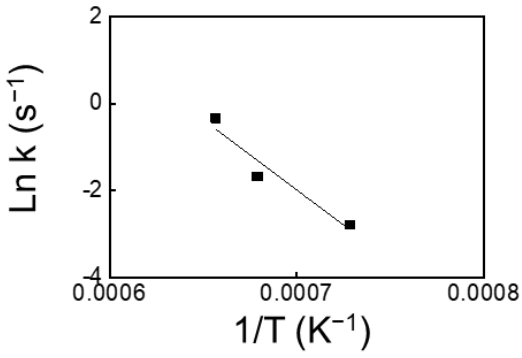

(e) Super DSS (type 329J4L).

Fig. 3.6 Arrhenius plots of the dissolution rates constants of the γ phase in the base material HAZs for the DSSs.

Table 3.6 Experimental temperature dependencies of the γ phase dissolution in DSSs (base materials).

Steel type	Time constant, n	The temperature dependency of dissolution rate [s^{-1}]	ΔG [kJ/mol]
Lean DSS (type 821L1)	0.93	$K=\exp(\frac{-3.43\times10^4}{T}+21.4)$	285
Standard DSS (type 329J3L)	0.64	$K=\exp(\frac{-4.05\times10^4}{T}+25.64)$	337
Super DSS (type 327L1)	0.72	$K=\exp(\frac{-3.26\times10^4}{T}+18.39)$	271
Lean DSS (lab)	0.49	$K=\exp(\frac{-2.47\times10^4}{T}+17.24)$	205
Super DSS (type 329J4L)	0.87	$K=\exp(\frac{-3.23\times10^4}{T}+20.62)$	268

3.3.2 Kinetics of γ dissolution phenomenon of the weld metals

As described in Introduction, the WM of DSSs are generally solidified as the F mode, and a γ phase comes to precipitate in the solidified a structure during cooling. In Section 3.3.2, we investigated the precipitation kinetics of γ phase in WM (reheated WM) for three kinds DSSs: lean (lab), standard (type 329J3L), and super (type 327L1). The dissolution heat treatment of weld metals was investigated based on the dissolution heat treatment method described in Table 3.4. Fig. 3.7 shows the effects of heat temperature and holding time on the volume fraction of γ phase in lean (lab), standard (type 329J3L), and super (type 327L1) DSSs. Fig. 3.8 shows an Austin–Rickett plot of the dissolution behavior of the γ phase in DSSs (reheated WM) in which a good linear relationship can be seen, and the time exponents (n) of the dissolution of the γ phase in lean (lab), standard (type 329J3L), and super (type 327L1) DSSs were found to be 0.55, 0.36 and 0.37. This shows that the dissolution kinetics of the γ phase in DSSs can be expressed by the Austin–Rickett equation.

The Arrhenius plots shown in Fig. 3.9 were obtained to investigate the temperature dependencies of the dissolution rate of the γ phase in DSSs. From the figure, it can be seen that ln k and $1/T$ have a good linear relationship. Then, the temperature dependencies of the dissolution rate of the γ phase in lean (lab), standard (type 329J3L), and super (type 327L1) DSSs were investigated, and the results are presented in Table 3.7.

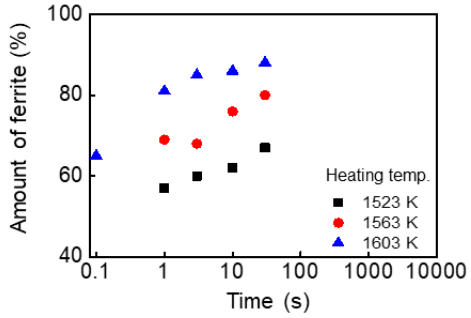

(a) Lean DSS (lab).

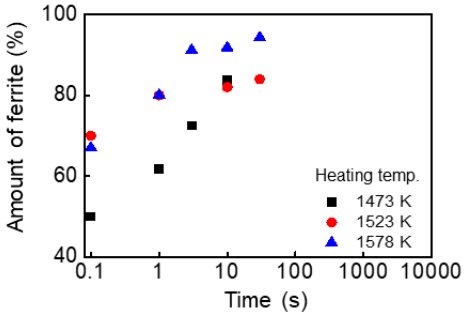

(b) Standard DSS (type 329J3L).

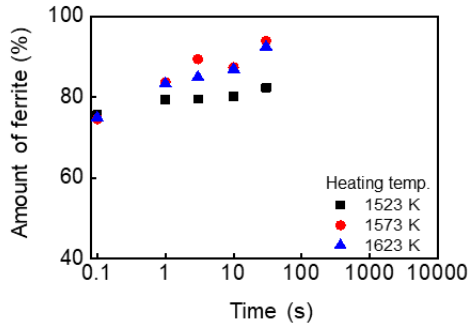

(c) Super DSS (type 327L1).

Fig. 3.7 Changes in the dissolved γ fraction for the DSSs at different temperatures.

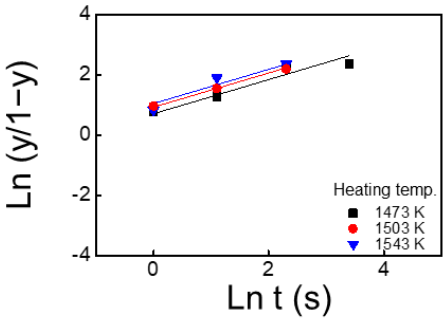

(a) Lean DSS (lab).

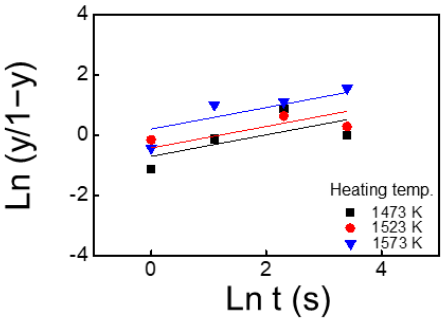

(b) Standard DSS (type 329J3L).

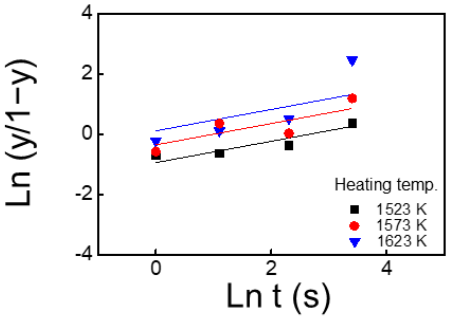

(c) Super DSS (type 327L1).

Fig. 3.8 Austin–Rickett plots of the γ phase dissolution behavior in the weld metals for the DSSs at different temperatures.

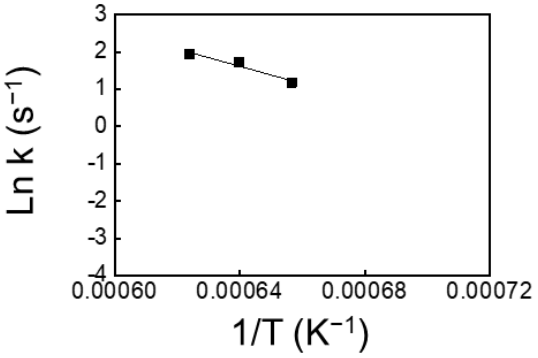

(a) Lean DSS (lab).

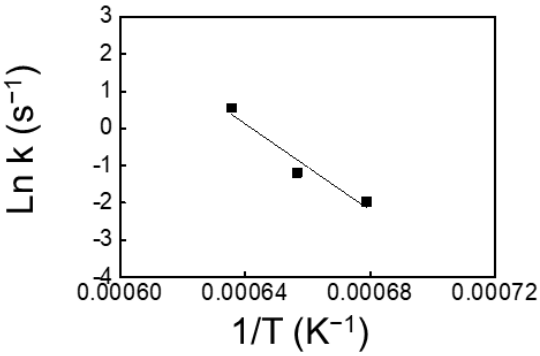

(b) Standard DSS (type 329J3L).

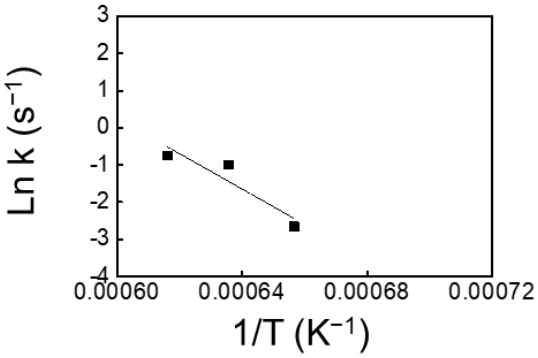

(c) Super DSS (type 327L1).

Fig. 3.9 Arrhenius plots of the dissolution rates constants of the γ phase in the weld metals for the DSSs.

Table 3.7 Experimental temperature dependencies of the γ phase dissolution in DSSs (weld metals).

Steel type	Time constant, *n*	The temperature dependency of dissolution rate [s^{-1}]	ΔG [kJ/mol]
Lean DSS (lab)	0.55	$K=\exp(\frac{-2.33\times10^4}{T}+16.5)$	193
Standard DSS (type 329J3L)	0.36	$K=\exp(\frac{-5.83\times10^4}{T}+37.4)$	484
Super DSS (type 327L1)	0.37	$K=\exp(\frac{-4.7\times10^4}{T}+28.8)$	395

3.3.3 Kinetics of γ precipitation phenomenon of the base materials

The change in microstructure of DSSs during the precipitation treatment was investigated.

Fig. 3.10 shows an example of microstructural change (phase mapping by EBSD analysis) in lean DSS (type 821L1) with the precipitation treatment condition. A γ phase was precipitated not only at the grain boundaries (GBs) (Widmanstätten–like) but also in the grains of α, and the amount of γ phase increased with an increase in the heating temperature. Similar precipitation behavior has been observed in standard and super DSSs. Fig. 3.11 shows the effects of heat temperature and holding time on the volume fraction of γ phase in lean (lab), standard (type 329J3L), super (type 327L1), lean (type 821L1), and super (type 329J4L) DSSs.

The fraction of γ phase was increased with an increase in the heat temperature and holding time, and saturated at an equilibrium fraction in all steels. As described in the dissolution phenomenon, the precipitation kinetics of the γ phase from previous studies [123–127, 167] were investigated using the Austin–Rickett equation, thereby verifying its applicability to the precipitation phenomenon. Fig. 3.12 shows an Austin–Rickett plot of the precipitation behavior of the γ phase in DSSs (base metal HAZs), in which a good linear relationship can be seen, and the time exponents (n), of the precipitation of the γ phase in lean (lab), standard (type 329J3L), super (type 327L1), lean (type 821L1), and super (type 329J4L) DSSs were found to be 0.95, 1.3, 0.57, 0.91, and 0.44, respectively as shown in table 3.8. According to Fig.3.12, the precipitation of γ phase in standard (type329J3L) and super (type 327L1) DSSs was fastest at the heating temperature around 1273 K, lean (lab) and lean (type 821L1) DSSs was fastest at the heating temperature around 1223 K, while that in super (type 329J4L) DSS around 1323 K.

The fact that the precipitation of γ phase in DSSs becomes fastest at the certain intermediate temperature (*i.e.*, possesses a "nose") means that the temperature dependency of precipitation rate would not followed by the simple Arrhenius–type equation as indicated by Eq. (3.4).

Therefore, the temperature dependency of precipitation rate of γ phase in DSSs, which indicates a C–curved diagram with a nose, was theoretically discussed. Assuming that precipitation of γ phase is controlled by the non–uniform nucleation in an α grain and at the α –GB, and grows inward an α grain, the non–uniform nucleation rate I can be expressed by Eq. (3.5) [168];

$$l = \nu n \left(\frac{d}{L}\right)^{3-j} \exp\left(-\frac{\Delta G_a - \Delta G^*}{RT}\right) \tag{3.5}$$

where ν is the frequency factor m is the number of atoms per unit volume, d is the effective GB thickness, L is the grain diameter, j is the dimensionality of site, ΔG^* is the minimum free energy required to form a nucleus, and ΔG_a is the free energy of activation for a nucleus to continue to grow. Terms in Eq. (3.5) which have temperature dependency are m, L and ΔG^*. However, the variation of m is negligible compared with the temperature dependency of exponential term, and L is regarded as constant because the starting specimen is a solution treated specimen at 1653 K for 60 s. Consequently, temperature dependent term in Eq. (3.5) is only ΔG^*, and can be expressed by Eq. (3.6) from the Spherical–Cap model [169];

$$\Delta G^* = \frac{16\pi(\sigma_{\alpha/\gamma})^3}{3\left(\Delta G v_{\alpha\leftrightarrow\gamma}\right)^2} f(\theta) \tag{3.6}$$

where $Gv_{\alpha\leftrightarrow\gamma}$ is the volume free energy change from α to γ phase, θ is the wetting angle of γ phase at the α–GB, and is expressed by the following relationships;

$$\Delta Gv_{\alpha\leftrightarrow\gamma} = \frac{\Delta H_{\alpha/\gamma}(T_E - T)}{V_m T_E} \tag{3.7}$$

$$\cos\theta = \frac{\sigma_{\alpha/\alpha} - \sigma_{\alpha/\gamma}}{\sigma_{\alpha/\gamma}} \tag{3.8}$$

$$f(\theta) = \frac{2 - 3\cos\theta + \cos^3\theta}{4} \tag{3.9}$$

where T_E is the starting temperature of precipitation of γ phase (γ solvus), $\Delta H_{\alpha/\gamma}$ is the change in enthalpy from α to γ phase at T_E, V_m is the molar volume, $\sigma_{\alpha/\alpha}$ and $\sigma_{\alpha/\gamma}$ are the interfacial energies between α and α phases, α and γ phases, respectively. Assuming that $\sigma_{\alpha/\alpha}$ and $\sigma_{\alpha/\gamma}$ are independent on temperature, ΔG^* in Eq. (3.5) is inversely proportional to the square of degree of undercooling from the starting temperature of the γ phase precipitation, $(T_E–T)^2$, and expressed by;

$$\Delta G^* = \frac{B^*}{(T_E - T)^2} \tag{3.10}$$

where B^* is an arbitrary coefficient. Consequently, the non–uniform nucleation rate I in Eq. (3.5) can be expressed by;

$$I = A^* \exp\left(-\frac{\Delta G_a}{RT}\right) \cdot \exp\left\{\frac{-B^*}{RT(T_E - T)^2}\right\} \tag{3.11}$$

Assuming that the progress in transformation from α to γ phase is controlled by the non–uniform nucleation, the temperature dependency of rate constant $K(T)$ can be also given by;

$$K(T) = A^* \exp\left(-\frac{\Delta G_a}{RT}\right) \cdot \exp\left\{\frac{-B^*}{RT(T_E - T)^2}\right\} \tag{3.12}$$

where A^* is an arbitrary coefficient. Fig. 3.13 schematically shows the temperature dependency of the rate constant $K(T)$ expressed by Eq. (3.12). The rate constant approaches asymptotically to two types of Arrhenius equation in the temperature ranges below/above a nose.

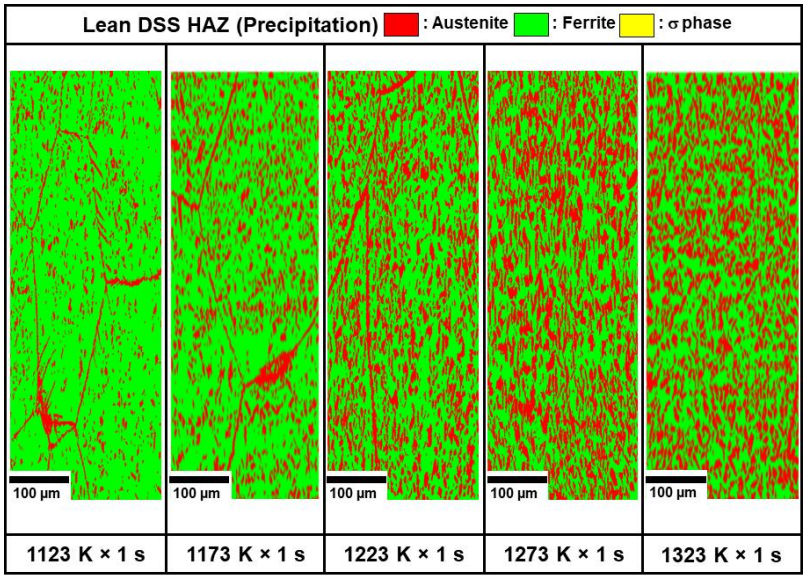

Fig. 3.10 Microstructural changes in lean DSS (type 821L1) with precipitation treatment.

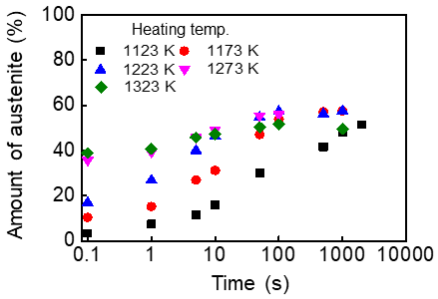

(a) Lean DSS (type 821L1).

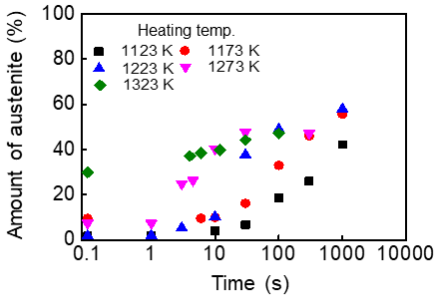

(b) Standard DSS (type 329J3L).

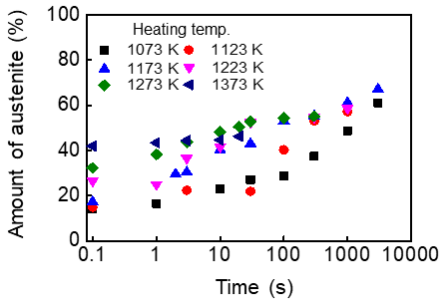

(c) Super DSS (type 327L1).

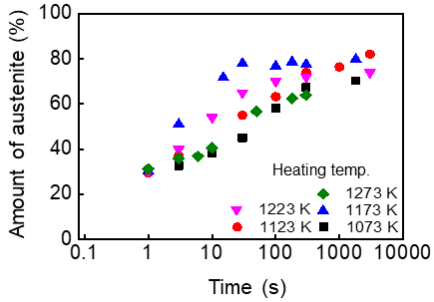

(d) Lean DSS (lab).

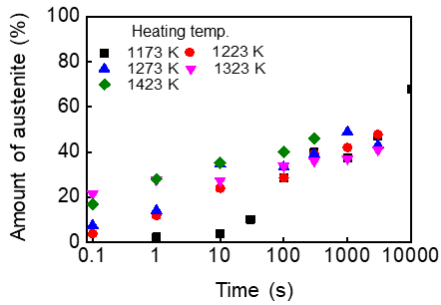

(e) Super DSS (type 329J4L).

Fig. 3.11 Changes in the precipitated γ fraction for the DSSs at different temperatures.

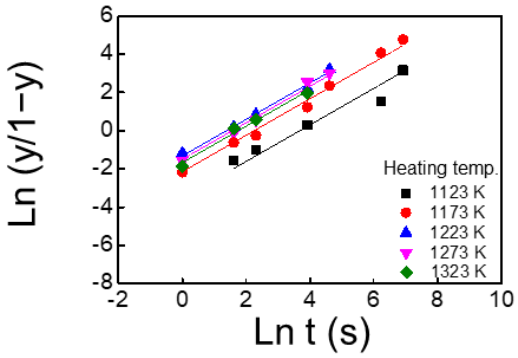

(a) Lean DSS (type 821L1).

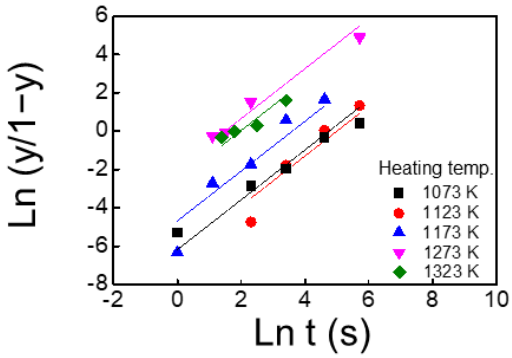

(b) Standard DSS (type 329J3L).

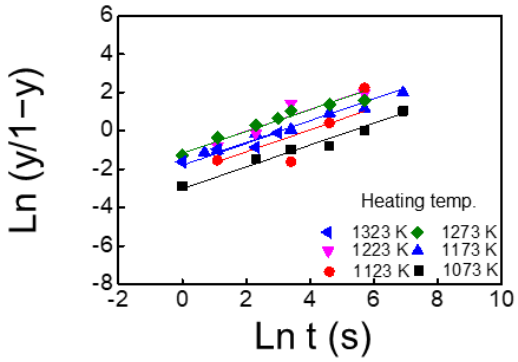

(c) Super DSS (type 327L1).

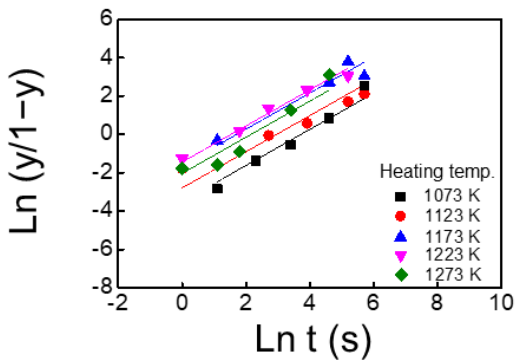

(d) Lean DSS (lab).

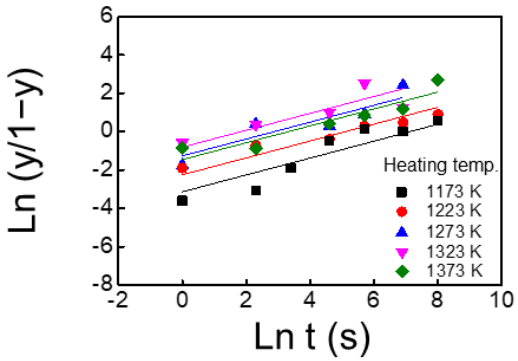

(e) Super DSS (type 329J4L).

Fig. 3.12 Austin–Rickett plots of the γ phase precipitation behavior in the base material HAZs for the DSSs at different temperatures.

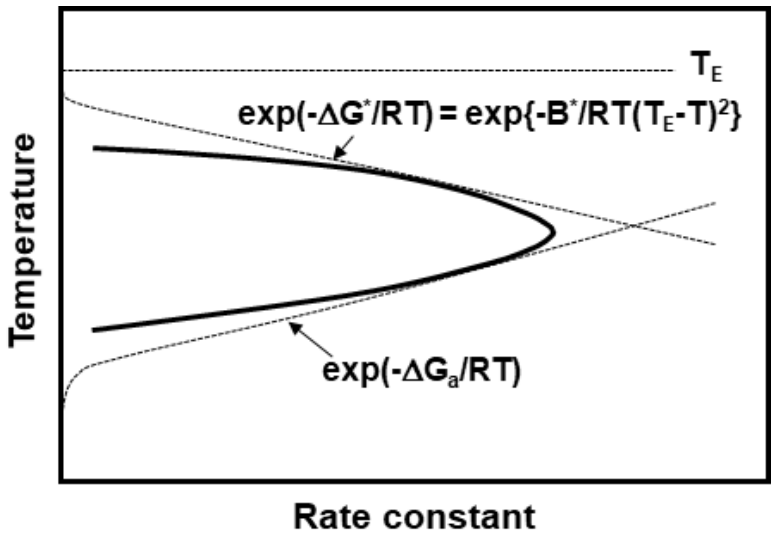

Fig. 3.13 Temperature dependency of rate constant.

On the other hand, from the fact that a γ phase in DSS welds grows as the Widmanstätten structure from α–GBs into grains, the precipitation amount of γ phase depends on both nucleation and growth. Namely, the fraction transformed y depends on the nucleation rate, diffusion speed and time, and dissolving a diffusion equation assuming the local equilibrium at the α/γ interface, the rate constant $K(T)$ can be approximately expressed by Eq. (3.13) [170];

$$K(T) = -\frac{16\sqrt{2}}{15} \cdot \pi \cdot D^{2/3} \left(\frac{C_\alpha - C_E}{C_\gamma - C_E} \right) \cdot I \tag{3.13}$$

where D is the diffusion constant (of N or Ni), C_α and C_γ are the solute concentrations (N or Ni) in α and γ phases, respectively, C_E is the equilibrium concentration of solute element (N or Ni) in α phase at the α/γ interface. The diffusion constant can be given by;

$$D = D_0 \exp\left(-\frac{\Delta G_a}{RT} \right) \tag{3.14}$$

Approximately assuming that C_α, C_γ and C_E are independent of the temperature and the amount of γ phase (*i.e.*, negligible small compared to the temperature dependency of exponential term), Eq. (3.13) can be transformed to;

$$K(T) = A^{**} \exp\left(-\frac{\Delta G_a}{RT} \right)^{2/3} \cdot \exp\left(\frac{\Delta G_a}{RT} \right) \cdot \exp\left\{ \frac{-B^*}{RT(T_E - T)^2} \right\} \tag{3.15}$$

where A^{**} is an arbitrary coefficient. Eq. (3.15) can be transformed to;

$$K(T) = A^{**} \exp\left(-\frac{5\Delta G_a}{3RT} \right) \cdot \exp\left\{ \frac{-B^*}{RT(T_E - T)^2} \right\} \tag{3.16}$$

Eq. (3.16) can be simplified by Eq. (3.17) using three undetermined coefficients A, B and C;

$$K(T) = A \exp\left(-\frac{B}{RT}\right) \cdot \exp\left\{\frac{-C}{RT(T_E - T)^2}\right\} \tag{3.17}$$

Based on the experimental results (Fig. 3.12), the temperature dependency of the precipitation rate constants of γ phase were determined by a regression analysis (T_E can be calculated by the phase computation software, Thermo–Calc, Database: TCFE6). Fig.3.14 shows the temperature dependency of the precipitation rate constants of γ phase in DSSs (regression analysis results of rate constants), and the results are presented in Table 3.8. The temperature dependency of precipitation rate of γ phase in base metal HAZs of DSSs, which indicates a C–curved diagram with a nose, could be obtained in the present study.

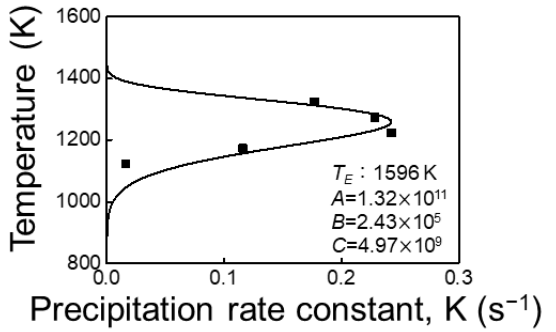

(a) Lean DSS (type 821L1).

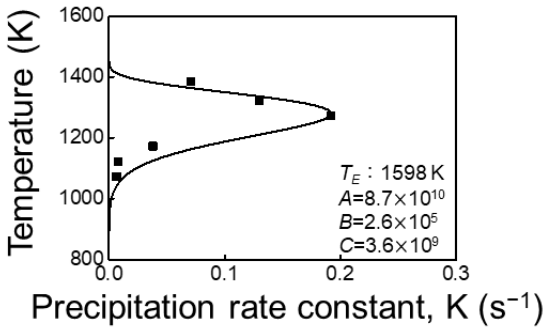

(b) Standard DSS (type 329J3L).

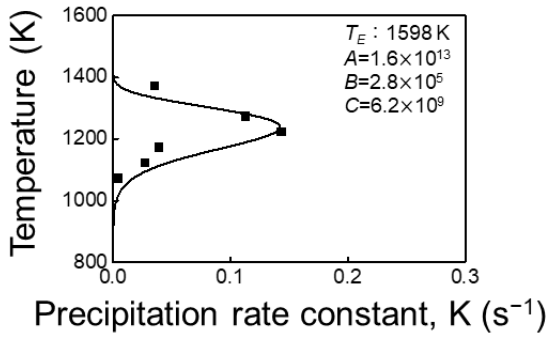

(c) Super DSS (type 327L1).

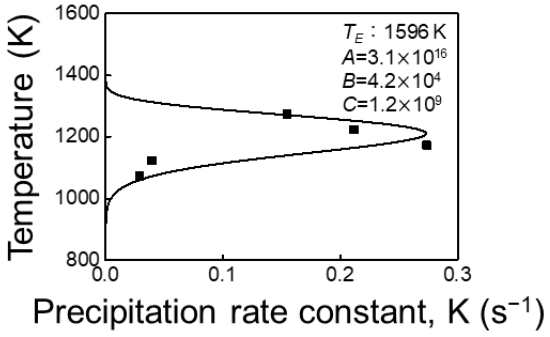

(d) Lean DSS (lab).

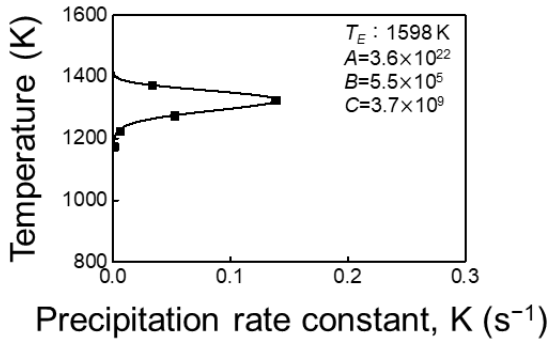

(e) Super DSS (type 329J4L).

Fig. 3.14 Regression analysis of the precipitation rate constants of the γ phase in the base material HAZs for the DSSs.

Table 3.8 Experimental time constant and rate constant of γ precipitation in DSSs (base materials).

Steel type	Time constant, n	Nose temperature (K)	Maximum value of the rate constant, K (s^{-1})
Lean DSS (type 821L1)	0.95	1258	0.24
Standard DSS (type 329J3L)	1.3	1273	0.192
Super DSS (type 327L1)	0.57	1223	0.143
Lean DSS (lab)	0.91	1173	0.27
Super DSS (type 329J4L)	0.44	1323	0.17

3.3.4 Kinetics of γ precipitation phenomenon of the weld metals

The precipitation heat treatment of weld metals was investigated based on the precipitation heat treatment method described in Table 3.4. Fig. 3.15 shows the effects of heat temperature and holding time on the volume fraction of γ phase in lean (lab), standard (type 329J3L), and super (type 327L1) DSSs. The fraction of γ phase was increased with an increase in the heat temperature and holding time, and saturated at an equilibrium fraction in all steels. The Austin–Rickett plots of precipitation behavior of γ phase in the WM of lean (lab), standard (type 329J3L), and super (type 327L1) DSSs are shown in Fig. 3.16. There were good linear relationships in the Austin–Rickett plot again, and gradients of the lines were almost identical for all steels. The time exponents (n) of the lean (lab), standard (type 329J3L), and super (type 327L1) DSSs WM were determined as 0.5, 0.85 and 0.67, respectively. The precipitation rates of γ phase in the DSSs WM also possess the temperature dependency with a nose. The nose temperature of precipitation in the lean (lab), standard (type 329J3L), and super (type 327L1) DSSs WM were around 1323 K. It follows that precipitation kinetics of γ phase in the reheated WM is also followed by the Austin–Rickett type equation. Based on the experimental results (Fig. 3.16), the temperature dependency of the precipitation rate constants of γ phase were determined by a regression analysis (T_E can be calculated by the phase computation software, Thermo–Calc, Database: TCFE6). Fig. 3.17 shows the temperature dependency of the precipitation rate constants of γ phase in DSSs (regression analysis results of rate constants), and the results are presented in Table 3.9. The temperature dependency of precipitation rate of γ phase in the reheated WM of DSSs could be also obtained in the present study.

Table 3.9 Experimental time constant and rate constant of γ precipitation in DSSs (weld metals).

Steel type	Time constant, *n*	Nose temperature (K)	Maximum value of the rate constant, *K* (s^{-1})
Lean DSS (lab)	0.5	1333	0.28
Standard DSS (type 329J3L)	0.85	1363	0.2
Super DSS (type 327L1)	0.67	1308	0.21

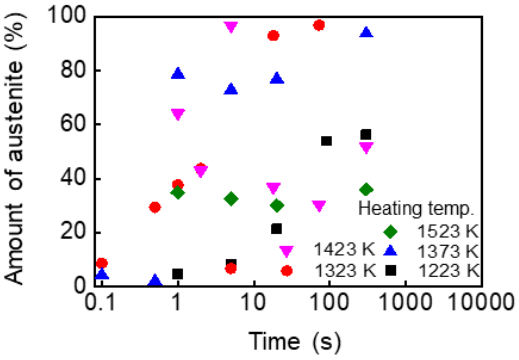

(a) Lean DSS (lab).

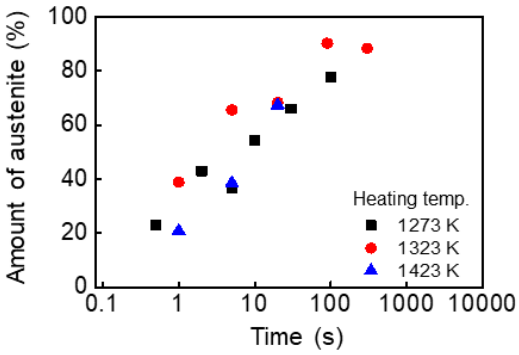

(b) Standard DSS (type 329J3L).

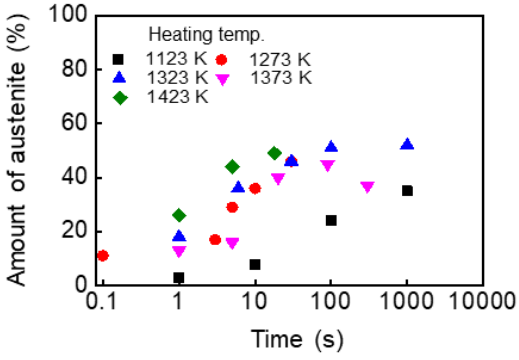

(c) Super DSS (type 327L1).

Fig. 3.15 Changes in the precipitated γ fraction for the DSSs at different temperatures.

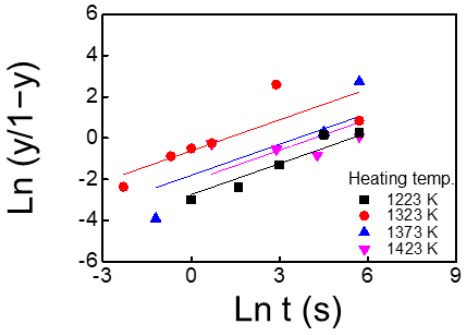

(a) Lean DSS (lab).

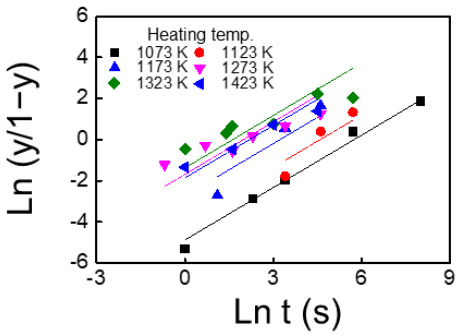

(b) Standard DSS (type 329J3L).

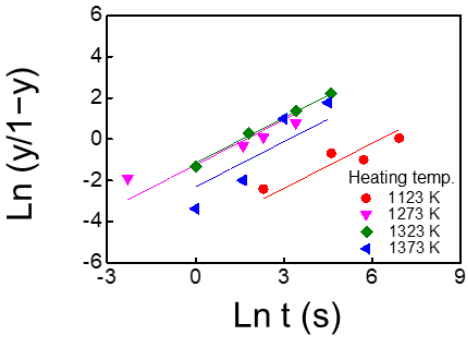

(c) Super DSS (type 327L1).

Fig. 3.16 Austin–Rickett plots of the γ phase precipitation behavior in the weld metals for the DSSs at different temperatures.

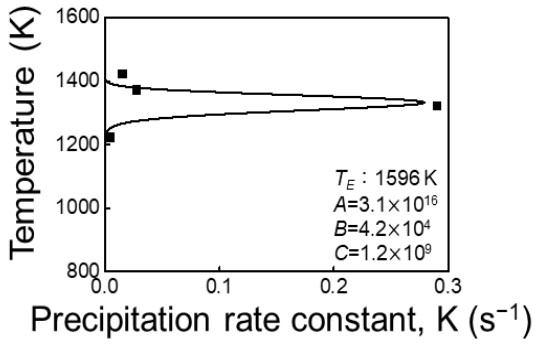

(a) Lean DSS (lab).

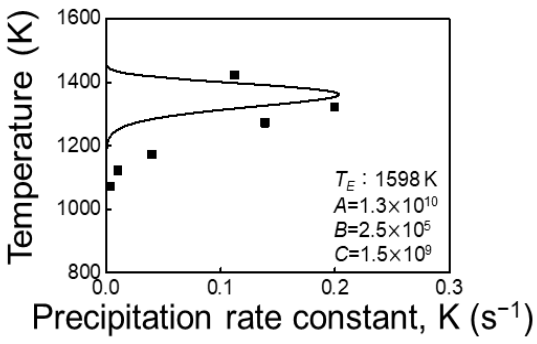

(b) Standard DSS (type 329J3L).

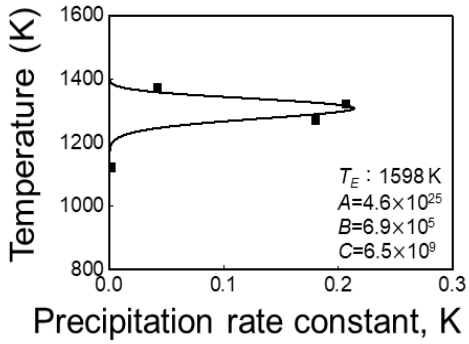

(c) Super DSS (type 327L1).

Fig. 3.17 Regression analysis of the precipitation rate constants of the γ phase in the weld metals for the DSSs.

3.4 Prediction of phase transformation in the multi–pass welds

3.4.1 Finite–element simulation model

In order to expand the isothermal kinetics of dissolution and precipitation determined above to the non–isothermal process such as thermal cycle processes, the incremental method was applied. The method of calculating the γ amount in the multi–pass welds were performed based on the previous study [126–127]. Besides, in this study, α/γ phase transformation prediction was conducted for five types of DSSs. Among them, lean (lab), standard (type 329J3L), and super (type 327L1) DSSs were predicted for multi–pass welds. Meanwhile, for lean (type 821L1), super (type 329J4L) DSSs, prediction for multi–pass HAZs was performed. The finite–element analysis model for predicting the γ amount in multi–pass welds was created using Quick–welder software (Research Center of Computational Mechanics, Japan). Fig. 3.18 shows the cross–sectional views and mesh division (weld pass sequence) of a multi–pass welds (GTAW) of Three types of DSSs used for numerical analyses of the thermal cycle and α/γ phase transformation (distribution of the α/γ phase fraction). The solid line represents the fusion line.

The minimum mesh size was approximately 0.25 mm × 0.25 mm. The α single–phasing and solidus temperature of lean (lab), standard (type 329J3L), and super (type 327L1) DSSs calculated using Thermo–Calc (Database; TCFE6) are summarized in Table 3.10. In addition, the thermal properties of the lean (lab), standard (type 329J3L), and super (type 327L1) DSSs [42] used in the thermal conduction analysis are shown in Fig. 3.19 (assuming to be identical regardless of the steel grade). The increment method [40–41] was applied to extend the experimentally determined isothermal kinetics of dissolution and precipitation to non–isothermal processes such as welding. A flowchart of the prediction process of the γ amount of multi–pass welding is shown in Fig. 3.20. To calculate the amount of precipitation or dissolution of the γ phase and the amount of γ phase at that time, the amount of γ phase at each stage is compared with the amount of the α/γ equilibrium. The temperature dependence of the equilibrium γ phase fraction of the lean (lab), standard (type 329J3L), and super (type 327L1) DSSs (determined based on the results of measurements combined with the values calculated using Thermo–Calc (Database; TCFE6) are shown in Fig. 3.21. The reflected process was repeatedly performed until the completion of the multi–pass welding (or the completion time of each pass). From these procedures, the dissolution and precipitation behavior of the γ phase during multiple thermal cycles was numerically simulated. In this study, we repeated these calculations for the entire weld area to visualize the distribution of γ phase fractions in multi–pass welding.

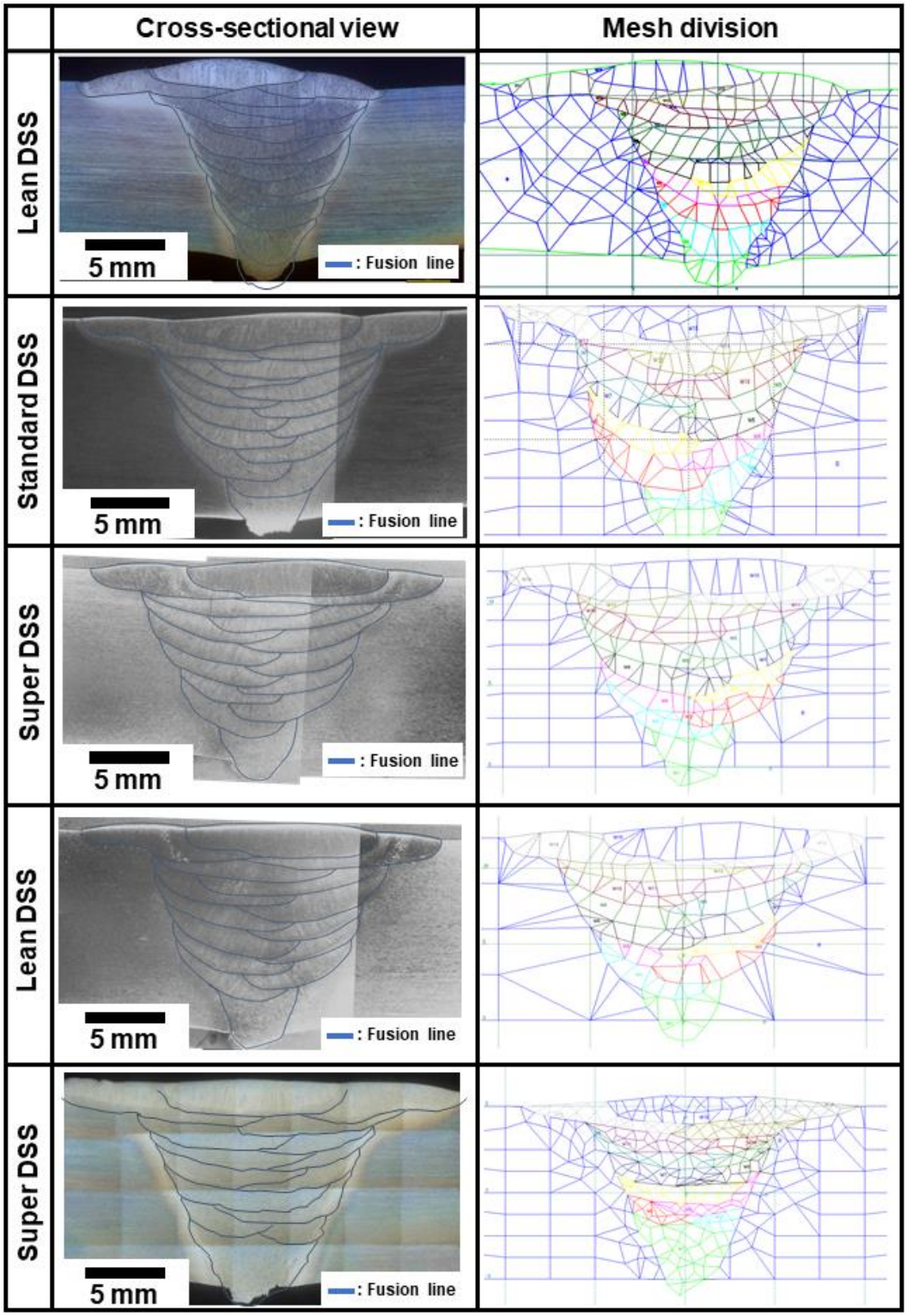

Fig. 3.18 Cross–sectional views and mesh division of multi–pass welds of DSSs.

Table 3.10 α single–phasing and solidus temperatures of DSSs.

Steel	α single–phasing temp.	Solidus temp.
Lean DSS (lab)	1596 K	1683 K
Standard DSS (type 329J3L)	1598 K	1647 K
Super DSS (type 327L1)	1598 K	1604 K

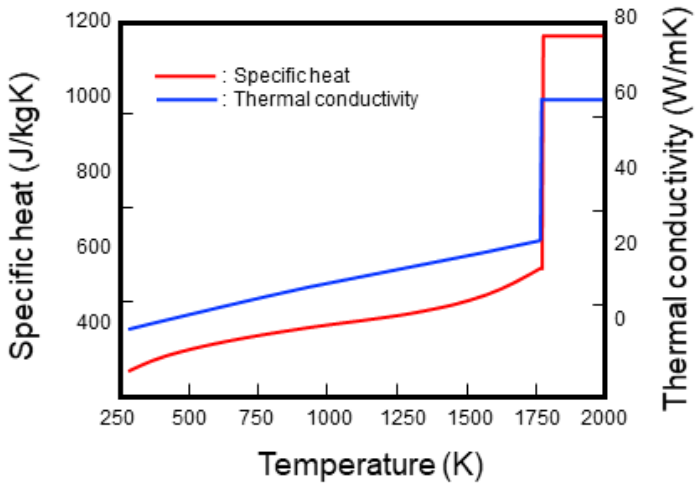

Fig. 3.19 Physical properties of DSS used for calculation.

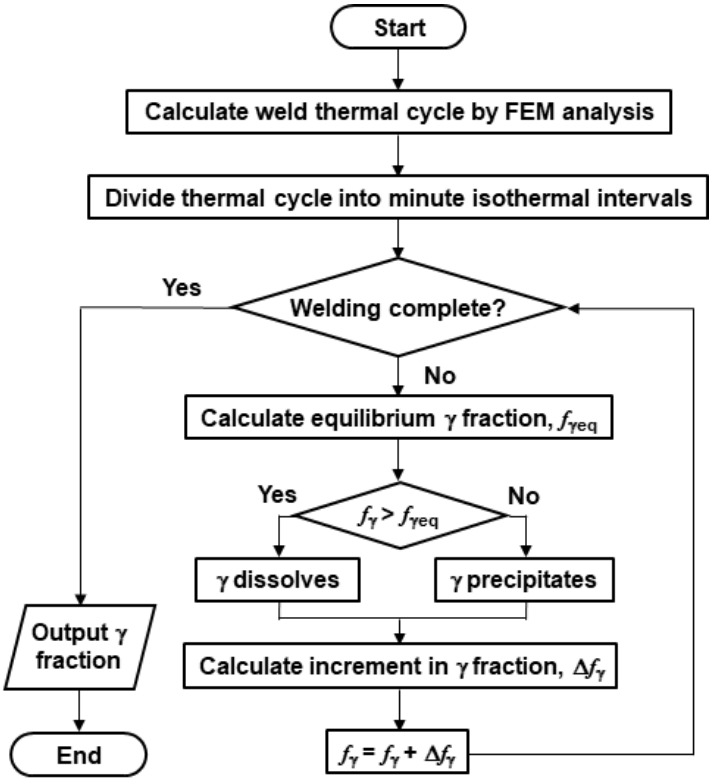

Fig. 3.20 Flowchart of computation of phase transformation in multi–pass welds.

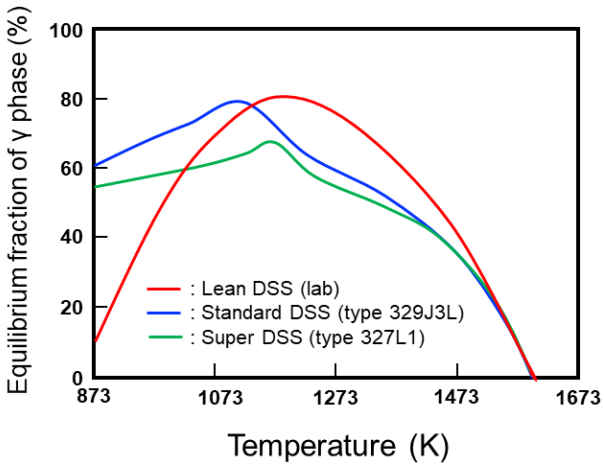

Fig. 3.21 Temperature dependency of equilibrium γ phase fraction of DSSs.

3.4.2 Computed results of austenitic phase fraction in multi–pass welds

Fig. 3.22 shows the distribution of the γ phase fraction (indicated by color contour) calculated in the multi–pass welds of lean (lab) DSS. This figure exhibits the entire history of the distribution of the γ phase fraction at the completion of each weld pass during multi–pass welding. The dashed lines in the figure indicate the fusion lines of weld passes. The γ phase fraction in the just solidified WM was considerably small in any weld passes, and the depleted zone of γ phase was formed adjacent to the fusion line ("under–bead" region) in the base material HAZs and reheated WMs. However, the γ phase fraction in the depleted zone was increased by the subsequent weld passes (the γ phase was re–precipitated by the thermal cycles in subsequent welding). Accordingly, the α/γ phase balance has been complexly varied in multi–pass welds, and the profile of the γ phase fraction was arranged in laminae in the WM roughly along the fusion lines. The minimum γ phase fraction in multi–pass welds was approx. 20 % located in the base material HAZ of the final weld layer, and the γ phase fraction in WMs was reduced to approx. 25 %. On the other hand, the γ phase fraction in a part of base material HAZ (low temperature HAZ) was exceeded to that in the base material, because of the additional precipitation of γ phase during multi–pass welding. The distribution of the γ phase fraction calculated in the multi–pass welds of standard (type 329J3L), and super (type 327L1) DSSs is also shown in Fig. 3.23 and Fig. 3.24, respectively. Quite similar tendencies to lean (lab) DSS welds were observed in the distribution of the γ phase fraction, that is, the γ phase fraction was reduced in the solidified WM and under–bead region of WM as well as the base material HAZ, while the γ phase fraction in the depleted zone was recovered by the subsequent weld passes. As a result, the α/γ phase balance has been complexly varied in multi–pass welds. Figs. 3.25–3.26 shows the result of the γ phase fraction calculated in the multi–pass HAZ.

Furthermore, it shows that the γ amount of the HAZ (base material) of the first pass is less than 30 %. However, as the pass progresses, re–precipitation occurs due to the thermal cycle in subsequent welding, thereby recovering the amount of γ. However, the amount of γ in the final weld is considerably reduced compared to that in other welds because the amount of γ is no longer affected by the subsequent thermal cycle. This is because the ratio of α/γ owing to the

insufficient amount of γ, becomes misaligned. Consequently, it was confirmed that the α/γ phase transformation in the multi–pass welded part exhibits a highly complex behavior, as in the results of Figs. 3.22–3.26. Additionally, in the case of lean (type 821L1) and super (type 329J4L) DSSs in this doctoral dissertation, the kinetics of weld metals were not conducted.

Therefore, only the multi–pass HAZs were to be predicted. In the future, if the kinetics of the weld metals are carried out, it is considered that it will be possible to predict the γ phase fraction of the multi–pass welds using the prediction technique applied in this study.

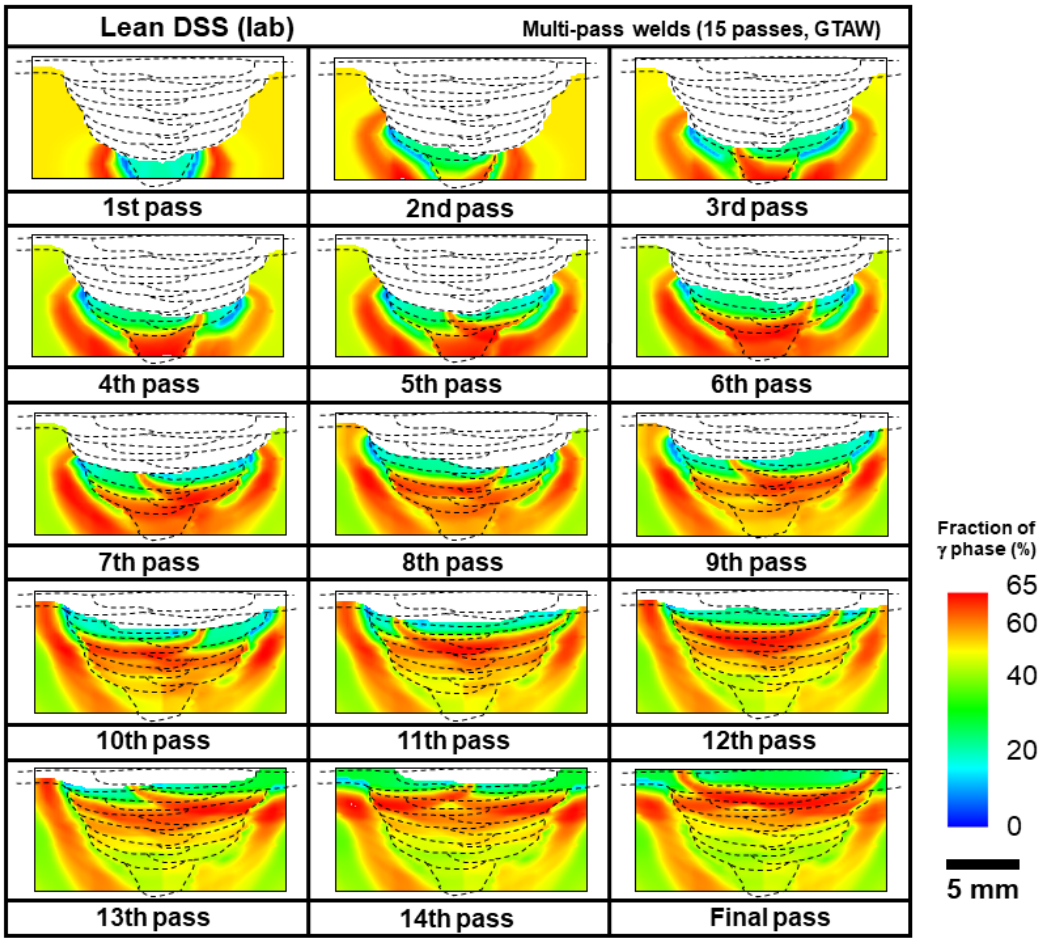

Fig. 3.22 Distribution of the γ phase fraction calculated in a multi–pass welds of lean DSS (lab).

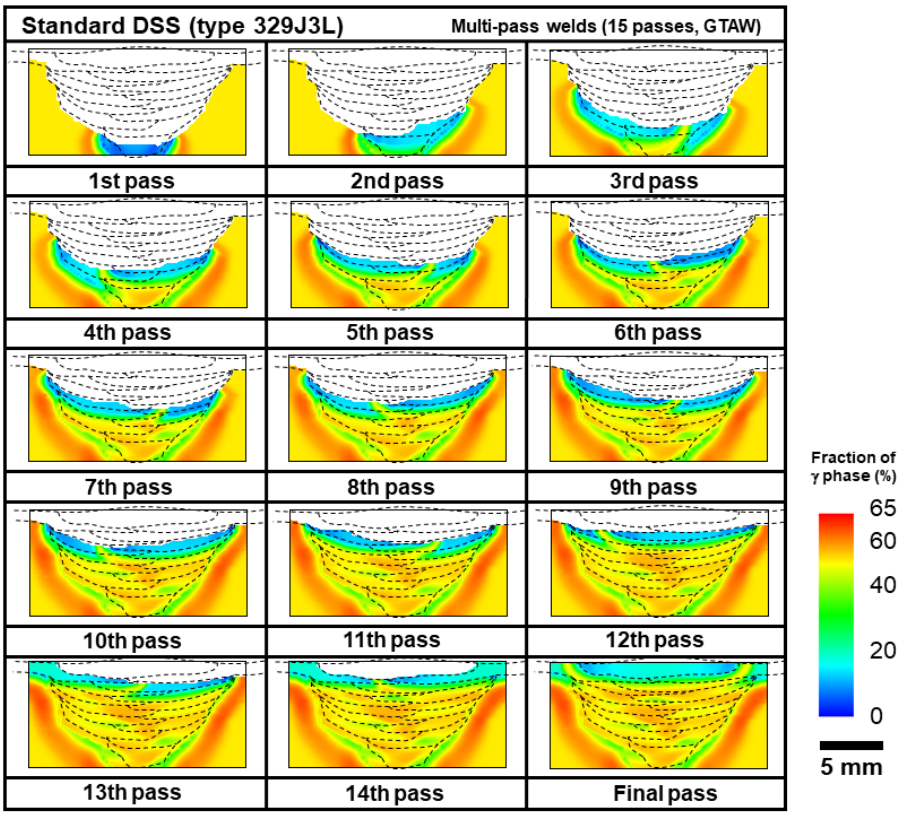

Fig. 3.23 Distribution of the γ phase fraction calculated in a multi–pass welds of standard DSS (type 329J3L).

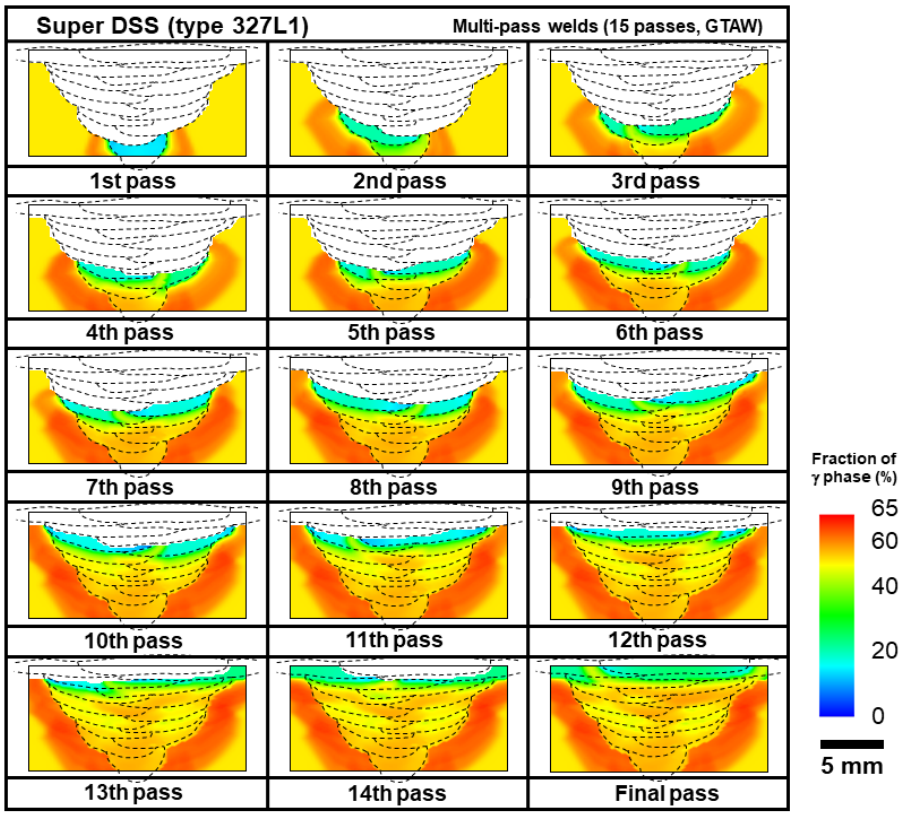

Fig. 3.24 Distribution of the γ phase fraction calculated in a multi–pass welds of super DSS (type 327L1).

.

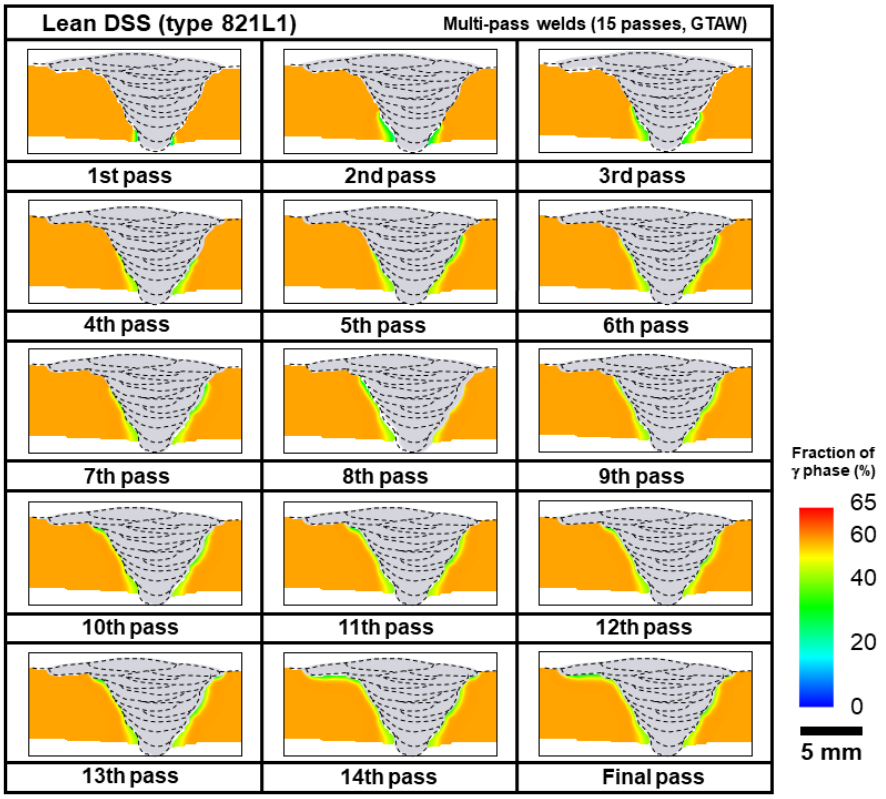

Fig. 3.25 Distribution of the γ phase fraction calculated in a multi–pass HAZs of lean DSS (type 821L1).

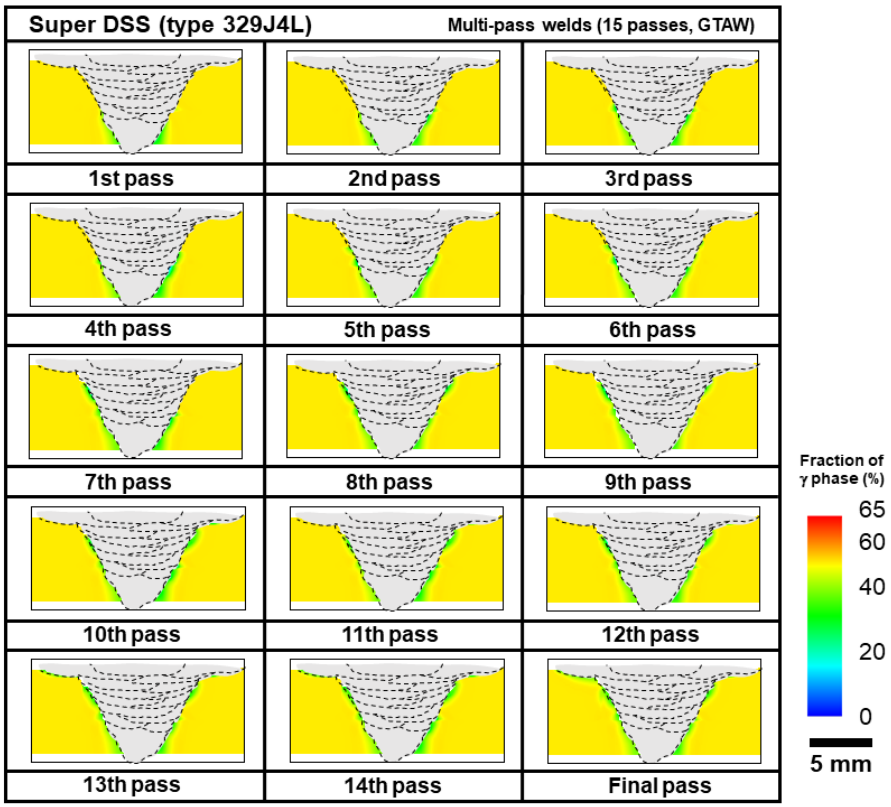

Fig. 3.26 Distribution of the γ phase fraction calculated in a multi–pass HAZs of super DSS (type 329J4L).

3.4.3 Comparison of calculated and measured austenitic phase fraction in multi–pass welds

In order to validate the predicted results of the α/γ phase transformation, the γ phase fraction in the multi–pass welds were compared between calculated and measured. Fig. 3.27 shows the example of microstructure (phase mapping by EBSD analysis) of multi–pass welds. A dashed line in Fig. 3.27 indicates the fusion line. The γ phase fraction at the various positions was measured in multi–pass welds. Fig. 3.28 shows the comparison of the γ phase fraction between calculated and measured in the multi–pass welds (GTAW) of lean, standard and super DSSs, respectively. In these figures, a fig. 3.28(a) indicates the analysis spots (positions) of the γ phase fraction, and a fig. 3.28(b) indicates the correlation between the calculated γ phase fraction and measured one. Although there were small scatters between the calculated and measured values, the calculated results were fairly consistent with measured ones (correlation coefficients; 0.7 –0.8) in all welds (in the WM, reheated WM as well as the base metal HAZ). It follows that the α/γ phase transformation in the DSSs multi–pass welds could be predicted semi–quantitatively by the present kinetic approach and computer simulation. In particular, the γ phase–depleted zone in the multi–pass welds, where the mechanical and corrosion properties would be potentially deteriorated, could be estimated with a high degree of accuracy.

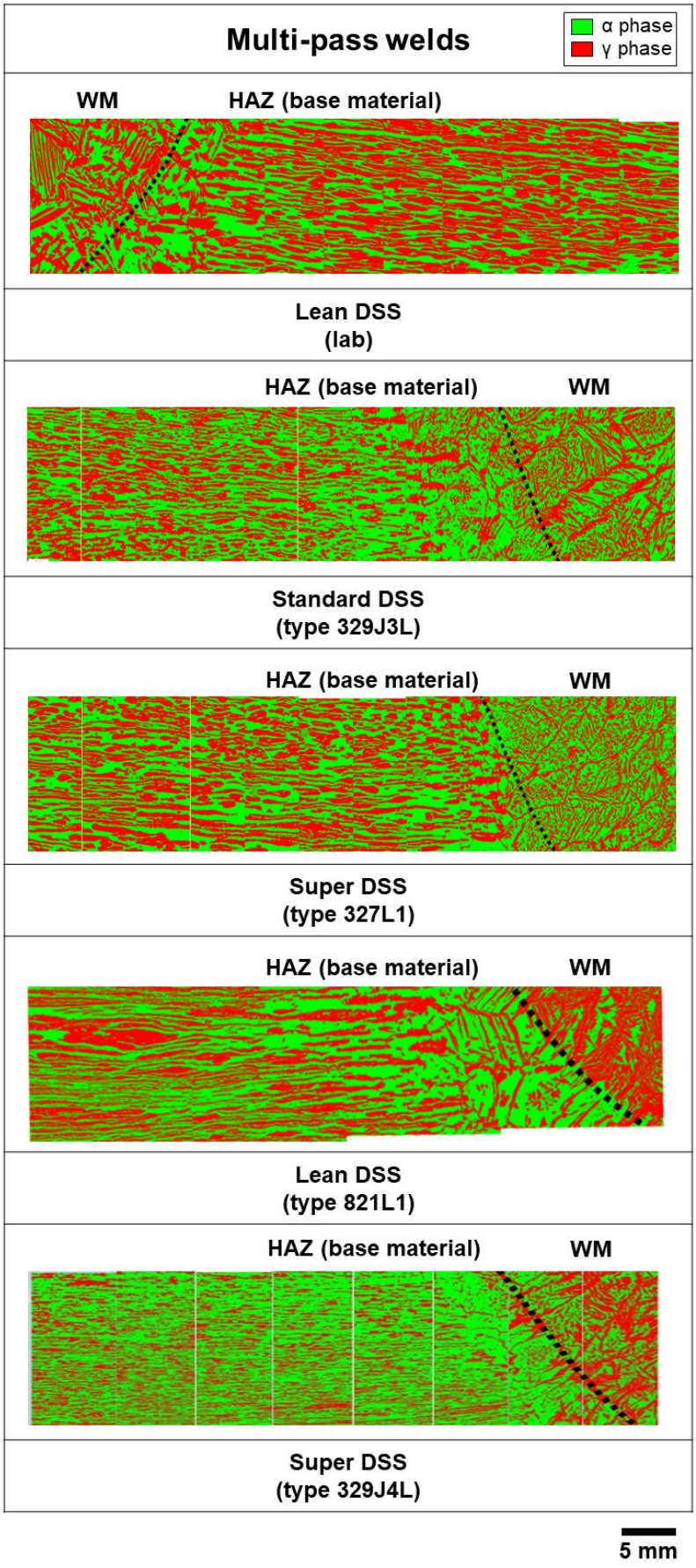

Fig. 3.27 Microstructures of WM and HAZ in multi–pass welds.

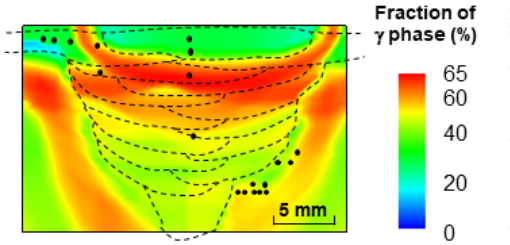

(a–1) Lean DSS (lab).

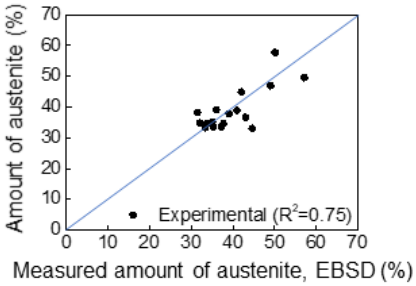

(b–1) Lean DSS (lab).

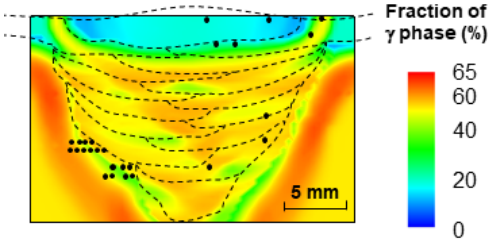

(a–2) Standard DSS (type 329J3L).

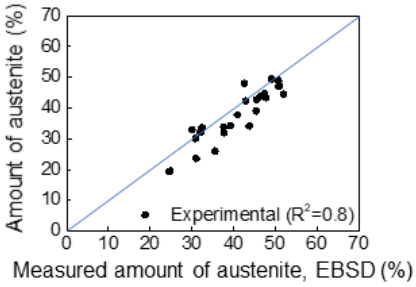

(b–2) Standard DSS (type 329J3L).

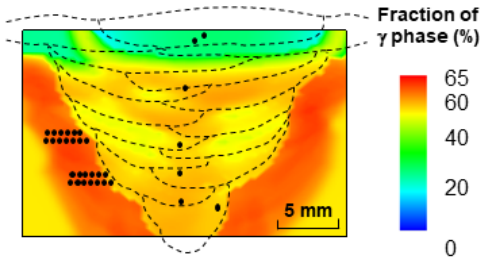

(a–3) Super DSS (type 327L1).

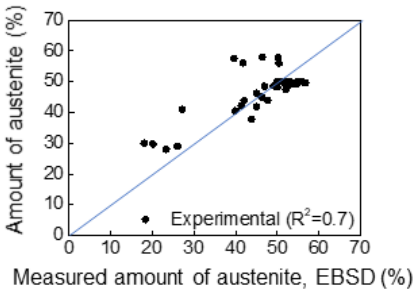

(b–3) Super DSS (type 327L1).

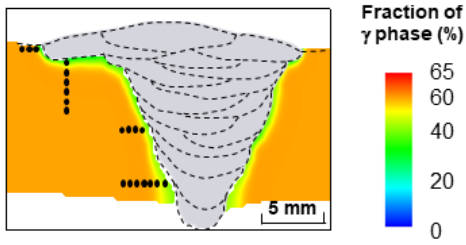

(a–4) Lean DSS (type 821L1).

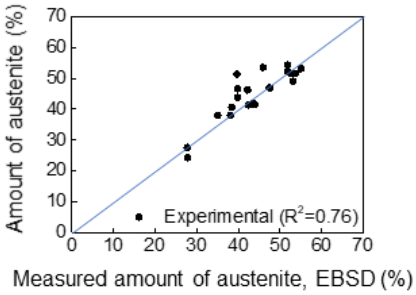

(b–4) Lean DSS (type 821L1).

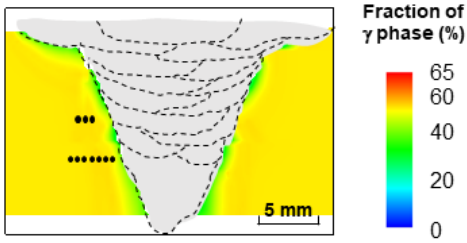

(a–5) Super DSS (type 329J4L).

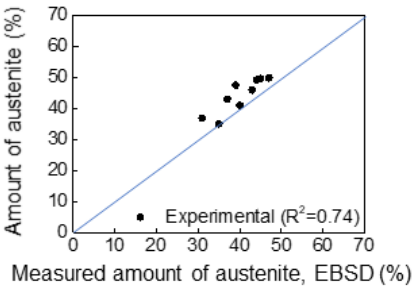

(b–5) Super DSS (type 329J4L).

(a) Analysis spots. (b) Correlation of γ phase fraction.

Fig. 3.28 Comparison of the calculated and measured γ phase fraction in welds.

3.5. Conclusions

In the present Chapter, the kinetic approach was made to the α/γ phase transformation phenomena in the multi–pass welds of DSSs. Both of the dissolution and precipitation behaviors of γ phase were kinetically investigated for the reheated WM as well as the base material HAZ, and the γ phase fraction in multi–pass welds of DSSs was numerically calculated. The results obtained are summarised as follows;

1) During the solution heat treatment of DSSs (base metal, welded metal), the fraction of γ phase was increased with an increase in heat temperature and holding time and saturated with equilibrium fraction in all DSSs.

2) The fraction of the derived γ phase was used in the Austin–Rickett equation to examine the dissolution kinetics. The results of the Austin–Rickett plot showed a good linear relationship, and a time exponents (n) was obtained. Consequently, the dissolution kinetics of the γ phase of all DSSs were followed by the Austin–Rickett equation. Besides, the temperature dependence of the dissolution rate was investigated using the Arrhenius–type equation.

3) During the precipitation heat treatment of DSSs (base metal, welded metal), the fraction of γ phase was increased with an increase in heat temperature and holding time and saturated with equilibrium fraction in all DSSs.

4) The fraction of the derived γ phase was used in the Austin–Rickett equation to examine the precipitation kinetics. The results of the Austin–Rickett plot showed a good linear relationship, and a time exponents (n) was obtained. As a result, the precipitation kinetics of the γ phase of all DSSs were followed by the Austin–Rickett equation.

5) From the results of the Austin–Rickett plot, it was confirmed that the precipitation of the γ phase in DSSs is fastest at the certain intermediate temperature, which cannot be considered for temperature dependence with a simple Arrhenius–type equation. Therefore, the temperature dependence on the precipitation rate of the γ phase in DSSs with a precipitation nose was theoretically examined using the non–uniform nucleation rate equation.

6) Based on the determined kinetic equation, the distribution of the γ phase fraction in the multi–pass welds of DSSs was calculated by combined with the results of heat conduction analysis using Quick–welder software. In the case of Lean (lab), standard (type 329J3L), and super (type 327L1) DSSs, the γ amount was semi–quantitatively predicted for the multi–pass welds, and Lean (type 821L1), super (type 329J4L) DSSs were also semi–quantitatively predicted for the multi–pass HAZs.

7) From the multi–pass welds prediction results, it was confirmed that the γ amount of the first pass HAZ (base material) was less than 30%. However, as the pass progresses, re–precipitation occurs due to the thermal cycle in subsequent welding, recovering the amount of γ. However, the amount of γ in the final welds was considerably reduced compared to that in other welds because the amount of γ was no longer affected by the subsequent thermal cycle.

8) In the predicted results, there were small scatters between the experimental and measured values, but the experimental results were in good agreement with the values measured (correlation coefficient: 0.7–0.8) in all welds (in the WM, reheated WM as well as the base metal HAZ). From the above facts, it was suggested that the α/γ phase transformation can be semi–quantitatively predicted by the present kinetic approach and computer simulation in multi-pass welds of DSSs.

Chapter 4 Theoretical consideration of α/γ phase transformation based on the phase–field method

4.1 Introduction

Duplex stainless steel (DSS) is being increasingly used in the chemical, petrochemical, nuclear, and marine industries mainly owing to its excellent corrosion performance and good mechanical properties. It is well known that DSS exhibits optimal properties when its ferrite–to–austenite (α/γ) volume ratio is approximately 1:1 and no other phases are present. However, during manufacturing processes, such as welding and other thermal cycling methods, the α/γ volume ratio may change owing to the precipitation of various compounds (e.g., Cr carbides and nitrides) and the formation of intermetallic phases, such as sigma (σ), chi (χ), and secondary austenite (γ_2)) [83–86]. Changes in the phase ratio of α/γ can reduce the mechanical properties and corrosion resistance of steel [95, 99, 105, 107–108]. Claudio Gennari et al [112]. were conducted on the mechanical behavior of 4 types of DSSs with different compositions. From the results of previous studies, it was shown that the elongation was uniformly increased, but it was suggested that if the alloy composition is different, it may lead to localized resistive heating due to the uneven distribution of electrical current and the difference in work hardening rate and that it affects the elongation rate. Besides, Lihua Zhang et al [113]. conducted a study on the characteristics of pitting corrosion resistance. From the results of the study, it was suggested that as the amount of γ was decreased, the pitting corrosion resistance was also decreased. Therefore, the quantitative prediction of the phase transformation that occurs during multi–pass welding is necessary. In previous studies [126–127, 167], the phase transformation behavior of α/γ in DSSs (lean, standard, and super) was reviewed, and the amount of γ precipitated during multi–pass welding in the heat affected zone (HAZ) and welded metal in different types of steel was derived by numerical simulations. The results confirmed that the γ precipitation and dissolution behavior obeyed the Austin–Rickett equation. In addition, by revealing the relationship between the rate constant and the temperature dependence, the kinetics of the phase transformation was clearly explained. However, in previous studies, to predict the phase transformation behavior of steels with different chemical compositions, it was inevitable to obtain the transformation rate equation experimentally based on the kinetics of each material. This means that depending on the steel type, there are limitations in terms of time and cost. Currently, simulation based on the phase–field model is one of the most actively researched and developed methods among the existing computer simulation technologies for predicting the microstructure and phase transformation of materials. The advantage of the phase–field model is that the parameters related to the free–energy equation and diffusion included in the governing equation can be applied for predicting the microstructure of the material using a commercially available database. Moreover, this model can consider all the changes (phase transformations) that occur in the microstructure of the material owing to external environmental variables (heat, stress, magnetic field, etc.) in terms of conservative (mass) and non–conservative (phase, interface, anisotropy, etc.) parameters. The phase–field

model has been extensively applied in various natural and applied science studies since it was first proposed by Fix [128] and Langer [129]. Recently, it has been applied to the prediction and analysis of non–diffusion phase transformation processes, such as dislocation kinetics [130–131], crack propagation [132–133], and martensitic transformation, and to almost all the phase transformations involving solid–solid phase transformation, grain growth [134], and recrystallization precipitation diffusion. The most actively used phase–field model is that for the solidification analysis of metallic materials. Solidification is a phase transformation phenomenon in which a solid phase crystallizes when the liquid phase is cooled below its melting temperature, which occurs during processes such as casting, welding, and crystal growth. This phenomenon frequently constitutes a problem in practical alloy manufacturing processes. Böttger [137–138] used phase–field simulation to analyze hot ductility during continuous casting and to study micro–segregation. Eiken [139] studied the growth behavior of magnesium by performing a three–dimensional phase–field simulation. Therefore, many studies have been conducted in other fields of study using the phase–field method. In the case of DSS, calculations of the microstructural changes during solidification were successfully performed under two different composition conditions using a non–equilibrium multiphase field combined with the CALPHAD database [143]. This method was also applied to investigate solidification in continuous casting and static recrystallization after hot rolling [171].

The precipitation behavior of DSS during the sigma phase and under continuous cooling was investigated using phase–field simulation [151]. However, there are few studies involving the quantitative investigation of the kinetics during the α/γ phase transformation of DSS using the phase–field method. Therefore, if the kinetics can be determined theoretically through numerical analysis, the limitations associated with determining the kinetics experimentally can be overcome. Furthermore, there is also the possibility of modeling the transformation kinetics resulting from chemical compositions regardless of the type of steel.

Therefore, in this study, a phase–field simulation model was constructed for Fe–Cr–Ni ternary compositions in terms of the Cr/Ni equivalent ratio of DSSs. In addition, numerical analysis of the dissolution and precipitation of the γ phase was performed and the possibility of deriving the dissolution and precipitation rate constant was examined.

4.2 Phase–field theory

4.2.1 Evolution equations

The phase–field method employed in this study is based on the conventional phase–field method [172–174]. The nonlinear evolution equations of the phase–field showing the α/γ phase transformation of the Fe–Cr–Ni ternary alloy are as follows:

$$\begin{aligned}\frac{\partial c_2}{\partial t} &= \nabla\cdot\left\{M_{22}(c_i,\phi,T)\nabla\frac{\delta G_{sys}}{\delta c_2} + M_{23}(c_i,\phi,T)\nabla\frac{\delta G_{sys}}{\delta c_3}\right\},\\ \frac{\partial c_3}{\partial t} &= \nabla\cdot\left\{M_{32}(c_i,\phi,T)\nabla\frac{\delta G_{sys}}{\delta c_2} + M_{33}(c_i,\phi,T)\nabla\frac{\delta G_{sys}}{\delta c_3}\right\},\end{aligned} \tag{4.1}$$

$$\frac{\partial \phi}{\partial t} = -M_{\phi}(c_i, \phi, T)\frac{\delta G_{sys}}{\partial \phi},$$

where *ci* is the local composition field of component *i*, at spatial position *r* and time (*t*) [174].

The subscripts i = 1, 2, and 3 correspond to Fe, Cr, and Ni, respectively. The phase–field variable $\phi(r, t)$ is the probability of finding the α and γ phases at position *r* and time *t*, so that $0 \leq \phi(r, t) \leq 1$; $\phi = 0$ and $\phi = 1$ correspond to the α (bcc) phase and γ (fcc) phase, respectively. G_{sys} is the total free energy of a microstructure, which is expressed as a function of c_i and ϕ. M_{ij} is the mobility of an atom during diffusion.

4.2.2 Evaluation of the total free energy of a microstructure

The equation for the total free energy is as follows:

$$G_{sys} = G_c + E_{surf} + E_{str}, \tag{4.2}$$

where the total free energy of a microstructure (G_{sys}) is defined as the sum of the chemical free energy (G_c), composition gradient energy (E_{surf}), and elastic strain energy (E_{str}). In addition, the chemical free energy in the phase–field method can be expressed as follows:

$$G_c(c_i, \phi, T) = G_c^{\alpha}(c_i, T)\{1 - h(\phi)\} + G_c^{\gamma}(c_i, T)h(\phi) + Wg(\phi), \tag{4.3}$$

$$h(\phi) \equiv \frac{\int_0^{\phi} g(\phi)\mathrm{d}\phi}{\int_0^{1} g(\phi)\mathrm{d}\phi} = \phi^3(6\phi^2 - 15\phi + 10), \tag{4.4}$$

$$g(\phi) \equiv \phi^2(1 - \phi)^2, \tag{4.5}$$

where $G_c^{\alpha}(c_i, T)$ and $G_c^{\gamma}(c_i, T)$ denote the Gibbs energies of the α and γ phases, respectively [175–178], which are expressed as functions of the composition (c_i) and temperature (T). The functions $g(\phi)$ and $h(\phi)$ in Eqs. (4.4) and (4.5) are defined as $h(\phi) = \phi^3(6\phi^2 - 15\phi + 10)$ and $g(\phi) = \phi^2(1 - \phi)^2$, respectively [179], and $Wg(\phi)$ is the energy barrier of the α/γ crystal transformation. In the Fe–Cr–Ni ternary system with magnetic contribution, the chemical free energy of phases α and γ are explained by a sub–regular solution approximation [175]:

$$\begin{aligned} G_c^{\alpha}(c_i, T) &= {}^{\circ}G_{Fe}^{\alpha}c_{Fe} + {}^{\circ}G_{Cr}^{\alpha}c_{Cr} + {}^{\circ}G_{Ni}^{\alpha}c_{Ni} + {}^{E}G_m^{\alpha} + {}^{mg}G_m^{\alpha} + RT(c_{Fe}\ln c_{Fe} + \\ &\quad c_{Cr}\ln c_{Cr} + c_{Ni}\ln c_{Ni}), \\ G_c^{\gamma}(c_i, T) &= {}^{\circ}G_{Fe}^{\gamma}c_{Fe} + {}^{\circ}G_{Cr}^{\gamma}c_{Cr} + {}^{\circ}G_{Ni}^{\gamma}c_{Ni} + {}^{E}G_m^{\gamma} + {}^{mg}G_m^{\gamma} + RT(c_{Fe}\ln c_{Fe} + \\ &\quad c_{Cr}\ln c_{Cr} + c_{Ni}\ln c_{Ni}), \end{aligned} \tag{4.6}$$

where ${}^{\circ}G_i^{\alpha}$ and ${}^{\circ}G_i^{\gamma}$ are the Gibbs energies of pure element *i* in the case of bcc and fcc crystal structures, which are expressed as functions of the temperature [176]. ${}^{E}G_m^{\alpha}$ and ${}^{E}G_m^{\gamma}$ are the excess free energies corresponding to the heat of mixing, ${}^{mg}G_m^{\alpha}$ and ${}^{mg}G_m^{\gamma}$ are the magnetic contributions to the Gibbs energy, and R and T are the gas constant and absolute temperature, respectively. The functions of ${}^{E}G_m^{\alpha}$, ${}^{E}G_m^{\gamma}$, ${}^{mg}G_m^{\alpha}$, and ${}^{mg}G_m^{\gamma}$ are defined as follows:

$$
\begin{aligned}
{}^{E}G_m^{\alpha} &\equiv L_{Fe,Cr}^{\alpha}(c_i,T)\,c_{Fe}c_{Cr} + L_{Fe,Ni}^{\alpha}(c_i,T)\,c_{Fe}c_{Ni} + L_{Cr,Ni}^{\alpha}(c_i,T)\,c_{Cr}c_{Ni} + \\
&\quad L_{Fe,Cr,Ni}^{\alpha}(c_i,T)\,c_{Fe}c_{Cr}c_{Ni}, \\
{}^{E}G_m^{\gamma} &\equiv L_{Fe,Cr}^{\gamma}(c_i,T)\,c_{Fe}c_{Cr} + L_{Fe,Ni}^{\gamma}(c_i,T)\,c_{Fe}c_{Ni} + L_{Cr,Ni}^{\gamma}(c_i,T)\,c_{Cr}c_{Ni} + \\
&\quad L_{Fe,Cr,Ni}^{\gamma}(c_i,T)\,c_{Fe}c_{Cr}c_{Ni},
\end{aligned} \tag{4.7}
$$

$$
\begin{aligned}
{}^{mg}G_m^{\alpha} &\equiv RT\ln(\beta^{\alpha}+1)f(\tau), \tau \equiv T/T_C^{\alpha}, \\
{}^{mg}G_m^{\gamma} &\equiv RT\ln(\beta^{\gamma}+1)f(\tau), \ \tau \equiv T/T_C^{\gamma},
\end{aligned} \tag{4.8}
$$

where the interaction parameters $L_{i,j}^{\alpha}$, $L_{i,j}^{\gamma}$, $L_{i,j,k}^{\alpha}$, and $L_{i,j,k}^{\gamma}$, Curie temperatures T_C^{α} and T_C^{γ}, and atomic magnetic moments β^{α} and β^{γ} are available from thermodynamic databases of equilibrium phase diagrams. These parameters have been determined for the Fe–Cr–Ni system by Miettinen [177].

In addition,

$$
\begin{aligned}
f(\tau) &= 1 - \frac{1}{D}\left\{\frac{79\tau^{-1}}{140p} + \frac{474}{497}\left(\frac{1}{p}-1\right)\left(\frac{\tau^3}{6} + \frac{\tau^9}{135} + \frac{\tau^{15}}{600}\right)\right\}, (\tau \le 1), \\
f(\tau) &= -\frac{1}{D}\left(\frac{\tau^{-5}}{10} + \frac{\tau^{-15}}{315} + \frac{\tau^{-25}}{1500}\right), (\tau > 1),
\end{aligned} \tag{4.9}
$$

$$
D = \frac{518}{1125} + \frac{11692}{15975}\left(\frac{1}{p}-1\right). \tag{4.10}
$$

For the α phase, $\tau \equiv T/T_C^{\alpha}$ and $p = 0.40$, whereas for the γ phase, $\tau \equiv T/T_C^{\gamma}$ and $p = 0.28$.

Furthermore, the slope energy (E_{surf}) in the phase–field method can be expressed as given in Eq. (4.11) and rearranged to give Eq. (4.12), which presents only independent variables (c_2, c_3, and ϕ).

$$
E_{surf}(\nabla c_i, \nabla\phi) = \frac{1}{2}\kappa_c \sum_{i=1}^{3}(\nabla c_i)^2 + \frac{1}{2}\kappa_c(\nabla\phi)^2 \tag{4.11}
$$

$$
E_{surf}(\nabla c_i, \nabla\phi) = \kappa_c(\nabla c_2)^2 + \kappa_c(\nabla c_3)^2 + \kappa_c(\nabla c_2)(\nabla c_3) + \frac{1}{2}\kappa_c(\nabla\phi)^2 \tag{4.12}
$$

In this analysis, the spatially steep interface appears only at the α/γ interface position and contributes to $1/2\cdot\kappa_c\left(\bigtriangledown\phi\right)^2$ for the slope energy of the part. In the actual calculation, all the composition gradient energy terms are omitted, and Eq. (4.13) is assumed.

$$
E_{surf}(\nabla\phi) = \frac{1}{2}\kappa_c(\nabla\phi)^2 \tag{4.13}
$$

The elastic strain energy (E_{str}) in the phase–field method can be expressed as given in Eq. (4.14) [180–181]:

$$E_{str} = \frac{1}{2} C_{ijkl}\{\varepsilon_{ij}^{c}(\boldsymbol{r}) - \varepsilon_{ij}^{0}(\boldsymbol{r})\}\{\varepsilon_{kl}^{c}(\boldsymbol{r}) - \varepsilon_{kl}^{0}(\boldsymbol{r})\} \tag{4.14}$$

where $\varepsilon_{ij}^{0}(\boldsymbol{r})$ is the eigen strain of the Fe–Cr–Ni ternary alloy, $\varepsilon_{ij}^{c}(\boldsymbol{r})$ is the total distortion, $\varepsilon_{ij}^{el}(\boldsymbol{r})$ is the elastic strain, and C_{ijkl} is the elastic constant. In this study, the eigen strain and elastic constants were calculated according to the microdynamics expressed as a function of concentration and phase–field variables [179]. In addition, the elastic strain energy was not considered in the calculation because a one–dimensional inconsistent DSS was assumed.

4.2.3 Calculation of evolution equations

Assuming that the mobility of an atom by diffusion is negligible, $M_{23}(\phi,T) = M_{32}(\phi,T) = 0$ in Eq. (4.1). In addition, because the composition gradient energy is omitted, as described previously, the evolution equation is given as follows:

$$\begin{aligned}
\frac{\delta G_{sys}}{\delta c_2} &= \frac{\partial G_c^{\alpha}(c_i,T)}{\partial c_2}\{1 - h(\phi)\} + \frac{\partial G_c^{\gamma}(c_i,T)}{\partial c_2} h(\phi), \\
\frac{\delta G_{sys}}{\delta c_3} &= \frac{\partial G_c^{\alpha}(c_i,T)}{\partial c_3}\{1 - h(\phi)\} + \frac{\partial G_c^{\gamma}(c_i,T)}{\partial c_3} h(\phi), \\
\frac{\partial G_{sys}}{\partial \phi} &= \{G_c^{\gamma}(c_i,T) - G_c^{\alpha}(c_i,T)\}\frac{\delta h}{\partial \phi} + W\frac{\delta g}{\partial \phi} - \kappa_{\phi}\nabla^2\phi.
\end{aligned} \tag{4.15}$$

The mobilities $M_{22}(\phi,T)$ and $M_{33}(\phi,T)$ are calculated from the diffusion potential of component *i* in phase $\phi(=\alpha,\gamma)$ as follows:

$$\begin{aligned}
M_{22}(\phi,T) &\equiv (1-\phi)M_{22}^{\alpha}(T) + \phi M_{22}^{\gamma}(T), \\
M_{33}(\phi,T) &\equiv (1-\phi)M_{33}^{\alpha}(T) + \phi M_{33}^{\gamma}(T),
\end{aligned} \tag{4.16}$$

where M_{22}^{α} and M_{22}^{γ} are the mobilities of the atoms by diffusion in component *Cr* in the phase $\phi(=\alpha,\gamma)$; M_{33}^{α} and M_{33}^{γ} are the mobilities of the atoms by diffusion in the Ni component in the phase $\phi(=\alpha,\gamma)$. The mobility by diffusion can be expressed by the mutual diffusion constant as follows:

$$\begin{aligned}
\widetilde{D_{22}^{\alpha}} &\equiv M_{22}^{\alpha}(T)\left(\frac{\partial^2 G_c^{\alpha}}{\partial c_2^2}\right), \widetilde{D_{33}^{\alpha}} \equiv M_{33}^{\alpha}(T)\left(\frac{\partial^2 G_c^{\alpha}}{\partial c_3^2}\right), \\
\widetilde{D_{22}^{\gamma}} &\equiv M_{22}^{\gamma}\left(\frac{\partial^2 G_c^{\gamma}}{\partial c_2^2}\right), \widetilde{D_{33}^{\gamma}} \equiv M_{33}^{\gamma}\left(\frac{\partial^2 G_c^{\gamma}}{\partial c_3^2}\right),
\end{aligned} \tag{4.17}$$

In this study, it was assumed that the mutual diffusion coefficient $\left(\widetilde{D_{22}^{\alpha}}, \widetilde{D_{33}^{\alpha}}, \widetilde{D_{22}^{\gamma}}, \widetilde{D_{33}^{\gamma}}\right)$ could be replaced by the impurity diffusion coefficient, $\left(D_{22}^{\alpha}, D_{33}^{\alpha}, D_{22}^{\gamma}, D_{33}^{\gamma}\right)$. Therefore, the mobilities by diffusion as functions of the temperature and concentration can be expressed as follows:

$$M_{22}^{\alpha}(T) \equiv \frac{D_{22}^{\alpha}(T)}{\left(\frac{\partial^2 G_c^{\alpha}}{\partial c_2^2}\right)_{c_2,c_3}}, M_{33}^{\alpha}(T) \equiv \frac{D_{33}^{\alpha}(T)}{\left(\frac{\partial^2 G_c^{\alpha}}{\partial c_3^2}\right)_{c_2,c_3}},$$
$$M_{22}^{\gamma}(T) \equiv \frac{D_{22}^{\gamma}(T)}{\left(\frac{\partial^2 G_c^{\gamma}}{\partial c_2^2}\right)_{c_2,c_3}}, M_{33}^{\gamma}(T) \equiv \frac{D_{33}^{\gamma}(T)}{\left(\frac{\partial^2 G_c^{\gamma}}{\partial c_3^2}\right)_{c_2,c_3}}, \quad (4.18)$$

Further, the interfacial mobility for the crystal transformation is given as follows:

$$\frac{\nu}{M_{\phi}(T)}\frac{\gamma_s V_m}{\kappa_{\phi}} = -\Delta F, \quad (4.19)$$

where ν is the speed of advancement of the α/γ interface, ΔF is the force moving the interface, γ_s is the energy density of the α/γ interface, and V_m is the molar volume of (Fe–bcc).

The relationship between the interfacial energy density and γ_s and the interfacial width d at the α/γ interface are given as Eq. (4.20), which is derived assuming that the phase–field at the interface always has a normal profile shape. κ_{ϕ} and W in Eq. (4.21) are derived from Eq. (4.20), and finally, $M_{\phi}(T)$ is obtained by applying Eq. (4.22).

$$\gamma_s V_m = \frac{\sqrt{\kappa_{\phi} W}}{3\sqrt{2}}, \; d = 2.2\sqrt{\frac{2\kappa_{\phi}}{W}} \quad (4.20)$$
$$\kappa_{\phi} = \frac{1.5}{1.1}\gamma_s V_m d, \; W = \frac{13.2\gamma_s V_m}{d} \quad (4.21)$$
$$M_{\phi}(T) = -\frac{\nu}{\Delta F}\frac{\gamma_s V_m}{\kappa_{\phi}} \quad (4.22)$$

These parameters have been determined for the Fe–Cr–Ni system by previous research [172,177]. The one–dimensional evolution equation (Eq. (4.1)) is differentially expanded, and the time variations in the composition and phase–field functions are calculated. Denoting the concentrations of Fe, Cr, and Ni and the phase–field positions x and t as $c_{Fe}(x,t)$, $c_{Cr}(x,t)$, $c_{Ni}(x,t)$, and $\phi(x,t)$, respectively, each concentration and phase–field after time t is expressed using the incremental method as follows:

$$\begin{aligned} c_{Fe}(x,t+\Delta t) &= 1 - c_{Cr}(x,t+\Delta t) - c_{Ni}(x,t+\Delta t), \\ c_{Cr}(x,t+\Delta t) &= c_{Cr}(x,t) + \frac{\partial c_{\mathrm{Cr}}}{\partial t}\Delta t, \\ c_{Ni}(x,t+\Delta t) &= c_{Ni}(x,t) + \frac{\partial c_{\mathrm{Ni}}}{\partial \mathrm{t}}\Delta t, \\ \phi\,(x,t+\Delta t) &= \phi\,(x,t) + \frac{\partial \phi}{\partial t}\Delta t. \end{aligned} \quad (4.23)$$

The differential development of the evolution equation can be expressed as follows:

$$\begin{aligned}
\frac{\partial c_2}{\partial t} &= \frac{\partial}{\partial x}\left\{M_{22}\left(\frac{\partial \mu_{sys,2}}{\partial x}\right)\right\},\\
\frac{\partial c_3}{\partial t} &= \frac{\partial}{\partial x}\left\{M_{33}\left(\frac{\partial \mu_{sys,3}}{\partial x}\right)\right\},\\
\frac{\partial \phi}{\partial t} &= -M_\phi\left[\left\{G_c^\gamma(c_i,T)-G_c^\alpha(c_i,T)\right\}\frac{\mathrm{d}h}{\mathrm{d}\phi}+W\frac{\mathrm{d}g}{\mathrm{d}\phi}-\kappa_\phi\left(\frac{\partial^2\phi}{\partial x^2}\right)\right]\\
&= -M_\phi\left[\mu_{chem}-\kappa_\phi\left(\frac{\partial^2\phi}{\partial x^2}\right)\right].
\end{aligned} \tag{4.24}$$

The diffusion potential $\mu_{sys,i}$ can be expressed as follows:

$$\mu_{sys,i}\equiv\frac{\delta G_{sys}}{\delta c_i}\left(=\frac{\partial G_c^\alpha}{\partial c_i}+\frac{\partial E_{surf}}{\partial c_i}+\frac{\partial E_{str}}{\partial c_i}\right),\ \mu_{chem}\equiv\left\{G_c^\gamma(c_i,T)-G_c^\alpha(c_i,T)\right\}\frac{\mathrm{d}h}{\mathrm{d}\phi}+W\frac{\mathrm{d}g}{\mathrm{d}\phi}$$

By modifying the first and second equations in Eq. (4.24), the following equations are obtained:

$$\begin{aligned}
\frac{\partial c_2}{\partial t} &= M_{22}\left(\frac{\partial^2\mu_{sys,2}}{\partial x^2}\right)+\left(\frac{\partial M_{22}}{\partial c_2}\right)\left(\frac{\partial c_2}{\partial x}\right)\left(\frac{\partial \mu_{sys,2}}{\partial x}\right),\\
\frac{\partial c_3}{\partial t} &= M_{33}\left(\frac{\partial^2\mu_{sys,3}}{\partial x^2}\right)+\left(\frac{\partial M_{33}}{\partial c_3}\right)\left(\frac{\partial c_3}{\partial x}\right)\left(\frac{\partial \mu_{sys,3}}{\partial x}\right),\\
\frac{\partial \phi}{\partial t} &= -M_\phi\left[\mu_{chem}-\kappa_\phi\left(\frac{\partial^2\phi}{\partial x^2}\right)\right].
\end{aligned} \tag{4.25}$$

It is efficient to calculate the difference directly based on the diffusion potential by approximating the right and left sides of Eq. (4.25) by the forward difference and central difference methods as follows:

$$\begin{aligned}
\frac{c_2^{t+\Delta t}-c_2^t}{\Delta t} &= M_{22}\left(\frac{\mu_2^{i+1}+\mu_2^{i-1}-2\mu_2^i}{\Delta x^2}\right)+\left(\frac{\partial M_{22}}{\partial c_2}\right)\left\{\frac{(c_2^{i+1}-c_2^{i-1})(\mu_2^{i+1}-\mu_2^{i-1})}{4\Delta x^2}\right\},\\
\frac{c_3^{t+\Delta t}-c_3^t}{\Delta t} &= M_{33}\left(\frac{\mu_3^{i+1}+\mu_3^{i-1}-2\mu_3^i}{\Delta x^2}\right)+\left(\frac{\partial M_{33}}{\partial c_3}\right)\left\{\frac{(c_3^{i+1}-c_3^{i-1})(\mu_3^{i+1}-\mu_3^{i-1})}{4\Delta x^2}\right\},\\
\frac{\phi^{t+\Delta t}-\phi^t}{\Delta t} &= -M_\phi\left\{\mu_{chem}-\kappa_\phi\left(\frac{\phi^{i+1}+\phi^{i-1}-2\phi^i}{\Delta x^2}\right)\right\}.
\end{aligned} \tag{4.26}$$

4.2.4 Thermodynamic parameters and material constants

The material constants and calculation constants used in this calculation are as follows. These parameters have been determined for the Fe–Cr–Ni system by previous research [172,177].

$$\begin{aligned} &\gamma_s = 0.5\ (\mathrm{J/m^2}) \\ &V_m = 7.1\times10^{-6}\ (\mathrm{m^3/mol}) \\ &\nu = 1.0\times10^{-6}\ (\mathrm{m/s}) \\ &\Delta F = -1000\ (\mathrm{J/mol}) \end{aligned} \tag{4.27}$$

4.2.5 Preliminary review of simulation calculation conditions

Since this simulation is a Fe–Cr–Ni ternary calculation, it is necessary to convert the multi–system composition into a ternary composition using Cr and Ni equivalents in order to calculate the actual DSSs. Schaeffler [182] and Delong [6] have proposed several Cr equivalents and Ni equivalents. In this study, Kokawa, et al. [183] used the following formula, obtained by quantitatively evaluating the N amount and organizational change in DSSs.

$$\begin{aligned} &\mathrm{Ni_{eq}} = \mathrm{Ni} + 30\mathrm{C} + 18.2\mathrm{N} + 0.5\mathrm{Mn} \\ &\mathrm{Cr_{eq}} = \mathrm{Cr} + \mathrm{Mo} + 1.5\mathrm{Si} + 0.5\mathrm{Nb} \end{aligned} \tag{4.28}$$

Since the phase–field method is a model that calculates the most efficient reduction of free energy, it is not possible to calculate a phenomenon in which the energy of the system is increased, such as nucleation. Therefore, in the calculation of microstructure formation in the phase–field method, the calculation is performed by giving the initial nucleation site [148–149,174,184]. As a characteristic of the austenite precipitation phenomenon of DSSs, it is conceivable to follow the Austin–Rickett type kinetic equation. In the Austin–Rickett type kinetic equation, the delay of the transformation rate due to the grain collision effect can be applied to the phenomenon, so it is important to reproduce the grain collision effect while reproducing and calculating the austenite phase analysis. In this section, to examine the nucleation site that reproduces the precipitation behavior according to the Austin–Rickett type kinetic equation, it was calculated under two conditions as shown in Fig. 4.1. Fig. 4.2 shows the results of the austenite growth process for both conditions. The α/γ transformation kinetics are described as the interfacial region of the part where the defined phase–field parameter $\phi(r, t)$ is continuously changed within the one–dimensional simulated microstructure as follows.

$\phi(r, t) = 1$, if the γ phase is present at position r and time t;
$\phi(r, t) = 0$, if the α phase is present at position r and time t.

In the case of Fig. 4.2(a), each austenite particle grows evenly, and each particle collides at once to complete the transformation. On the other hand, when the nucleation sites are arranged

by varying the spacing (Fig. 4.2(b)), collisions occur sequentially starting with the spacing of each austenite particle close to each other, suppressing growth, and gradually completing the transformation. Fig. 4.3 shows the change of the austenite amount with time under the two conditions set in Fig. 4.1. In the case of Fig. 4.3(a), the precipitation rate was suddenly decreased around 80 % and rapidly reaches the saturation value. However, in the case of 4.3(b), the precipitation rate was gradually decreased from around 60 % to completion of transformation and reaches the saturation value. By combining the above results, an Austin–Rickett plot was conducted to examine the transformation kinetic due to the grain collision effect, and the results are shown in Fig. 4.4. Fig. 4.4(a) greatly deviated from the linearity at the late of the transformation, and Fig. 4.4(b) maintained good linearity until the transformation was completed. Therefore, the conditions of the nucleation site in this study were adopted in Fig. 4.1(b). Like the precipitation phenomenon, the same conditions were adopted for the dissolution phenomenon and the calculation was carried out.

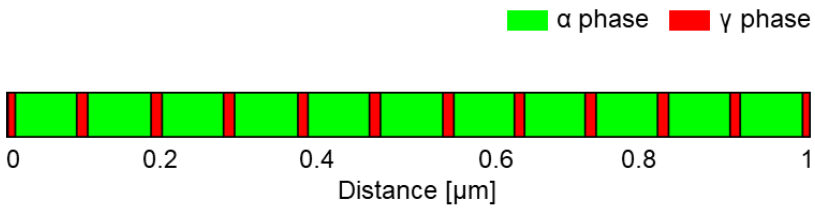

(a) Placed at equal intervals.

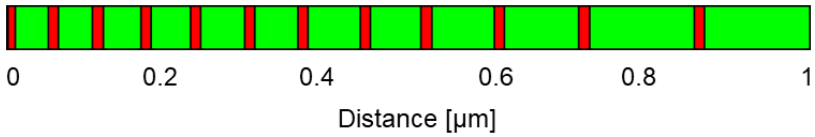

(b) Placed at various intervals.

Fig. 4.1 Location of nucleation site.

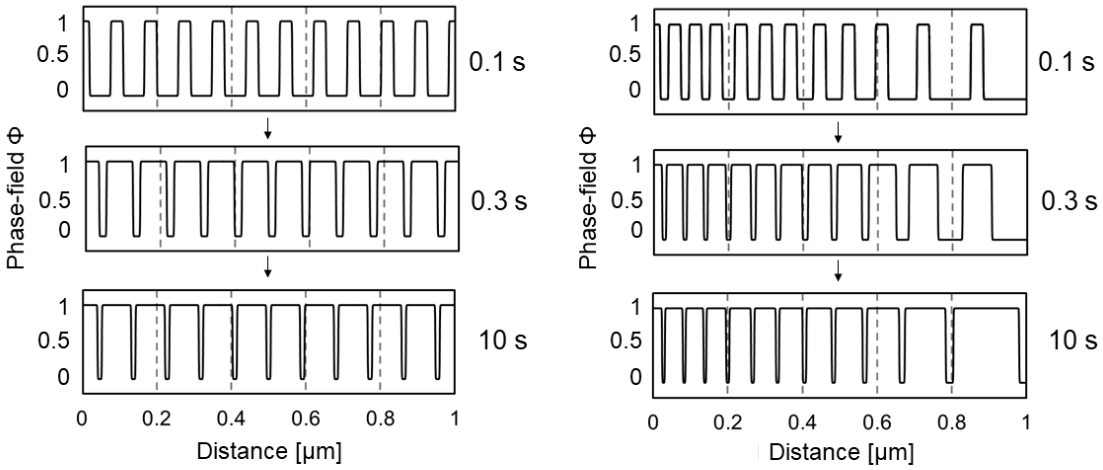

(a) Equally spaced nucleation site condition. (b) Variously spaced nucleation site condition.

Fig. 4.2 Time evolution of "ϕ" distribution.

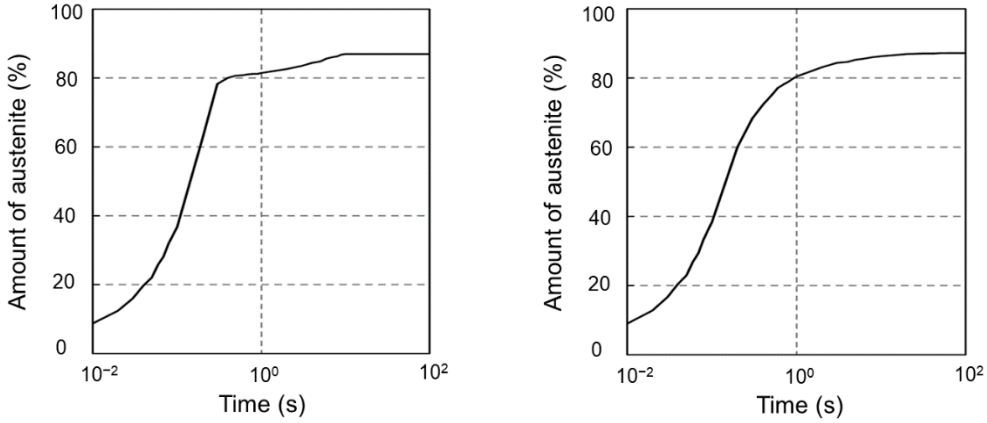

(a) Equally spaced nucleation site condition. (b) Variously spaced nucleation site condition.

Fig. 4.3 Change in austenite fraction.

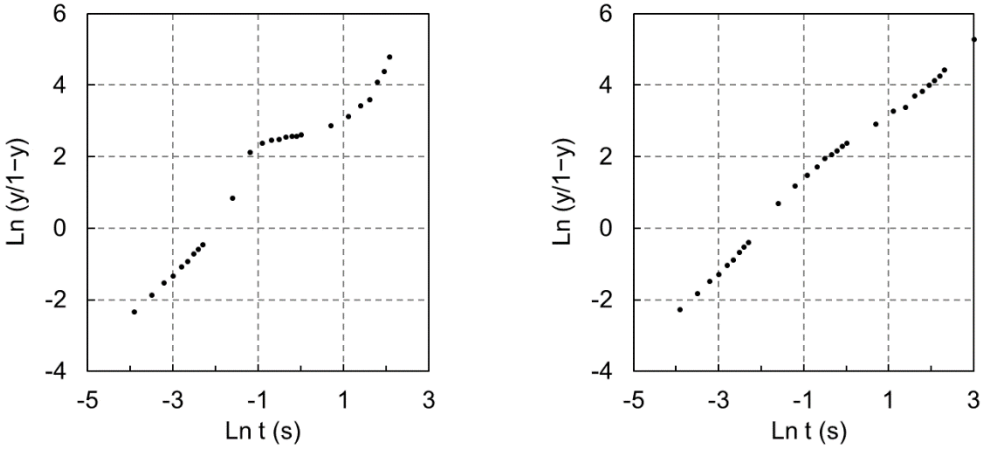

(a) Equally spaced nucleation site condition. (b) Variously spaced nucleation site condition.

Fig. 4.4 Austin–Rickett plots of austenite precipitation behavior.

4.3 Kinetics of the phase transformation behavior through numerical analysis

4.3.1 Kinetics of the calculated dissolution results of the base materials

For the lean (type 821L1), standard (type 329J3L), and super (type 327L1) DSSs used in Chapter 3, a kinetic review of the dissolution phenomenon of the base materials using the phase–field method was conducted. The composition is shown in Table 4.1. In Chapter 3, we have already confirmed that the γ phase precipitation and dissolution phenomena can be expressed by the Austin–Rickett equation. Furthermore, the relationship between the temperature dependence of the rate of precipitation and dissolution was also investigated to prove its validity. The research flow in this Chapter was also carried out based on the flow in Chapter 3. The γ dissolution behavior was calculated considering the Fe–Cr–Ni ternary composition obtained by converting the DSS composition into its Cr and Ni equivalents using Eq. (4.28). The calculations results are shown in Fig. 4.5. Regardless of the alloy composition,

the saturated dissolution was increased with an increase in heating temperature. The Austin–Rickett plot of the dissolution behavior of the γ phase in the DSS (base material HAZ s) demonstrated a strong linear relationship, as shown in Fig. 4.6. The time exponents (n) of the dissolution of the γ phase in the lean, standard, and super DSSs were measured to be 1.93, 2.02, and 1.97, respectively. This confirms that the dissolution kinetics of the γ phase in DSS can be approximately expressed by the Austin–Rickett equation. To investigate the temperature dependence of the γ phase dissolution phenomena, the rate constant $k(T)$ was calculated using the Arrhenius–type equation (Eq 3.4). The Arrhenius plots shown in Fig. 4.7 were obtained. From the figure, it can be seen that ln k and $1/T$ have a good linear relationship. Then, the temperature dependencies of the dissolution rate of the γ phase in lean, standard, and super DSSs were investigated, and the results are presented in Table 4.2.

Table 4.1 Chemical composition of the base materials in this study (mass %).

Steel	C	Si	Mn	P	S	Ni	Cr	Mo	Cu	N	Fe
Lean DSS (type 821L1)	0.017	0.42	3.21	0.024	<0.001	2.24	20.88	0.48	1.05	0.17	Bal.
Standard DSS (type 329J3L)	0.008	0.56	1.82	0.025	0.0002	5.75	22.55	3.08	0.16	0.161	Bal.
Super DSS (type 327L1)	0.009	0.31	0.51	0.024	0.0009	6.56	25.11	3.72	0.21	0.259	Bal.

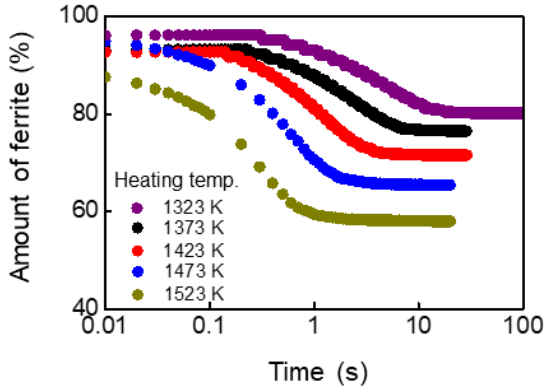

(a) Lean DSS (type 821L1).

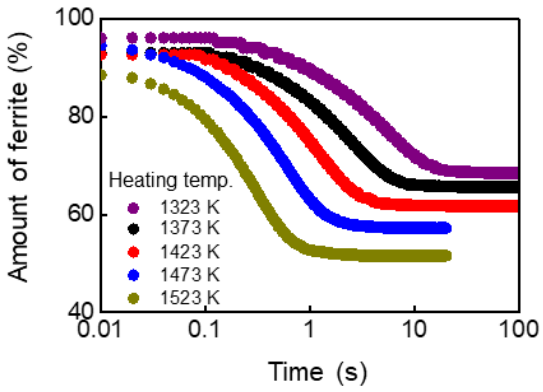

(b) Standard DSS (type 329J3L).

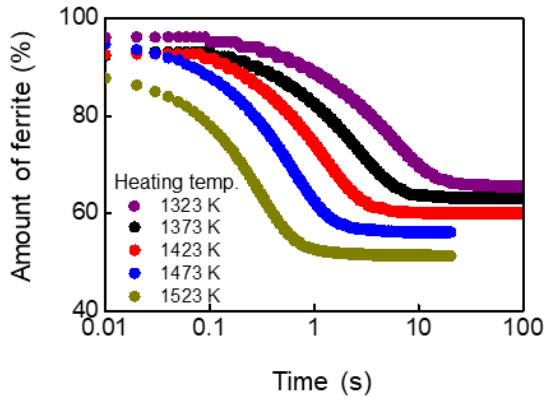

(c) Super DSS (type 327L1).

Fig. 4.5 Changes in the dissolved γ fraction for the DSSs at different temperatures.

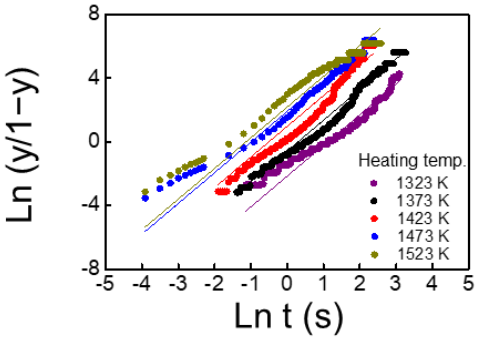

(a) Lean DSS (type 821L1).

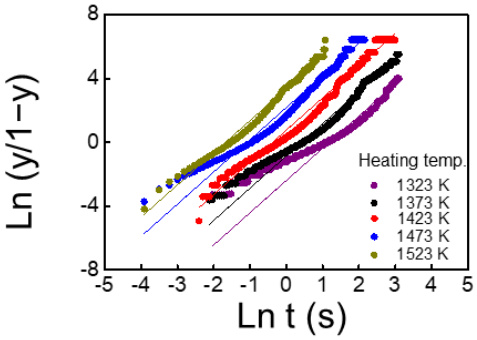

(b) Standard DSS (type 329J3L).

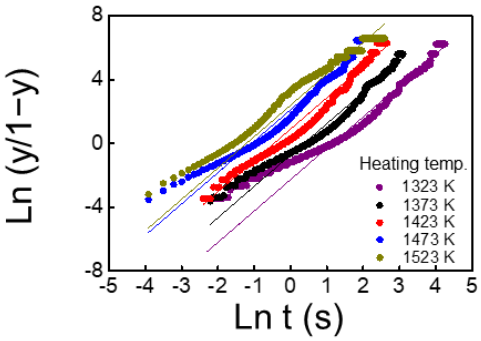

(c) Super DSS (type 327L1).

Fig. 4.6 Austin–Rickett plots of the γ phase dissolution behavior in the base material HAZs the DSSs at different temperatures.

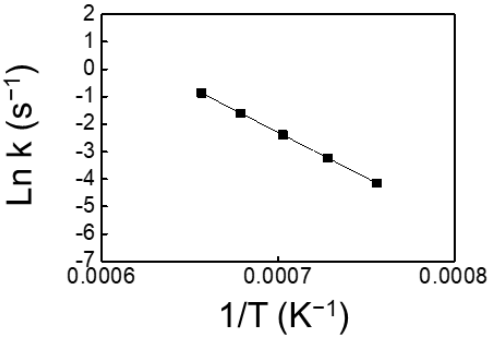

(a) Lean DSS (type 821L1).

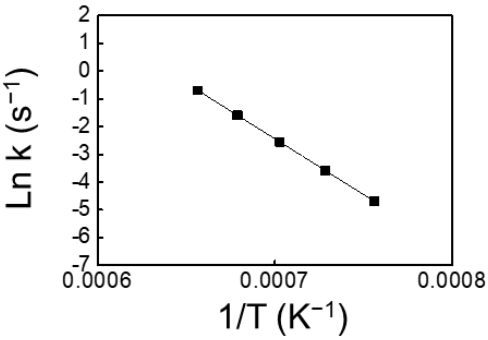

(b) Standard DSS (type 329J3L).

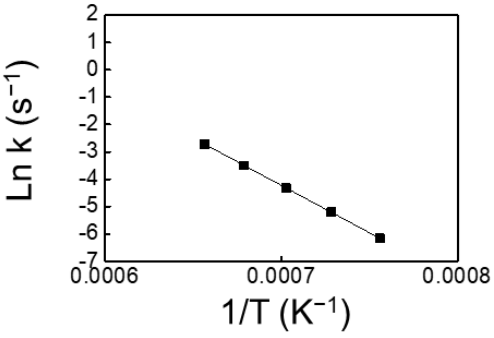

(c) Super DSS (type 327L1).

Fig. 4.7 Arrhenius plots of the dissolution rates constants of the γ phase in the base material HAZs for the DSSs.

Table 4.2 Experimental temperature dependencies of the γ phase dissolution in DSSs (base materials).

Steel type	Time constant, n	The temperature dependency of dissolution rate [s^{-1}]	ΔG [kJ/mol]
Lean DSS (type 821L1)	1.93	$K=\exp(\frac{-2.36\times10^4}{T}+16.84)$	196
Standard DSS (type 329J3L)	2.02	$K=\exp(\frac{-2.92\times10^4}{T}+20.9)$	242
Super DSS (type 327L1)	1.97	$K=\exp(\frac{-2.51\times10^4}{T}+17.93)$	209

4.3.2 Kinetics of the calculated dissolution results of the weld metals

For the lean (lab), standard (type 329J3L), and super (type 327L1) DSSs used in Chapter 3, a kinetic review of the dissolution phenomenon of the weld metals using the phase–field method was conducted. The composition is shown in Table 4.3. Fig. 4.8 shows the results of calculating the dissolution of γ behavior using the Fe–Cr–Ni ternary composition obtained by converting the composition of DSSs by Cr and Ni equivalents in Eq. (4.28). Regardless of the alloy composition, the saturated dissolution was increased with an increase in heating temperature. Fig. 4.9 shows the results of the Austin–Rickett plot for the γ phase dissolution behavior of DSSs. In the case of the dissolution phenomenon, the time exponents (n) of lean (lab), standard (type 329J3L), and super (type 327L1) DSSs were determined as 1.8, 2.04, and 2.2, respectively. Arrhenius plot was performed based on the results in Fig. 4.9, and the results are shown in Fig. 4.10. There are good linear relationships between ln k and $1/T$ for both steels, and therefore, $k(T)$ of Eq (3.4) can be obtained as in Table 4.4.

Table 4.3 Chemical composition of the weld metals in this study (mass %).

Steel	C	Si	Mn	P	S	Ni	Cr	Mo	Cu	N	Fe
Lean DSS (lab)	0.014	0.35	1.49	0.024	0.0004	3.06	20.85	0.30	0.09	0.177	Bal.
Standard DSS (type 329J3L)	0.012	0.56	1.81	0.024	0.0005	5.72	22.46	3.07	0.17	0.169	Bal.
Super DSS (type 327L1)	0.013	0.31	0.48	0.025	0.0005	6.83	24.98	4.03	0.2	0.265	Bal.

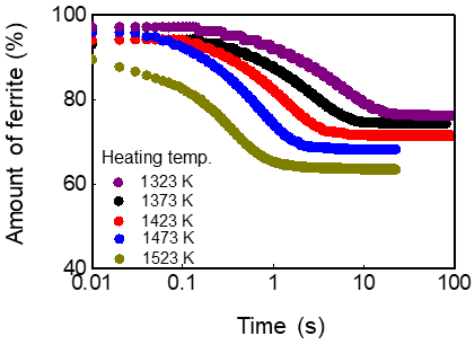

(a) Lean DSS (type 821L1).

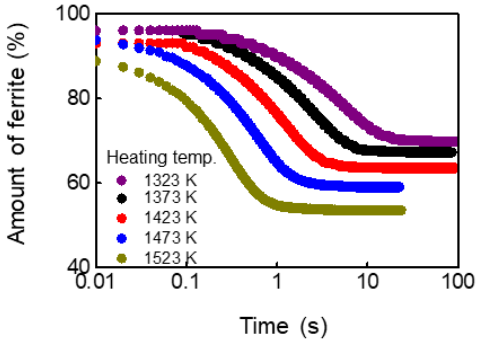

(b) Standard DSS (type 329J3L).

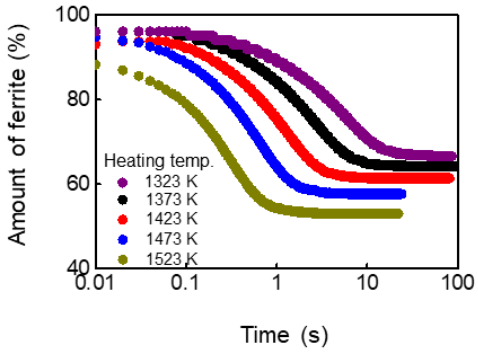

(c) Super DSS (type 327L1).

Fig. 4.8 Changes in the dissolved γ fraction for the DSSs at different temperatures.

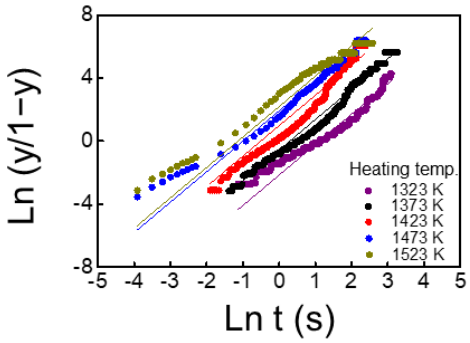

(a) Lean DSS (lab).

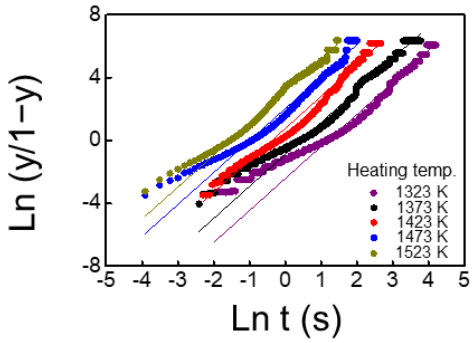

(b) Standard DSS (type 329J3L).

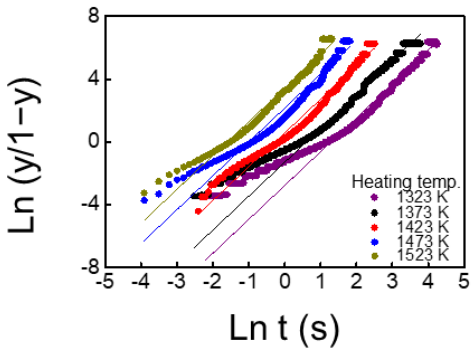

(c) Super DSS (type 327L1).

Fig. 4.9 Austin–Rickett plots of the γ phase dissolution behavior in the weld metals for the DSSs at different temperatures.

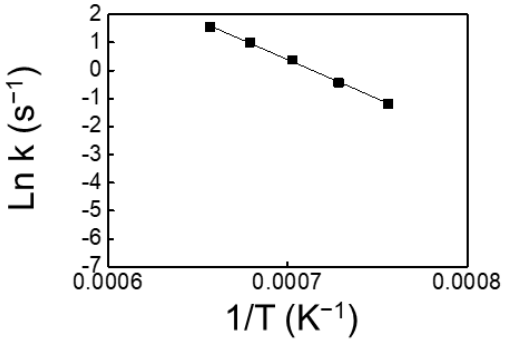

(a) Lean DSS (lab).

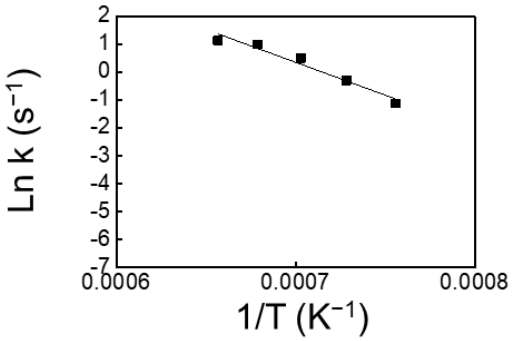

(b) Standard DSS (type 329J3L).

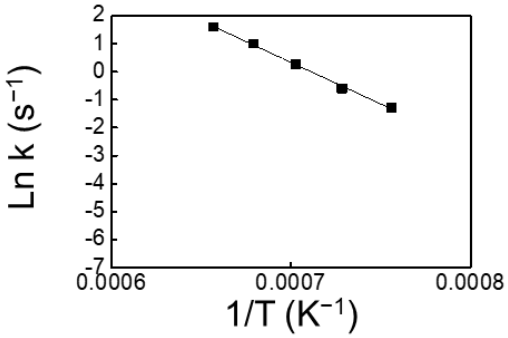

(c) Super DSS (type 327L1).

Fig. 4.10 Arrhenius plots of the dissolution rates constants of the γ phase in the weld metals for the DSSs.

Table 4.4 Experimental temperature dependencies of the γ phase dissolution in DSSs (weld metals).

Steel type	Time constant, n	The temperature dependency of dissolution rate [s^{-1}]	ΔG [kJ/mol]
Lean DSS (lab)	1.8	$K=\exp(\frac{-1.78\times10^4}{T}+17.1)$	148
Standard DSS (type 329J3L)	2.04	$K=\exp(\frac{-2.8\times10^4}{T}+19.9)$	232
Super DSS (type 327L1)	2.2	$K=\exp(\frac{-2.97\times10^4}{T}+21.1)$	247

4.3.3 Kinetics of the calculated precipitation results of the base materials

Fig. 4.11 shows the calculation results for the γ phase precipitation behavior of the Fe–Cr–Ni ternary system converted into Cr and Ni equivalents according to Eq. (4.28). Regardless of the alloy composition, the amount of saturated γ phase precipitated was increased with an increase in the temperature from 948 K to 1023 K, reaching a maximum at 1023 K. At higher temperatures, this amount was decreased. Fig. 4.12 shows Austin–Rickett plots for the precipitation behavior of the γ phase in the investigated DSSs. The plots indicate a good linear relationship, and the slope of the line is almost the same regardless of the heating temperature.

The temperature–dependent rate constant and time exponents (*n*) can be derived according to temperature from the aforementioned Austin–Rickett plots in Fig. Fig. 4.12, and the results are presented in Table 4.5. The time exponents (*n*) for lean, standard, and super DSSs were determined to be 1.01, 0.82, and 0.77, respectively. Consequently, the precipitation kinetics of the γ phase in all base metal HAZs were followed by the Austin–Rickett equation. In addition, it can be observed from Table 4.5 that the precipitation is fastest at 1073 K for lean and standard DSSs and at 1023 K for super DSS. Fig. 4.13 shows the regression analysis results of the phase–field calculated values. In Fig. 4.13, the precipitation rate constant curve derived from the calculations represents a C–curve diagram with a nose. The calculated rate constants of lean (type 821L1), standard (type 329J3L), and super (type 327L1) DSSs were 8.2, 5.2, and 4.5, respectively. Besides, the calculated nose temperatures were 1073 K, 1073 K, and 1023 K for lean (type 821L1), standard (type 329J3L), and super (type 327L1) DSSs, respectively

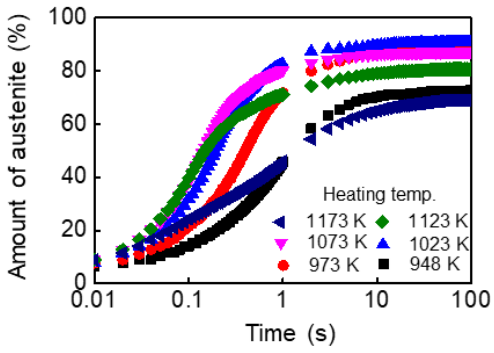

(a) Lean DSS (type 821L1).

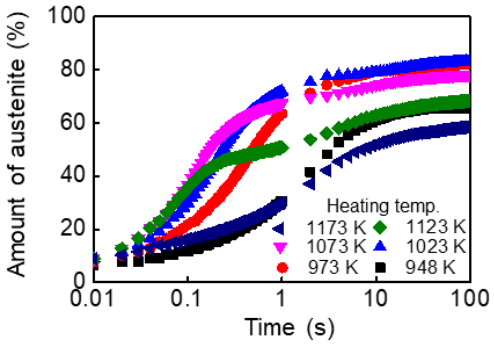

(b) Standard DSS (type 329J3L).

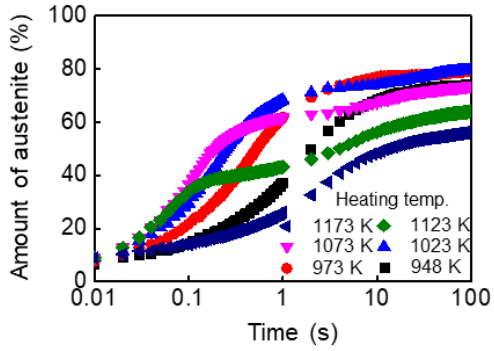

(c) Super DSS (type 327L1).

Fig. 4.11 Changes in the precipitated γ fraction for the DSSs at different temperatures.

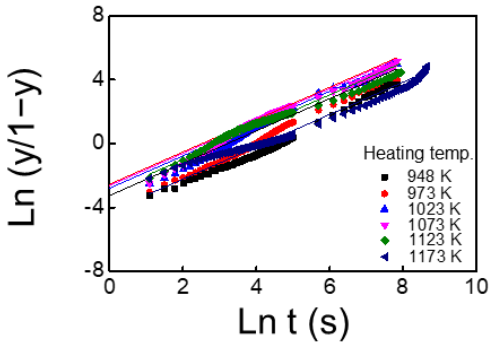

(a) Lean DSS (type 821L1).

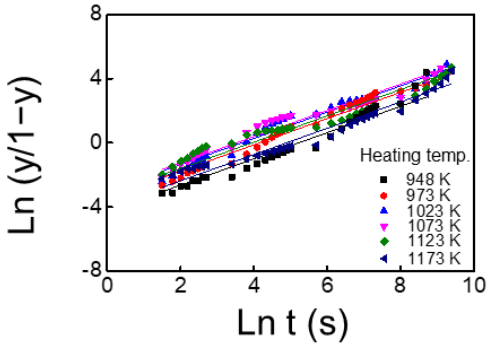

(b) Standard DSS (type 329J3L).

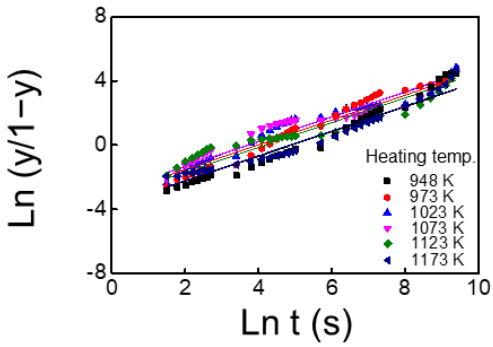

(c) Super DSS (type 327L1).

Fig. 4.12 Austin–Rickett plots of the γ phase precipitation behavior in the base material HAZs for the DSSs at different temperatures.

Table 4.5 Experimental time constant and rate constant of γ precipitation in DSSs (base materials).

Steel type	Time constant, *n*	Nose temperature (K)	Maximum value of the rate constant, *K* (s^{-1})
Lean DSS (type 821L1)	1.01	1073	8.21
Standard DSS (type 329J3L)	0.82	1073	5.24
Super DSS (type 327L1)	0.77	1023	4.51

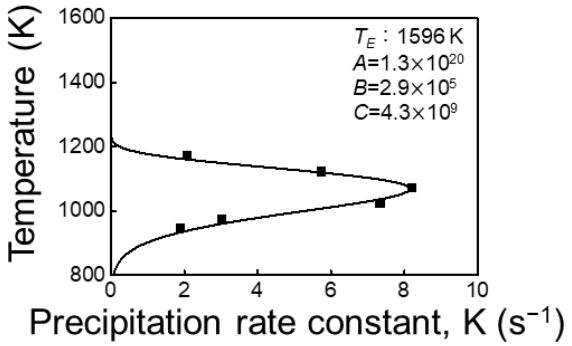

(a) Lean DSS (type 821L1).

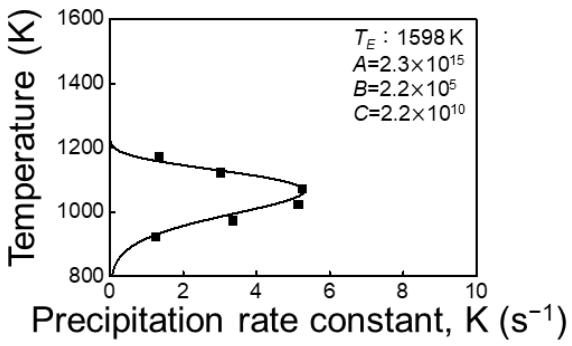

(b) Standard DSS (type 329J3L).

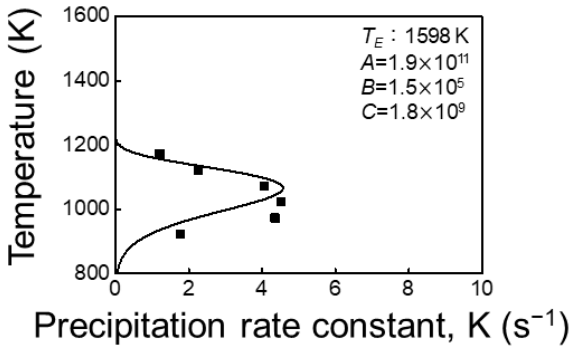

(c) Super DSS (type 327L1).

Fig. 4.13 Regression analysis of the precipitation rate constants of the γ phase in the base material HAZs for the DSSs.

4.3.4 Kinetics of the calculated precipitation results of the weld metals

Fig. 4.14 shows the results of calculation the γ precipitation behavior using the Fe–Cr–Ni ternary composition converted by Cr, Ni equivalent in Eq. (4.28). Regardless of the alloy compositions, when the temperature was increased from 923 K to 1023 K, the saturated precipitation amount was increased and the saturated precipitation amount at 1023 K temperature became maximum. At a temperature higher than that, the amount of saturated precipitation was decreased. Fig. 4.15 shows the results of the Austin–Rickett plot for the γ phase precipitation behavior of DSSs. In the case of the precipitation phenomenon, the time exponents (n) of lean (lab), standard (type 329J3L), and super (type 327L1) DSSs were determined to be 1.1, 1.01, and 0.74, respectively. The regression analysis of the precipitation phenomenon was based on the results obtained in Fig. 4.15. The regression analysis results for each steel type are shown in Fig. 4.16, and the determined time constant and rate constant are summarized in Table 4.6. The precipitation rate constant derived from the calculation result in Fig. 4.16 has a nose.

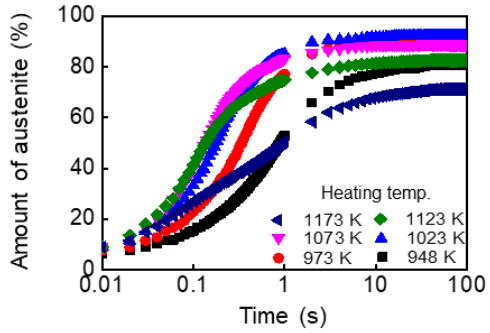

(a) Lean DSS (lab).

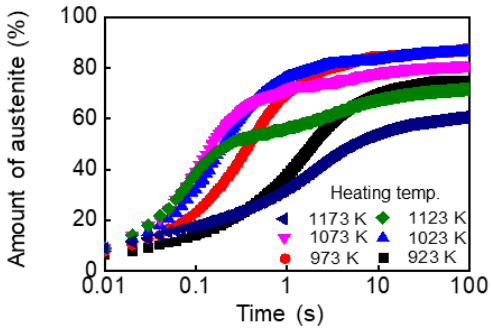

(b) Standard DSS (type 329J3L).

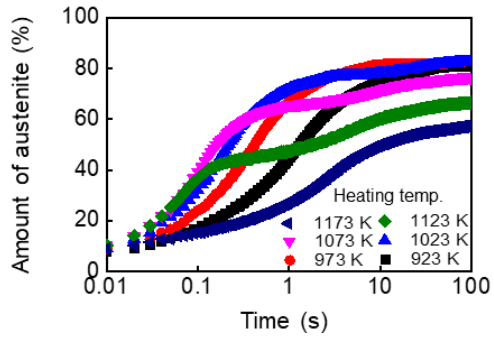

(c) Super DSS (type 327L1).

Fig. 4.14 Changes in the precipitated γ fraction for the DSSs at different temperatures.

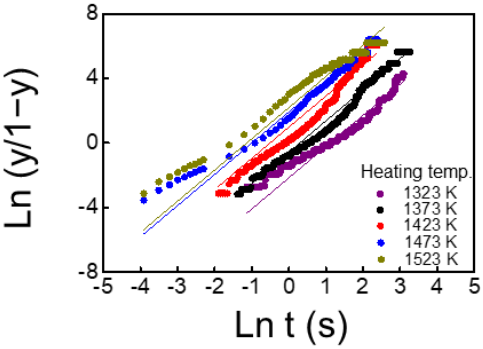

(a) Lean DSS (lab).

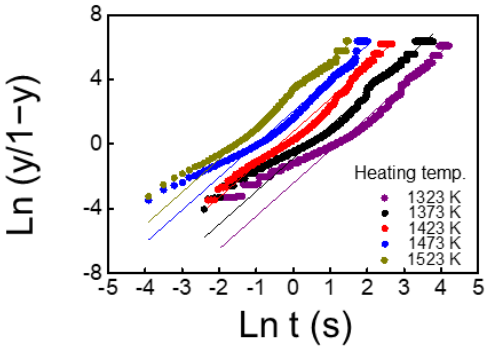

(b) Standard DSS (type 329J3L).

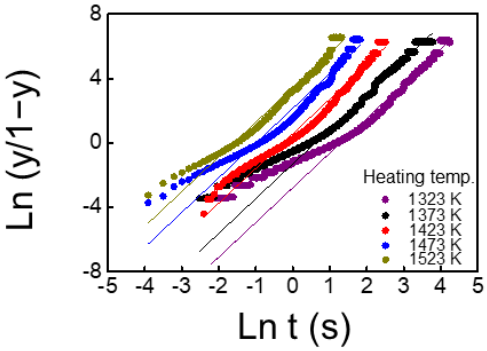

(c) Super DSS (type 327L1).

Fig. 4.15 Austin–Rickett plots of the γ phase precipitation behavior in the weld metals for the DSSs at different temperatures.

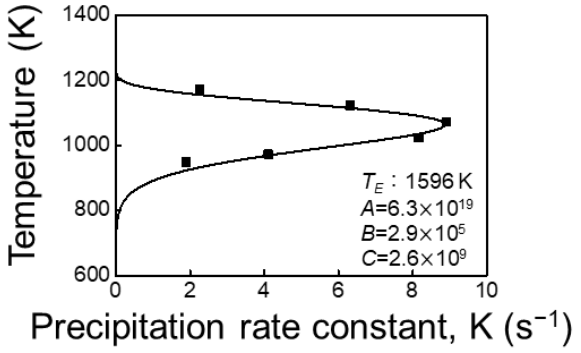

(a) Lean DSS (lab).

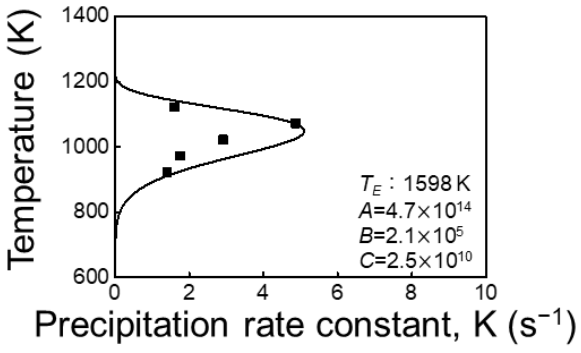

(b) Standard DSS (type 329J3L).

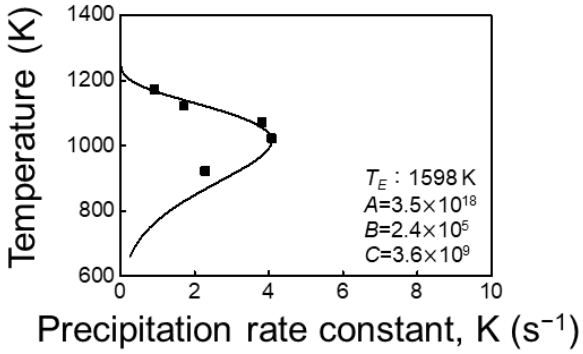

(c) Super DSS (type 327L1).

Fig. 4.16 Regression analysis of the precipitation rate constants of the γ phase in the weld metals for the DSSs.

Table 4.6 Experimental time constant and rate constant of γ precipitation in DSSs (weld metals).

Steel type	Time constant, *n*	Nose temperature (K)	Maximum value of the rate constant, *K* (s^{-1})
Lean DSS (lab)	1.1	1073	8.9
Standard DSS (type 329J3L)	1.01	1073	4.4
Super DSS (type 327L1)	0.74	973	4.1

4.4. Conclusions

A theoretical approach for the prediction of the γ phase dissolution and precipitation behavior of DSSs was developed by applying phase–field theory. The main results and conclusions of this study are summarized as follows:

1) The fraction of γ phase during the solution heat treatment of the multi–system composition DSSs converted to ternary composition using Cr and Ni equivalents was derived from phase–field simulation. During the solution heat treatment of DSSs (base metal, welded metal), the fraction of γ phase derived from the phase–field simulation was increased with an increase in heat temperature and holding time and saturated with equilibrium fraction in all steels.

2) The fraction of γ phase derived from the phase–field simulation was used in the Austin–Rickett equation to examine the dissolution kinetics. The results of the Austin–Rickett plot showed a good linear relationship, and a time exponents (n) was obtained. Consequently, the dissolution kinetics of the γ phase of all DSSs were approximately followed by the Austin–Rickett equation. Besides, the temperature dependence of the dissolution rate was investigated using the Arrhenius–type equation.

3) The fraction of γ phase during the precipitation heat treatment of the multi–system composition DSSs converted to ternary composition using Cr and Ni equivalents was derived from phase–field simulation. During the precipitation heat treatment of DSSs (base metal, welded metal), the fraction of γ phase derived from the phase–field simulation was increased with an increase in heat temperature and holding time and saturated with equilibrium fraction in all steels.

4) The fraction of γ phase derived from the phase–field simulation was used in the Austin–Rickett equation to examine the precipitation kinetics. The results of the Austin–Rickett plot showed a good linear relationship, and a time exponents (n) was obtained. As a result, the precipitation kinetics of the γ phase of all DSSs were approximately followed by the Austin–Rickett equation.

5) From the results of the Austin–Rickett plot, it was confirmed that the precipitation of the γ phase in DSSs is fastest at the certain intermediate temperature, which cannot be considered for temperature dependence with a simple Arrhenius–type equation. Therefore, the temperature dependence on the precipitation rate of the γ phase in DSSs with a precipitation nose was theoretically examined using the non–uniform nucleation rate equation.

6) In this study, a kinetics was performed using the amount of γ derived from the phase-field simulation. In the case of the dissolution phenomenon, it was calculated using the Arrhenius–type equation to investigate the temperature dependence of the dissolution rate, and a good linear relationship was shown between ln k and $1/T$. The temperature dependence of the precipitation phenomenon was theoretically investigated using the non-uniform nucleation rate equation, and the derived precipitation rate constant curve showed a C–curve with a nose similar to the experimental results. From the above facts, it was judged that the kinetics using the phase–field simulation constructed in this study was valid.

Chapter 5 Determination of rate constant of α/γ phase transformation based on the phase–field method

5.1 Introduction

With the continuous advance of technology, computer simulations have become a powerful tool for material design. Because of the low development costs, they can be applied to any type of steel and allow the modeling of the kinetics of the transformation, based on the chemical composition. In recent years, the phase–field method has been applied to simulate the phase transformations and microstructural evolutions of materials. The phase–field method was originally proposed to simulate the dendritic growth in pure undercooled melts [185–188].

Later, it was extended to the solidification of alloys with one [189–191] or two [192–193] solid phases. Using a phase–field method derived by Steinbach et al. [194], the austenite to ferrite phase transformation during controlled cooling was investigated for both C–Mn–Nb steels and C–Mn steels [145,195]. Yeon et al. [146] simulated the isothermal austenite to ferrite transformation in a Fe–Mn–C system under para–equilibrium. Using the model of Steinbach et al., Pariser et al. [147] modeled the austenite to ferrite transformation in an ultra–low carbon steel and in an interstitial–free steel during cooling at a medium cooling rate. In addition, Koyama et al. [148–149] investigated the phase decomposition of elemental Ni and Mn during the spinodal decomposition in Fe–Cu–Ni–Mn quaternary alloys. Nevertheless, the kinetics of the α/γ phase transformation of DSSs have been rarely investigated quantitatively using the phase–field method, which does not involve any experimental derivation. Accordingly, we investigated the dissolution and precipitation of the γ phase in DSSs with an Fe–Cr–Ni ternary system composition converted to its Cr/Ni equivalent using the phase field method in Chapter 4. However, in the calculated value and the experimental value of the DSSs assumed as a ternary system, inconsistency of values may occur due to the difference in the magnetic diffusion coefficient of Cr and Ni and the difference in the degree of equilibrium.

Therefore, in this study, the verification of validity and introduction of correction factors were reviewed by comparing the calculated values obtained in Chapter 4 with the measured values.

5.2 Correction factor for γ dissolution phenomenon in base materials

5.2.1 Comparison between temperature dependences of dissolution rate constant determined experimentally and numerically

The chemical composition used to apply the correction factor used the chemical composition already discussed in Table 4.1 in Chapter 4. The Arrhenius plots shown in Fig. 5.1 were obtained to compare the experimental and calculated results. From the figure, it can be seen that ln k and $1/T$ have a good linear relationship. Then, the temperature dependencies of the dissolution rate of the γ phase in lean (type 821L1), standard (type 329J3L), and super (type 327L1) DSSs were investigated, and the results are presented in Table 5.1. In Fig. 5.1, there is a difference in the experimental and calculated values; however, a relationship between them

was observed. Therefore, an attempt was made to correct the calculation results to better approximate the experimental results. In the Arrhenius plots shown in Fig. 5.1, the slope depends on the value of the activation energy, and ln k is related to the k_0 value in Eq. (3.4).

Therefore, we show the comparison of the activation energy and the k_0 values obtained experimentally and numerically in Table 5.2, and the correction constant was derived by comparing these values. From Table 5.2, it can be seen that the experimental activation energy and k_0 are approximately 1.38 and 1.33 times greater than the calculated ones. These values were used as correction factors.

Table 5.1. Experimental and calculated temperature dependencies of the γ phase dissolution.

Experimental value			Calculated value		
Steel type	The temperature dependency of dissolution rate [s^{-1}]	ΔG [kJ/mol]	Steel type	The temperature dependency of dissolution rate [s^{-1}]	ΔG [kJ/mol]
Lean DSS (type 821L1)	$K=\exp(\frac{-3.43\times10^4}{T}+21.4)$	285	Lean DSS (type 821L1)	$K=\exp(\frac{-2.36\times10^4}{T}+16.84)$	196
Standard DSS (type 329J3L)	$K=\exp(\frac{-4.05\times10^4}{T}+25.64)$	337	Standard DSS (type 329J3L)	$K=\exp(\frac{-2.92\times10^4}{T}+20.9)$	242
Super DSS (type 327L1)	$K=\exp(\frac{-3.26\times10^4}{T}+18.39)$	271	Super DSS (type 327L1)	$K=\exp(\frac{-2.51\times10^4}{T}+17.93)$	209

Table 5.2. Experimental and calculated activation energies and frequency factors.

Activation energy [kJ/mol]			Frequency factor [s^{-1}]		
Steel type	Experimental value	Calculated value	Steel type	Experimental value	Calculated value
Lean DSS (type 821L1)	285	196	Lean DSS (type 821L1)	1.97×10^9	7.87×10^8
Standard DSS (type 329J3L)	337	242	Standard DSS (type 329J3L)	1.36×10^{11}	1.11×10^{11}
Super DSS (type 327L1)	271	209	Super DSS (type 327L1)	9.65×10^7	3.97×10^8

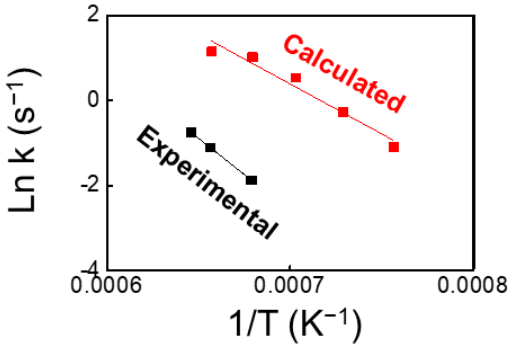

(a) Lean DSS (type 821L1).

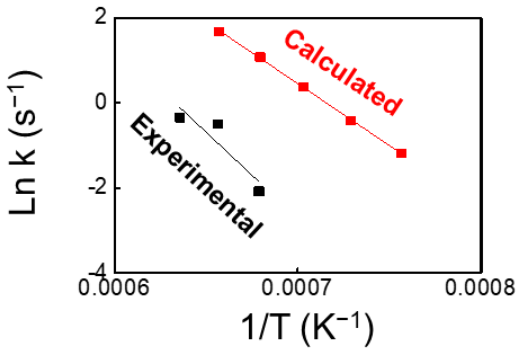

(b) Standard DSS (type 329J3L).

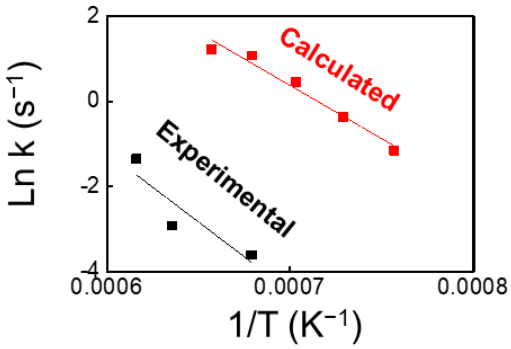

(c) Super DSS (type 327L1).

Fig. 5.1 Arrhenius plots of the dissolution rates constants of the γ phase in the base material HAZs for the DSSs.

5.2.2 Validation of the correction factors

Table 5.3 shows the temperature dependencies obtained by applying the correction factors derived in Section 5.2.1. Fig. 5.2 shows the Arrhenius plots of the γ phase dissolution rates obtained experimentally and by applying the correction factors. The higher correlation between the experimental and calculated values validates the correction factors. Furthermore, the general applicability of the average correction factors was investigated by applying them to DSSs with different compositions.

Table 5.3. Temperature dependencies of the γ phase dissolution rates obtained experimentally and by the corrected calculation.

Experimental value			Calculated value		
Steel type	The temperature dependency of dissolution rate [s^{-1}]	ΔG [kJ/mol]	Steel type	The temperature dependency of dissolution rate [s^{-1}]	ΔG [kJ/mol]
Lean DSS (type 821L1)	$K=\exp(\frac{-3.43\times10^4}{T}+21.4)$	285	Lean DSS (type 821L1)	$K=\exp(\frac{-3.3\times10^4}{T}+20.8)$	271
Standard DSS (type 329J3L)	$K=\exp(\frac{-4.05\times10^4}{T}+25.64)$	337	Standard DSS (type 329J3L)	$K=\exp(\frac{-4.02\times10^4}{T}+25.7)$	334
Super DSS (type 327L1)	$K=\exp(\frac{-3.26\times10^4}{T}+18.39)$	271	Super DSS (type 327L1)	$K=\exp(\frac{-3.46\times10^4}{T}+20)$	288

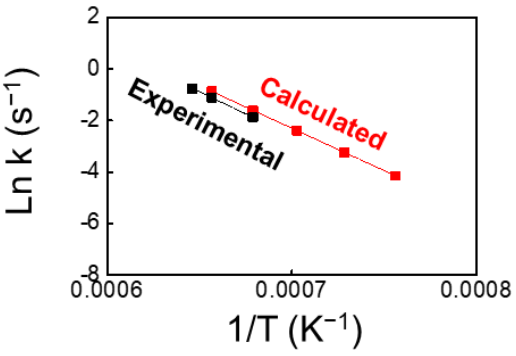

(a) Lean DSS (type 821L1).

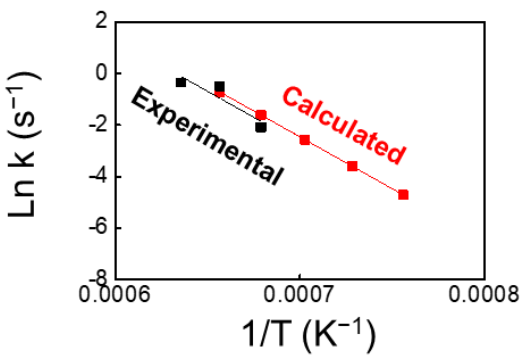

(b) Standard DSS (type 329J3L).

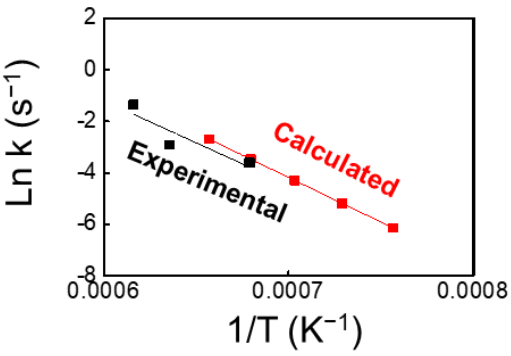

(c) Super DSS (type 327L1).

Fig. 5.2 Arrhenius plots of the dissolution rates constants of the γ phase in the base material HAZs for the DSSs.

5.2.3 Applicability of the proposed model to other steel grades

The generality of the phase–field method established in this study was evaluated using a lean (lab) and super (type 329J4L) DSSs with the chemical composition shown in Table 5.4. Fig. 5.3 shows the calculation results for the γ phase dissolution behavior using the Fe–Cr–Ni ternary system composition converted into Cr and Ni equivalents according to Eq. (4.28). As the temperature was increased from 1323 K to 1523 K, the amount of saturated γ phase dissolved was increased, reaching a maximum at 1523 K. Fig. 5.4 shows Austin–Rickett plots for the dissolution behavior of the γ phase in the investigated DSSs. From the figure, it can be seen that the Austin–Rickett plot exhibits a good linear relationship; thus, the dissolution kinetics of the γ phase are considered to approximately follow the Austin–Rickett equation. To investigate the temperature dependence of the γ phase dissolution phenomena, the rate constant $k(T)$ was calculated using the Arrhenius–type equation (Eq. 3.4). In addition, the results obtained are compared with the experimental values as in Section 5.2.1, and the results are shown in Fig. 5.5. Like the previous results, there is clearly a difference in absolute value between the calculated value and the experimental value, but it can be seen that a similar trend is observed.

Therefore, we applied the correction factor applied in Section 5.2.1 and compared the result with the experimental value. Fig. 5.6 shows the result of comparing the temperature dependence of the γ phase dissolution phenomena between the corrected calculated value and the experimental value. It can be seen that the result after correction correlated better with the experimental value than the uncorrected result. Table. 5.5 shows the results of the temperature dependence of the γ phase dissolution rate of the lean (lab) and super (type 329J4L) DSSs. The temperature dependence of the γ phase dissolution constant derived by the phase–field method was extremely well–correlated with the experimental values. This indicates that the model proposed in this study for deriving the γ phase dissolution rate using the phase–field method can potentially be applied to other DSSs. In this study, three types of DSSs were used to derive the correction factor. The investigation of more types of DSSs could increase the reliability of the correction factor. In future studies, the temperature dependence of the precipitation rate will be investigated and the α/γ phase transformation behavior of the multi–pass welds will be predicted using the temperature dependence of precipitation and dissolution phenomena.

Table 5.4 Chemical composition of the duplex stainless steels in this study (mass %).

Steel	C	Si	Mn	P	S	Ni	Cr	Mo	Cu	N	Fe
Lean DSS (lab)	0.014	0.35	1.49	0.024	0.0004	3.06	20.85	0.30	0.09	0.177	Bal.
Super DSS (type 329J4L)	0.025	0.33	0.73	0.031	<0.001	6.33	24.69	3.21	0.06	0.17	Bal.

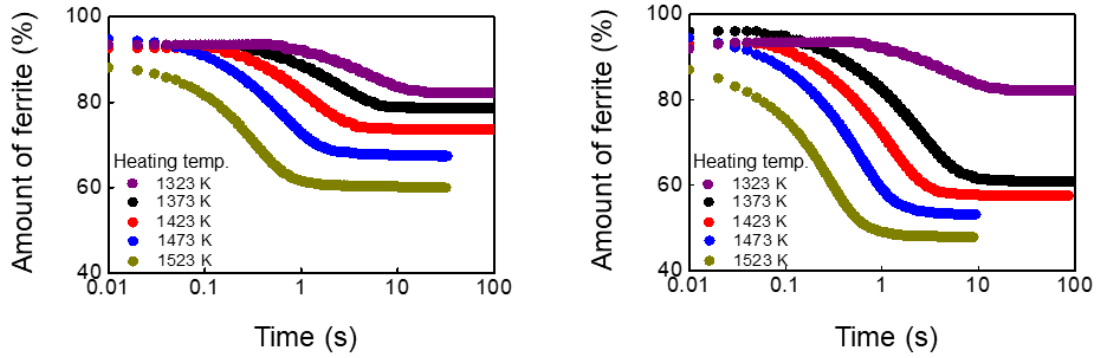

(a) Lean DSS (lab). (b) Super DSS (type 329J4L).

Fig. 5.3 Changes in the dissolved γ fraction for the DSSs at different temperatures.

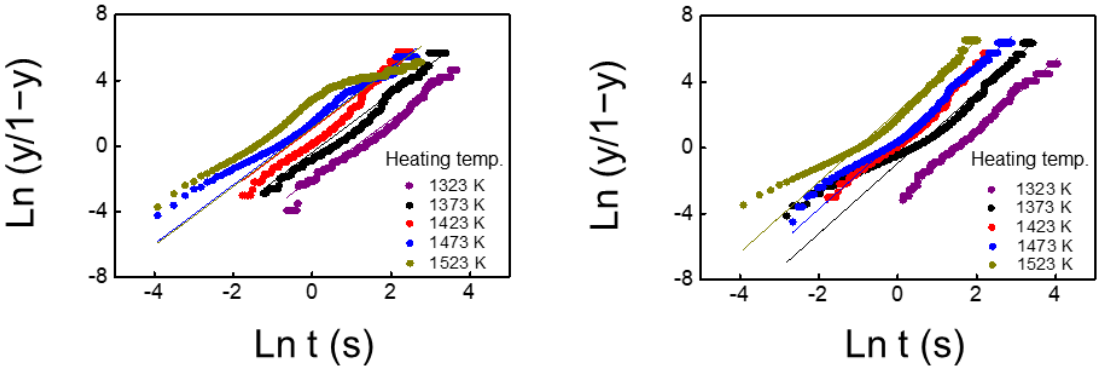

(a) Lean DSS (lab). (b) Super DSS (type 329J4L).

Fig. 5.4 Austin–Rickett plots of the γ phase dissolution behavior in the base material HAZs for the DSSs at different temperatures.

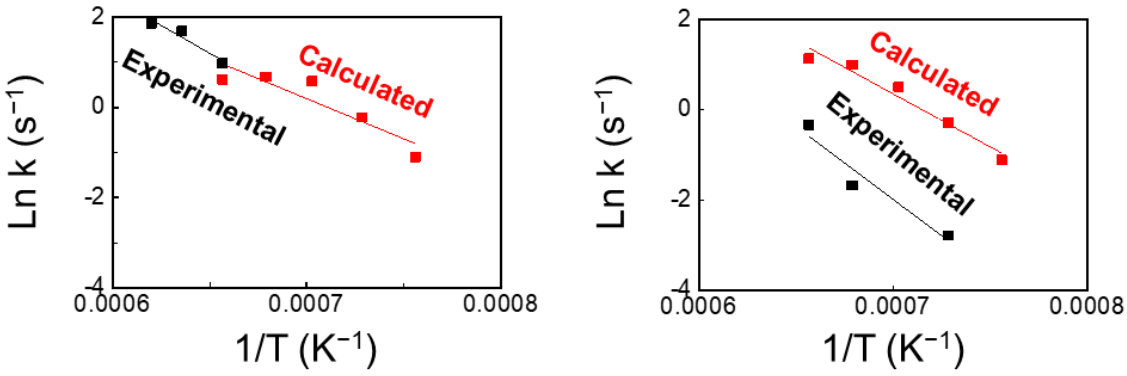

(a) Lean DSS (lab). (b) Super DSS (type 329J4L).

Fig. 5.5 Arrhenius plot of dissolution rate of γ phase in HAZ before introduction of correction factor for the DSSs.

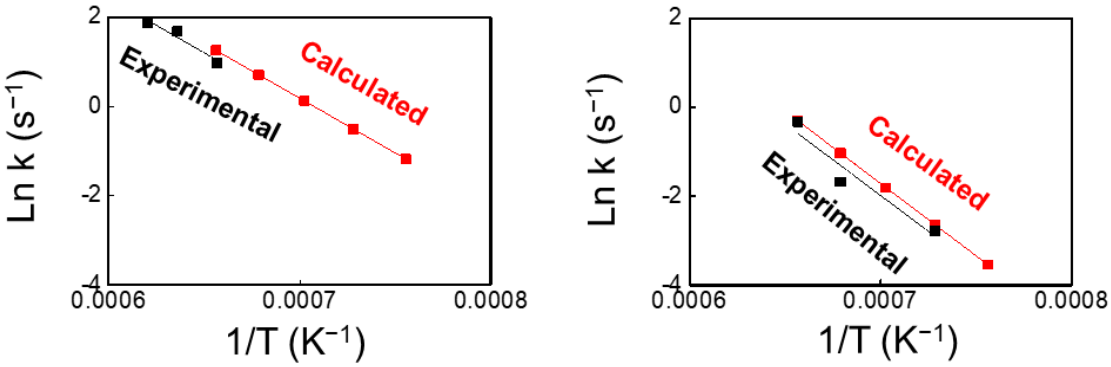

(a) Lean DSS (lab). (b) Super DSS (type 329J4L).

Fig. 5.6 Arrhenius plot of dissolution rate of γ phase in HAZ after introduction of correction factor for the DSSs.

Table 5.5. Temperature dependencies of the γ phase dissolution rates obtained experimentally and by the corrected calculation.

Experimental value			Calculated value		
Steel type	The temperature dependency of dissolution rate [s^{-1}]	ΔG [kJ/mol]	Steel type	The temperature dependency of dissolution rate [s^{-1}]	ΔG [kJ/mol]
Lean DSS (lab)	$K=\exp(\frac{-2.47\times10^4}{T}+17.24)$	285	Lean DSS (lab)	$K=\exp(\frac{-2.46\times10^4}{T}+17.42)$	271
Standard DSS (type 329J4L)	$K=\exp(\frac{-3.22\times10^4}{T}+20.62)$	271	Standard DSS (type 329J4L)	$K=\exp(\frac{-3.25\times10^4}{T}+21.1)$	288

5.3 Correction factor for γ dissolution phenomenon in weld metals

5.3.1 Comparison between temperature dependences of dissolution rate constant determined experimentally and numerically

The chemical composition used to apply the correction factor used the chemical composition already discussed in Table 4.3 in Chapter 4. Fig. 5.7 shows the results of calculating the dissolution of γ behavior using the Fe–Cr–Ni ternary composition obtained by converting the composition of duplex stainless steel by Cr and Ni equivalents in Eq. (4.28). Regardless of the alloy composition, the saturated dissolution was increased with an increase in heating temperature. Fig. 5.8 shows the results of the Austin–Rickett plot for the γ phase dissolution behavior of DSSs. In the case of the dissolution phenomenon, the time exponents (n) of lean (lab), standard (type 329J3L), and super (type 327L1) DSSs were determined as 1.8, 2.04, and 2.2 (table 4.4 in Chapter 4), respectively. In order to investigate the temperature dependence, the dissolution phenomenon was investigated using Eq. (3.4). Arrhenius plot was performed based on the results in Fig.5.8, and the results are shown in Fig. 5.9. There are good linear relationships between ln k and $1/T$ for both steels, and therefore, $k(T)$ of Eq. (3.4) can be obtained as in table 5.6. As can be seen from Fig 5.9, there is clearly a difference in absolute value between the calculated value and the experimental value, but it can be seen that a similar trend is observed. Therefore, in order to derive a result close to the experimental value, correction was performed by introducing the correction factor applied in the Section 5.2.1.

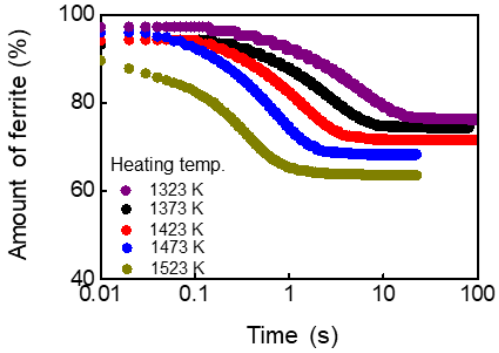

(a) Lean DSS (lab).

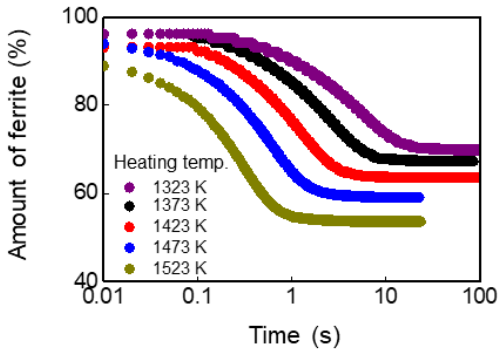

(b) Standard DSS (type 329J3L).

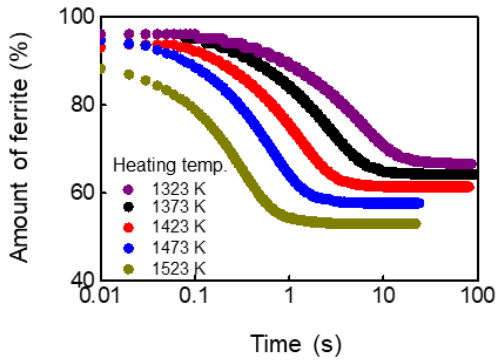

(c) Super DSS (type 327L1).

Fig. 5.7 Changes in the dissolved γ fraction for the DSSs at different temperatures.

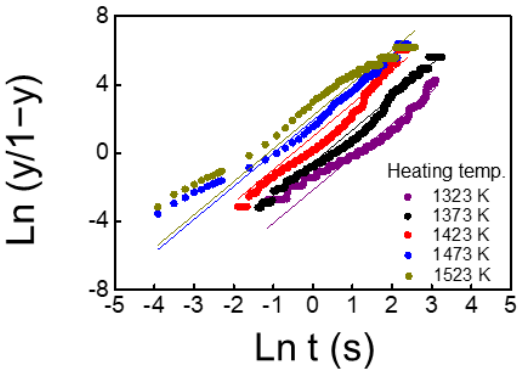

(a) Lean DSS (lab).

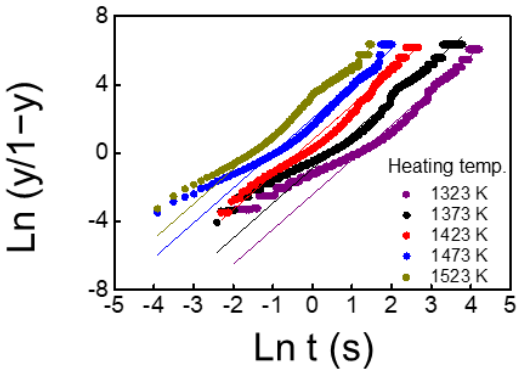

(b) Standard DSS (type 329J3L).

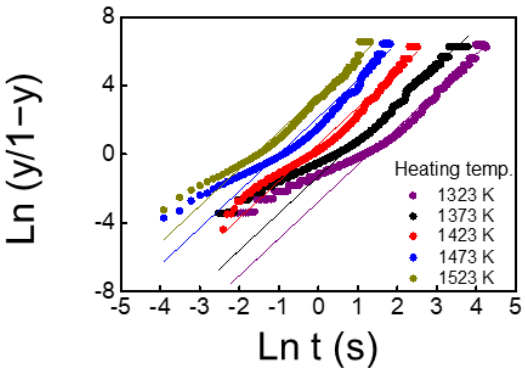

(c) Super DSS (type 327L1).

Fig. 5.8 Austin–Rickett plots of the γ phase dissolution behavior in the weld metals for the DSSs at different temperatures.

Table 5.6 Calculated temperature dependencies of the γ phase dissolution.

Steel type	The temperature dependency of dissolution rate [s^{-1}]	ΔG [kJ/mol]
Lean DSS (lab)	$K=\exp(\frac{-1.78\times10^4}{T}+17.1)$	148
Standard DSS (type 329J3L)	$K=\exp(\frac{-2.8\times10^4}{T}+19.9)$	232
Super DSS (type 327L1)	$K=\exp(\frac{-2.97\times10^4}{T}+21.1)$	247

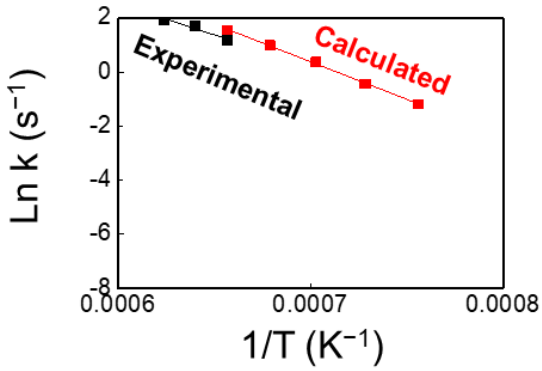

(a) Lean DSS (lab).

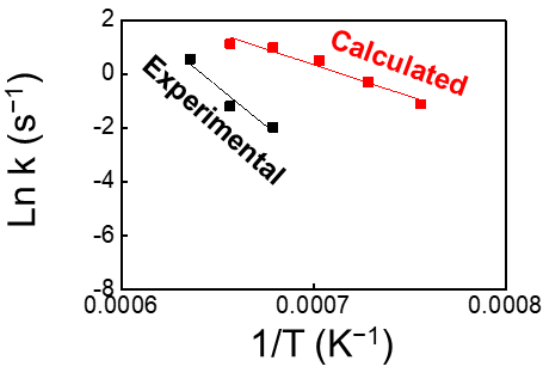

(b) Standard DSS (type 329J3L).

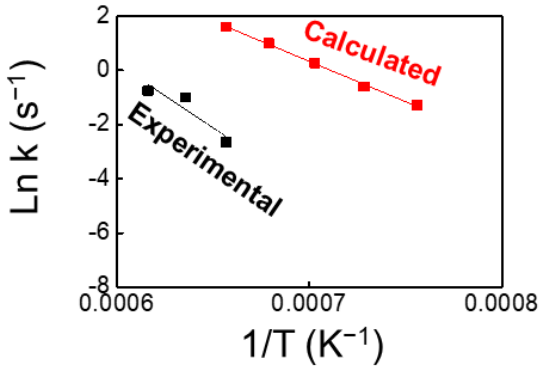

(c) Super DSS (type 327L1).

Fig. 5.9 Arrhenius plots of the dissolution rates constants of the γ phase in the weld metals for the DSSs.

5.3.2 Validation of the correction factors

Fig. 5.10 shows the results of Arrhenius plot by applying the correction factor. Fig. 5.10 shows the result of comparison with the calculated value after correction and the experimental value. From Fig. 5.10, since the correlation between the calculated value and the experimental value after the correction was increased, the correction factor introduced in the Section 5.2.1 is judged to be reasonable. Besides, the results on the rate constant and temperature dependence of the calculated values after correction are summarized in Table 5.7.

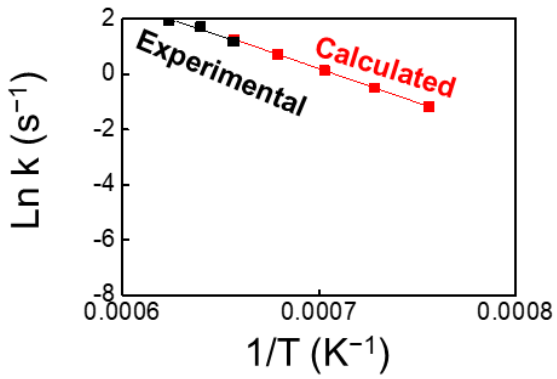

(a) Lean DSS (lab).

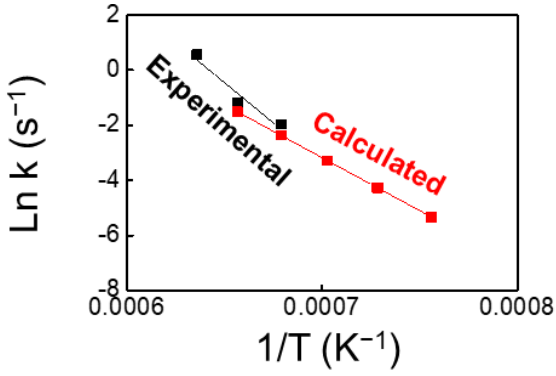

(b) Standard DSS (type 329J3L).

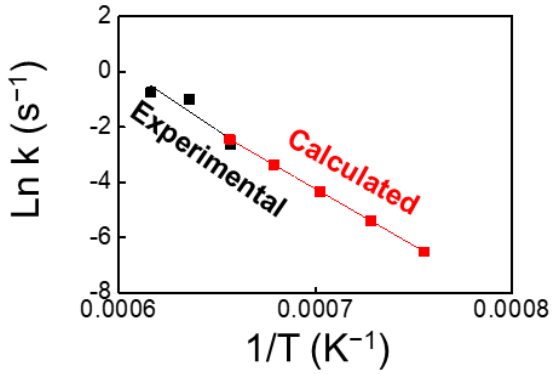

(c) Super DSS (type 327L1).

Fig. 5.10 Arrhenius plots of the dissolution rates constants of the γ phase in the weld metals for the DSSs.

Table 5.7 Temperature dependencies of the γ phase dissolution rates obtained by the corrected calculation.

Steel type	The temperature dependency of dissolution rate [s^{-1}]	ΔG [kJ/mol]
Lean DSS (lab)	$K=\exp(\frac{-2.46\times10^4}{T}+17.42)$	204
Standard DSS (type 329J3L)	$K=\exp(\frac{-3.84\times10^4}{T}+23.7)$	319
Super DSS (type 327L1)	$K=\exp(\frac{-4.1\times10^4}{T}+24.5)$	341

5.4 Correction factor for γ precipitation phenomenon in base materials

5.4.1 Comparison between temperature dependences of precipitation rate constant determined experimentally and numerically

The results of the temperature dependence of the precipitation rate constant according to the steel type are derived using the temperature–dependent rate constant and time exponents (n) derived in Chapter 4 (phase–field calculated values) and Chapter 3 (experimental values). Fig. 5.11(a) shows the regression analysis results of the phase–field calculated values, whereas Fig. 5.11(b) shows the regression analysis results of the experimental values. In Fig. 5.11, the precipitation rate constant curve derived from the calculations represents a C–curve diagram with a nose similar to the experimental results. It can be observed from Fig. 5.11 that there is a difference between the absolute value of the calculation and experiment results; however, the trend of the two sets of values is similar. Fig. 5.12 shows the maximum rate constant and the nose temperature from Fig. 5.11 The calculated rate constants of lean (type 821L1), standard (type 329J3L), and super (type 327L1) DSSs were 8.2, 5.2, and 4.5 (table 4.5 in Chapter 4), respectively, and the experimental values were 0.24, 0.2, and 0.14 (table 3.8 in Chapter 3), respectively. Besides, the calculated nose temperatures were 1073 K, 1073 K, and 1023 K (table 4.5 in Chapter 4) for lean (type 821L1), standard (type 329J3L), and super (type 327L1) DSSs, respectively, and the experimental values were 1258 K, 1273 K, and 1223 K (table 3.8 in Chapter 3), respectively. It can be observed from Fig. 5.12 that the absolute value is different in the calculation and experimental results; however, the rate constants and nose temperatures of the different steels are correlated. Therefore, it seems possible to obtain accurate results by correcting the calculation–based rate constant and nose temperature. The differences between the experimental and calculated values of the rate constant are attributed to the difference in the magnetic diffusion coefficients of Cr and Ni because DSS was assumed to be a ternary system. The differences in the nose temperatures could occur because of the dissimilarities originating from the differences in the equilibrium degree of DSS and ternary alloys. Therefore, the rate constant was corrected by multiplying it by a correction factor of 0.0314 and the nose temperature was corrected by adding 213 K to the calculated value.

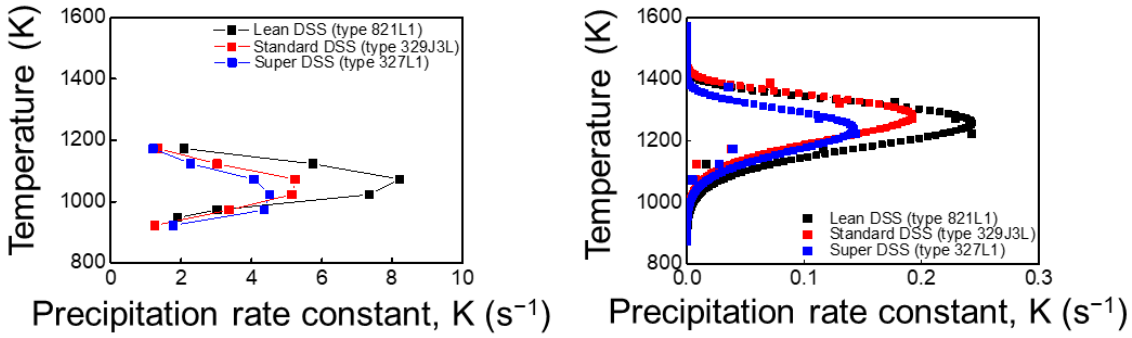

(a) Calculated results. (b) Experimental results.

Fig. 5.11 Regression analysis of the precipitation rate constants of the γ phase in the base metal HAZs for the DSSs.

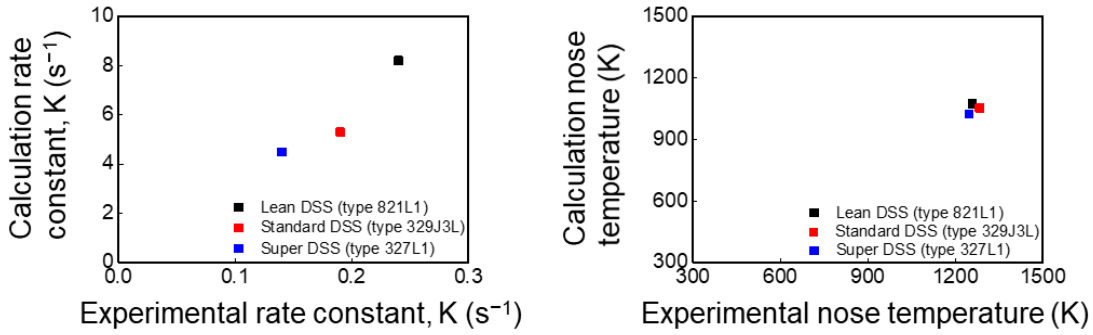

(a) Maximum value of the rate constant. (b) Nose temperature.

Fig. 5.12 Correlation between experimental and calculated results.

5.4.2 Validation of the correction factors

Fig. 5.13 (a)–(b) show the corrected calculation results and the regression analysis outcome for the experimental results. These figures indicate that the correction is valid because the degree of correlation between the experimental and calculated values were increased on introducing the correction factors. To investigate the applicability of this approach, we applied the average correction factor of the three steel grades to DSSs having different compositions, as described in Section 5.3.1.

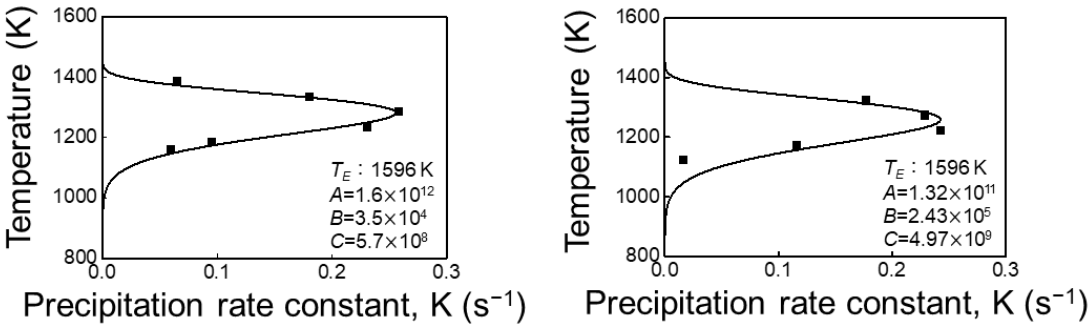

(a–1) Lean DSS (type 821L1).

(b–1) Lean DSS (type 821L1).

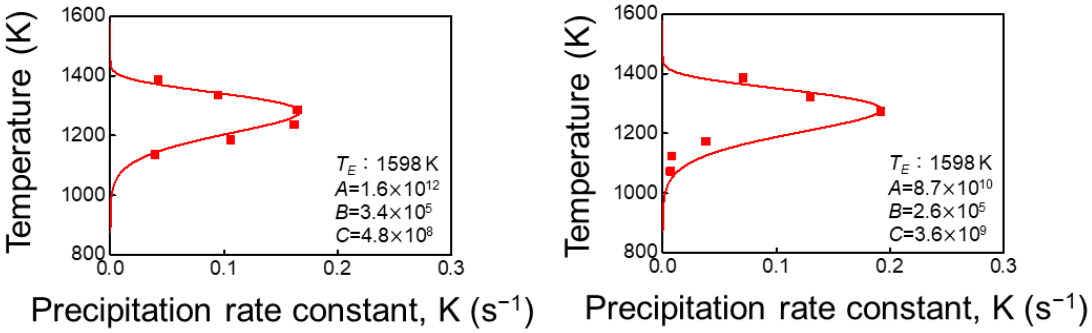

(a–2) Standard DSS (type 329J3L).

(b–2) Standard DSS (type 329J3L).

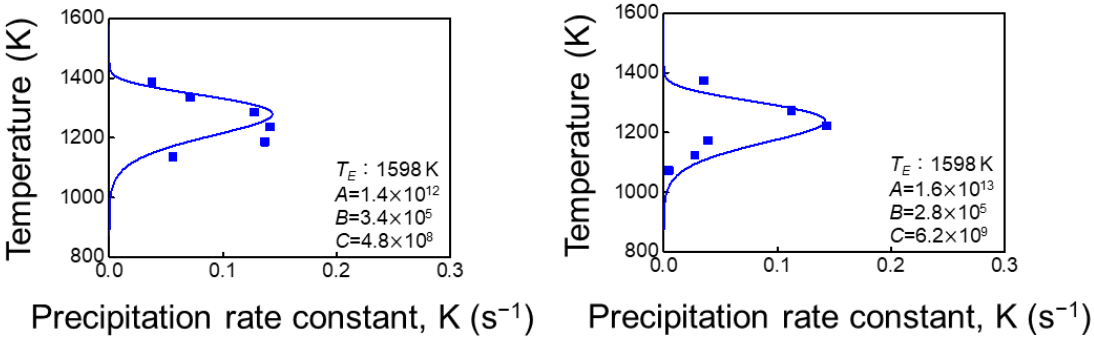

(a–3) Super DSS (type 327L1).

(b–3) Super DSS (type 327L1).

(a) Corrected calculation values.

(b) Experimental values.

Fig. 5.13 Comparison of the temperature–precipitation rate constant curves for the DSSs.

5.4.3 Applicability of the proposed model to other steel grades

To evaluate the applicability of the phase–field method established in this study to other steels, we investigated DSSs with different chemical compositions. The chemical composition of the lean (lab) and super (type 329J4L) DSSs used in the aforementioned evaluation is given in Table 5.4. Fig. 5.14 shows the calculation results for the γ phase precipitation behavior using the Fe–Cr–Ni ternary system composition converted into Cr and Ni equivalents according to Eq. (4.28). As the temperature increases from 948 K to 1023 K, the amount of saturated γ phase precipitated was increased, reaching a maximum at 1023 K. At higher temperatures, this amount was decreased. Fig. 5.15 shows the Austin–Rickett plots for the precipitation behavior of the γ phase in the investigated DSSs. The plots indicate a good linear relationship; therefore, the precipitation kinetics of the γ phase was approximately followed by the Austin–Rickett

equation. Using the correction factors mentioned in Section 5.3.1, the values obtained from the horizontal and vertical axes were corrected; the results obtained through regression analysis are shown in Fig. 5.16 (a), and the regression analysis outcome for the experimental results is shown in Fig. 5.12(b) for comparison. Figs. 5.16 (a) and 5.16 (b) show that although there are some differences on the temperature axis, the experimental and calculated values are generally in good agreement. Fig. 5.17 shows the maximum rate constant and the nose temperature for the four steel grades investigated; it can be observed from the figure that the calculated and experimental values present a one–to–one relationship. Therefore, similar to the discussion on the dissolution phenomenon in Chapter 5.2, the γ phase precipitation behavior model based on the phase–field method can be extended to other DSSs. However, there are a few things to overcome in the future. There is some temperature difference, which is believed to be due to the fact that only three data points were used to derive the correction factor. However, the accuracy of the model will improve with the accumulation of calculation data in the future.

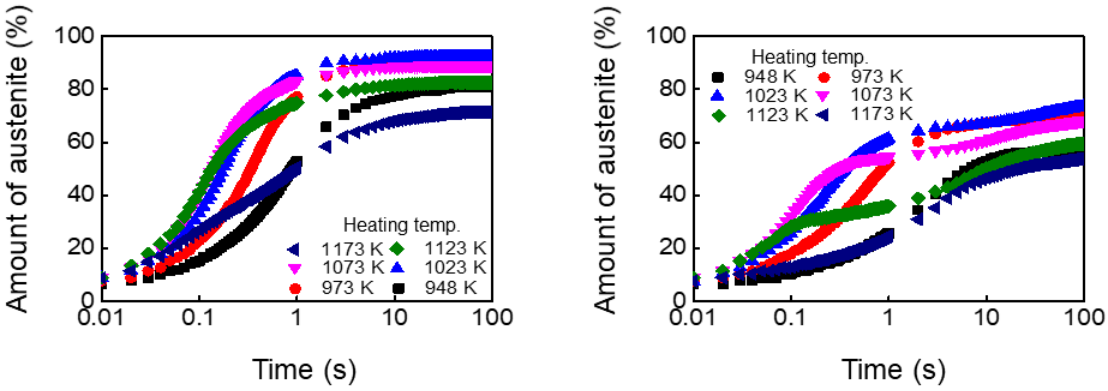

(a) Lean DSS (lab). (b) Standard DSS (type 329J3L).

Fig. 5.14 Changes in the precipitated γ fraction for the DSSs at different temperatures.

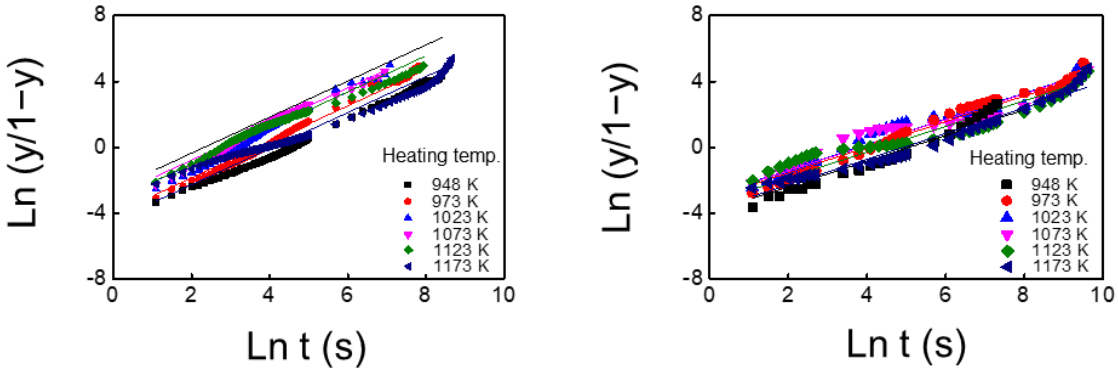

(a) Lean DSS (lab). (b) Standard DSS (type 329J3L).

Fig. 5.15 Austin–Rickett plots of the γ phase precipitation behavior in the base material HAZs for the DSSs at different temperatures.

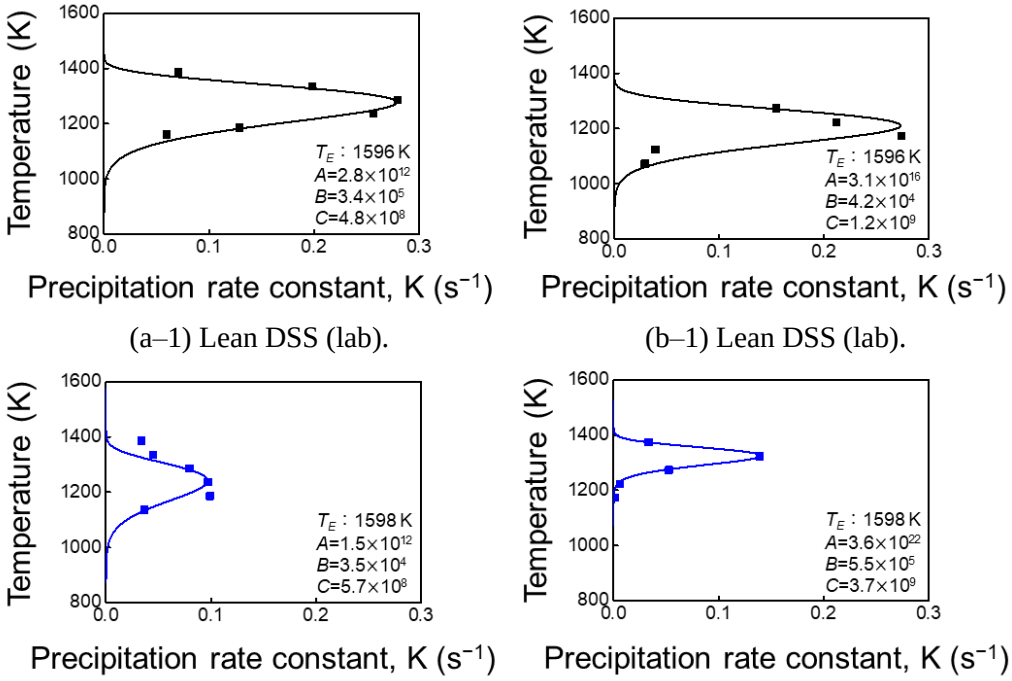

(a–1) Lean DSS (lab).

(b–1) Lean DSS (lab).

(a–2) Super DSS (type 329J4L).

(b–1) Super DSS (type 329J4L).

(a) Corrected calculation values.

(b) Experimental values.

Fig. 5.16 Comparison between the experimental and calculated rate constant curves for the DSSs.

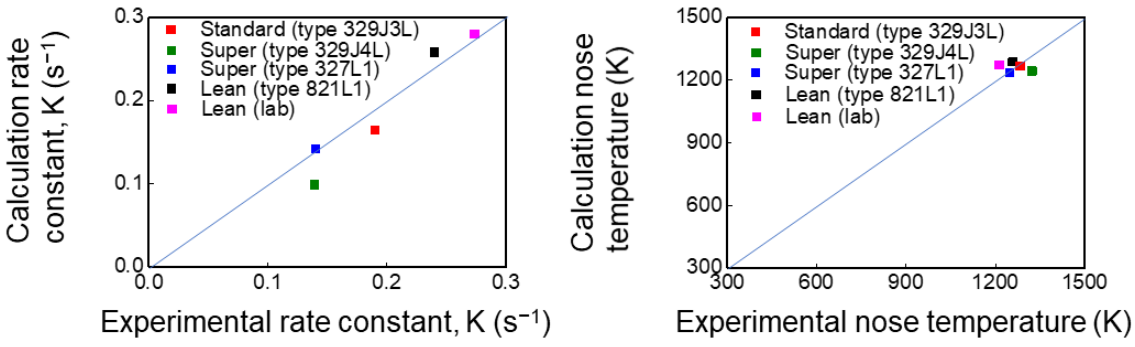

(a) Maximum value of the rate constant.

(b) Nose temperature.

Fig. 5.17 Correlation between experimental and calculated results.

5.5 Correction factor for γ precipitation phenomenon in weld metals

5.5.1 Comparison between temperature dependences of precipitation rate constant determined experimentally and numerically

Fig. 5.18 shows the results of calculation the γ precipitation behavior using the Fe–Cr–Ni ternary composition converted by Cr, Ni equivalent in Eq. (4.28). Regardless of the alloy composition, as the temperature increases from 923 K to 1023 K, the saturated precipitation amount was increased and the saturated precipitation amount at 1023 K temperature became maximum. At a temperature higher than that, the amount of saturated precipitation was decreased. Fig. 5.19 shows the results of the Austin–Rickett plot for the γ phase precipitation behavior of DSSs. In the case of the precipitation phenomenon, the time exponents (n) of lean (lab), standard (type 329J3L), and super (type 327L1) DSSs were determined to be 1.1, 1.01 and 0.74 (table 4.6 in Chapter 4), respectively. From the results showing a good linear relationship, it means that the behavior of γ phase precipitation and dissolution can be approximately expressed by the Austin–Rickett equation. In order to investigate the temperature dependence, the precipitation phenomenon was investigated using Eq. (3.17). The regression analysis of the precipitation phenomenon was based on the results obtained in Fig. 5.19. The regression analysis results for each steel type are shown in Fig. 5.20, and the determined time constant and rate constant are summarized in Table 5.8. The precipitation rate constant derived from the calculation results in Fig. 5.20 has a nose like the experimental value. As can be seen from Fig 5.20, there is clearly a difference in absolute value between the calculated value and the experimental value, but it can be seen that a similar trend is observed. Therefore, in order to derive a result close to the experimental value, correction was performed by introducing the correction factor applied in the Section 5.3.1.

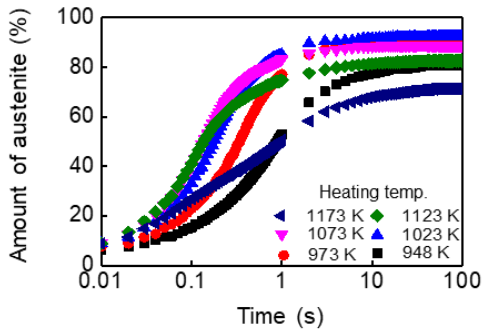

(a) Lean DSS (lab).

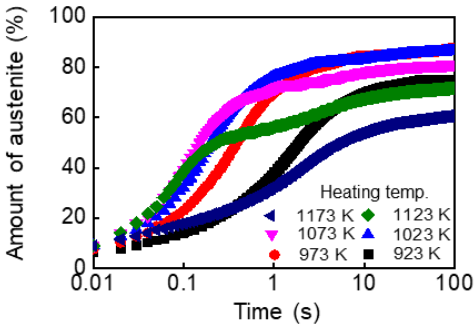

(b) Standard DSS (type 329J3L).

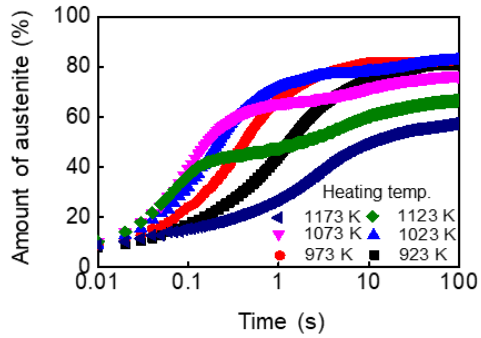

(c) Super DSS (type 327L1).

Fig. 5.18 Changes in the precipitated γ fraction for the DSSs at different temperatures.

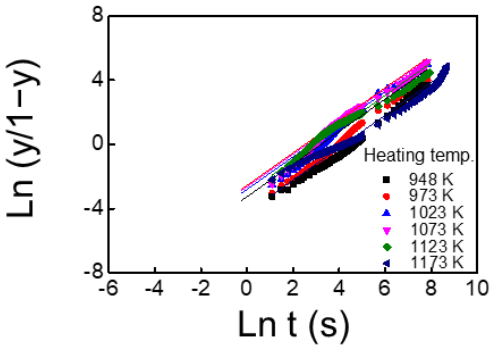

(a) Lean DSS (lab).

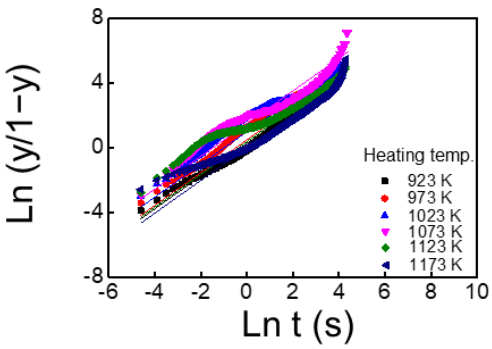

(b) Standard DSS (type 329J3L).

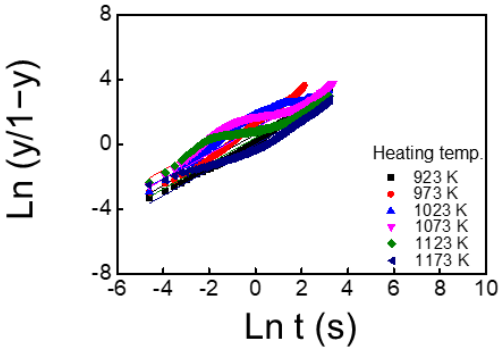

(c) Super DSS (type 327L1).

Fig. 5.19 Austin–Rickett plots of the γ phase precipitation behavior in the weld metals for the DSSs at different temperatures.

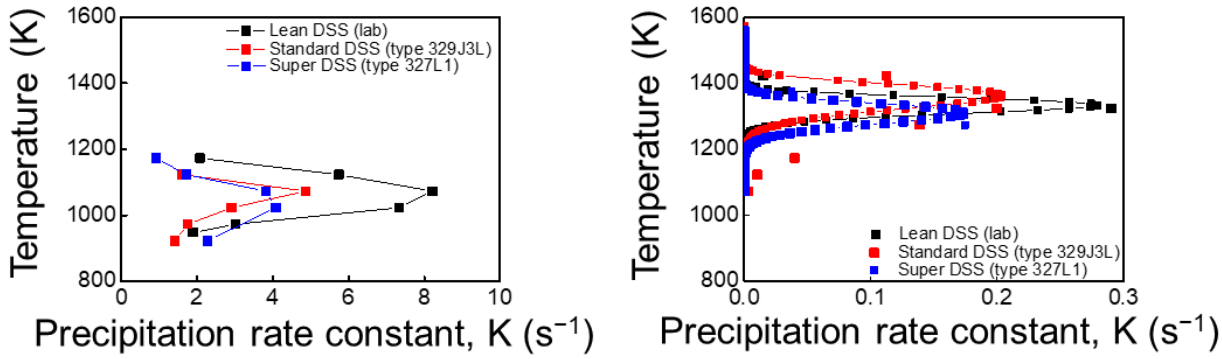

(a) Calculated results.

(b) Experimental results.

Fig. 5.20 Regression analysis of the precipitation rate constants of the γ phase in the weld metals for the DSSs.

Table 5.8 Calculated time constant and rate constant of γ precipitation in DSSs.

Steel type	Time constant, *n*	Nose temperature (K)	Maximum value of the rate constant, *K* (s^{-1})
Lean DSS (lab)	1.1	1073	8.9
Standard DSS (type 329J3L)	1.01	1073	4.4
Super DSS (type 327L1)	0.72	973	4.1

5.5.2 Validation of the correction factors

Fig. 5.21 shows the results of regression analysis by applying the correction factor. Fig. 5.21 shows the result of comparison with the calculated value after correction and the experimental value. From Fig. 5.21, since the correlation between the calculated value and the experimental value after the correction was increased, the correction factor introduced in the Section 5.3.1 is judged to be reasonable. Besides, the results on the rate constant and temperature dependence of the calculated values after correction are summarized in Table 5.9.

Table 5.9 time constant and rate constant of γ precipitation obtained by the corrected calculation.

Steel type	Nose temperature (K)	Maximum value of the rate constant, K (s^{-1})
Lean DSS (lab)	1278	0.28
Standard DSS (type 329J3L)	1263	0.16
Super DSS (type 327L1)	1228	0.13

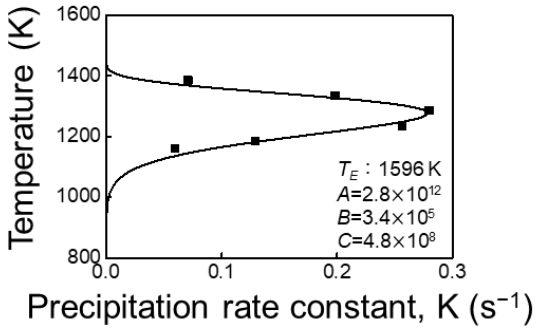

(a–1) Lean DSS (lab).

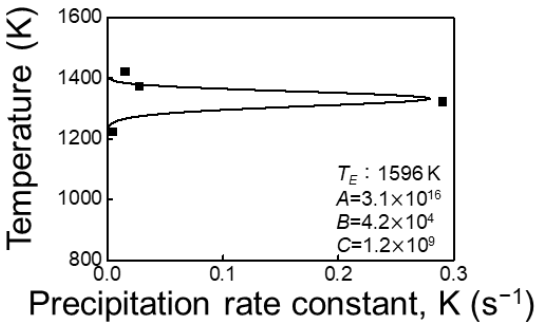

(b–1) Lean DSS (lab).

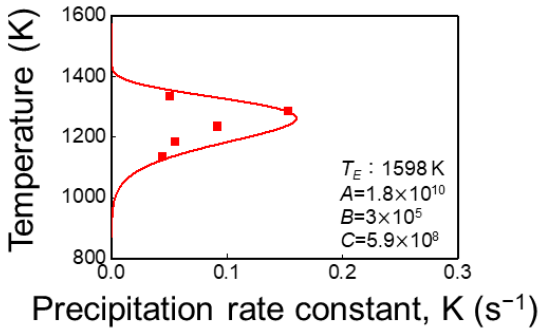

(a–2) Standard DSS (type 329J3L).

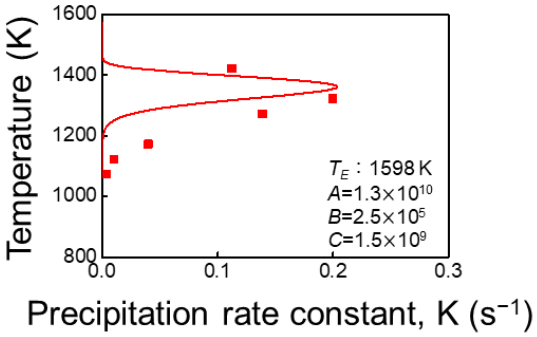

(b–2) Standard DSS (type 329J3L).

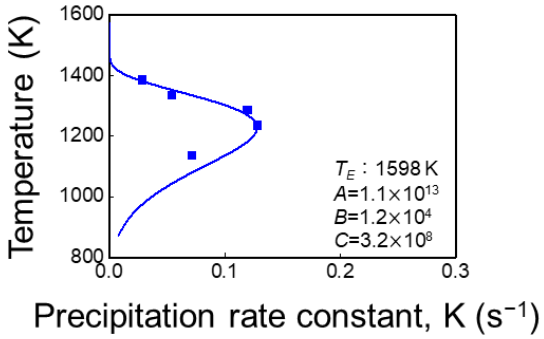

(a–3) Super DSS (type 327L1).

(a) Corrected calculation values.

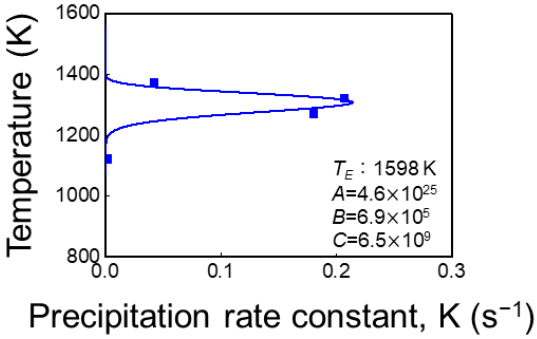

(b–3) Super DSS (type 327L1).

(b) Experimental values.

Fig. 5.21 Comparison of the temperature–precipitation rate constant curves for the DSSs.

5.6 Conclusions

In this study, three types of DSSs were used to derive the correction factor. The c orrection factor was derived by comparing the calculated value with the experimental value. Using the derived correction factor, a review on the applicability to other steel grades and weld metals was conducted. The main results and conclusions of this stud y are summarized as follows:

1) As a result of comparing the correlation between the temperature dependence on the dissolution rate between the experimental values and the calculated values to introduce a correction factor to the calculated values of the dissolution phenomenon, it was confirmed that a good correlation was shown between the calculated values and the experimental value.

2) In the case of the correction factor for the dissolution phenomenon, it was introduced through the comparison of the activation energy and the k_0 value, which affects the temperature dependence of the dissolution rate. As a result of comparing the calculated values and the experimental values, the activation energy and k_0 of the experimental values differed by about 1.38 and 1.33 times from the calculated values, and correction was performed as much as the difference. It was found that there was a high correlation between the temperature dependence of the corrected calculated values and the experimental values.

3) As a result of comparing the correlation between the temperature dependence on the precipitation rate between the experimental values and the calculated values to introduce a correction factor to the calculated values of the precipitation phenomenon, it was confirmed that a good correlation was shown between the calculated values and the experimental values.

4) For the correction factor of the precipitation phenomenon, the difference in the maximum rate constant (multiply the calculated values by 0.0314) and the precipitation nose temperature (add 213 K to the calculated values) of the calculated values and the experimental values were compared, and the correction was performed by the difference. It was confirmed that there was a high correlation between the temperature dependence between the corrected calculated values and the experimental values.

5) To evaluate the applicability of the reviewed correction factors for lean (type 821L1), standard (type 329J3L), and super (type 327L1) DSSs three steel grades, it was applied to lean (lab) and super (type 329J4L) DSSs under different conditions. In DSSs of different compositions, the effectiveness of the correction factor was proved because it was shown a high correlation between the temperature dependence of the experimental values and the calculated values through the introduction of the correction factor. In addition, it was confirmed that the application of the correction

factor in the weld metals also showed a high level of correlation. From the above facts, it was suggested that the rate constant (dissolution and precipitation) determined using the phase–field method established in this study is applicable to other steel types as well.

Chapter 6 Prediction of α/γ phase transformation in multi–pass welds using phase–field model

6.1 Introduction

The microstructural evolution of a system occurs owing to a tendency for reduction in the total free energy of the system under non–equilibrium conditions. The traditional approach used to model the evolution of the microstructure of a material treats regions that separate different domains as zero–thickness regions (sharp interface between domains). The motion of this sharp interface explains the kinetics toward equilibrium. However, a sharp interface model is difficult to implement because it requires a solution to the diffusion equation according to the moving boundary conditions at the interface. This approach in which the interface (boundary) must be determined as part of the solution is commonly referred to as the free boundary problem. The free boundary approach can succeed in changing the topology with simple geometries, but it is impractical for more complex two– or three–dimensional systems. Recently, a more convenient method of phase–field simulation of microstructure evolution and phase transformation has become a powerful tool. The phase–field method is effective for understanding complex motions that are nonuniform during phase transformation. This is because there are useful frameworks that include a static approach based on the total free energy of the microstructure and a kinetic approach that explains the evolution of complex microstructures. [179, 196–198].

Thus, the phase–field model has been widely used for explaining microstructure evolution and phase transformation phenomena [145–147, 143, 151, 171, 191, 195, 199–205]. However, there are few studies involving the quantitative investigation of the kinetics during the α/γ phase transformation of DSS using the phase–field method. That is why we investigated the dissolution and precipitation of the γ phase in DSSs with a ternary composition of Fe–Cr–Ni converted to Cr/Ni equivalents using the phase–field method in Chapters 4 and 5. Besides, in relation to the discrepancy between the calculated value and the experimental value, the validity of the correction factor was verified and the possibility of expansion to other steel types was evaluated. In this study, quantitative prediction of the α/γ phase transformation phenomenon of multi–pass welds of DSSs was performed using the rate constants verified in Chapters 4 and 5.

6.2 Prediction of phase transformation in the multi–pass welds

The method of predicting multi–pass welds using the rate constant derived through the phase–field method was investigated using the method already discussed in Chapter 3. In the case of the 3D analysis model to obtain the thermal history of the multi–pass welds, the thermal history was obtained using the model shown in Fig. 3.18. Besides, in this study, α/γ phase transformation prediction was conducted for five types of DSSs. Among them, lean (lab), standard (type 329J3L), and super (type 327L1) DSSs were predicted for multi–pass welds.

Meanwhile, for lean (type 821L1), super (type 329J4L) DSSs, prediction for multi–pass HAZs was performed. Furthermore, to verify the validity of the phase–field method, the results

of the multi–pass welds predicted by the rate constant derived from the phase–field were compared with the experimental values predicted in Chapter 3.

6.2.1 Computed results of austenitic phase fraction in multi–pass welds

Fig. 6.1 shows the result of predicting the γ phase fraction (indicated by color contour) of the multi–pass welds of lean (lab) DSS by using the rate constant derived from the phase–field method. This figure exhibits the entire history of the distribution of the γ phase fraction at the completion of each weld pass during multi–pass welding. The dashed lines in the figure indicate the fusion lines of weld passes. The γ phase fraction in the just solidified WM was considerably small in any weld passes, and the depleted zone of γ phase was formed adjacent to the fusion line ("under–bead" region) in the base material HAZs and reheated WMs. However, the γ phase fraction in the depleted zone was increased by the subsequent weld passes (the γ phase was re–precipitated by the thermal cycles in subsequent welding). Accordingly, the α/γ phase balance has been complexly varied in multi–pass welds, and the profile of the γ phase fraction was arranged in laminae in the WM roughly along the fusion lines. The minimum γ phase fraction in multi–pass welds was approx. 20 % located in the base material HAZ of the final weld layer, and the γ phase fraction in WMs was reduced to approx. 25 %. On the other hand, the γ phase fraction in a part of base material HAZ (low temperature HAZ) was exceeded to that in the base material, because of the additional precipitation of γ phase during multi–pass welding.

The distribution of the γ phase fraction calculated in the multi–pass welds of standard (type 329J3L), and super (type 327L1) DSSs is also shown in Fig. 6.2 and Fig. 6.3, respectively. Quite similar tendencies to lean (lab) DSS welds were observed in the distribution of the γ phase fraction, that is, the γ phase fraction was reduced in the solidified WM and under–bead region of WM as well as the base material HAZ, while the γ phase fraction in the depleted zone was recovered by the subsequent weld passes. As a result, the α/γ phase balance has been complexly varied in multi–pass welds. Figs. 6.4–6.5 shows the result of the γ phase fraction calculated in the multi–pass HAZ. Furthermore, it shows that the γ amount of the HAZ (base material) of the first pass is less than 30 %. However, as the pass progresses, re–precipitation occurs due to the thermal cycle in subsequent welding, thereby recovering the amount of γ.

However, the amount of γ in the final weld is considerably reduced compared to that in other welds because the amount of γ is no longer affected by the subsequent thermal cycle. This is because the ratio of α/γ owing to the insufficient amount of γ, becomes misaligned.

Consequently, it was confirmed that the α/γ phase transformation in the multi–pass welded part exhibits a highly complex behavior, as in the results of Figs. 6.1–6.5.

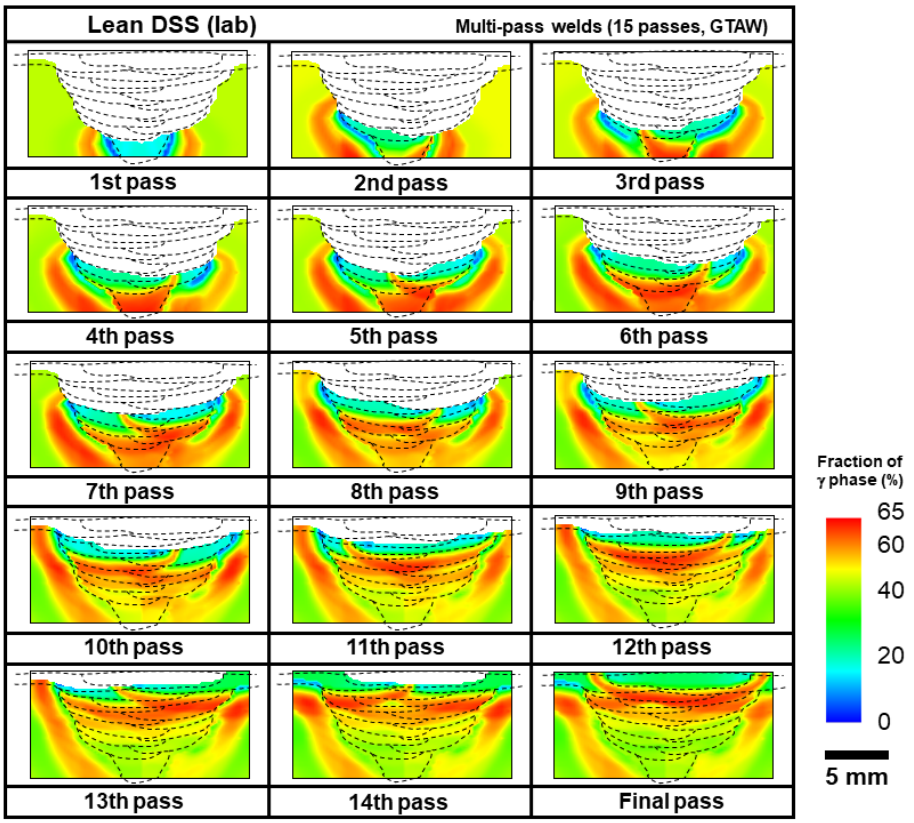

Fig. 6.1 Distribution of the γ phase fraction calculated in a multi–pass welds of lean DSS (lab).

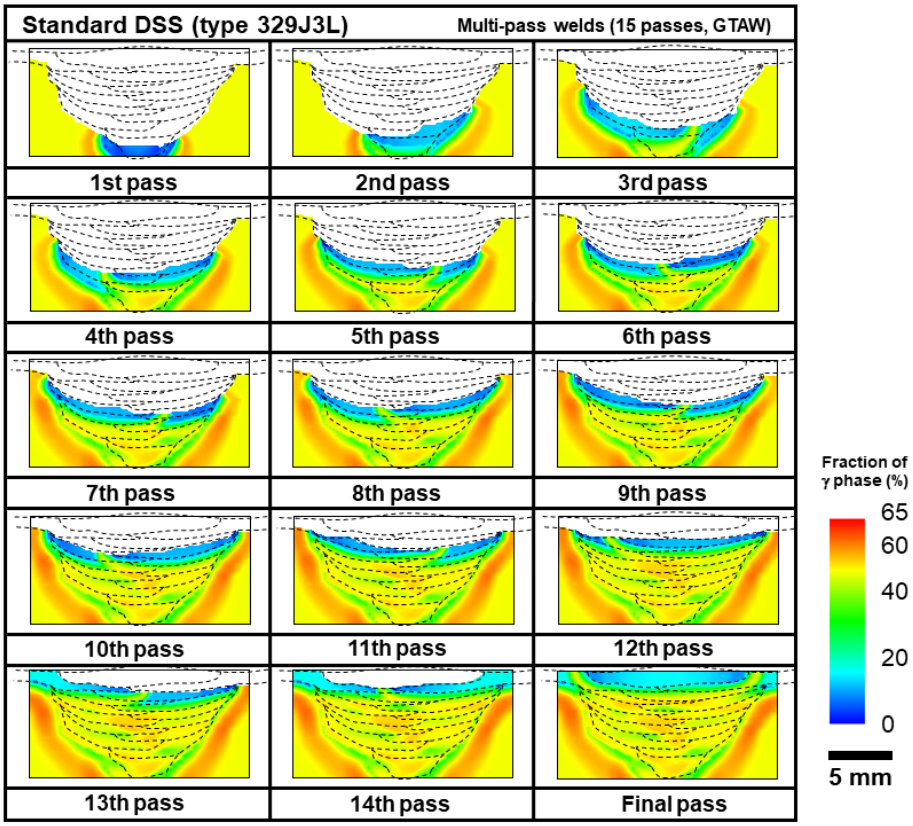

Fig. 6.2 Distribution of the γ phase fraction calculated in a multi–pass welds of standard DSS (type 329J3L).

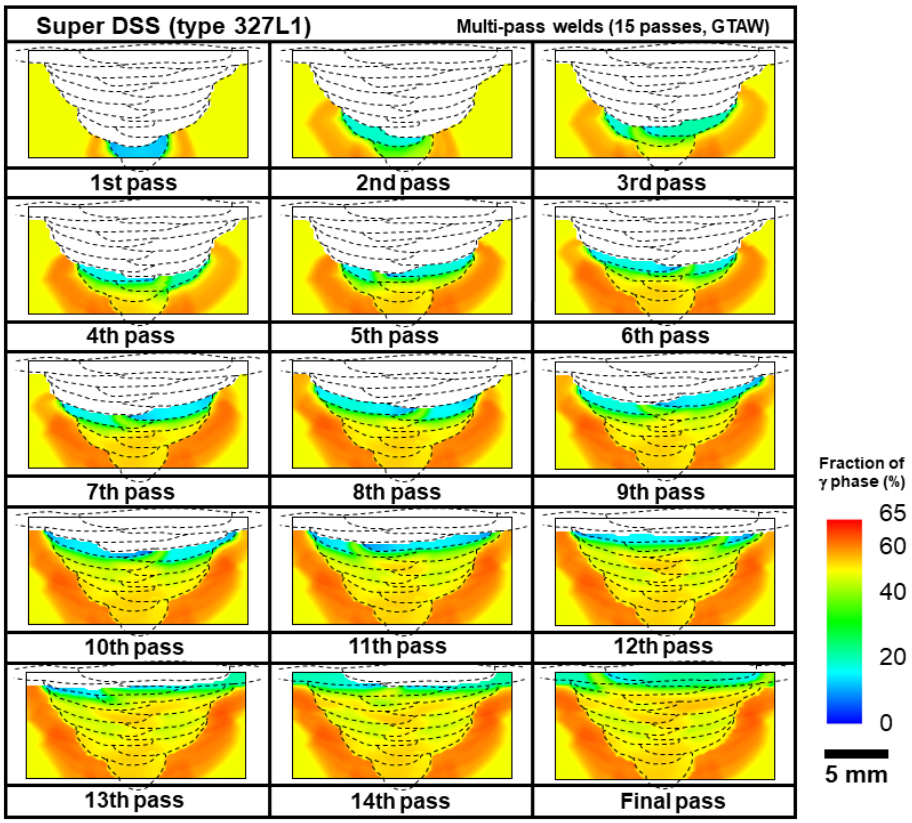

Fig. 6.3 Distribution of the γ phase fraction calculated in a multi–pass welds of super DSS (type 327L1).

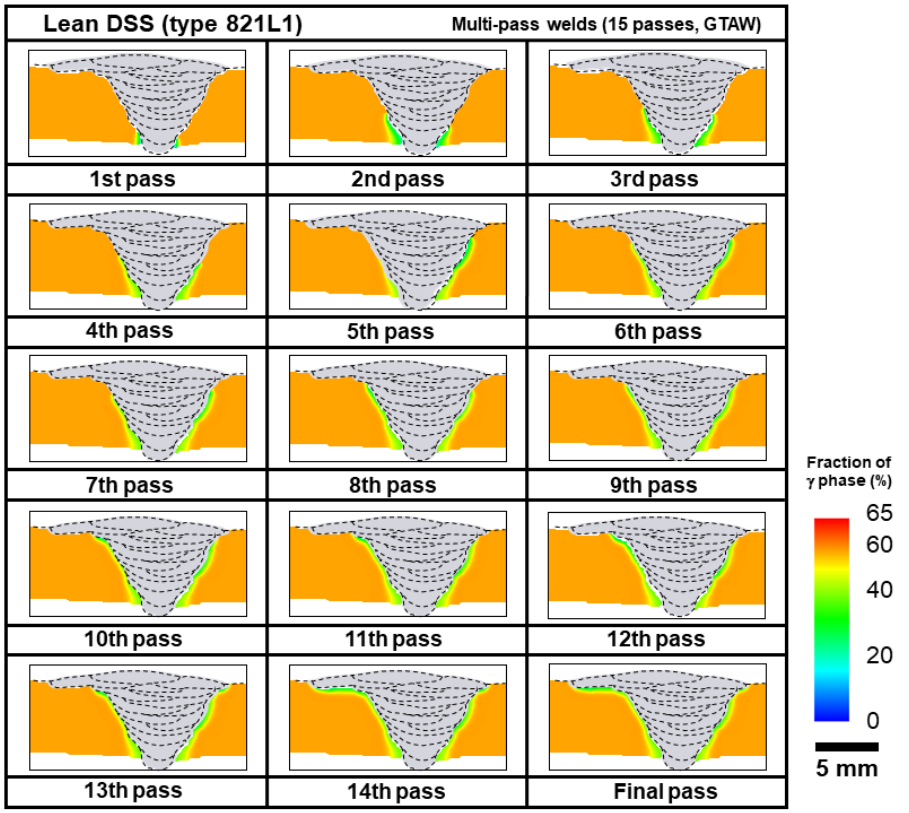

Fig. 6.4 Distribution of the γ phase fraction calculated in a multi–pass HAZs of lean DSS (type 821L1).

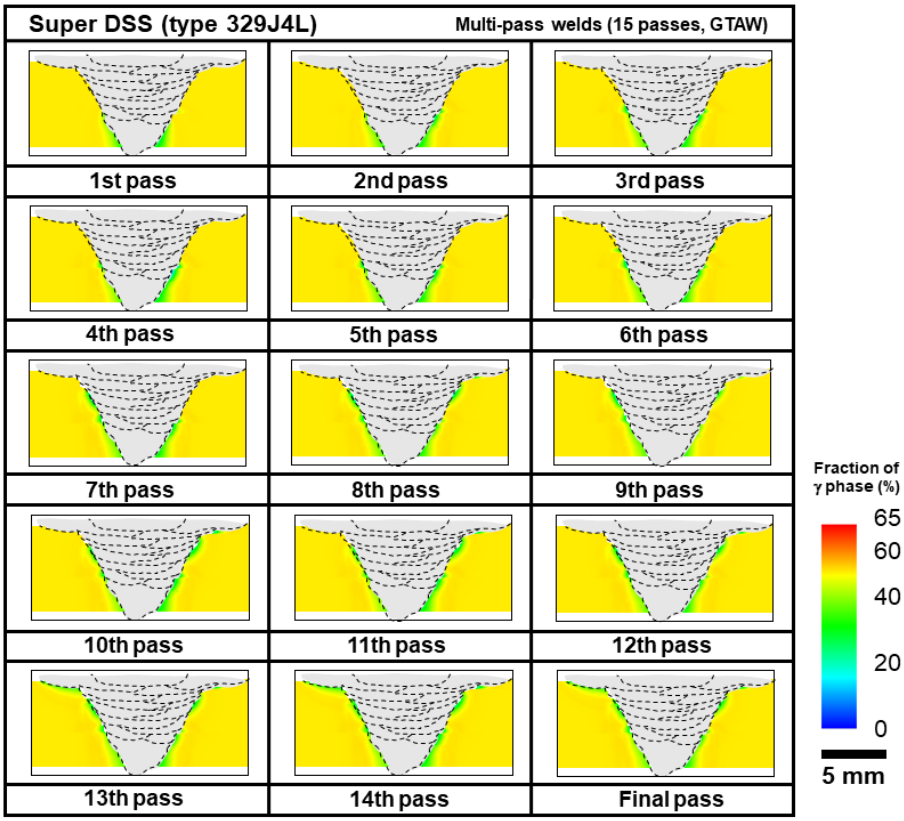

Fig. 6.5 Distribution of the γ phase fraction calculated in a multi–pass HAZs of super DSS (type 329J4L).

6.2.2 Comparison of experimental and theoretical γ amount in multi–pass welds

Fig. 6.6 shows the comparison of the γ phase fraction between calculated and measured in the multi–pass welds (GTAW) of lean, standard and super DSSs using the rate constants derived from the phase–field respectively. In these figures, a fig. 6.6(a) indicates the analysis spots (positions) of the γ phase fraction, and a fig. 6.6(b) indicates the correlation between the calculated γ phase fraction and measured one. Although there were small scatters between the calculated and measured values, the calculated results were fairly consistent with measured ones (correlation coefficients; 0.7–0.8) in all welds (in the WM, reheated WM as well as the base metal HAZ). In addition, when comparing the experimentally predicted results of the multi–pass welds in Chapter 3, it can be seen that the overall γ amount is slightly lower by about 3 % to 5 %. This is because it was derived using three types of DSSs when deriving the correction coefficient mentioned in Chapter 5, it is difficult to accurately match the experimental value due to the occurrence of an error in the correction coefficient. This problem is convinced that the accuracy of the model will improve as the sample of the correction factor increases in the future. Based on the above prediction results, the α/γ phase transformation of DSSs multi–pass welds can be semi–quantitatively predicted by phase–field–based kinetics and computer simulations. In particular, the γ phase–depleted zone in the multi–pass welds, where the mechanical and corrosion properties would be potentially deteriorated, could be estimated with a high degree of accuracy.

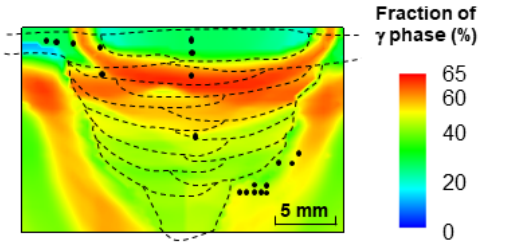

(a–1) Lean DSS (lab).

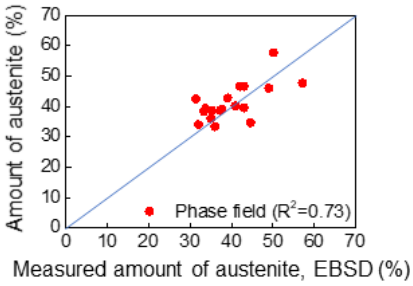

(b–1) Lean DSS (lab).

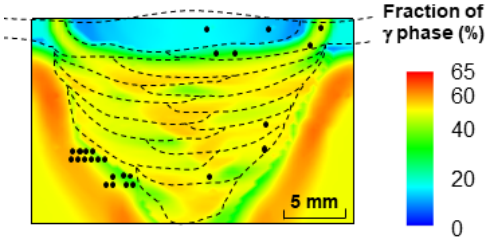

(a–2) Standard DSS (type 329J3L).

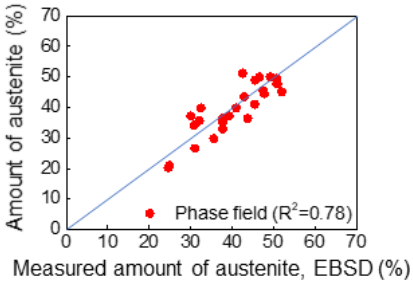

(b–2) Standard DSS (type 329J3L).

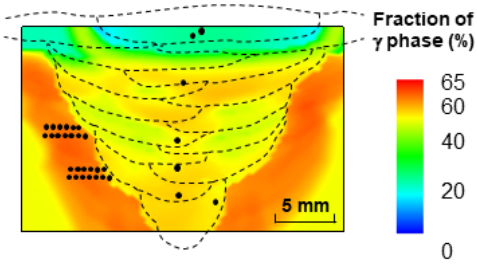

(a–3) Super DSS (type 327L1).

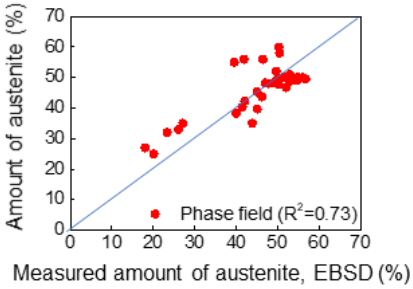

(b–3) Super DSS (type 327L1).

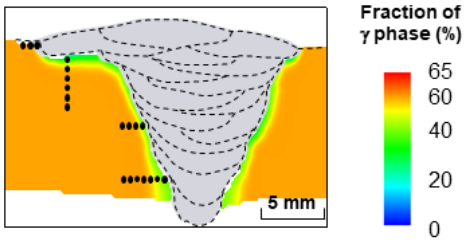

(a–4) Lean DSS (type 821L1).

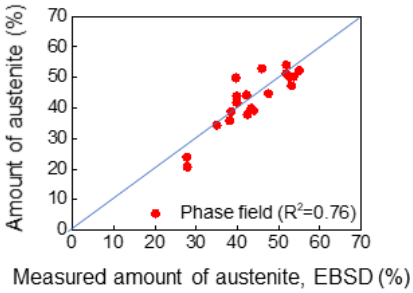

(b–4) Lean DSS (type 821L1).

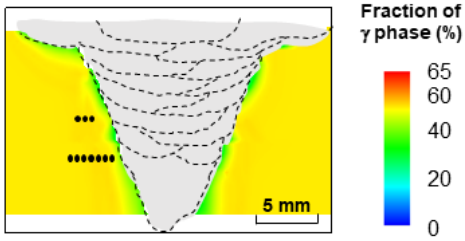

(a–5) Super DSS (type 329J4L).

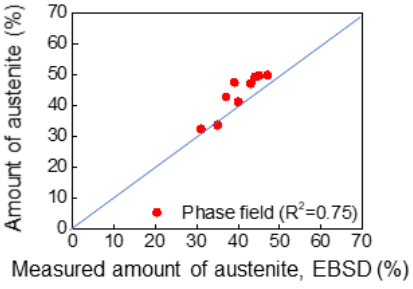

(b–5) Super DSS (type 329J4L).

(a) Analysis spots.

(b) Correlation of γ phase fraction.

Fig. 6.6 Comparison of the calculated and measured γ phase fraction in welds.

6.3 Conclusions

In this study, the γ amount of the multi–pass welds were predicted using the rate constant derived from the phase–field method (in the Chapters 4 and 5). Besides, the validity of the phase–field method was verified through comparison with the experimentally predicted γ amount in Chapter 3. The main results and conclusions of this study are summarized as follows:

1) Based on the rate constants derived using phase–field simulation, the distribution of the γ phase fraction in the multi–pass welds of DSSs was calculated by combined with the results of heat conduction analysis using Quick–welder software.

2) In the case of Lean (lab), standard (type 329J3L), and super (type 327L1) DSSs, the γ amount was semi–quantitatively predicted for the multi–pass welds, and Lean (type 821L1), super (type 329J4L) DSSs were also semi–quantitatively predicted for the multi–pass HAZs.

3) From the predicted results, it was found that the γ phase fraction of the just solidified WM was relatively low, and the depleted region of the γ phase was formed adjacent to the fusion line of the base material HAZs and the reheated WM. However, it was found that the γ amount was recovered by re–precipitation by thermal cycles in the subsequent welding.

4) In the case of the final weld, the amount of γ is considerably insufficient compared to other welds because it can no longer be affected by the subsequent thermal cycles. This lack of γ amount affected the entire α/γ ratio, so it was judged that the α/γ phase transformation behavior of the multi–pass welds was very complex.

5) It was confirmed that the amount of γ was lower by about 3 % to 5 % through comparison with the experimental values semi–quantitatively predicted in Chapter 3. This is because in this study, only three data points were used to derive the correction factor. In the future, if the data of the correction factor are accumulated, the accuracy of the prediction result of the γ amount is expected to be improved.

6) There were small scatters between the calculated and measured values from the predicted results, but the calculated results were in good agreement with the values measured (correlation coefficient: 0.7–0.8) in all welds (in the WM, reheated WM as well as the base metal HAZ).

7) The rate constants derived from the phase–field simulation constructed by converting the multi–system composition DSSs into a ternary composition was corrected through comparison with the experimental value, and the γ amount of the multi–pass welds was semi–quantitatively predicted using the corrected rate constants. The predicted γ amount was verified for validity through comparison with the measured values, and it was confirmed that there was a high level of correlation (correlation coefficients; 0.7–0.8) between the calculated values and the measured values. Thus, it has been proven that the prediction technique using the phase–field simulation constructed in this study is useful.

Chapter 7 Proposal for microstructural improvement to recover γ amount in HAZ

7.1 Introduction

We proved in Chapters 3 and 6 that prediction of the γ phase fraction in multi–pass welds is possible with the current approach based on the determined kinetic equation (phase–field, experimental). Additionally, the amount of γ phase decreases in the HAZ of each welding pass; however, it can be recovered by subjecting it to the heat effect of the subsequent pass. However, for the HAZ of the final welding pass, the ratio of α/γ becomes misaligned. This is due to the insufficient precipitation of γ because the heat of the subsequent pass remains unaffected. These α/γ phase ratio changes can reduce the mechanical properties and corrosion resistance of duplex stainless steels (DSSs) [95,105–107]. Claudio Gennari et al [112]. were conducted on the mechanical behavior of 4 types of DSSs with different compositions. From the results of previous studies, it was shown that the elongation was uniformly increased, but it was suggested that if the alloy composition is different, it may lead to localized resistive heating due to the uneven distribution of electrical current and the difference in work hardening rate and that it affects the elongation rate. Besides, Lihua Zhang et al [113]. conducted a study on the characteristics of pitting corrosion resistance. From the results of the study, it was suggested that as the amount of γ was decreased, the pitting corrosion resistance was also decreased. For reasons mentioned above, it is judged that it is important not only to quantitatively predict the phase transformation phenomenon of the multi–pass welds but also to suggest improvement measures for insufficient precipitation region. To improve the above problem, in this section we proposed a new microstructure improvement welding process to restore the γ fraction of the final weld based on computer predictions. Besides, to verify the validity of the optimal conditions derived from the simulation, the verification through microstructural improvement welding was conducted.

7.2 Materials and experimental procedures

7.2.1 Materials used

The duplex stainless steels (DSSs) used in the microstructural improvement welding process (reheat–bead welding) is lean DSSs and its chemical composition are shown in Table 7.1 and 7.2.

Table 7.1 Chemical composition of the duplex stainless steels in this study (mass %).

Steel	C	Si	Mn	P	S	Ni	Cr	Mo	Cu	N	Fe
Lean DSS (lab)	0.014	0.35	1.49	0.024	0.0004	3.06	20.85	0.30	0.09	0.177	Bal.
Lean DSS (type 821L1)	0.017	0.42	3.21	0.024	<0.001	2.24	20.88	0.48	1.05	0.17	Bal.

Table 7.2 Chemical composition of the filler metals in this study (mass %).

Steel	C	Si	Mn	P	S	Ni	Cr	Mo	Cu	N	Fe
Lean DSS (lab)	0.014	0.35	1.49	0.024	0.0004	3.06	20.85	0.30	0.09	0.177	Bal.
Lean DSS (type 821L1)	0.01	0.38	1.43	0.017	–	8.62	23.11	3.27	0.06	0.15	Bal.

7.2.2 Experimental procedures

Table 7.3 shows a specification of reheat–bead welding. The reheat–bead welding specifications were as follows: arc current, 100 A; arc voltage, 14 V; welding speed, 9 cm/min; shielding gas, Ar + 2 % N_2 (flow rate, 15 L/min).

Table 7.3 Conditions for reheat bead welding.

Parameters	Values
Arc voltage	14 V
Arc current	100 A
Welding speed	1 mm/s, 1.5 mm/s
Shield gas	Ar + 2 % N_2
Shield gas flow rate	15 L/min

7.3 Basic concept of reheat–bead welding

A reheat–bead welding technique was used for microstructural improvement welding. A schematic of the process is illustrated in Fig. 7.1; the region where the amount of γ phase is dissolved and decreased in the HAZ of the base metal is indicated in yellow, while that where re–precipitation is expected to occur due to the heat effect of reheat–bead welding is indicated in green. This process is similar to the technique of temper bead welding. It is aimed at improving the lack of the γ phase of the HAZ by re–precipitating the γ phase using melt–run welding or the like to give an appropriate heat effect to the γ–deficient region.

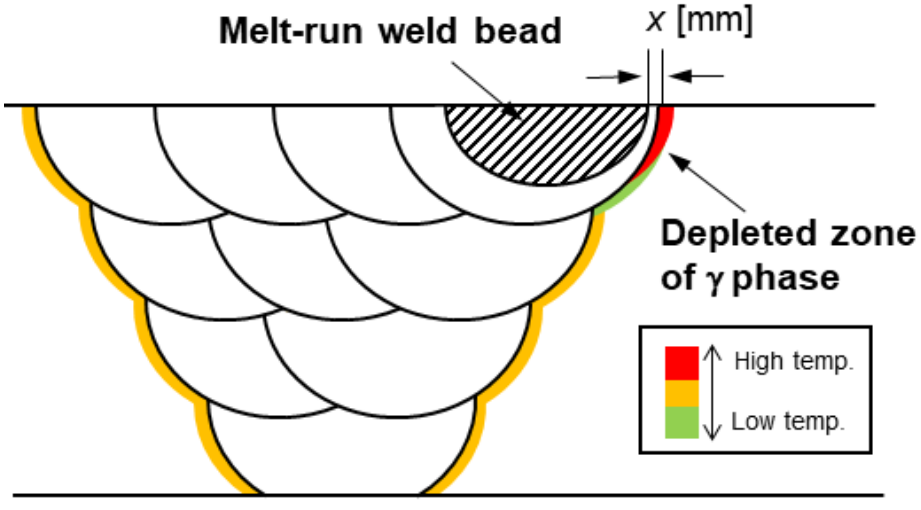

Fig. 7.1 Schematic of reheat–bead welding.

7.4 Proposal for microstructural improvement of the welding process

7.4.1 Finding out the change in the amount of γ phase recovery according to the welding location and conditions

In this Section, quantitative prediction conditions for the change in the amount of γ phase recovery according to the welding location and conditions were investigated prior to the application of the microstructure improvement welding of the multi–pass welds. As for the investigation method, the welds created through single–pass welding were assumed as the final weld as shown in Fig. 7.1, and the predicted conditions were quantified through finite element analysis. The heat input condition was carried out in 4 conditions as shown in Table 7.4. Also, the cross–sectional views created according to the amount of heat input are shown in Fig. 7.2.

Through finite element analysis, the thermal history of the microstructure improvement welding according to the heat input and distance was derived, and the results are shown in Fig. 7.3. From the results, it was confirmed that the cooling rate became slower as the amount of heat input was increased, and the amount of γ was predicted using the method of deriving the amount of γ discussed in Chapter 3. Fig. 7.4 shows the result of the recovery amount of the γ amount according to the distance, *x*. From the results, the recovery of γ amount was observed through microstructure improvement welding regardless of the amount of heat input, and it can be seen that the higher the amount of heat input, the greater the amount of γ recovered. This is believed to be due to the expansion of the region where the γ amount was recovered due to the high amount of heat input. Also, Fig. 7.5 shows the relationship between the nose temperature (Chapter 3) and the amount of γ. It can be seen that the amount of γ recovered was the greatest around the nose temperature of 1173K. In order to investigate the effect of the distance, *x*, on the recovery of the γ amount, the relationship between the thermal history and the precipitation rate constant of the γ phase was compared, and the results are shown in Fig. 7.6. The thermal history shown in Fig. 7.6 is the result of the heat input of 3000 J/mm, and it is judged that the amount of γ was recovered from the fact that the holding time in the vicinity of the precipitation nose temperature (1173K) becomes long when the distance, *x*, was 1.25 mm is the maximum.

Table 7.4 Conditions for GTAW.

	Welding current [A]	Arc voltage [V]	Welding speed [mm/s]	Heat input [J/mm]
Small heat input	200	11	3.33	660
Medium heat input	220	12	2.00	1320
Large heat input	250	16	2.00	2000
Extra large heat input	300	20	2.00	3000

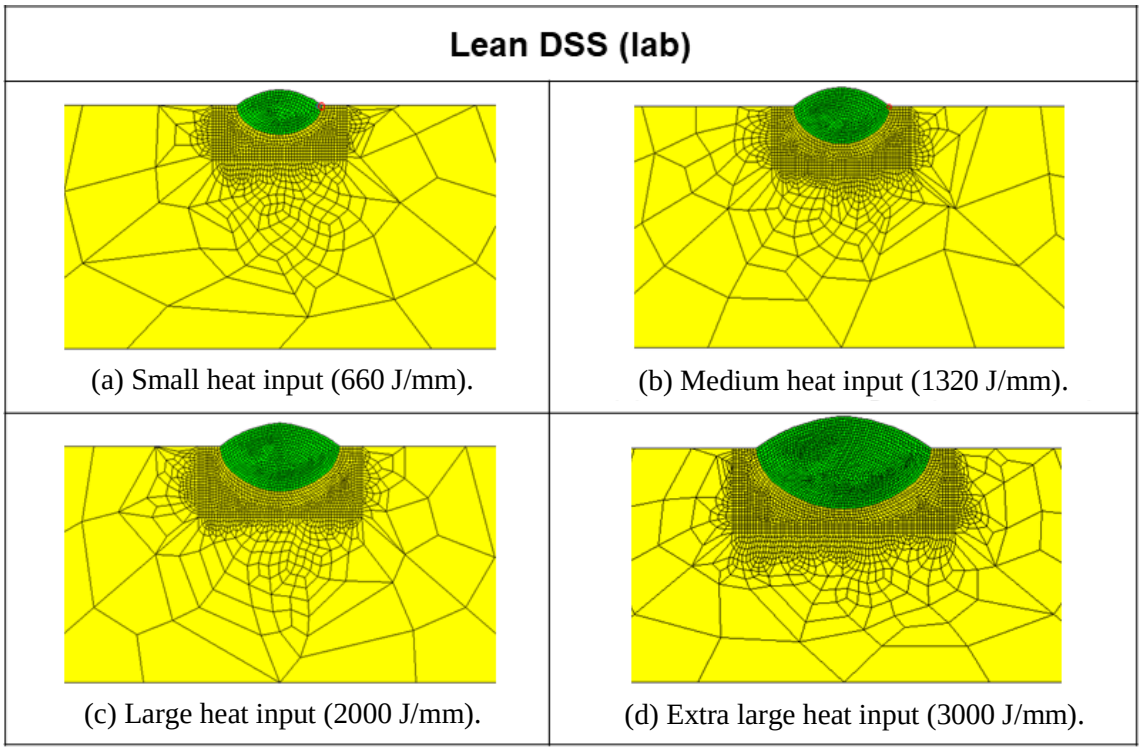

(a) Small heat input (660 J/mm).

(b) Medium heat input (1320 J/mm).

(c) Large heat input (2000 J/mm).

(d) Extra large heat input (3000 J/mm).

Fig. 7.2 FEM mesh model of multi–pass welding of lean (lab) DSS.

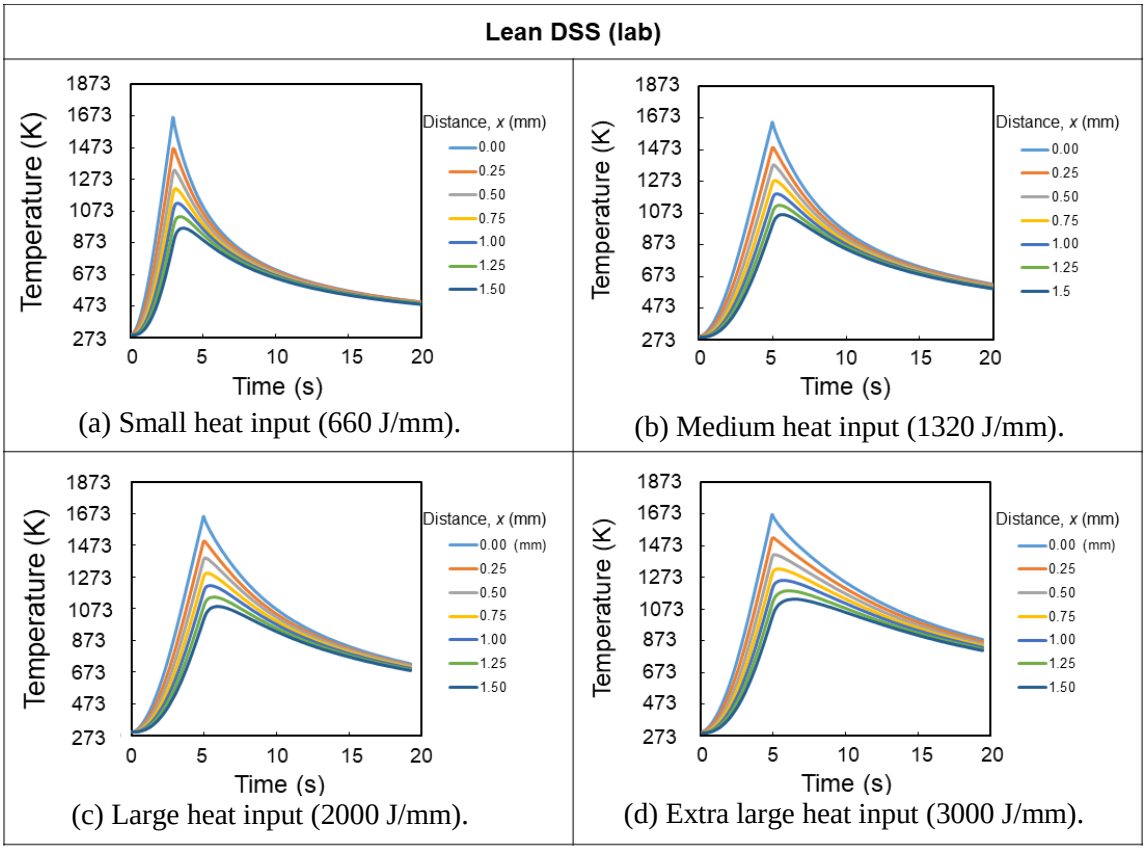

(a) Small heat input (660 J/mm).

(b) Medium heat input (1320 J/mm).

(c) Large heat input (2000 J/mm).

(d) Extra large heat input (3000 J/mm).

Fig. 7.3 Thermal history of lean (lab) DSS.

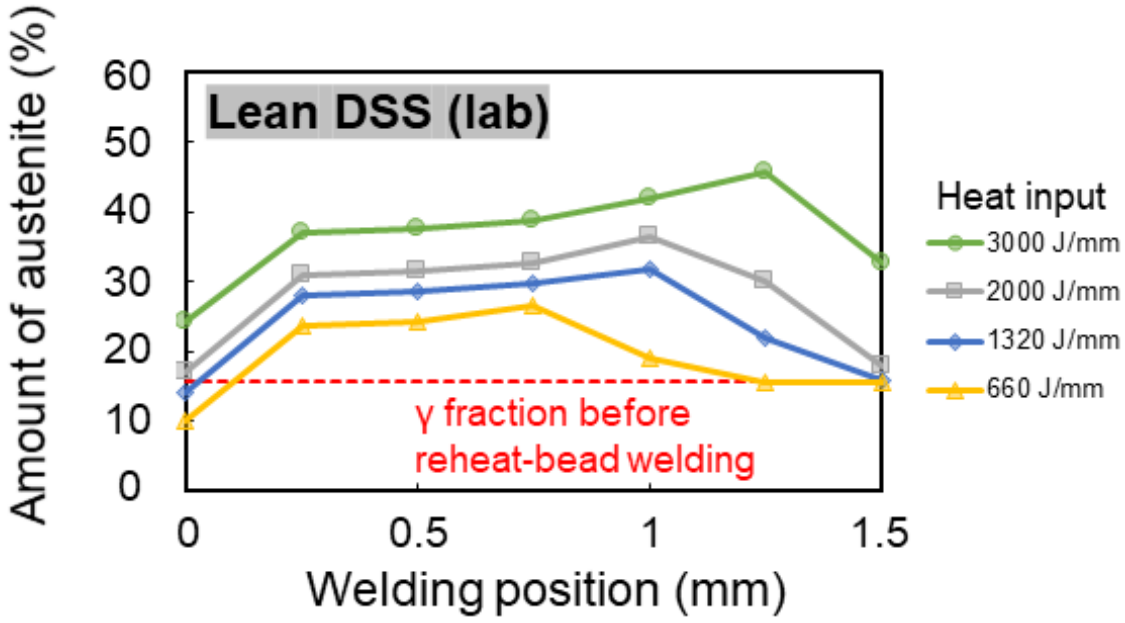

Fig. 7.4 Relationship of γ fraction and Welding position.

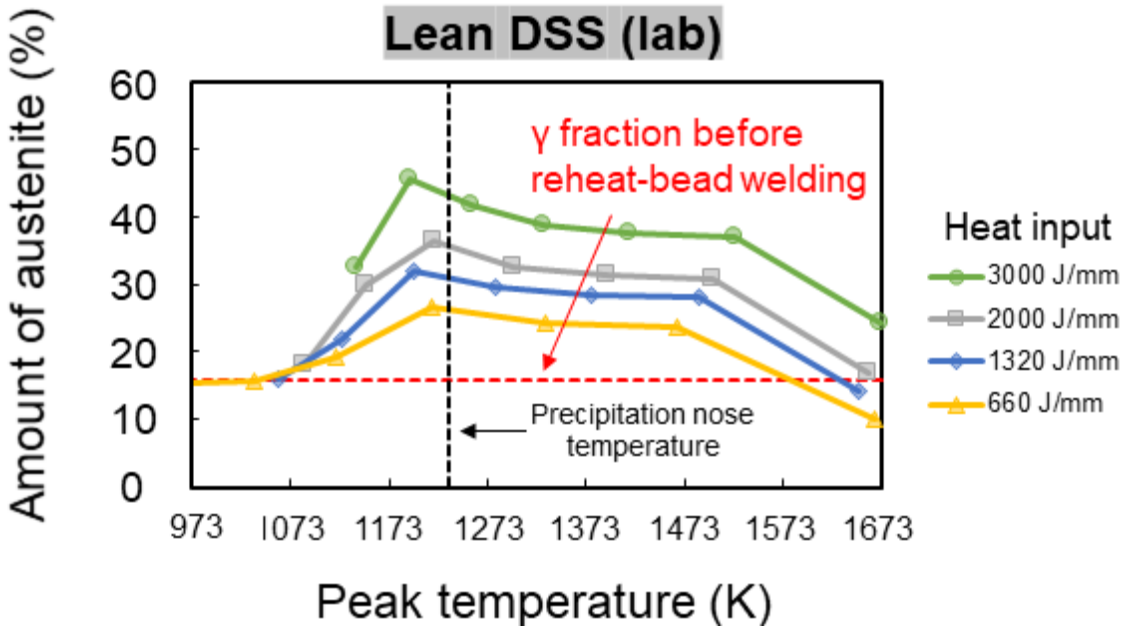

Fig. 7.5 Relationship of γ fraction and peak temperature.

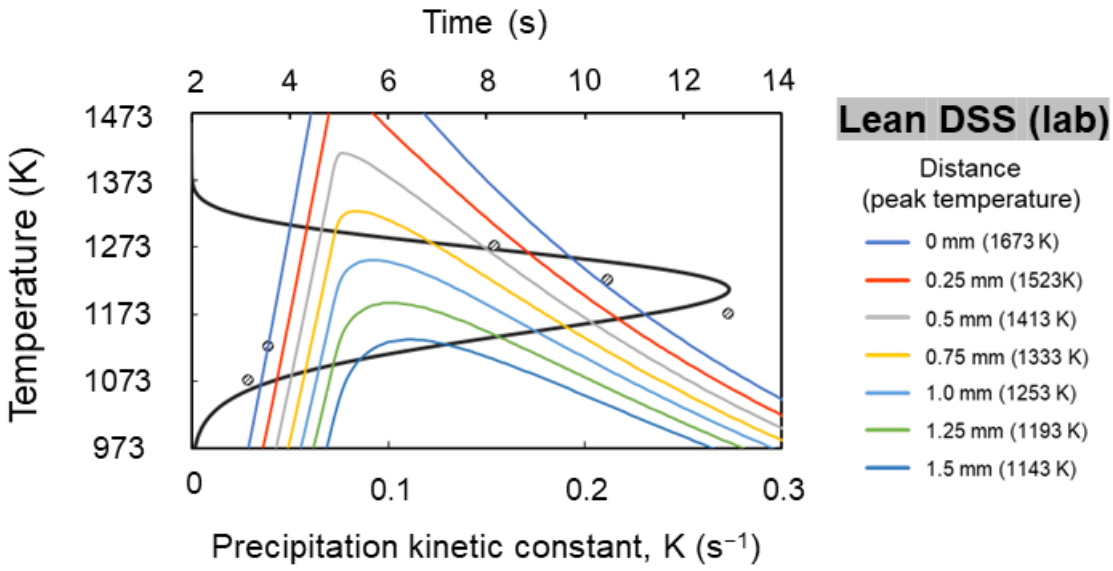

Fig. 7.6 Relationship between thermal history and rate constant of γ precipitation.

7.4.2 Identify the range of appropriate conditions for microstructure improvement welding

Based on the results of Section 7.3.1, the prediction results of the γ amount by welding conditions are arranged in a color contour, and the results are shown in Fig. 7.7. From the above results, it was suggested that for HAZ, where the γ amount is insufficient due to the absence of subsequent heat during welding, it is possible to recover the appropriate γ amount according to the welding conditions. It is known that the corrosion resistance and mechanical properties of DSS also affect the composition ratio of alloy elements such as Cr and Ni. This means that the phase ratio of α/γ may differ depending on the steel type. It is judged that the microstructure improvement welding process successfully predicted in this study can be sufficiently useful in examining the standard value of the γ amount according to the other steel type.

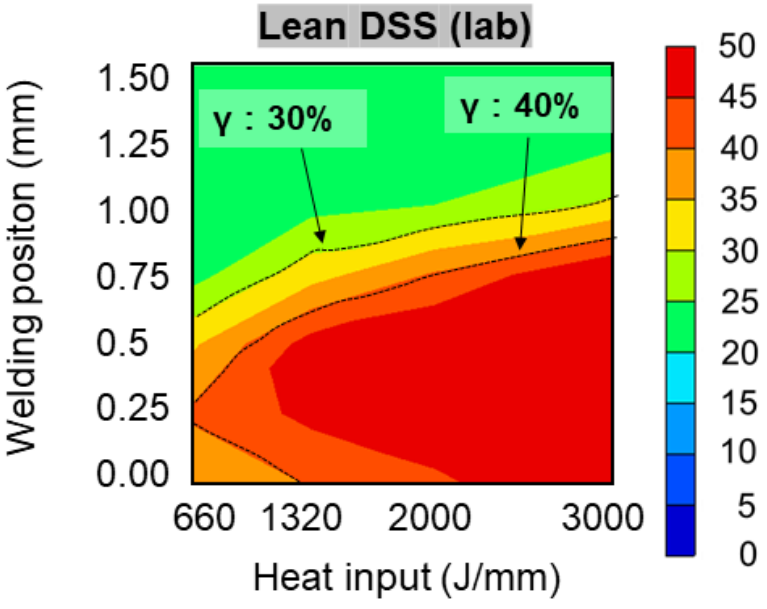

Fig. 7.7 Calculation result of γ fraction by welding condition.

7.4.3 Experimental verification of microstructural improvement welding method

In this Section, reheat–bead welding was constructed using the conditions of 1400 J/mm of heat input and 1 mm of welding position in Fig. 7.7. In addition, the amount of γ around the fusion line in the vicinity of the surface before and after reheat–bead welding was measured by EBSD, and its validity was verified. Fig. 7.8 shows the amount of γ before and after reheat–bead welding. The position of 0 mm on the horizontal axis means the fusion line of the multi–pass weld, and the position of 1 mm to the left is the fusion line of the reheat–bead. After reheat–bead welding, the recovery of the γ amount was observed in the range of 1–2 mm from the fusion line of the multi–pass weld. In addition to the HAZ, recovery of the γ amount was observed at the position of −1 mm to 0 mm, which is the weld metal of the multi–pass weld. In particular, in the region of up to 0.5 mm, which is very close to the fusion line of the multi–pass weld, the amount of γ recovered to about 50 %, which is equivalent to the base metal. It was able to show the feasibility of microstructure improvement welding process. In order to increase the reliability of the microstructure improvement welding process successfully reviewed in Chapter 7.4, the possibility of expansion to DSS of different compositions was investigated, and the evaluation of the applicability is described in detail in the next Chapter.

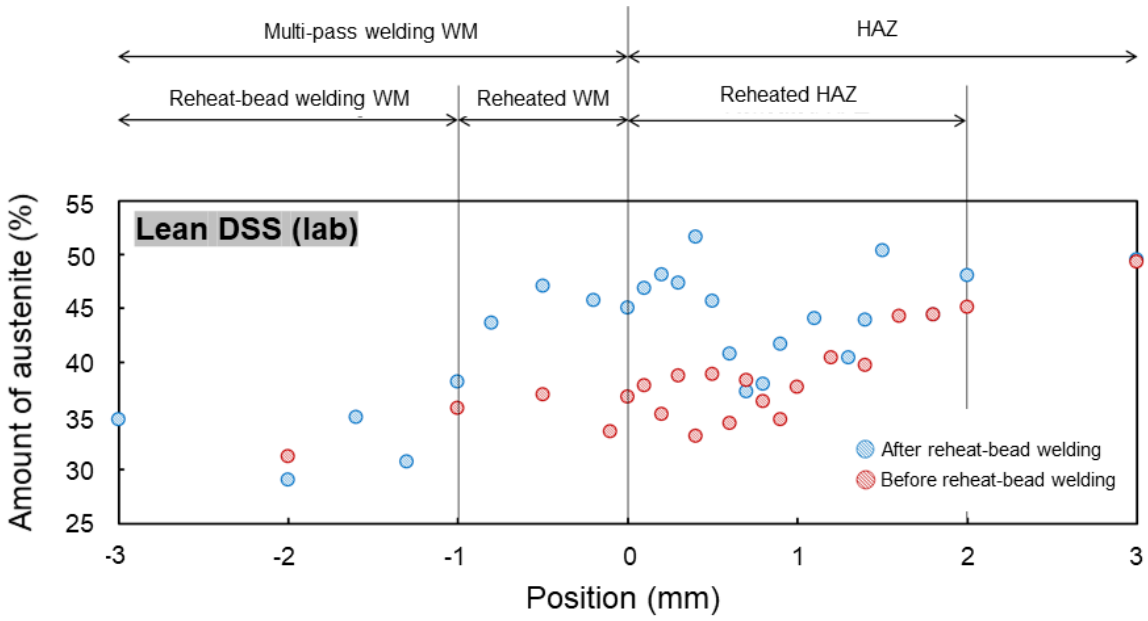

Fig. 7.8 Measured γ phase fraction after reheat–bead welding.

7.5 Evaluation of the applicability of the microstructure improvement welding to other steels

7.5.1 Optimization of welding conditions based on experimental values

Based on the content of Chapter 7.4, the optimal welding position of the reheat–bead was derived using 933 J/mm heat input. The distance, *x*, of the fusion line of the final pass of the multi–pass welding changed from 0.25 mm to 1.0 mm, and the amount of γ phase after welding under each condition was calculated. The method of predicting the amount of γ according to the distance was predicted using the rate constant and procedure already discussed in Chapter 3. Fig. 7.9 shows a schematic of reheat–bead welding and the results calculated under each position. Further, the amount of γ phase according to the reheat–bead welding position was calculated, and the results shown in Fig. 7.10. As seen in Fig. 7.10, the largest amount of γ is re–precipitated at x = 0.5 mm. Therefore, this condition was adopted in the actual process.

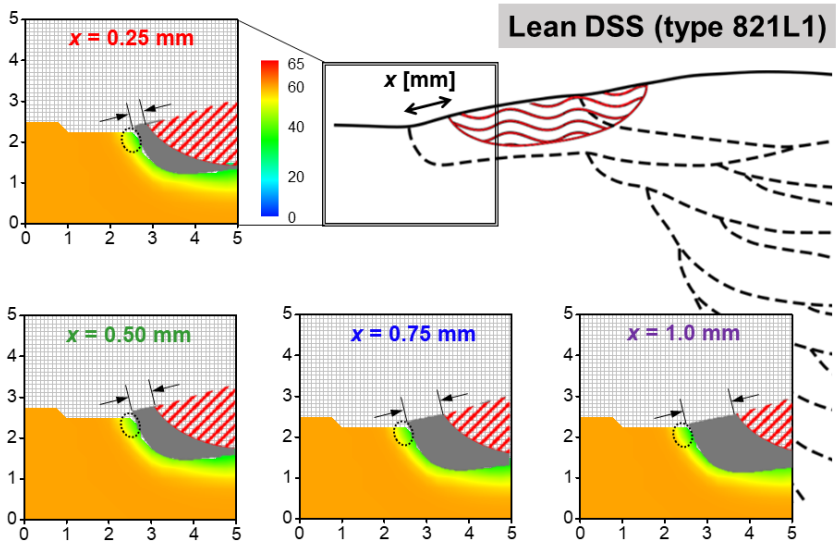

Fig. 7.9 Phase transformation the prediction results at each reheat–bead welding application position.

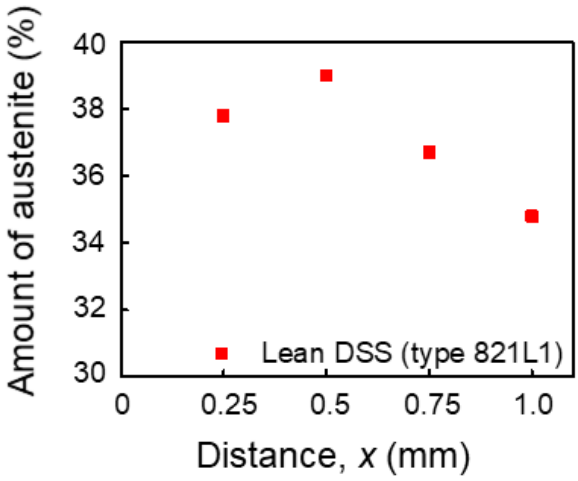

Fig. 7.10 Relationship between reheat–bead welding application position and austenite fraction.

7.5.2 Optimization of welding conditions based on phase–field

In this Section, the amount of γ according to distance is predicted using the rate constant of lean DSS (type 821L1) verified in Chapters 4,5, and 6. The distance, *x*, of the fusion line of the final pass of the multi–pass welding changed from 0.25 mm to 1.0 mm, and the amount of γ phase after welding under each condition was calculated. Fig. 7.11 shows the schematic of the reheat–bead welding derived using the phase–field rate constant and the result of the calculated γ amount at each position. Further, the amount of γ phase according to the reheat–bead welding position was calculated, and the results shown in Fig. 7.12. There is a difference in value between the γ amount predicted by the phase–field rate constant (Fig. 7.12) and the γ amount predicted using the experimental value (Fig. 7.10), but the trend is similar. The predicted result using the phase–field rate constant also has the largest amount of γ precipitated at x = 0.5 mm, similar to the result of Fig. 7.10.

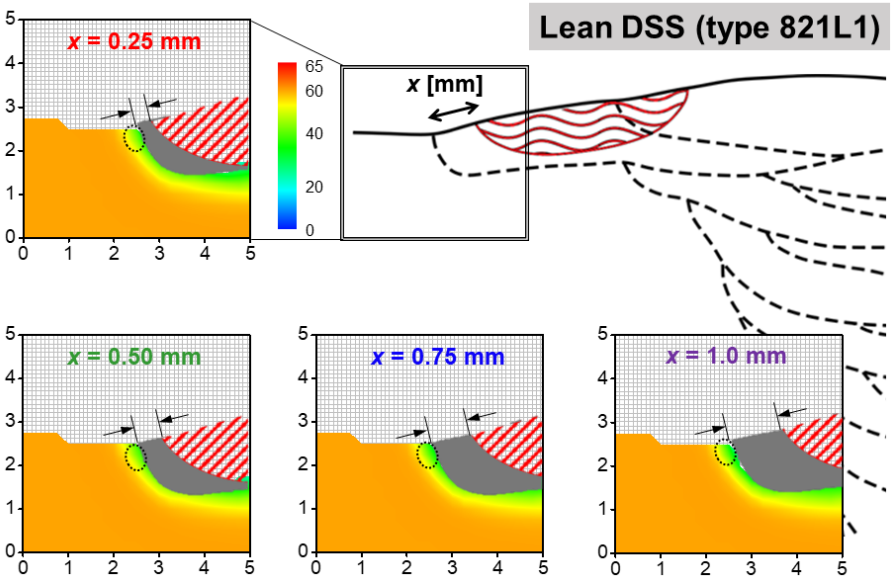

Fig. 7.11 Phase transformation the prediction results at each reheat–bead welding application position.

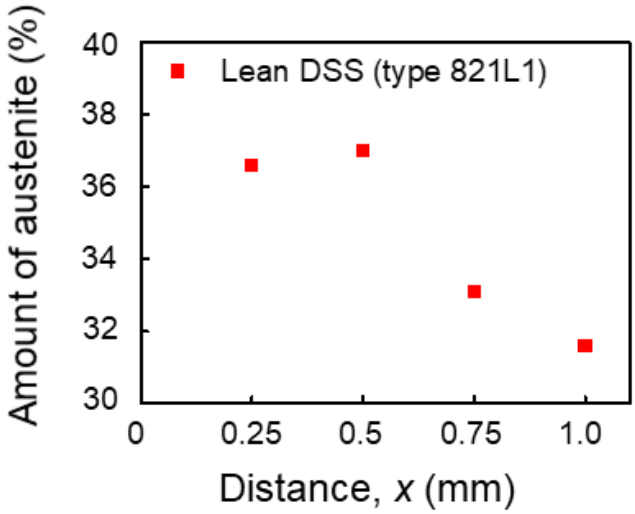

Fig. 7.12 Relationship between reheat–bead welding application position and austenite fraction.

7.5.3 Experimental verification of microstructural improvement welding method

Based on the results presented in Figs. 7.10 and 7.12, it was confirmed that the recovery of the amount of γ, when x = 0.5 mm and the welding was performed under these conditions was the largest. Additionally, the appearance of beads before and after reheat–bead welding is shown in Fig. 7.13. Fig. 7.14 shows cross–sectional views and EBSD results after performing reheat–bead welding. The amount of γ phase in the HAZ (yellow part of the phase map) 250 μm from the fusion line was 40.5 %. Compared to the amount of the γ phase, which was less than 30 % before reheat–bead welding was performed, it was observed that recovery could be effectively achieved. Furthermore, from the results presented in Figs. 7.10 and 7.12, it can be ascertained that the correspondence between the results of x = 0.5 mm (phase–field value = 37 %, experimental value = 39 %) predicted via computer simulation and the experimental results (γ = 40.5 %) is very high.

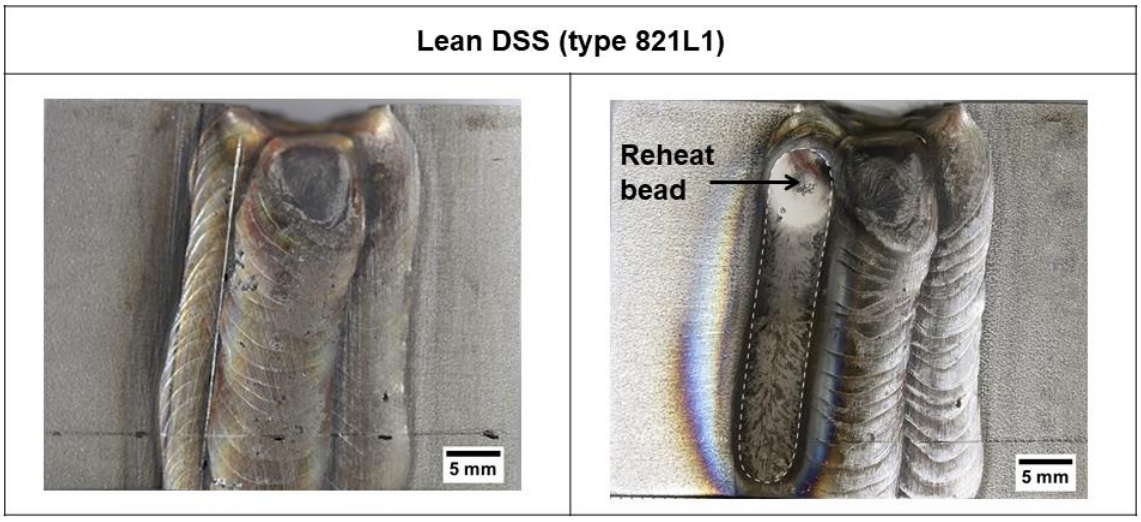

(a) Before reheat-bead. (b) After reheat-bead.

Fig. 7.13 Appearance of reheat–bead welded joint; (a) before reheat–bead and (b) after reheat–bead.

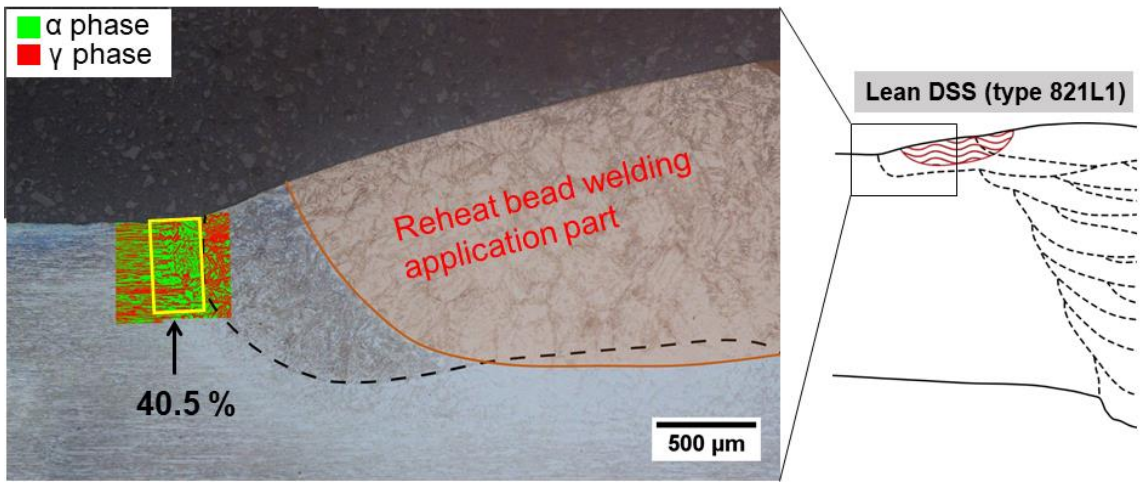

Fig. 7.14 Microstructure and EBSD analysis result of reheat–bead welded joint.

7.6 Consideration on the microstructural improvement welding method

The α/γ phase transformation of the multi–pass welds of DSSs was quantitatively predicted using numerical simulation. Through microstructural analysis, the results were showed that the calculated and the experimental results of the multi–pass welds were identical (Chapters 3 and 6). However, through the prediction results, the region where the γ amount of the multi–pass welds is insufficient was identified, and a microstructure improvement welding process was proposed in Chapter 7 to restore the γ amount of the final welds based on the numerical simulation. First, for lean (lab) DSS, a color contour was created by quantifying the change in the amount of recovery of the γ phase according to the welding location and welding conditions.

Besides, by comparing the relationship between the thermal history derived through the simulation and the amount of precipitation of the γ phase, the change in the amount of γ according to the welding location and welding conditions was investigated. Moreover, to increase the reliability of the microstructure improvement welding process, its reliability was evaluated by applying it to a lean (type 821L1) DSS having a different composition. For lean (type 821L1) DSS, the γ amount for 4 welding positions (x = 0.25, 0.5, 0.75, and 1.0 mm) was derived through numerical simulation. For the simulation result, the validity was verified through comparison with the measured value. Besides, another significant thing in this study is that it was possible to predict the γ amount by using the rate constant derived from the phase–field simulation through the correction factor in Chapters 4, 5, and 6. Moreover, it is noteworthy that there is a very high correlation between the results predicted by the simulation and the measured values. In DSSs, the phase ratio of α/γ is of paramount importance, and if the ratio is misaligned, there is a concern about precipitation of the secondary phases, which adversely affects mechanical properties and corrosion resistance. Therefore, since the phase ratio of α/γ may vary depending on the steel type, a quantified method was needed to recover the insufficient amount of γ.

In the study in Chapter 7, the information on the welding conditions according to the required amount of γ can be known, so it is considered to be useful in recovering the region where the amount of γ is insufficient in other steel types. From the above, it is judged that we have derived the research results which are very interesting and have very high engineering application value.

7.7 Conclusions

In Chapter 7, we proposed a new microstructure improvement welding process to restore the γ fraction of the final weld based on computer predictions. Besides, to verify the validity of the optimal conditions derived from the simulation, the verification through microstructural improvement welding was conducted. The results obtained are summarised as follows;

1) To apply microstructure improvement welding, prediction conditions for γ phase recovery change were investigated for Lean (lab) DSS according to various welding positions and heat input conditions. From the results of deriving the thermal history according to the amount of heat input, it was confirmed that the cooling rate became slower as the amount of heat input was increased. In the case of the amount of γ recovered, the amount of γ recovered was increased with an increase in the heat input. Besides, when the distance, x, was 1.25 mm, the amount of γ recovered was maximum.

2) To investigate the effect of distance, x, on the recovery of γ amount, the relationship between the thermal history and the precipitation rate constant of the γ phase was investigated. When the distance, x, was 1.25 mm, the recovery of the γ amount was maximized due to the longer holding time near the precipitation nose temperature. Based on the above, a quantified color contour was created.

3) The microstructure improvement welding process was proved its validity through experimental verification. After reheat–bead welding of lean (lab) DSS, in the region of up to 0.5 mm close to the fusion line, the amount of γ recovered to about 50 %, which is equivalent to the base metal, showing the feasibility of the microstructure improvement welding process. Furthermore, to increase the reliability of the microstructure improvement welding reviewed in Lean (lab) DSS, scalability investigation and applicability evaluation were conducted for Lean (type 821L1) DSS.

4) To evaluate the applicability to lean (type 821L1) DSS, the γ amount was derived through numerical simulation for 4 welding positions (x = 0.25, 0.5, 0.75, and 1.0 mm). When x = 0.5 mm (γ = 39 %), the amount of γ was the maximum. The validity of the derived γ amount was verified through comparison with the measured value, and it was confirmed that there was a high correlation between the experimental value (γ = 39 %) and the measured value (γ = 40.5 %).

5) The microstructure improvement welding process was applied to lean (type 821L1) DSS using the rate constant reviewed in chapters 4, 5, and 6 (phase–field simulation). In the case of the rate constant derived from the phase–field simulation, the γ amount was shown the maximum value when x = 0.5 mm (γ = 37 %). Furthermore, it was confirmed that there was a high correlation between the experimental value (γ = 39 %) and the measured value (γ = 40.5 %).

6) As a result of proposing a microstructure improvement welding process using lean (lab, type 821L1) DSSs, it was found that there was a good correlation between calculated, experimental, and measured values. Therefore, it is judged that the microstructure improvement welding proposed in this study is a useful technique for recovering the region where the γ amount is insufficient.

Chapter 8 Conclusions

The purpose of this study is to semi–quantitatively predict the complex α/γ phase fraction during thermal cycles in multi–pass welds. By determining the kinetics through experimental and theoretical numerical analysis (phase–field method), the α/γ phase fraction of the multi–pass welds was semi–quantitatively predicted. To verify the validity of the phase–field model constructed through theoretical consideration, it was proved through comparison with the experimental values. Based on the above, we introduce the phase–field model, a new technology that overcomes the limitation of experimentally determining the kinetics and predicts only by simulation.

The Chapter 1 is an introductory part, describing the purpose and flow of the study.

In Chapter 2, a general review of the welding metallurgical problem of stainless steels was conducted. Besides, we examined how the phase–field simulation technique, which is a powerful tool for predicting microstructures, is applied to various alloys. Furthermore, future tasks and prospects that can develop the conventional technology with phase–field simulation are also described.

In Chapter 3, the kinetic approach was made to the α/γ phase fraction in the multi–pass welds of DSSs. Both of the dissolution and precipitation behaviors of γ phase were kinetically investigated for the reheated WM as well as the base material HAZ, and the γ phase fraction in multi–pass welds of DSSs was numerically calculated by coupling with the heat conduction analysis during multi–pass welding. Finally, the predicted results of α/γ phase fraction in multi–pass welds were verified by the experimental examination.

1) From the kinetic evaluation of the dissolution and precipitation phenomenon of DSSs, the efficiency of the Austin–Rickett type equation was confirmed. Additionally, the rate constants for dissolution and precipitation were derived based on the equation.

2) Based on the kinetic equations determined, the distribution of the γ phase fraction in multi–pass welds of DSSs was calculated combined with the heat conduction analysis in welding process. The incremental method was applied to expand the dissolution and precipitation kinetics to the non–isothermal process. As a result of predicting the phase transformation behavior of the multi–pass welds using the rate constant obtained by the kinetic evaluation, a good agreement with the measured result was obtained. Therefore, the α/γ phase fraction prediction technique was ascertained to be valid.

3) From the predicted results in the multi–pass welds, at the time of completion of each welding pass, the amount of γ in the HAZ was temporarily lowered, but it was suggested that the γ phase re–precipitated under the influence of heat from the subsequent pass. However, in the HAZ of the final pass, there was little recovery of the γ phase owing to the absence of subsequent thermal cycles.

In Chapter 4, a phase–field simulation model was constructed for Fe–Cr–Ni ternary compositions in terms of the Cr/Ni equivalent ratio of DSSs. In addition, numerical analysis of the dissolution and precipitation of the γ phase was performed and the possibility of deriving the dissolution and precipitation rate constant was examined. Furthermore, the relationship between the temperature dependence of the rate of dissolution and precipitation dissolution was also investigated.

1) The calculation results of the γ phase dissolution and precipitation behavior, which were obtained using the composition of the Fe–Cr–Ni ternary system in terms of Cr and Ni equivalents, showed that the kinetics of the γ phase in all the base metal HAZs and weld metals of the studied DSSs were approximately followed by the Austin–Rickett equation.

2) Arrhenius plots of the γ phase dissolution rate demonstrated that there was a good correlation and that the use of the developed phase–field simulation was valid.

3) When a regression analysis was performed based on the calculation results, the precipitation rate constant curve presented a nose, as shown in the actual experimental curve.

In Chapter 5, the verification of validity and introduction of correction factors were reviewed by comparing the calculated values obtained in Chapter 4 with the experimental values. For the correction factor, three types of DSSs were used to derive the correction factor, and it was derived by comparing the calculated values with the experimental values. The feasibility of the established phase–field method was verified by conducting a review on the applicability to other steel grades and weld metals using the derived correction factors.

1) The Arrhenius plot of the γ phase dissolution rate showed a good correlation between the calculated and experimental values. Besides, when the regression analysis was performed based on the calculation results, as can be seen in the experimental curve, the precipitation rate constant curve showed a nose. Therefore, the introduction of a correction factor was considered.

2) Correction factors were introduced by comparing the temperature dependence of the experimental values with that of the calculated values, which improved the degree of correlation between these values.

3) When the applicability of the proposed method was evaluated using DSSs with different compositions and weld metals, the temperature dependences of the experimental and calculated values mostly showed good agreement. From the above facts, it was suggested that the precipitation rate constant determined using the phase–field method established in this study is applicable to other steel types.

In Chapter 6, the γ amount of the multi–pass welds were semi–quantitatively predicted using the rate constant derived from the phase–field method (in Chapters 4 and 5). Besides, the validity of the phase–field method was verified through comparison with the experimentally predicted γ amount in Chapter 3.

1) Based on the determined kinetic equations (phase–field), the distribution of the γ phase fraction in multi–pass DSS welds was calculated, and the heat conduction analysis in the welding process was also conducted.

2) The calculated results (phase–field) of the γ phase fraction in multi–pass welds was consistent with the measured results. In addition, it was confirmed that the amount of γ was lower by about 3 % to 5 % through comparison with the experimental values. It is believed that this is due to an error in the correction coefficient.

3) Based on the prediction results, the α/γ phase transformation of DSSs multi–pass welds can be semi–quantitatively predicted by phase–field–based kinetics and computer simulations.

The prediction of the γ phase fraction in multi–pass welds has been demonstrated with the current approach based on the kinetic equation (phase–field, experimental) determined in the studies of Chapters 3 and 6. However, in the case of the HAZ of the final welding pass, since the heat of the subsequent pass remains unaffected, there is a concern that the precipitation of γ will be insufficient. To improve the above problem, in Chapter 7, we proposed a new microstructure improvement welding process to restore the γ fraction of the final weld based on computer predictions. Besides, to verify the validity of the optimal conditions derived from the simulation, the verification through microstructural improvement welding was conducted.

1) Based on the computer prediction, the microstructural improvement welding ("reheat–bead welding") process, with analogous concept to the temper bead welding technique, was newly proposed for recovering the γ phase fraction in weld even in the as–welded situation.

2) In the lean (lab) DSS, the amount of γ was predicted according to the heat input and the welding position, and a color contour was created based on the prediction result.

3) After reheat–bead welding of lean (lab) DSS, in the region of up to 0.5 mm close to the fusion line, the amount of γ recovered to about 50 %, which is equivalent to the base metal, showing the feasibility of the microstructure improvement welding process.

4) As a result of deriving the optimization conditions according to the distance, x, of the fusion line of the lean (type 821L1) DSS, the largest amount of γ was precipitated at x = 0.5 mm (phase–field value = 37 %, experimental value = 39 %).

5) By constructing reheat–bead welding on lean (type 821L1) DSS under optimized conditions, the amount of γ phase in the final pass was effectively recovered.

Acknowledgments

I would like to express my sincere gratitude to my research guide Professor Kazuyoshi Saida for his valuable comments, remarks, and suggestions throughout the duration of this study. I believe it is a privilege to have worked with a world–class welding process expert, and through discussions with him, I learned a lot of new things in the field of phase transformation. Moreover, he gave me support not only on my research but also on my career, which has played an important role in both my professional and personal development.

My deep appreciation is due to Professor Hiroshige Inoue, Professor Akio Hirose for an excellent opportunity to finish this thesis at Osaka University. I would also like to thank Associate Professor Tomo Ogura, Assistant Professor Shotaro Yamashita for providing me essential comments and advice as the research and experiments proceeded. Also, my appreciations are due to Associate Professor Yu Lina for very pleasant cooperation in carrying out the important scientific research of this study.

It is my pleasure to acknowledge the collaboration with the whole personnel of Saida Laboratory, which made this thesis possible and to thank past, and present members.

Special thanks are to Messrs. Y. Tanabe, T. Matsumura, R. Hamada, and J. Tokunaga for their cooperation and support in this study.

I would also like to appreciate my sincere gratitude for the guidance and encouragement of Professor Tae–Hyun Nam of Materials Engineering and Convergence Technology, Gyeongsang National University, Republic of Korea.

Finally, I would like to thank my beloved parents (Gwang–Su Kim, Mo–Hwa Yoon), younger brother (Dong–Seok Kim), and girlfriend (Hye–Ju Choi) for their patience and support.

I would also like to appreciate my sincere gratitude to paternal grandparents (Hyo–Won Kim, Ok–Nang Lee) in heaven, aunt (Tae–Sun Kim), and uncles (Han–Su Kim, Chang–Su Kim, Yeong–Su Kim, Jong–Su Kim, Gi–Su Kim, Du–Su Kim). I would also like to express my gratitude to maternal grandparents (Dae–Jin Yoon, Sun–Yeon Sung), aunt (Chun–Hwa Yoon), and uncles (Yeo–Hong Yoon, Yeo–Seong Yoon, Bin Yoon).

References

1. Cunat PJ. Alloying elements in stainless steel and other chromium–containing alloys. *ICDA, Paris*. 2004.
2. Lippold, J.C., Kotecki, D.J. *Welding metallurgy and weldability of stainless steels*. John Wiley & Sons, New Jersey, USA, 2005
3. 李 齋炯. Solidification Cracking Prevention by Thermal Strain Control [dissertation]. Osaka (Japan): Osaka University at Japan; 2021.
4. Inoue Y, Kikuchi M. Present and future trends of stainless steel for automotive exhaust system. *High–temperature*. 2003 Jul;950:750.
5. Nygren E, Folke G, Molin S, Ljungberg L. Sandvikens Handbok: Järnets och stålets metalografi. *Esselte Tryck, Stockholm*, Sweden. 1970.
6. W. T. DeLong: *Welding Journal*, 54 (1974), 273s.
7. Boellinghaus T, Lippold JC, Cross CE, editors. *Cracking phenomena in welds IV*. Springer International Publishing; 2016 Feb 10.
8. Lippold JC, Kotecki DJ, Wagoner RH, Chenot JL, Westbrook JH, Fleischer RL. *Welding Metallurgy. In Weldability of Stainless Steels* 2005. John Wiley & Sons New Jersey.
9. Nissley NE, Collins MG, Guaytima G, Lippold JC. Development of the strain–to–fracture test for evaluating ductility–dip cracking in austenitic stainless steels and Ni–base alloys. *Welding in the World*. 2002 Jul 1;46(7–8):32–40.
10. Hemsworth B, Boniszewski T, Eaton NF. Classification and definition of high–temperature welding cracks in alloys. *Metal Construction*. 1969 Feb;1(2):5–16.
11. Wolf M, Schobbert H, Böllinghaus T. Influence of the weld pool geometry on solidification crack formation. In *Hot Cracking Phenomena in Welds* 2005 (pp. 245 –268). Springer, Berlin, Heidelberg.
12. Böllinghaus, Th.; Herold, H, editors. *Hot cracking phenomena in welds*. Springer–Verlag, Berlin Heidelberg, 2005.
13. Böllinghaus T, Herold H, Cross CE, Lippold JC, editors. *Hot cracking phenomena in welds II*. Springer Science & Business Media; 2008 Aug 7.
14. Lippold J, Böllinghaus T, Cross CE, editors. *Hot cracking phenomena in welds III*. Springer Science & Business Media; 2011 May 3.
15. Kannengießer T. Recent developments in nickel base material welding considering the influence of shielding gas on the hot cracking resistance, 2004.
16. Goodwin GM. The effects of heat input and weld process on hot cracking in stainless steel. *Welding Journal*. 1988 Apr 1;67(4):88–94.
17. Shankar V, Gill TP, Mannan SL, Sundaresan S. Solidification cracking in austenitic stainless steel welds. *Sadhana*. 2003 Jun 1;28(3–4):359–82.
18. Cross CE. On the origin of weld solidification cracking. In *Hot cracking phenomena in welds* 2005 (pp. 3–18). Springer, Berlin, Heidelberg.
19. Folkhard E. *Welding metallurgy of stainless steels*. Springer Science & Business Media; 2012 Dec 6.
20. Kou S. Welding metallurgy. *New Jersey*, USA. 2003 Sep:431–46.

21. Fredriksson H. Transition from Peritectic to Eutectic Reaction in Iron Base Alloys. In *Solidification and Casting of Metals\ Proc. Conf.*\, Sheffield, England, July 1977, 1979 (pp. 131–138).
22. David SA, Goodwin GM, Braski DN. *Solidification behavior of austenitic stainless steel filler metals*. Oak Ridge National Lab., TN (USA); 1980 Feb 1.
23. Matsuda F, Nakagawa H, Nakata K, Okada H. The VDR cracking test for solidification crack susceptibility on weld metals and its application to aluminum alloys (materials, metallurgy, weldability). *Transactions of JWRI*. 1979;8(1):85–95.
24. Koseki T, Matsumiya T, Yamada W, Ogawa T. Numerical modeling of solidification and subsequent transformation of Fe–Cr–Ni alloys. *Metallurgical and Materials Transactions A*. 1994 Jun 1;25(6):1309–21.
25. Kelly TF, Cohen M, Vander Sande JB. Rapid solidification of a droplet–processed stainless steel. *Metallurgical Transactions A*. 1984 May;15(5):819–33.
26. Bhadeshia HK, David SA, Vitek JM. Solidification sequences in stainless steel dissimilar alloy welds. *Materials Science and Technology*. 1991 Jan 1;7(1):50–61.
27. Olson DL. Prediction of austenitic weld metal microstructure and properties. *Welding journal*. 1985 Oct 10;64(10):281s–95s.
28. Hammar O. Influence of steel composition on segregation and microstructure during solidification of austenitic stainless steels. *Solidification and casting of metals*. 1979;401.
29. Suutala N, Moisio T. Solidification technology in the foundry and casthouse. *The Metals Society, London*. 1980 Sep;310.
30. Suutala N. Effect of solidification conditions on the solidification mode in austenitic stainless steels. *Metallurgical Transactions A*. 1983 Feb 1;14(1):191–7.
31. Siewert TA, McCowan CN, Olson DL. Ferrite number prediction to 100 FN in stainless steel weld metal. *Welding Journal*. 1988 Dec 1;67(12):289–98.
32. Kotecki DJ, Siewert TA. WRC–1992 constitution diagram for stainless steel weld metals: a modification of the WRC–1988 diagram. *Welding Journal*. 1992 May 1;71(5):171–8.
33. Babu SS, Vitek JM, Iskander YS, David SA. New model for prediction of ferrite number of stainless steel welds. *Science and Technology of Welding and Joining*. 1997 Dec 1;2(6):279–85.
34. Vitek JM, Iskander YS, Oblow EM. Improved Ferrite Number prediction in stainless steel arc welds using artificial neural networks–Part 1: Neural network development. WELDING JOURNAL–NEW YORK–. 2000 Feb 1;79(2):33s–40s.
35. Lippold JC. *Welding metallurgy and weldability*. USA: John Wiley & Sons Incorporated; 2015.
36. Hull FC. Effect of delta ferrite on the hot cracking of stainless steel. *WELD J*. 1967;46(9):399.
37. Bardeen J. Imperfections in nearly perfect crystals. In *Symposium Held at Pocono Manor*, 1950 1952 (Vol. 261). Wiley.
38. A. Gueussier and R. Castro, Rev. *Metall*., 57 (1960), p. 117.
39. Borland JC, Younger RN. Some aspects of cracking in welded Cr–Ni austenitic steels. *British Welding Journal*. 1960 Jan 7;7(1):22–59.

40. Thomas, R. D. Jr., *Metals Prog*., 70: 73, 1956.
41. Medovar, B. I., *Avtomatischeskaya Svarka*, 6: 3, 1953.
42. Curran RM, Rankin AW. Welding Type 347 stainless steel for 1100 F turbine operation. *Welding J.(NY)*. 1955 Mar 1;34.
43. Rollason EC, Bystram MC. HOT–CRACKING OF AUSTENITIC WELDS WITH SPECIAL REFERENCE TO 18/13/1 CR–NI–NB ALLOY. *Journal of the Iron and Steel Institute*. 1951 Jan 1;169(4):347.
44. Masumoto I. Hot cracking of austenitic steel weld metal. *J. JWS*. 1972;41(11):1306–14.
45. Kujanpaa V, Suutala N, Takalo T, Moisio T. Correlation between solidification cracking and microstructure in austenitic and austenitic–ferritic stainless steel welds. *Welding Research International*. 1979;9(2):55–75.
46. Chun EJ, Baba H, Nishimoto K, Saida K. Evaluation of solidification cracking susceptibility in austenitic stainless steel welds using laser beam welding transverse–varestraint test. In *Cracking phenomena in welds IV* 2016 (pp. 161–206). Springer, Cham.
47. 金東助, 小椋智, 田辺祥大, 山下正太郎, 才田一幸. 二相ステンレス鋼の凝固割れ感受性評価と計算機シミュレーションによる凝固偏析解析. *溶接学会論文集*. 2020;38(2):76–84.
48. Lee CH. *Weldability and microstructural analysis of nuclear–grade austenitic stainless steels*. Teledyne Brown Engineering, Huntsville, AL (USA); 1988 Jan 1.
49. Hull FC. *Effects of Alloying Additions on Hot Cracking of Austeitic Chromium–nickel Stainless Steels*. 1960.
50. Matsuda F, Nakagawa H, Lee JB. Weld Cracking in Duplex Stainless Steel (Report II): Modelling of Cellular Dendritic Growth during Weld Solidification (Materials, Metallurgy & Weldability). *Transactions of JWRI*. 1989;18(1):107–17.
51. Matsuda F, Nakagawa H, Lee JB. Weld Cracking in Duplex Stainless Steel (Report III): Numerical Analysis on Solidification Brittleness Temperature Range in Stainless Steel (Materials, Metallurgy & Weldability). *Transactions of JWRI*. 1989;18(1):119–26.
52. Matsuda F, Katayama S, Arata Y. Solidification crack susceptibility in weld metals of fully austenitic stainless steels – solidification crack susceptibility and amount of phosphide and sulphide in SUS 310 weld metal. *Trans. Jpn. Weld. Res. Inst.* 1981;10: 201–212
53. Lundin CD, Lee CH, Menon R, Osorio V. Weldability evaluations of modified 316 and 347 austenitic stainless steels: Part I–preliminary results. *Welding Journal*. 1988 Feb 1;67(2):35s–46s.
54. Kujanpää VP. Effects of steel type and impurities in solidification cracking of austenitic stainless steel welds. *Metal Construction*. 1985;17(1):40R–6R.
55. Brooks JA. Effect of alloy modifications on HAZ cracking of A–286 stainless steel. *Welding journal*. 1974 Nov;53(11):517s–23s.
56. Matsuda F, Nakagawa H, Katayama S, Arata Y. Solidification Crack Susceptibility in Weld Metals of Fully Austenitic Stainless Steels (Report VI): Effect of La or REM Addition on Solidification Crack Resistance (Materials Metallurgy and Weldability). *Transactions of JWRI*. 1982;11(1):79–94.
57. Arata Y, Matsuda F, Saruwatari S. Varestraint test for solidification crack susceptibility in

weld metal of austenitic stainless steels. *Transactions of JWRI*. 1974;3(1):79–88.
58. CLESLAK M, MJ C, AM R, WF S. Solidification cracking and analytical electron microscopy of austenitic stainless steel weld metals.
59. Matsuda F, Nakagawa H, Katayama S, Arata Y. Solidification Crack Susceptibility in Weld Metals of Fully Austenitic Stainless Steels (Report VIII): Effect of Nitrogen on Cracking in SUS 304 Weld Metal (Materials, Metallurgy & Weldability). *Transactions of JWRI*. 1983;12(1):89–95.
60. Lundin CD, Chou CP, Sullivan CJ. Hot cracking resistance of austenitic stainless steel weld metals. *Welding journal*. 1980 Apr;59(8):226s–32s.
61. ZHITNIKOV N. THE HOT CRACKING RESISTANCE OF AUSTENITIC CR–NI WELD METAL IN RELATION TO NITROGEN CONTENT.
62. Metals handbook, 8 end, Vol. 8, 424;1973, Metals Park, OH, *American Society for Metals*.
63. Castro R. JJ de. Cadenet:'Welding Metallurgy of Stainless and Heat–Resisting Steels' Canbrige University Press, London, 1974.
64. Uhlig HH, King CV. Corrosion and corrosion control. *Journal of the Electrochemical Society*. 1972 Dec 1;119(12):327C.
65. Kou S, Le Y. The effect of quenching on the solidification structure and transformation behavior of stainless steel welds. *Metallurgical Transactions A*. 1982 Jul 1;13(7):1141–52.
66. Pease GR. The practical welding metallurgy of nickel and high–nickel alloys. *Welding journal*. 1957 Jul;36(7):3.
67. Christoffel RJ, Nippes EF, Solomon HD. Weldments: *Physical Metallurgy and Failure Phenomena*. Bolton Landing. 1978:1979.
68. Lippold JC, Kotecki DJ, Wagoner RH, Chenot JL, Westbrook JH, Fleischer RL. *Welding Metallurgy. In Weldability of Stainless Steels* 2005. John Wiley & Sons New Jersey.
69. Principles and Technology of the Fusion Welding of Metals, Vol.1, Mechanical Engineering Publishing Co., Peking, China, 1970.
70. Ikawa, H., Nakao, Y., and Nishimoto, K., *Technol. Repts. Osaka Univ.*, 29(1648): 1979.
71. Magula V, Liao J, Ikeuchi K, Kuroda T, Kikuchi Y, Matsuda F. New Aspects of Sensitization Behavior in Recent 316 Type Austenitic Stainless Steels Austenitic Stainless Steels (Materials, Metallurgy & Weldability). *Transactions of JWRI*. 1996;25(1):49–58.
72. Linnert, G. E., in *Source Book on Stainless Steels*, *American Society for Metals*, Metals Park, OH, 1976, p. 237.
73. Charles J. Duplex stainless steels, a review after DSS'07 in Grado. *Revue de Métallurgie–International Journal of Metallurgy*. 2008 Mar;105(3):155–71.
74. Benson M. Applications utilising the advantageous properties of LDX 2101. *Proceedings Stainless Steel World*. 2005:171–6.
75. Alfonsson E. Lean duplex—The first decade of service experience. In *Proceedings of the 8th Duplex Stainless Steels Conference, Beaune, France* 2010 Oct (pp. 13–15).
76. Nilsson JO, Wilson A, Josefsson B, Thorvaldsson T. Relationship between pitting corrosion, toughness and microstructure for isothermally heat treated super duplex stainless steel. *Applications of Stainless Steel*' 92. 1992 Jun;1:280–9.
77. Soulignac P. Celebrating the 70+ years of duplex stainless steels in Europe. In *Proceedings of*

the 8th Duplex Stainless Steels Conference, Beaune, France 2010 Oct (pp. 13–15).
78. STEELS OD. PRACTICAL GUIDELINES FOR THE FABRICATION OF DUPLEX STAINLESS STEELS. *Metallurgy*.;3:2.
79. Charles J. Composition and properties of duplex stainless steels. *Welding in the World/Le Soudage Dans Le Monde*. 1995(36):43–54.
80. Smuk O. *Microstructure and properties of modern P/M super duplex stainless steels* (Doctoral dissertation, Materialvetenskap).
81. Miranda Pérez AF. Solid state phase transformations in Advanced Steels.
82. Chen TH, Yang JR. Effects of solution treatment and continuous cooling on σ–phase precipitation in a 2205 duplex stainless steel. *Materials Science and Engineering: A*. 2001 Jul 31;311(1–2):28–41.
83. Miura M, Koso M, Kudo T, Tsuge H. Effect of nickel and nitrogen on microstructure and corrosion resistance of duplex stainless steel weldment. *Q. J. Jpn. Weld. Soc*. 1989 Feb;7(1):94–100. (in Japanese).
84. KAMIYA O, KUMAGAI K, KIKUCHI Y, ENJO T. Effect of microstructure on fracture toughness of SUS329J1 duplex stainless steel welds. *Transactions of the Japan Welding Society*. 1989;20(2):152–9. (in Japanese).
85. McPherson NA, Li Y, Baker TN. Microstructure and properties of as welded duplex stainless steel. *Science and technology of welding and joining*. 2000 Aug 1;5(4):235–44.
86. Badji R, Bouabdallah M, Bacroix B, Kahloun C, Belkessa B, Maza H. Phase transformation and mechanical behavior in annealed 2205 duplex stainless steel welds. *Materials Characterization*. 2008 Apr 1;59(4):447–53.
87. Deng B, Jiang YM, Gao J, Li J. Effect of annealing treatment on microstructure evolution and the associated corrosion behavior of a super–duplex stainless steel. *Journal of Alloys and Compounds*. 2010 Mar 18;493(1–2):461–4.
88. Atamert S, King JE. Elemental partitioning and microstructural development in duplex stainless steel weld metal. *Acta metallurgica et materialia*. 1991 Mar 1;39(3):273–85.
89. Putz A, Althuber M, Zelić A, Westin EM, Willidal T, Enzinger N. Methods for the measurement of ferrite content in multipass duplex stainless steel welds. *Welding in the World*. 2019 Jun;63(4):1075–86.
90. Pickle T, Henry N, Morriss P, Tennis L, Wagner D, Baumer RE. Root pass microstructure in super duplex stainless steel multipass welds. *Welding Journal*. 2019 May 1;98(5):123s–34s.
91. Hosseini VA, Wessman S, Hurtig K, Karlsson L. Nitrogen loss and effects on microstructure in multipass TIG welding of a super duplex stainless steel. *Materials & design*. 2016 May 15;98:88–97.
92. Hosseini VA, Bermejo MA, Gårdstam J, Hurtig K, Karlsson L. Influence of multiple thermal cycles on microstructure of heat–affected zone in TIG–welded super duplex stainless steel. *Welding in the World*. 2016 Mar 1;60(2):233–45.
93. Vahman M, Shamanian M, Golozar MA, Jalali A, Sarmadi MA, Kangazian J. The effect of welding heat input on the structure–property relationship of a new grade super duplex stainless steel. *steel research international*. 2020 Jan;91(1):1900347.
94. Menezes AJ, Abreu H, Kundu S, Bhadeshia HK, Kelly PM. Crystallography of Widmanstätten

austenite in duplex stainless steel weld metal. *Science and Technology of Welding and Joining*. 2009 Jan 1;14(1):4–10.

95. Ramirez AJ, Brandi SD, Lippold JC. Secondary austenite and chromium nitride precipitation in simulated heat affected zones of duplex stainless steels. *Science and Technology of Welding and Joining*. 2004 Aug 1;9(4):301–13.
96. Nilsson JO, Huhtala T, Jonsson P, Karlsson L, Wilson A. Structural stability of super duplex stainless weld metals and its dependence on tungsten and copper. *Metallurgical and Materials Transactions A*. 1996 Aug 1;27(8):2196–208.
97. Badji R, Bouabdallah M, Bacroix B, Kahloun C, Bettahar K, Kherrouba N. Effect of solution treatment temperature on the precipitation kinetic of σ–phase in 2205 duplex stainless steel welds. *Materials Science and Engineering: A*. 2008 Nov 25;496(1–2):447–54.
98. Nishimoto K, Saida K, Katsuyama O. Prediction of sigma phase precipitation in super duplex stainless steel weldments. *Welding in the World*. 2006 Mar;50(3):13–28.
99. Yousefieh M, Shamanian M, Saatchi A. Influence of heat input in pulsed current GTAW process on microstructure and corrosion resistance of duplex stainless steel welds. *Journal of iron and steel research, international*. 2011 Sep 1;18(9):65–9.
100. Sugimoto I, Park SH, Hirano S, Saito H, Hata S. Microscopic observation of precipitation behavior at friction stirring zone of super duplex stainless steel. *Materials Transactions*. 2019 Sep 1;60(9):2003–7.
101. Valiente Bermejo MA, Hurtig K, Eyzop D, Karlsson L. A New Approach to the Study of Multi–Pass Welds–Microstructure and Properties of Welded 20–mm–Thick Superduplex Stainless Steel. *Applied Sciences*. 2019 Jan;9(6):1050.
102. Hosseini VA, Hurtig K, Karlsson L. Bead by bead study of a multipass shielded metal arc–welded super–duplex stainless steel. *Welding in the World*. 2020 Feb;64(2):283–99.
103. Guilherme LH, Reccagni P, Benedetti AV, Fugivara CS, Engelberg DL. Corrosion assessment of ASME qualified welding procedures for grade 2101 lean duplex stainless steel. *Corrosion*. 2019 Oct 1;75(10):1216–29.
104. Badji R, Bouabdallah M, Bacroix B, Kahloun C, Belkessa B, Maza H. Phase transformation and mechanical behavior in annealed 2205 duplex stainless steel welds. *Materials Characterization*. 2008 Apr 1;59(4):447–53.
105. Kang DH, Lee HW. Study of the correlation between pitting corrosion and the component ratio of the dual phase in duplex stainless steel welds. *Corrosion Science*. 2013 Sep 1;74:396–407.
106. Yousefieh M, Shamanian M, Saatchi A. Influence of heat input in pulsed current GTAW process on microstructure and corrosion resistance of duplex stainless steel welds. *Journal of iron and steel research, international*. 2011 Sep 1;18(9):65–9.
107. Baeslack W. Phase transformation behaviour in duplex stainless steel weldments. *Metal construction*. 1988 Jan;20:26.
108. Nilsson JO. Super duplex stainless steels. *Materials science and technology*. 1992 Aug 1;8(8):685–700.
109. Okayasu M, Ishida D. Effect of microstructural characteristics on mechanical properties of austenitic, ferritic, and γ–α duplex stainless steels. *Metallurgical and Materials Transactions A*. 2019 Mar 15;50(3):1380–8.

110. Arabi SH, Pouranvari M, Movahedi M. Pathways to improve the austenite–ferrite phase balance during resistance spot welding of duplex stainless steels. *Science and Technology of Welding and Joining*. 2019 Jan 2;24(1):8–15.
111. Zhang Y, Cheng S, Wu S, Cheng F. The evolution of microstructure and intergranular corrosion resistance of duplex stainless steel joint in multi–pass welding. *Journal of Materials Processing Technology*. 2020 Mar 1;277:116471.
112. Gennari C, Pezzato L, Simonetto E, Gobbo R, Forzan M, Calliari I. Investigation of electroplastic effect on four grades of duplex stainless steels. *Materials*. 2019 Jan;12(12):1911.
113. Zhang L, Zhang W, Jiang Y, Deng B, Sun D, Li J. Influence of annealing treatment on the corrosion resistance of lean duplex stainless steel 2101. *Electrochimica Acta*. 2009 Sep 30;54(23):5387–92.
114. Johnson WA. Reaction kinetics in processes of nucleation and growth. *Am. Inst. Min. Metal. Petro. Eng.*. 1939;135:416–58.
115. Avrami M. Kinetics of phase change. I General theory. *The Journal of chemical physics*. 1939 Dec;7(12):1103–12.
116. Avrami M. Kinetics of phase change. II transformation-time relations for random distribution of nuclei. *The Journal of chemical physics.* 1940 Feb;8(2):212–24.
117. Kolmogoroff AN. On the statistical theory of the crystallization of metals. *Bull. Acad. Sci. USSR Mat. Ser*. 1937;1:355–9.
118. Austin JB. Kinetics of the decomposition of austenite at constant temperature. *Transactions of the American Institute of Mining and Metallurgical Engineers*. 1939;135:396–415.
119. Magnabosco R. Kinetics of sigma phase formation in a duplex stainless steel. *Materials Research*. 2009 Sep;12(3):321–7.
120. Dos Santos DC, Magnabosco R. Kinetic study to predict sigma phase formation in duplex stainless steels. *Metallurgical and Materials Transactions A*. 2016 Apr 1;47(4):1554–65.
121. Ferro P, Bonollo F, Timelli G. Sigma phase precipitation modelling in a UNS S32760 superduplex stainless steel. La Metallurgia Italiana. 2012.
122. Wilson A, Nilsson JO. Modelling the CCT–diagram of intermetallic phase precipitation in duplex stainless steels from isothermal experiments. *Scandinavian journal of metallurgy*. 1996;25(4):178–85.
123. Nakao Y, Nishimoto K, Inoue S. Kinetics of the Formation of Austenite at Constant Temperature: Study on the Phase Transformation in Welded Joints of Duplex Satinless Steels (Report 1). *Transactions of the Japan Welding Society*. 1982;13(2):65.
124. Nakao Y, Nishimoto K, Inoue S. Quantitative Analysis of Austenite Formation in HAZ: Study on the Phase Transformation in Welded Joints of Duplex Stainless Steels (Report 2). *Transactions of the Japan Welding Society*. 1982;13(2):81.
125. Yasuda K, Gunn RN, Gooch TG. Prediction of austenite phase fraction in duplex stainless steel weld metals. *Quarterly Journal of the Japan Welding Society* (Japan). 2002 Feb;20(1):68–77.
126. K. Saida, K. Nishimoto, H. Inoue and Y. Oikawa, Prediction of Phase Transformation in Duplex Stainless Steel Welds, *Mathematical Modelling of Weld Phenomena 11*, ed. by C. Sommitsch, N. Enzinger and P. Mayr, (2016), p.109–122.

127. Ogura T, Tanabe Y, Inoue H, Oikawa Y, Saida K. Kinetics of Phase Transformation in Weld Heat Affected Zone of Duplex Stainless Steels. In *9th European Stainless Steel Conference–Science & Market (ESSC2017) & 5th European Duplex Stainless Steel Conference & Exhibition (DUPLEX 2017)* 2017.
128. G.J. Fix, Phase field problems for free boundary problems, in Free Boundary Problems: Theory and Applications, Vol. II, A. Fasano and M. Primicerio, eds., *Pitman, Boston*, 1983, p.580.
129. Langer JS. Models of pattern formation in first–order phase transitions. In *Directions in Condensed Matter Physics: Memorial Volume in Honor of Shang–Keng Ma* 1986 (pp. 165–186).
130. Wang YU, Jin YM, Cuitino AM, Khachaturyan AG. Nanoscale phase field microelasticity theory of dislocations: model and 3D simulations. *Acta Materialia*. 2001 Jun 13;49(10):1847–57.
131. Wang YU, Jin YM, Cuitino AM, Khachaturyan AG. Phase field microelasticity theory and modeling of multiple dislocation dynamics. *Applied Physics Letters*. 2001 Apr 16;78(16):2324–6.
132. Henry H, Levine H. Dynamic instabilities of fracture under biaxial strain using a phase field model. *Physical review letters*. 2004 Sep 2;93(10):105504.
133. Chen LQ, Yang W. Computer simulation of the domain dynamics of a quenched system with a large number of nonconserved order parameters: The grain–growth kinetics. *Physical Review B*. 1994 Dec 1;50(21):15752.
134. D. Rodney, Y. Le Bouar, A. Finel, Phase field methods and dislocations, *Acta Mater*. 51 (2003) 17–30.
135. Collins JB, Levine H. Diffuse interface model of diffusion–limited crystal growth. *Physical Review B*. 1985 May 1;31(9):6119.
136. Kobayashi R. Modeling and numerical simulations of dendritic crystal growth. *Physica D: Nonlinear Phenomena*. 1993 Mar 15;63(3–4):410–23.
137. Böttger B, Stratemeier S, Subasic E, Göhler K, Steinbach I, Senk D. Modelling of Hot Ductility during Solidification of Steel Grades in Continuous Casting–Part II. *Advanced Engineering Materials*. 2010 Mar;12(3):101–9.
138. Böttger B, Carré A, Eiken J, Schmitz GJ, Apel M. Simulation of microstructure formation in technical aluminum alloys using the multiphase–field method. *Transactions of the Indian Institute of Metals*. 2009 Oct 1;62(4–5):299–304.
139. Eiken J. Phase–field simulation of microstructure formation in technical magnesium alloys. *International journal of materials research*. 2010;101(4):503–9.
140. Hu SY, Chen LQ. Solute segregation and coherent nucleation and growth near a dislocation—a phase–field model integrating defect and phase microstructures. *Acta materialia*. 2001 Feb 8;49(3):463–72.
141. Aranson IS, Kalatsky VA, Vinokur VM. Continuum field description of crack propagation. *Physical review letters*. 2000 Jul 3;85(1):118.
142. Karma A, Kessler DA, Levine H. Phase–field model of mode III dynamic fracture. *Physical Review Letters*. 2001 Jul 3;87(4):045501.

143. Nomoto S, Mori K, Segawa M, Yamanaka A. Solidification Simulation of Fe–Cr–Ni–Mo–C Duplex Stainless Steel Using CALPHAD–Coupled Multi–phase Field Model with Finite Interface Dissipation. In *Proceedings of the 4th World Congress on Integrated Computational Materials Engineering (ICME 2017)* 2017 (pp. 283–292). Springer, Cham.
144. Oba M, Nomoto S, Mori K, Yamanaka A. Development of Microstructure–Based Multiscale Simulation Process for Hot Rolling of Duplex Stainless Steel. In *Proceedings of the 4th World Congress on Integrated Computational Materials Engineering (ICME 2017)* 2017 (pp. 345–352). Springer, Cham.
145. Mecozzi MG, Sietsma J, Van Der Zwaag S, Apel M, Schaffnit P, Steinbach I. Analysis of the γ→ α transformation in a C–Mn steel by phase–field modeling. *Metallurgical and Materials Transactions A*. 2005 Sep 1;36(9):2327–40.
146. Yeon DH, Cha PR, Yoon JK. A phase field study for ferrite–austenite transitions under para–equilibrium. *Scripta materialia*. 2001 Sep 28;45(6):661–8.
147. Pariser G, Schaffnit P, I, Bleck W. Simulation of the γ–α-transformation using the phase-field method. *Steel research*. 2001 Sep;72(9):354–60.
148. Koyama T, Onodera H. Computer simulation of phase decomposition in Fe–Cu–Mn–Ni quaternary alloy based on the phase–field method. *Materials transactions*. 2005;46(6):1187–92.
149. Koyama T, Hashimoto K, Onodera H. Phase–field simulation of phase transformation in Fe–Cu–Mn–Ni quaternary alloy. *Materials transactions*. 2006;47(11):2765–72.
150. Tsukada Y, Shiraki A, Murata Y, Takaya S, Koyama T, Morinaga M. Phase–field simulation of nucleation and growth of M23C6 carbide and ferromagnetic phases during creep deformation in Type 304 steel. *Journal of nuclear materials*. 2010 Jun 1;401(1–3):154–8.
151. Malik A, Odqvist J, Höglund L, Hertzman S, Ågren J. Phase–field modeling of sigma–phase precipitation in 25Cr7Ni4Mo duplex stainless steel. *Metallurgical and Materials Transactions A*. 2017 Oct;48(10):4914–28.
152. Yeddu HK. Phase–field modeling of austenite grain size effect on martensitic transformation in stainless steels. *Computational Materials Science*. 2018 Nov 1;154:75–83.
153. Bhogireddy VS. *Phase Field modeling of sigma phase transformation in duplex stainless steels: Using FiPy–Finite Volume PDE solver* (Doctoral dissertation, KTH).
154. Zhu JZ, Liu ZK, Vaithyanathan V, Chen LQ. Linking phase–field model to CALPHAD: application to precipitate shape evolution in Ni–base alloys. *Scripta Materialia*. 2002 Mar 11;46(5):401–6.
155. Böttger B, Grafe U, Ma D, Fries SG. Simulation of microsegregation and microstructural evolution in directionally solidified superalloys. *Materials science and technology*. 2000 Nov 1;16(11–12):1425–8.
156. Kobayashi H, Ode M, Kim SG, Kim WT, Suzuki T. Phase–field model for solidification of ternary alloys coupled with thermodynamic database. *Scripta materialia*. 2003 Mar 17;48(6):689–94.
157. Qin RS, Wallach ER. A phase–field model coupled with a thermodynamic database. *Acta materialia*. 2003 Dec 8;51(20):6199–210.
158. Loginova I, Ågren J, Amberg G. On the formation of Widmanstätten ferrite in binary Fe–C–

phase–field approach. *Acta Materialia*. 2004 Aug 2;52(13):4055–63.
159. Wu K, Chang YA, Wang Y. Simulating interdiffusion microstructures in Ni–Al–Cr diffusion couples: a phase field approach coupled with CALPHAD database. *Scripta materialia*. 2004 Apr 1;50(8):1145–50.
160. Zhu JZ, Wang T, Zhou SH, Liu ZK, Chen LQ. Quantitative interface models for simulating microstructure evolution. *Acta materialia*. 2004 Feb 23;52(4):833–40.
161. Ohno M, Mohri T. Disorder–L10 transition investigated by phase field method with CVM local free energy. *Materials Transactions*. 2001;42(10):2033–41.
162. Poduri R, Chen LQ. Non–classical nucleation theory of ordered intermetallic precipitates—application to the Al–Li alloy. *Acta materialia*. 1996 Oct 1;44(10):4253–9.
163. Vaks VG. Microscopic derivation of Ginzburg–Landau–type functionals for alloys and their application to studies of antiphase and interphase boundaries. *Journal of Experimental and Theoretical Physics Letters*. 2002 Jul 1;76(2):93–8.
164. Llorca–Isern N, López–Luque H, López–Jiménez I, Biezma MV. Identification of sigma and chi phases in duplex stainless steels. *Materials Characterization*. 2016 Feb 1;112:20–9.
165. Zhang B, Jiang Z, Li H, Zhang S, Feng H, Li H. Precipitation behavior and phase transformation of hyper duplex stainless steel UNS S32707 at nose temperature. *Materials Characterization*. 2017 Jul 1;129:31–9.
166. Zhao Y, Sun Y, Li X, Song F. In–situ observation of δ↔ γ phase transformations in duplex stainless steel containing different nitrogen contents. *ISIJ International*. 2017:ISIJINT–2017.
167. Kim DC, Ogura T, Hamada R, Yamashita S, Saida K. Establishment of a theoretical model based on the phase–field method for predicting the γ phase precipitation in Fe–Cr–Ni ternary alloys. *Materials Today Communications*. 2020 Dec 3:101932.
168. Cahn JW. The kinetics of grain boundary nucleated reactions. *Acta metallurgica*. 1956 Sep 1;4(5):449–59.
169. Johnson WC, White CL, Marth PE, Ruf PK, Tuominen SM, Wade KD, Russell KC, Aaronson HI. Influence of crystallography on aspects of solid–solid nucleation theory. *Metallurgical Transactions A*. 1975 Apr 1;6(4):911.
170. K.Hirano: 'Goukin no Gikou Katei to sono Kaishaku', *Kinzokugakkai Seminar*, (1968), p.1–28 (in Japanese).
171. Nomoto S, Oba M, Mori K, Yamanaka A. Microstructure–based multiscale analysis of hot rolling of duplex stainless steel using various simulation software. *Integrating Materials and Manufacturing Innovation*. 2017 Mar 1;6(1):69–82.
172. Cahn JW, Hilliard JE. Free Energy of a Nonuniform System. I. Interfacial Free Energy and Free Energy of a Nonuniform System. III. Nucleation in a Two-Component Incompressible Fluid. *The Selected Works of John W. Cahn*. 1998 Sep 1:25–8.
173. J.E. Hilliard, Spinodal decomposition, in: H.I. Aaronson (Ed.), Phase Transformation, *American Society for Metals*, Ohio, 1970, pp. 497–560.
174. Koyama T, Onodera H. Phase–Field simulation of phase decomposition in Fe− Cr− Co alloy under an external magnetic field. *Metals and Materials International*. 2004 Jul;10(4):321–6.
175. Saunders N, Miodownik AP, editors. CALPHAD *(calculation of phase diagrams): a comprehensive guide*. Elsevier; 1998 Jun 9.

176. Dinsdale AT. SGTE data for pure substances. *Calphad*. 1991;15(4):317–425.
177. Miettinen J. Thermodynamic reassessment of Fe–Cr–Ni system with emphasis on the iron–rich corner. *Calphad*. 1999 Jun 1;23(2):231–48.
178. Hillert M, Jarl M. CALPHAD: ComputCoupling. *Phase Diagrams Thermochem*. 1978;2:227–38.
179. T. Koyama, Recent development and future perspective of phase–field method, *Mater*. Jpn. 42 (2003) 397–404.
180. Khachaturyan AG. Theory of Structural Transformations in Solids John Wiley & Sons Inc. *New York*. 1983.
181. T. Mura, Micromechanics of Defects in Solids, second rev. ed., *Springer*, New York, 1991.
182. Schaeffler AL. Constitution diagram for stainless steel weld metal. *Metal progress*. 1949;56(11):680.
183. 粉川博之, 岡田純二, 桑名武. 二相ステンレス鋼溶接金属の窒素吸収と組織. *溶接学会論文集*. 1992 Nov 5;10(4):496–502.
184. 小山敏幸. フェーズフィールド法に基づく組織形成シミュレーションとその材料開発への応用. *日本金属学会誌*. 2009;73(12):891–905.
185. Sietsma J, van der Zwaag S. A concise model for mixed–mode phase transformations in the solid state. *Acta Materialia*. 2004 Aug 16;52(14):4143–52.
186. K.J. Lee, K.B. Kang, J.K. Lee, O. Kwon, R.W. Chang, in: Int. Symp. Math. Model. Hot Roll. Steel, *Canadian Institute of Mining and Metallurgy*, Hamilton, Ontario, Canada, (1990) 435.
187. T. Gladman, in: N. Hansen, A.R. Jones (Eds.), Recryst. Grain Growth Multi–Phase Part. Contain. *Mater*., (1980) 183.
188. R.W.K. Honeycombe, in: *Proc. Int. Conf. HSLA Steel*, (1985) 243–50.
189. C.M. Sellars, in: HSLA Steels Metall. Appl., *ASM International*, (1986) 73–81.
190. F. Steinbach, F. Pezzola, B. Nestler, M. Seeßelberg, R. Prieler, G.J. Schmitz, J.L.L. Rezende, A phase field concept for multiphase systems, *Phys. D*. 94 (1996) 135–147.
191. J. Tiaden, B. Nestler, H.J. Diepers, I. Steinbach, The multiphase–field model with an integrated concept for modelling solute diffusion, *Phys. Nonlinear Phenom*. 115 (1998) 73–86.
192. B. Sundman, B. Jansson, J.–O. Andersson, The thermo–calc databank system, *Calphad*. 9 (1985) 153–190.
193. MICRESS®, Technical University of Aachen, n.d.
194. I. Steinbach, F. Pezzolla, B. Nestler, M. Seeβelberg, R. Prieler, G.J. Schmitz and J.L.L. Rezende, *Physica D*, 94 (1996) 135–47.
195. M.G. Mecozzi, J. Sietsma, S. van der Zwaag, Analysis of $\gamma \rightarrow \alpha$ transformation in a Nb micro–alloyed C–Mn steel by phase field modelling, *Acta Materialia*. 54 (2006) 1431–1440.
196. T. Koyama, Ferrum (*Bulletin of The Iron and Steel Institute of Japan*) 9 (2004) 240, 301, 376, 497,905.
197. Chen LQ. Phase–field models for microstructure evolution. *Annual review of materials research*. 2002 Aug;32(1):113–40.
198. Boettinger WJ, Warren JA, Beckermann C, Karma A. Phase–field simulation of solidification. *Annual review of materials research*. 2002 Aug;32(1):163–94.
199. A.A. Wheeler, W.J. Boettinger, G.B. McFadden, *Phys. Rev. A*, 45 (1992) 7424–39.

200. G. Gaginalp, *Phys. Rev. A*, 39 (1989) 5887–96.
201. S.G. Kim, W.T. Kim, T. Suzuki, *Phys. Rev. E*, 58 (1998) 3316–23.
202. Karma, *Phys. Rev. E*, 49 (1994) 2245–50.
203. Loginova, J. Odqvist, G. Amberg, J. Ågren. *Acta Mater*., 51 (2003) 1327–39.
204. C.J. Huang, D.J. Browne, S. McFadden*, Acta Mater*. 54 (2006) 11–21.
205. Karma, W.J. Rappel, *Phys. Rev. Lett*. 77 (1996) 4050–53.

Published or Accepted Papers in Regards to This Thesis

1. **Kim, D. C**., Ogura, T., Yamashita, S., & Saida, K. (2019). Hot Cracking Susceptibility and Solidification Segregation Analysis by Computer Simulation in Duplex Stainless Steels. *JAPAN WELDING SOCIETY*, *38*(2), pp.76–84.
2. Ogura, T., Matsumura, T., Yu, L., **KIM, D**., Inoue, H., Oikawa, Y., & Saida, K. (2019). Numerical simulation of ferrite/austenite phase fraction in multipass welds of duplex stainless steels. In *Mathematical Modelling of Weld Phenomena 12* (pp. 93–123). Verlag der Technischen Universität Graz Graz.
3. **Kim, D. C**., Ogura, T., Yamashita, S., Oikawa, Y., & Saida, K. (2020). Computer prediction of α/γ phase fraction in multi–pass weld of duplex stainless steel and microstructural improvement welding process. *Materials & Design*, *196*, 109154.
4. **Kim, D. C**., Ogura, T., Hamada, R., Yamashita, S., & Saida, K. (2020). Establishment of a theoretical model based on the phase–field method for predicting the γ phase precipitation in Fe–Cr–Ni ternary alloys. *Materials Today Communications*, 101932.
5. **Kim, D. C**., Ogura, T., Hamada, R., Yamashita, S., & Saida, K. (2021). Theoretical phase–field–method–based model of the γ phase dissolution of base metals in duplex stainless steels. *Materials Today Communications*, 102150.
6. **Kim, D. C**., Ogura, T., Hamada, R., Yamashita, S., & Saida, K. (2021). Prediction of reversible α/γ phase transformation in multi–pass weld of Fe–Cr–Ni ternary alloy by phase–field method. *Journal of Advanced Joining Processes*, 100067.

Presentations

1. **Dong–cho Kim**, SAIDA Kazuyoshi. 二相ステンレス鋼の凝固割れ感受性評価. 2019. 04. 17–19. Spring Conference of the Japan Welding Society, Tokyo, Japan
2. **Dong–cho Kim**, SAIDA Kazuyoshi. Hot cracking susceptibility in duplex stainless steel welds. 2019. 07. 07–12. IIW ANNUAL ASSEMBLY AND INTERNATIONAL, Bratislava, Slovakia
3. **Dong–cho Kim**, Shotaro Yamshita, Tomo Ogura and Kazuyoshi Saida, Prediction of reversible α⇄γ phase transformation in HAZ of multi–pass welded duplex stainless steel by the phase–field method. 2021. 04. 14–19. Spring Conference of the Japan Welding Society, WEB 開催（オンデマンド方式）